NORTHWESTERN UNIVERSITY

Revealing Vibronic Coupling and Coherence in Molecular Aggregates with Multidimensional

Spectroscopy: Experiment and Theory

A DISSERTATION

SUBMITTED TO THE GRADUATE SCHOOL

IN PARTIAL FULFILLMENT OF THE REQUIREMENTS

for the degree

DOCTOR OF PHILOSOPHY

Field of Chemistry

By

Jonathan David Schultz

EVANSTON, ILLINOIS

September 2022

Abstract

Revealing Vibronic Coupling and Coherence in Molecular Aggregates with Multidimensional

Spectroscopy: Experiment and Theory

Jonathan David Schultz

Quantum mechanical phenomena are playing tremendous roles in many areas of chemistry

and materials science research. In recent years, the potential role of coupling between electronic

and vibrational degrees of freedom in photochemical processes has been widely researched.

Despite its potential to improve molecular technologies, the lack of studies focusing on small,

highly controlled molecular systems has precluded efforts to harness vibrational-electronic

(*vibronic*) coupling. Understanding the generalized functions of and tunable parameter space for

vibronic coupling is vital for integrating molecular vibrations as a design element in next-

generation optoelectronic devices.

This dissertation focuses on investigations of vibronic phenomena in the photodriven

dynamics of model dimeric compounds. We begin in Chapter 4 by exploring the role of steric

hindrance between chromophores in driving changes to vibronic coherences in a series of

substituted perylenediimide (PDI) cyclophane dimers. Using a combination of two-dimensional

electronic spectroscopy (2DES) and femtosecond stimulated Raman spectroscopy (FSRS), we

report differences in wavepacket evolution between these systems that are attributable to sterically

driven distortions of the PDI cores.

Chapter 5 focuses on the vibronic mechanism of sub-50 fs singlet fission (SF) in a linear

terrylenediimide (TDI) dimer. We observed that ultrafast SF in this dimer is accompanied by the

transfer of low-frequency coherent wavepackets which, in conjunction with theoretical analysis of the vibronic eigenstates, reveals that interactions between low-frequency singlet modes and high-frequency correlated triplet pair motions lead to mixing of the diabatic electronic states. This work highlights how multi-mode vibronic couplings can impact ultrafast singlet fission.

In Chapter 6, we transition to a joint experimental and theoretical study of quantum beats in 2DES signals, which are well-known to provide direct insight into the intra- and interchromophoric couplings within a chemical system. We expand traditional theories to account for multiple Franck-Condon active vibrations and compared simulated spectra directly to experimental results from two organic semiconductors and biomedical dyes. We find that coupling between purely harmonic vibrational wavepackets can significantly impact signatures and interpretations of coherences measured by 2DES.

This dissertation contributes insight into the factors that can impact vibronic coupling in multichromophoric systems and the influence that vibronic coupling may have on photophysical dynamics in organic molecular assemblies. In addition, the analytical and theoretical tools developed for these studies serve as quality starting points for future researchers utilizing nonlinear spectroscopy to investigate quantum phenomena in chemistry.

Acknowledgements

Where do I even begin? I have anticipated writing this text for years, and it is an honor to finally be at this point in my career. Words cannot express how grateful I am to those that I have learned, laughed, celebrated, grown, and lived life with over the past 27 years. I am forever thankful to the wonderful people who have continued to support my passions and dreams over the years. The following is my attempt at the **impossible** task of expressing my gratitude to you.

My journey through education and science has been continuously fostered by countless teachers and mentors. I want to first thank Professor Michael Wasielewski for giving me the freedom to explore fascinating scientific questions and grow as an independent researcher over the last five years. I am lucky to have interacted with the extraordinarily wide range of chemistry that Mike and my fellow group members practice. Mike, I can hardly believe that five years have passed since I started in your group as a zero-year student! Thank you so much for all the opportunities and support that you have given me.

For the first three years of my graduate studies, I had the pleasure of working with Professor Mark Ratner and his group. Mark is one-of-a-kind. His care for people and passion for life are absolutely captivating. Thank you, Mark, for all your support and advice – I will never forget the smile on your face that I would inevitably see upon entering your office! You and your group fostered my interest in the theoretical side of physical chemistry, which is ultimately what I am pursuing next in my career! I would also like to thank Nancy Ratner for showing me such kindness, care, and support.

I would like to thank the members of my advisory committee, Professors Michael Wasielewski, Lin Chen, Emily Weiss, Roel Tempelaar, and Eric Weitz, for all their valuable help,

guidance, and support over the years. After many years of dreading the qualifying exam, I was pleasantly surprised that the event ended up being an engaging discussion with successful scientists that treated me with respect. I am grateful for the time that my committee members have invested in helping me become an independent researcher.

I am very grateful to Professor Ryan Young, who I have worked extensively with in Mike's lab. Ryan, your unwavering interests in fundamental chemistry and my growth as a scientist have been constant resources for me throughout my graduate career. Thank you for everything that you do to support students and maintain a functioning lab! On a similar note, I want to thank Professor Kevin Kohlstedt for his continuing support and interest in my research.

While in Mike's group, I had the opportunity to learn from several wonderful and talented postdoctoral researchers. Thank you, Dr. Eileen Foszcz, for your incredibly hard work in establishing Femto C! Because of you and Aritra, I was able to dive into 2DES measurements right away in my graduate tenure. Speaking of Aritra, I cannot possibly thank Dr. Aritra Mandal enough for all his support, camaraderie, teachings, and advice. Aritra, I cannot imagine graduate school without you! You taught me so much and pushed me (a healthy amount!) to become an independent researcher. I will forever value our friendship and the time we got to work together! I should also note that I have continued to spread *many* elements of advice that you shared with me over the years to other students and colleagues. We all appreciate your guidance.

I had the pleasure of meeting Dr. Taeyeon Kim in New Zealand at the 2019 Time-resolved Vibrational Spectroscopy (TRVS) conference. Little did I know that we would end up becoming colleagues and great friends a year and a half later (academia is truly a small world)! Taeyeon, you have been a constant source of sanity for me since you arrived in Evanston. From jamming to *Juice*

Wrld in the office to revolutionizing our wavepacket signatures and time resolution, I have sincerely enjoyed every moment of our time together! It is bittersweet leaving, but I know we will continue to stay in contact (and perhaps collaborate)! Again, thank you so much Taeyeon.

The work that I discuss in this dissertation would not have been possible without the expertise and generosity of numerous individuals that synthesized the molecules that I studied! Dr. Adam Coleman, Jeremy Fisher, Dr. Michelle Chen, Dr. Xingang Zhao, and Jillian Bradley dedicated countless hours in the wet lab to making exotic new molecules that I had the pleasure of characterizing. The collaboration between chemical synthesis and advanced experimental techniques forms the backbone for this dissertation, and I am truly grateful to these talented researchers and their generosity. Dr. Adam Coleman is the mastermind behind the series of perylenediimide dimers that were in the spotlight of my qualifying exam and eventually led to my first publication (Chapter 4). Jeremy Fisher has worked tirelessly in our pursuit to understand quantum interference phenomena in ultrafast electron transfer research, and although these results are not featured in this dissertation, I have no doubt that we will share our findings with the world very soon! Dr. Michelle Chen and Dr. Xingang Zhao paved the way for numerous studies of the fascinating photophysics that their terrylenediimide-based compounds exhibit (Chapters 5 and 6). The compounds that they selflessly shared with me became the subjects of my first joint experiment-theory works, of which I am particularly proud. I also want to thank Jillian Bradley for your hard work in synthesizing compounds for us to explore with our most complex experiment on Femto C! Last, but not least, thank you Dr. Nikolai Tcyrulnikov for your unwavering willingness to help me and others purify and characterize compounds for our own research projects.

I would like to express a tremendous thank-you to Professor Roel Tempelaar for all his support and enthusiasm for science and teaching. A quick glance at the References in this dissertation illustrates the extent to which I have followed and learned from Roel's research publications. After I had already been studying his papers for years, the intertwined nature of academia truly became clear to me when Roel started as an assistant professor at Northwestern! During the pandemic, Roel graciously met with me for hours over Zoom to answer my unending questions about response functions, spectral simulations, and model Hamiltonians. Thank you so much Roel for all your help – you have played a substantial role in my passion for theoretical chemistry research!

Graduate school is a turbulent time filled with constant ups and downs and everything in between. I cannot thank my colleagues at Northwestern enough for all the friendship and support that they have given me. Within the Wasielewski group, I am so thankful to have worked alongside and mentored James O'Connor, Karen Ji, and Jeremy Fisher. You are all skilled scientists and wonderful people! I have truly enjoyed watching you all grow as researchers, and I cannot wait to attend your Ph.D. defenses! Thank you to Dr. Leighton Jones and Professor Martin Mosquera for all your help with DFT computations and theoretical chemistry in general. I cherish all the fun times that we had at the Celtic Knot and Whiskey Thief Tavern in downtown Evanston! Thank you to Dr. Gyeongwon Kang for all your help and guidance in calculating resonance Raman spectra (Chapter 5). Thank you to my fellow classmates of 2022, Dr. Laura Bancroft and (soon-to-be Dr.) Haochuan Mao, for embarking on this graduate school journey with me all the way back in 2017. I have also very much enjoyed working alongside Dr. Carolyn Ramirez and (soon-to-be Dr.) Yue Qi over these past few years. Thank you to Dr. Brian Phelan for the countless hours over

which we discussed and investigated coherent electron transfer. Cryogenic liquid helium experiments are incredibly challenging and tiring, but Brian still managed to bring some fun to them. Thank you, Dr. Itai Schlesinger, for sharing your expertise with me and everyone else around you! I very much appreciate your fascination with life and the universe at large, as well as the many hobbies for which you and I share interest. Thank you, Dr. Jordan Nelson, for teaching me everything I know about Linux and maintaining a computational cluster. You taught me the value of being confident in myself to scour manuals and forums on the internet and find solutions to the relentless complexities of Linux.

The members of the Wasielewski group have helped me in *so many* ways that it would take an additional chapter to do them justice. I want to extend my gratitude to Dr. Youn Jue Bae, Dr. Jenna Logsdon, and Dr. Brian Phelan for all the fun times we had as officemates! I also thank Paige Brown, Malik Williams, Emmaline Lorenzo, Leanna Kantt, Chenjian Lin, Oscar Huang, Dr. Natalia Powers-Riggs, Dr. Samantha Harvey, Dr. Su Chen, Dr. Joaquin Alzola, Colin Tichvon, Hannah Eckvahl, Elisabeth Latawiec, Jon Palmer, and Professor Matthew Krzyaniak for your friendship, kindness, and support. A HUGE thank you to the group administrators that have supported the Wasielewski group in countless ways over the past five years, Amanda Mahoney Clybor, Melanie Sandberg, and Corey Drennon! Amanda is one of the most thoughtful, genuine people I have ever had the pleasure of meeting.

The friendships that I am lucky to have forged with people beyond the Wasielewski group have been vital to my mental health over the past five years. Thank you so much to Waleed Helweh for all the delicious food, fun times, and warm hugs that we have shared in our journeys together! I also would like to thank Dr. Megan Wasson, Sylvia Hanna, Kenton Hicks, Dr. Tim Goetjen, Dr.

Meghan Ward Dukes, Megan Kaster, Craig Laing, Nick Weingartz, and Dr. Shawn Zhao for your camaraderie and all the wonderful memories!

Shortly before the 2020 pandemic lockdowns, Mike and Ryan provided me the opportunity to travel to Duke University for a meeting with the Center for Synthesizing Quantum Coherence (CSQC). This trip sparked two years of productive conversations about coherence and collaborations, along with new friendships and mentors! Thank you to Dr. Jonathon Yuly, Dr. Kelsey Parker, Reshmi Dani, Sohang Kundu, Kaydren Orcutt, Professor Peng Zhang, Dr. Eric Arsenault, Zachary Widel, Niven Singh, Zhendian Zhang, Kai Liu, Sutirtha Chowdhury, Jesus Valdiviezo, and Kiriko Terai for all the fun conversations and fascinating science we have worked on together! My association with the CSQC ultimately revealed to me the path that I will be embark on following the conclusion of my Ph.D.: working with Professor David Beratan at Duke University! Thank you so much David for your passions for people and science alike. I deeply admire your spirit and am grateful to know and work with you.

My desire to pursue a Ph.D. originated at the University of Minnesota-Twin Cities (UMTC), where I did my undergraduate studies. I am so grateful to Professor Kenneth Leopold of the UMTC Department of Chemistry. I entered his undergraduate general chemistry classroom in the fall of 2013 with little interest in pursuing chemistry. To my surprise, Professor Leopold's course immediately captivated me. Thank you, Professor Leopold, for all the time you spent discussing chemistry with me during your office hours. My passion for physical chemistry was first sparked by you!

I am lucky to have worked with so many outstanding faculty mentors in the UMTC Chemistry department. Professor Lee Penn, thank you for accepting me (an inexperienced

sophomore) into your research lab in the fall of 2018. Before working with you, I had very few ideas of what scientific research involved. You opened my eyes to the fun and excitement of academic research! While working with Lee, I had the pleasure of working alongside my first graduate student mentor, Dr. Jennifer Strehlau, who I cannot thank enough for all that she did to help me become an independent researcher. Thank you, Jen!

I owe a tremendous thank-you to Professor Renee Frontiera for helping me solidify and pursue my passion for physical chemistry. I am grateful to Renee for her trust in me as an undergraduate student to work with intricate and expensive laser spectroscopy equipment in her research lab. My confidence as a researcher and questioner soared during my time in Renee's group. Thank you, Renee, for your unwavering support and kindness over the past decade! I cannot imagine what I would be doing in life without your guidance and help.

Thank you, Professor David Blank, for your dedication to teaching and helping students find their paths in life. Your advice continues to resound in my mind and steer my life to this day. As an undergraduate, I also had the pleasure of working with Professor Ben Lear at the Pennsylvania State University. Thank you, Ben, for your enthusiasm for science and for people! My summer at Penn State is such a positive memory for me, for which I have you to thank!

Teaching and helping others are passions that keep me moving in life. I have had the outstanding opportunity to professionally develop these passions through Northwestern's Searle Center for Advancing Learning and Teaching. Thank you so much to Dr. Nancy Ruggeri, Kate Flom Derrick, and Dr. Katie Pierson for always believing in me and bringing me so many opportunities to grow as a teacher. Thank you to the Searle community at large (especially Dr. Bethany Sump, Janine Chow, Warren Snead, Keary Watts, and Dr. Grace Bellinger) and the

Northwestern Chemistry teaching faculty, Professors Katie Gesmundo, Stephanie Knezz, and Veronica Berns, for equipping me with the skills I need to help others find and pursue their own passions. In addition to all these marvelous individuals, I would also like to thank Dr. Youn Jue Bae, Hasan Munshi, Felicia Ko, Jonic Zhehao Zhu, Professor Chad Mirkin, and Professor Sarah Hurst Petrosko for your extensive help in realizing my graduate teaching fellowship project, from which I gained lots of valuable experience in both teaching and science education contexts.

The last five years have taught me the vital importance of mental health, which my growing appreciation for has incredibly shaped my personality and outlook on life. I have so many people and resources to thank in this regard, but most importantly, I want to thank Dr. Ann Kogen, who I have conversed extensively with for five years. Ann has helped me overcome some of the greatest internal challenges of my life and has helped me clarify my values and dreams in life. On a lower level, I want to thank the comfort that Bob Ross and his show "The Joy of Painting" have brought me over the past two hectic years. Bob, your positive outlook on life and passion for helping people find happiness continue to resonate with me.

I am so grateful to all my amazing friends that I have made over the years. I want to extend a special shout-out to my cohort that helped me maintain sanity through the chemical engineering program at UMTC. Ethan Loosbrock, Jon Morris, Dr. Steph Hart, Dr. Grant Marsden, Eric Madsen, Prakash Paul, Matt McClannahan, Heather Fong, Elizabeth Drantch, and Madeline Hanson, you all have a special place in my heart. I am so thankful to have you all in my life. Thank you to all of you, as well as Alex Najafalipour, Colin Lake, Shefali Jain, and Dawn Duan, for the years of friendship and beautiful memories that we have and will continue to forge together!

Above all, I want to thank my family for everything they have done to support me throughout my life. I am so fortunate to have been raised by my loving parents alongside my two brothers, Christopher and Jacob. Christopher, you taught me the importance of empathy and being thankful for what I have. Though you left this life early, you continue to shape my life every single day. Jacob, I am so lucky to have such a fun younger brother like you. When I am feeling stressed out, I know that I can always contact you for some laughs and a relaxing night of video games! You are well on your way to becoming an adult and I cannot wait to see all the amazing places you go in life. My extended family, *especially* my loving grandparents, Bill and Kay Ward and Beverly and Gene Schultz, have and always will be sources of joy and comfort for me. I cannot thank you all enough for the everlasting love and support you give me.

Though they likely will not read this document (but who knows what technological advances will bring about), I am deeply thankful for my precious cats, Ziti and Gnocchi. They are my children at heart, and I cannot imagine how the last couple of years would have been without the laughter, cuddles, and love that they bring to our family. On this note, it is about time that I thank my wonderful, extraordinary life partner, Jenny Wang. Of all the positive aspects that emerged from my time at Northwestern, my relationship with Jenny is by far the greatest. Jenny, I cannot put into words the comfort, joy, happiness, understanding, and love that you give me. In this crazy life and universe, I know I can always find peace with you. I also want to thank Jenny's family for welcoming me into their lives and continually supporting Jenny and me! A huge shout out to Guifang (Jo) Xu, who opened my eyes to so many delicious foods!

I am indescribably grateful to my parents for all their love and support. Thank you, Dad, for always believing in and rooting for me. I am so proud of your own progress over these past

five years and am so thankful to have you in my life. Thank you, Bob, for loving and supporting me as your own son. Your and mom's generous financial support is the very reason that I was able to attend UMTC and discover my passions for chemistry in the first place. No matter what happens in life, I know that I have your support.

Last, *but certainly not least*, I want to thank my extraordinary mother. My mother means the world to me, and I cannot put into words the extent to which she brightens my life. My mother is my role model. She has overcome an unbelievably long list of obstacles and has truly found herself. Mom, I think I speak for everyone else when I say ***thank you*** for your selflessness, generosity, and warmth. You are a glowing soul on this Earth, and I am so lucky to have you in my life. I love you so much and thank you for your unconditional support, understanding, advice, respect, and love. Your presence in my life over the past 27 years has truly set me on a course for happiness, and for that I am forever grateful.

Preface

As an aspiring physical chemist, I have invested appreciable time into studying the meaning, effects, and implications of *coherence*. Still, I find myself questioning others' and, quite frankly, my own usage of the word. Coherence phenomena have a long and ever-expanding history in the context of chemistry, yet much progress remains to be made in harnessing coherence as a system design parameter. This lag in realizing chemical and material applications of coherence is thought to be, at least in part, attributable to issues of science communication. Professor Tomáš Mančal wrote in 2020[1] that

> "*...critical assessment of the problems of communication between different scientific disciplines would deserve an attention of the sociologists and philosophers of science, as well as those responsible for its funding and management.*"

I would like to preface this dissertation with special attention to interdisciplinary science communication. Research throughout the fields of science, technology, engineering, and mathematics (STEM) is evolving to address questions that are increasingly broad in scope and disciplinary breadth. As Professor Mančal stated, promoting, exercising, and enforcing effective science communication are responsibilities shared not only by researchers, but with funding organizations and those leading scientific research. Those devoted to the advancement of STEM must prioritize clear *and* accurate communication, especially when interfacing with funding agencies and policymakers.

To the best of my ability, I have written this thesis to uphold these standards and offer something to all readers, regardless of background. Chapter 1, especially the first two sections, is written with special attention to accessibility. The connections between coherence and chemistry are vast in scope and can be extremely nuanced at times, but the big picture is always important to

keep in mind. I implore all readers to feel free to contact me with any questions that they may encounter.

Dedication

I dedicate this thesis to my loving mother.

You have and will always be my hero.

Table of Contents

List of Figures

List of Tables

Chapter 1: Introduction

1.1. Solar energy: Prospects and mechanisms

An age-old dream of scientists and engineers is to harness one of the most widely available and sustainable sources of energy: the sun. Ancient humans used the sun to make fire and light their homes with mirrors. Today, photovoltaic (PV) cells collect sunlight and convert it into electricity that we can use in our homes and store for later. While solar technologies have evolved tremendously since their conception, their efficiency in harvesting and repurposing energy from the sun remains a bottleneck in their development.[2] Current silicon-based photovoltaics are intrinsically limited to a maximum of ~34% efficiency due to their narrow bandgap in comparison to the broad solar spectrum.[3] This barrier severely hinders the development of solar devices capable of rivaling the efficiency and economics of fossil fuel-driven processes. To circumvent the limitations plaguing current technologies, new photovoltaic materials and strategies are required.

Recent years have seen enormous advances in numerous photovoltaic frameworks. A particularly notable platform is organic photovoltaics (OPVs), which continue to climb rapidly in record efficiency (greater than 17% as of 2020).[4] Unlike silicon, OPV systems feature cheap solution processability, a range of mechanical properties, and most importantly, a virtually unlimited playground of molecular pairings.[2, 4-7] The expansive tunability of OPVs and the exotic photophysics that they exhibit offer many channels that may enable OPVs to circumvent the ~34% efficiency limit constraining silicon devices.

An essential step toward advancing any methodology for harvesting solar energy is a mechanistic understanding of what occurs following excitation via sunlight. There are a daunting number of factors that govern the efficiency of an OPV cell.[4, 6, 8] Many key characteristics can be

traced back to fundamental chemical properties of the materials that compose the solar cell.[9] Therefore, building a thorough understanding of how material properties impact solar energy conversion and leveraging this knowledge to guide the design of highly efficient OPV devices is imperative. One approach to examine the chemical properties and behaviors of photovoltaic materials is to *watch* them in real time as they facilitate energy conversion. When light is shined on a solar cell, the material within the cell absorbs some of the light, leaving one or more molecules in an excited state, as represented by (1) in Figure 1.1. This deposited energy takes the form of an *exciton*, which is a bound electron and hole pair. The exciton must then (2) migrate through the device to a region where it can be (3) separated into free charge carriers (unbound electrons and holes) that are ready for collection (4).[2, 9] Once collected, these charge carriers can be used to supply electricity.
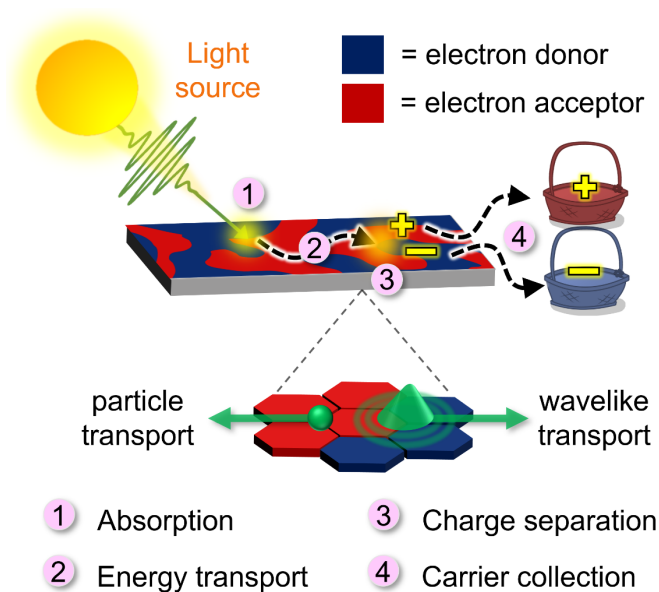
Figure 1.1. Cartoon schematic of the four key processes that underlie solar energy harvesting: energy absorption, energy transport, and charge separation to harvestable charge carriers within photovoltaic materials and devices.

The first three processes numbered in Figure 1.1 often transpire on extremely short timescales, sometimes on the order of a millionth of a billionth of a second! Adding additional complexity, sunlight covers a broad energy spectrum ranging from high-energy ultraviolet rays to low-energy infrared light.[10] Due to the vast ranges of relevant wavelengths of light and short time scales, advanced experimental methods and theoretical tools are key to forming a complete picture of efficient energy conversion. In this regard, ultrafast spectroscopy[11] offers an incredibly useful toolset for illuminating the inner workings of excitation dynamics in OPVs.

The term *spectroscopy* derives from the words *spectron* (Latin for ghosts) and *skopein* (Greek for *to see* or *to look in*).[12] Spectroscopic techniques offer insight into a chemical system by measuring that system's response (ghosts) to incident light. To date, a vast number of optical spectroscopies, both steady-state and time-resolved, are performed across an extraordinarily wide range of scientific disciplines. In the context of light harvesting, time-resolved spectroscopy affords a direct view of how, following photoexcitation, non-equilibrium groups of chromophores transport and manipulate energy in an effort to return to equilibrium.[13] Many techniques, especially those with high time resolution, rely on pulsed laser light to mimic the effects of incident sunlight on chemicals and materials while maintaining several handles of experimental control in the lab. Such techniques commonly provide rich structural and dynamical information about systems ranging from single atoms and molecules[14] to bulk materials.[15]

Substantial evidence provided by ultrafast spectroscopy suggests that light-harvesting organisms in nature have evolved to take advantage (in some capacity) of *quantum coherence* to boost their effectiveness in harnessing sunlight. While abstract-sounding, we all experience the concept of *coherence* in our daily lives. Coherence is known by many definitions in and outside

of the scientific community, but in general, coherence plays a role whenever two or more organisms, sounds, motions, signals, etc. are synchronized with each other. In our experience, we know coherence to be a convenience, which facilitates communication with each other and our interaction with the world. On the scales of molecular processes, coherence may offer conveniences that extend to the macroscale world.

The possible connections between coherence and biological organisms have been explored extensively over the past several decades.[1, 16] This flavor of research is focused on the increasingly fleeting details of how coherence between neighboring molecules can affect their collective behavior, such as in harvesting light and transporting energy. Chemists have developed countless strategies over hundreds of years figuring out how to manipulate materials at the smallest scales. Such tools are motivating researchers to leverage knowledge of molecular design to elucidate and control coherence in synthetic systems.[17-19]

1.2. Coherence: concepts and contexts

Adding more specificity to our definition, *coherence refers to temporal and/or spatial correlations between two waveforms.*[13, 16] These correlations are often discovered by generating interference patterns in an observation of the waveforms. For example, suppose you toss a stone into a pond. Contact between the stone and the water creates ripples, which travel radially outward and away from the point of contact (Figure 1.2). Now imagine you toss two stones (stone *a* and stone *b*) into the pond, thus creating two individual sets of ripples. The relationship between the ripples created by stones *a* and *b* refers to their coherence with each other.
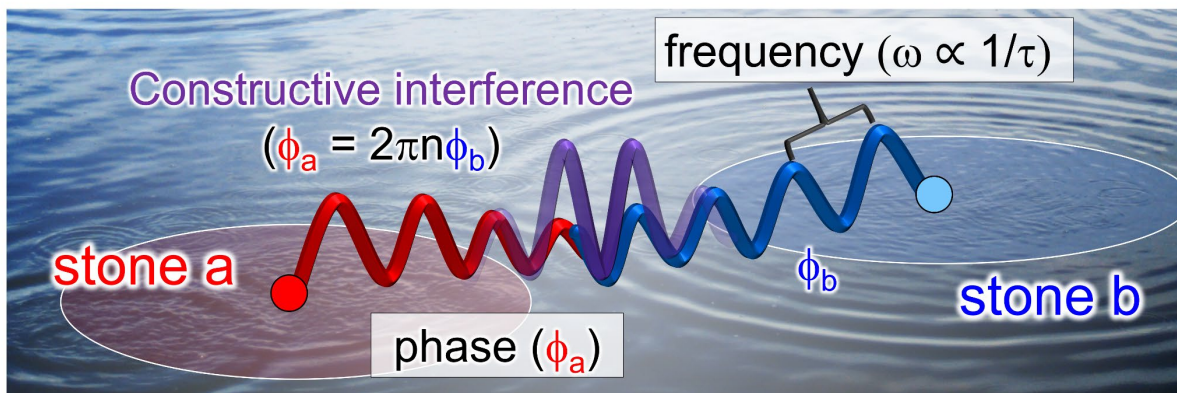
Figure 1.2. Key concepts relating to waves and coherence depicted in the context of ripples on a pond. If two stones (*a* and *b*) are tossed into the water, they will both launch ripples that expand radially away from the entry point of the stone. These sets of ripples are both described by amplitudes (which are related to the energy that the stone imparts upon the water), frequencies (which represent how quickly a wave is oscillating up and down), and phase (which is a constant value that serves as a reference point when discussing how two or more waves relate to each other). When two waves are "in-phase" with each other (i.e., their phases are related by a factor of 2π multiplied by any integer *n*), they can constructively interfere if they overlap in time and space.

In general, interactions between two or more "things," such as ripples on a pond, can *create* coherence or, in other words, be coherent with each other. This remains true for interactions at the molecular scale. As shown on the left of Figure 1.3, when molecules are positioned near each other in space, their electrons can couple to create *coherent superpositions*, or configurations that resemble mixtures of both electrons (for example, think of localized atomic orbitals versus delocalized molecular orbitals). In the case of two sources of ripples in a pond, superpositions occur when the ripples overlap in space and time, which creates new waveforms. Similarly, electronic superposition states often exhibit substantially different chemical properties and behaviors compared to the non-interacting constituents, which is very exciting because these differences can be directly tuned by parameters such as the intermolecular distances and angles, as well as individual molecular structure.
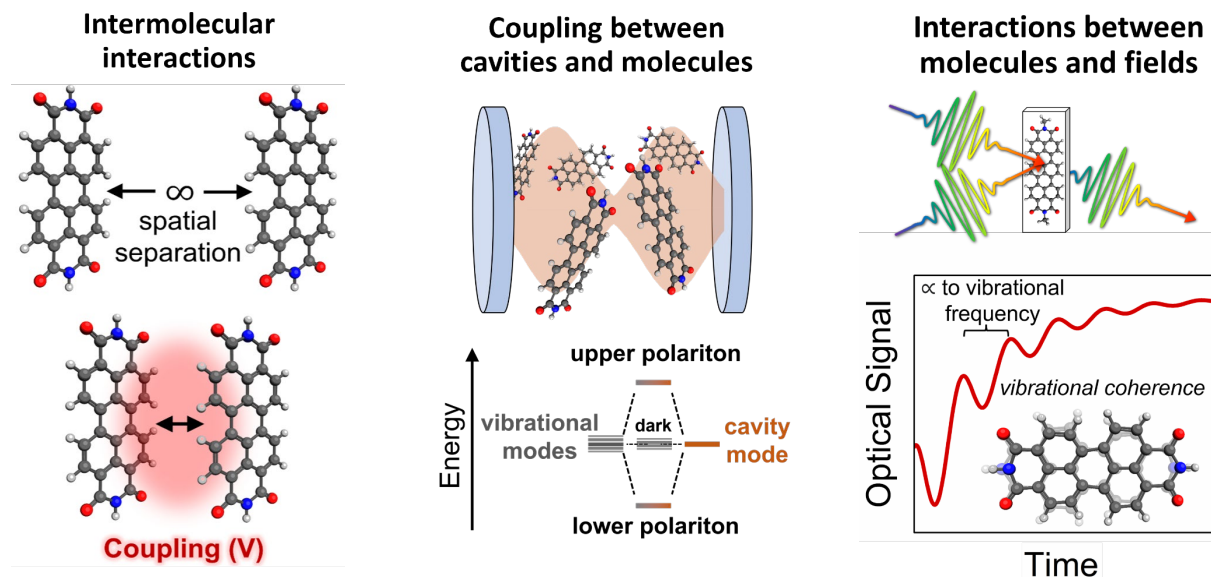
Figure 1.3. Schematic examples illustrating how interactions between molecules and other molecules (left), molecules and macroscopic objects (middle), and molecules and electromagnetic radiation (right) can create coherence.

Coherence can also emerge from interactions between molecules and macroscale objects, such as the cavity shown in the middle of Figure 1.3. Cavities, which can be thought of as mirrors positioned so close together that they support only particular frequencies of light in the space between them (we refer the reader elsewhere[20] for further information), can couple to molecular excitons and vibrations to produce hybridized states (called *polaritons*). In this case, since the cavity is a macroscale object, we can directly engineer its characteristics, such as distance between the walls, to vary the cavity-molecule coherence and steer the resulting chemistry. Similarly, as shown on the right of Figure 1.3, molecules also interact with light sources to create coherence, which is a phenomenon that is often used to measure coherence effects in chemistry (*vide infra*, Section 1.5). In this example, coherence between ultrashort laser pulses and molecular vibrations can lead to oscillations in signals detected experimentally, which can be detected and analyzed to understand chemical properties such as structure and coherent reaction dynamics.

On the other hand, interactions can destroy coherence. Imagine again that we are interested in the coherence between two sets of ripples on a pond (Figure 1.2). If the pond and the air above are both perfectly still, we should be able to observe the coherence between the ripples with high accuracy. However, if the wind begins to blow and apply force to the ripples, or if additional stones are thrown into the pond at a similar time and place, we will very quickly lose a sense of the coherence between our original two sets of ripples. The wind and additional stones are both analogous to what physical chemists call *the bath*, which is the complex environment that surrounds a system of interest. For example, a chemical dissolved in solvent is encapsulated by a vast, disordered sea of solvent molecules, which becomes increasingly complicated at higher temperatures (i.e., room temperature).

Interaction between a molecular system and the surrounding bath is well-known to destroy coherence. In Figure 1.4, the system on the left represents two coupled chromophores isolated in spacetime, where their coherence is maintained. In contrast, the two chromophores on the right of Figure 1.4 are surrounded by solvent molecules and irradiated with light, which both interact with the chromophores and erase the coherence between them.
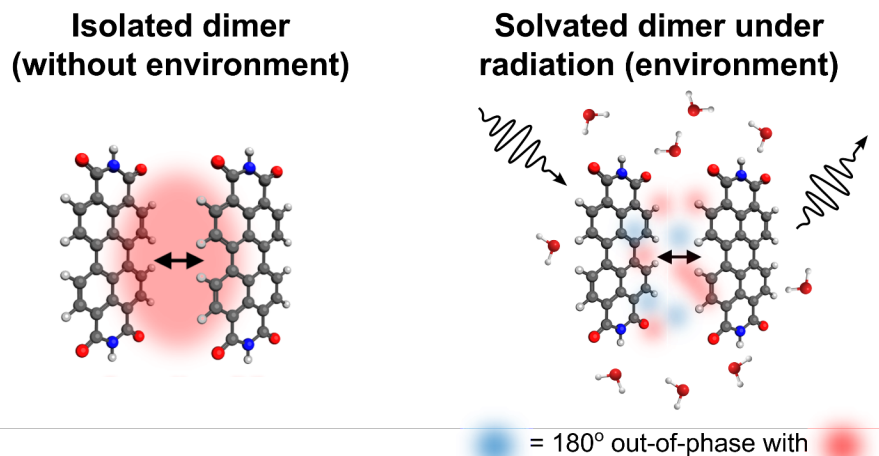
Figure 1.4. A schematic comparing a coupled molecular dimer that is isolated (left) versus solvated and subjected to irradiation. Blue glow represents waveforms that are 180° out-of-phase with red glow.

1.3. Quantum coherence

Quantum mechanics famously posits a wave-particle duality of matter. Many features of waves such as phase and linear superposition are intrinsically connected to coherence phenomena, which immediately suggests that coherence concepts might play a role in quantum mechanical processes. Coherence in the context of chemistry is typically used to indicate correlations between either (1) *signals emerging from a system* or (2) *the state of components within a system*. The system in this case could be an isolated molecule, or an ensemble of molecules surrounded by a thermal bath.

To see the emergence of coherence in quantum mechanics, we now delve a bit deeper into the mathematical formalism. All physical states of a quantum system belong to a vector space (Hilbert space) denoted as $\boldsymbol{H}$. For instance, let us define the set $B = (\phi_1, \phi_2, ..., \phi_n)$, which contains n distinct states (ϕ_n) that encompass all possible outcomes of a specific physical observable (e.g., position, spin angular momentum, etc.) measured from the quantum system. In this case, B is said

to be an *orthonormal basis* of **H**. Importantly, quantum mechanics tells us that *any possible state*

of the system may be expressed as a *superposition of states* in *B*. Using Dirac's bra/ket notation,[21]

a general wavefunction of the system (Ψ) is therefore written as a sum over these states:

$$|\Psi\rangle = \sum_n c_n |\phi_n\rangle \qquad \text{Eq. 1}$$

The coefficients c_n are in general complex numbers and represent the overlap between Ψ and a

particular ϕ_n discrete state. The coefficient c_n is also connected to the probability for observing the

system in state ϕ_n when *B* is measured, which is given by Born's rule

$$P_n = |\langle\phi_n|\Psi\rangle|^2 = |c_n|^2 \qquad \text{Eq. 2}$$

Eqs. 1 and 2 describe the hallmark superposition principle of quantum mechanics, which is

intrinsically connected to many usages of the term quantum coherence.

To illustrate the connection between superposition and quantum coherence, let us consider

a generic two-state system. In this example, we are not introducing time evolution, but rather

focusing on instantaneous snapshots of the system wavefunction (or perhaps initial conditions). In

this two-dimensional Hilbert space, we can express the total wavefunction at any given time using

the following form:

$$|\Psi\rangle = c_1|\phi_1\rangle + c_2|\phi_2\rangle \qquad \text{Eq. 3}$$

An equivalent picture to describe the wavefunction of Eq. 3 as a density operator[22] is

$$\hat{\rho}_\Psi = |\Psi\rangle\langle\Psi| = c_1{}^2|\phi_1\rangle\langle\phi_1| + c_2{}^2|\phi_2\rangle\langle\phi_2| + c_1{}^*c_2|\phi_1\rangle\langle\phi_2| \qquad \text{Eq. 4}$$
$$+ c_2{}^*c_1|\phi_2\rangle\langle\phi_1|$$

The coefficients of the first two outer products in Eq. 4 give us the probabilities of observing the

system collapse into either of the pure states ϕ_1 and ϕ_2 as $c_1{}^2$ and $c_2{}^2$, respectively. These outer

products are often called populations, referring to the fact that they represent the probability

density associated with a single state. In contrast, the latter two outer products in Eq. 4 each contain

a mixture of ϕ_1 and ϕ_2 and take the form of interference terms with complex coefficients $c_1{}^*c_2$ and

$c_2{}^*c_1$. These outer products are thus referred to as coherences. It is important to note that the

interference phenomenon exemplified by Eq. 4 emerges directly from the superposition principle

in quantum mechanics. The diagram in Figure 1.5, which is adapted from Young's classic double

slit experiment, illustrates how the coherence terms in Eq. 4 lead to an interference pattern

observed on the detector if an entity with wave-like nature passes through both slits 1 and 2 (as

opposed to the single peaks on the detector that emerge from the non-interfering population terms).
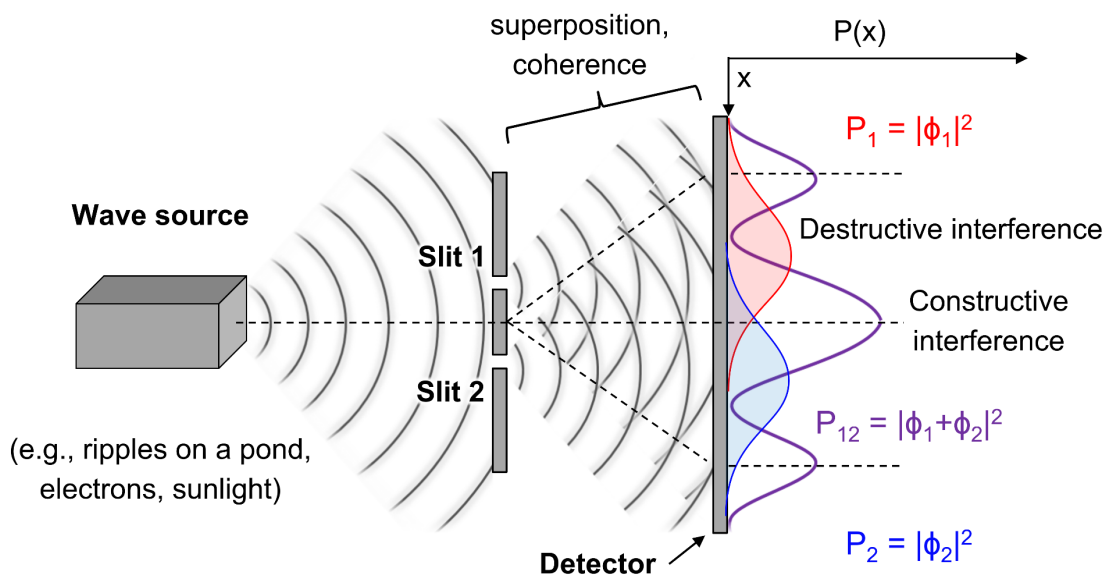
Figure 1.5. A schematic detailing Young's famous double slit experiment, in which the observation of an interference pattern on a spatially resolved detector (right) signifies the wave character of the entities emerging from the source (left).

We have now arrived at a common framework associated with the term quantum

coherence: *quantum coherence involves a coherent superposition between two or more quantum*

states that results in interference determined by their relative phase. Some works refer to the

specific case of superposition between local states (or standing waves) as *state coherence*.[13, 23] This

picture becomes increasingly complex as we consider additional aspects, such as time-dependence, initial condition, and *basis of representation*. The latter consideration is especially troublesome as the off-diagonal density matrix elements are completely dependent on the basis of representation. A change of basis does not reflect any change in the physical state or dynamics of the system (provided the change of basis is consistently applied to all operators and vectors), and changing basis is routinely performed to simplify mathematical expressions or clarify approximations. A common change of basis occurs when one rotates from a "local" basis to the energy eigenstate basis[16] (which is often delocalized), as in the molecular exciton example in Section 1.4.2. While changing basis is allowed and often beneficial for rationalizing quantum systems, communication surrounding quantum coherence as off-diagonal elements is completely meaningless without the specification of a particular basis, as there almost always exists a basis in which coherence terms are present.[1] This ambiguity is similar to reporting the position of an object but not specifying an origin or point of reference against which that position is measured.[24]

1.4. An overview of coherence research in chemistry

Research of coherence phenomena in chemistry has an extensive history that continues to expand as experimental and theoretical tools provide deeper perspectives into chemical reactions. For example, the advent of nuclear magnetic resonance (NMR) spectroscopy nearly 90 years ago[25,26] sparked widespread efforts to use coherent fields of light to launch and probe unitary evolution of nuclear spins. As is true for modern-day NMR and many other spectroscopic experiments, the purpose of this capability was to uncover information about the chemical properties (e.g., electron shielding and spin-spin couplings in the case of NMR) of molecular systems. On the other hand, many have sought to use the coherence of classical light fields not only to *probe* chemical

dynamics, but to *steer* and *control* them.[27-32] The distinctions *and* connections between how these, and other, coherence contexts enter the realm of chemical research are key to forming meaningful hypotheses and productive research directions. This section aims to explore these distinctions and connections in action through case studies spanning numerous facets of chemical research. We recognize our limited abilities to address all corners of coherence research in chemical contexts and reiterate that these sections are not exhaustive.

1.4.1. External control of quantum coherence

Coherent control is a facet of coherence research in chemistry that has persisted in some form (*vide infra*) over 80 years. Early works in the field of coherent control focused on driving particular chemical reactions through the selectivity of molecular vibrations.[27-32] However, as several references[27, 29, 32] discuss in great detail, the often-unavoidable process of intramolecular vibrational redistribution (IVR) hindered this direction. Recognizing the possibility of harnessing quantum interferences through theories of optimal control,[27, 33] the objective of coherent control shifted to manipulating chemical reaction dynamics using precisely controlled, coherent laser light. In other words, this approach to controlling reactivity aims to impart the coherence of classical electromagnetic fields onto the unitary evolution of quantum mechanical systems, which in turn directs reactivity. The nature of the coherent laser light is therefore a defining characteristic for coherent control schemes. For example, Brumer and Shapiro[31] suggested that using properties of narrowband laser fields (continuous-wave or temporally long)[34] to manipulate the superposition state that is initially prepared by exciting degenerate, optical transitions can theoretically translate to manipulation of the branching ratio between the ensuing reaction pathways. A myriad of additional control schemes were proposed and are discussed at length elsewhere.[11, 34, 35]

Methods of coherent control based on ultrashort laser pulses became particularly enticing as the field of femtochemistry progressed.[11] In general, heightened motivations for coherent control research ensue upon advancements in methodologies *to probe* coherence. In [Section 1.5](#), we discuss how spectroscopic techniques enable characterization of coherence effects in molecules across broad energy- and time-scales. From the perspective of coherent control research endeavors, the notion of coherence in molecular states and dynamics moves out of the "probing" spotlight and, instead, into the toolbox for external manipulation of chemistry. This intrinsic connection between experimental methods and ambitions of coherent control is masterfully captured by Ref. [11], an article from the late Professor Ahmed H. Zewail (the father of femtochemistry). In the article, to which and the references therein we refer the reader, Zewail discusses how progress in using ultrashort laser pulses to coherently prepare and study the evolution of nuclear wavepackets led directly to the idea to use such pulses to achieve selective chemistry.[11, 36] As we discuss below, the products of coherent control research in the 1980s and 1990s are pervasive in many fields of science today, especially those relating to coherence phenomena.

In noting that the control methodology put forth by Brumer and Shapiro[30, 31] is analogous to Young's double slit experiment, Gordon and coworkers[27] state:

> *"In Young's experiment, the phases are determined by the relative positions of the slits*
>
> *and the screen and the refraction index of the medium through which the waves travel,*
>
> *whereas in coherent control they are determined by properties of the molecular target*
>
> *and the laser photon."*

This distinction between the properties of these two puzzle pieces (i.e. the molecular system and the laser field) is critical to recognize. Over the last two decades, research efforts of the coherent

control "flavor" have continued to place more emphasis to the quantum mechanical properties of the molecular system and the surrounding bath. In some cases, the "control" element remains at the center stage. For example, in the context of condensed-matter physics, many efforts have been and are being made to optically dress and manipulate phonon states to drive non-equilibrium processes.[17, 37, 38] For example, Horstmann and coworkers[37] recently used ultrafast optical and diffraction-based experiments to achieve coherent control over a structural phase transition of atomic indium wires. They observed that not only did the photoswitching efficiency depend on the time delay between two coherent pump pulses, but this dependence displayed a marked interference pattern that matches phonon frequencies within the system. Such a finding is reminiscent of studies performed by the Zewail group on the bimolecular reaction between iodine and xenon gas,[39] with the crucial distinction that the study from Horstmann and coworkers was conducted in the vastly more complex condensed phase. We refer the reader to a recent review article by de la Torre and coworkers[17] that explores previous and ongoing coherent control research endeavors on condensed-phase matter. An interesting connection between this branch of coherent control and earlier work is evident in their respective terminology: References to *phononic control*[17] and *Floquet engineering*[17, 40] in the context of condensed-phase materials have direct analogies with the term *vibrational selectivity* used in early coherent control research of small-molecule, gas-phase chemistry.[32]

Another ongoing branch of coherent control exists within the field of quantum biology. For example, Paul et al. recently reported that the light-invoked ionic current from Channelrhodopsin-2 (ChR2) in living brain tissue can be manipulated by the phase characteristics of the coherent excitation field.[41] They suggest that this tunability is afforded by control of quantum

coherences within the retinal chromophore, or rather the production of vibrational wavepackets that influence the light-driven isomerization event of ChR2. This work builds on a high-profile 2006 report,[42] and related studies that followed,[43, 44] from Prokhorenko and coworkers that put forth experimental evidence for coherent control of retinal isomerization yield within bacteriorhodopsin.[42]

Variation in the balance between focus on molecular properties versus properties of the laser field(s) for achieving coherent control has also inspired modern research regarding electronic and vibronic coherence effects in ultrafast photochemistry (see Sections 1.4.4 and 1.6). The factor that distinguishes these fields of research from traditional coherent control is the usage of ultrashort laser pulses as probes of molecular coherence, rather than as a handle for control. However, the boundary between probing and controlling coherence is quite obscure in some cases. For example, recent theoretical work from Tomasi and coworkers[45] suggests that not only can excitonic coherence enhance light-harvesting efficiency in photosynthetic aggregates, but can also be controlled by the nature of the excitation field(s). In an example that directly shifts the handle for control to properties of the molecular sample, Alvertis and coworkers[46] found that ultrafast singlet fission (see Chapter 5) in a covalent dimer of the organic semiconductor tetracene proceeds through either a coherent or an incoherent mechanism depending on the extent of charge-transfer state stabilization (altered through solvent dielectric). A similar train of thought was implemented by Paulus and coworkers, where in their 2020 report[47] they provided evidence that information afforded by spectroscopic probes of coherence can be leveraged in synthetic design to control excited-state dynamics (in this case, the lifetime of a metal-to-ligand charge-transfer (MLCT) state).

The discussion up until now has focused on coherent control of photochemical reactions. Recent work from Pan and Liu[48] demonstrated that the extent of the reaction between Cl and CH_3D to form CH_2D and HCl can be manipulated by dressing the initial superposition state of the CH_3D reactant with a distinct vibrational phase. The authors show that this coherent control is successfully achieved through interferences between two Fermi-coupled vibrations of CH_3D, which can be modulated based on the IR excitation that prepares the initial state.[48]

It is important to note that technological limitations have and continue to play major roles in coherent control research, often as limiting factors.[32] As the branching of this field over the past 20 years indicates, the technological developments in the 21st century continue to renew interest in questions rooted in coherent control. Massive improvements in pulse shap- ing equipment have revolutionized spectroscopy over the past three decades by enabling, for example, extraordinarily efficient pulse compression,[49] precise phase cycling methods,[50, 51] high repetition-rate shaping,[52] and facile upgrading of one- to multi-dimensional experiments.[53, 54] We refer the reader to several references[55-57] (along with the citations therein) for more information.

1.4.2 Coherence from electronic coupling

The term *quantum coherence* can refer to the general superposition of two or more quantum states. Therefore, *how* a superposition configuration is initialized adds a distinguishing characteristic to the coherence context. In Section 1.4.1, we discussed how traditional coherent control research aims to steer chemistry by manipulating quantum superpositions in the energy eigenstate basis using external electromagnetic fields. As Gordon and coworkers[27] point out, an alternative degree of freedom in coherent control are the properties of the molecular system. In the site- basis Hamiltonian of the chemical system, these properties emerge as off-diagonal couplings

between interacting local states of the system. This section to overviews some, but certainly not all, quantum mechanical mechanisms that create coupling elements and pathways in molecular systems. Though communication about these mechanisms is commonly done using the site basis,[58] recall that their effect(s) on macroscopic observables is basis-independent (i.e. couplings in the site-basis alter the energy and composition of the system eigenstates). In addition, even though our descriptions of these coupling mechanisms are primarily time-independent, they most certainly impact the time evolution of chemical systems (*vide infra*).

A prerequisite for quantum mechanical couplings is spatio-temporal proximity (i.e., molecules separated infinitely in spacetime will exhibit infinitesimally small coupling). As such, couplings are of vital importance for understanding the properties and dynamics of closely packed molecular systems, such as covalent multimers or condensed-phase aggregates.[59] At separation scales of nanometers to Angstroms, electronic couplings and dipole-dipole interactions become increasingly important in dictating chemistry.
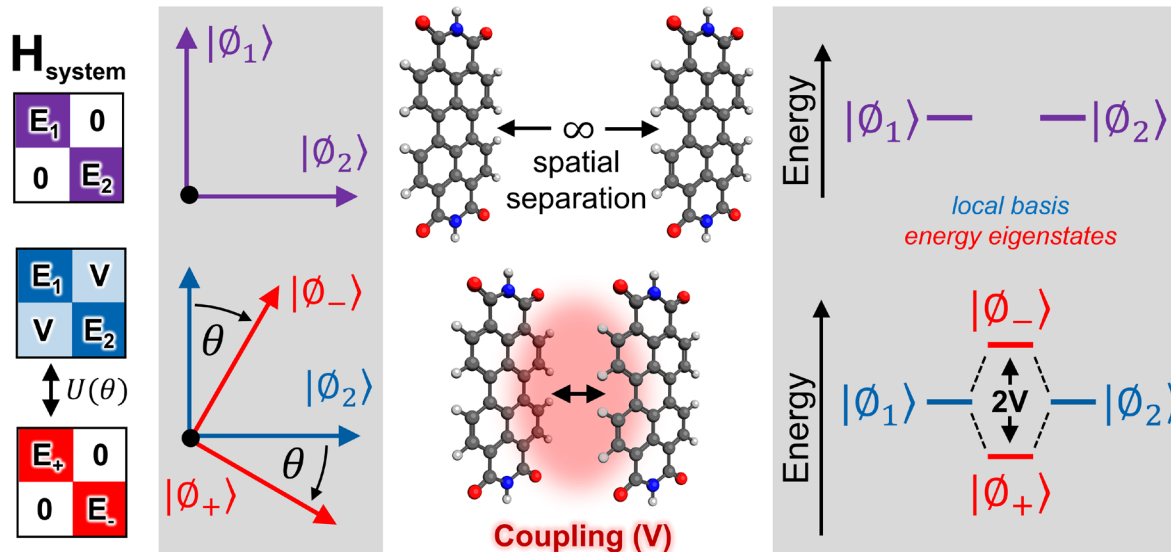
Figure 1.6. Illustration of the change of basis from local excitation states $|\phi_1\rangle$ and $|\phi_2\rangle$ to the stationary energy eigenstates (exciton states) $|\phi_+\rangle$ and $|\phi_-\rangle$ of two chromophores with excitonic coupling V. The angle θ (equal to 45° if the chromophores are identical) parameterizes the unitary operator $\hat{U}(\theta)$ generating the relative phase between the $|\phi_1\rangle, |\phi_2\rangle$ basis and the $|\phi_+\rangle, |\phi_-\rangle$ basis.

Consider the minimal case of a two-level system (2LS) involving two chromophores, as shown in Figure 1.6. We label the states with an elementary excitation on the left and right chromophores as the states $|\phi_1\rangle$ and $|\phi_2\rangle$, respectively. If the chromophores are infinitely separated in space and time, they can be assumed as completely uncoupled and non-interacting, so that the stationary states of the entire system (energy eigenstates) equate to the local states. However, if we bring these two states into close spatiotemporal proximity, interactions between the chromophores can arise due to interchromophoric interactions, such as transition dipole moment coupling[59, 60] and orbital-overlap.[59]

The interaction between the chromophores at finite distance results in a change in the stationary states of the system, by the emergence of an excitation coupling energy V between $|\phi_1\rangle$ and $|\phi_2\rangle$. To see how this coupling impacts the optical response (and any ensuing chemistry) from this 2LS, we must perform a change in basis. The unitary operator (U) represents our rotation from

the local (or site) basis to the energy eigenstate basis, in which the Hamiltonian is diagonal. In contrast to the uncoupled system, where excitations are localized on either chromophore, the coupled system exhibits *delocalized* eigenstates. For states that are electronic in nature, these are referred to as *excitons*, which are quantum superpositions of the local electronic wavefunctions of each chromophore within the aggregate. We can represent the exciton states as $|\phi_+\rangle$ and $|\phi_-\rangle$, which according to Eq. 3 are superpositions of the local states $|\phi_1\rangle$ and $|\phi_2\rangle$, where c_1 and c_2 are functions of V. If the energy of the uncoupled, local states (infinite separation) are equivalent, then the energy splitting between exciton states due to the interaction V is given by 2V. As we discuss further in Section 1.6, exciton wavefunctions are generally delocalized over many chromophores and play important roles in energy/charge transfer and photosynthetic light harvesting.

Note that the 2LS in Figure 1.6 is applicable to quantum states in general, not just electronic states (e.g., vibrational, vibronic, spin, etc.). For instance, a mathematically equivalent change-of-basis (though distinct chemical and physical interactions) connects local atomic orbital states to hybridized bonding and anti-bonding molecular orbitals[19] in the study of chemical bonding, and connects charge-localized diabatic states to charge delocalized adiabatic states in the study of electron and/or proton transfer.

The Kasha exciton model is ubiquitously applied when rationalizing the optical response of molecular aggregates.[59-61] This model considers coupling between electronic transition dipole moments as a function of intermolecular geometric parameters such as angles, spatial separation, and slip-stacking distance. This coupling, which is often written as J_{Coul} and calculated using the point-dipole approximation, originates from the Coulomb interaction and forms the foundation for Förster or fluorescence resonance energy transfer (FRET).[59, 62] J_{Coul} is proportional to the third

power of the intermolecular separation distance (R),[59] which manifests the R^6 dependence of the FRET rate.[63, 64] Hence, J_{Coul} is often referred to as long-range coupling since it can drive energy transfer on the nanometer scale.[62] In the context of the Kasha exciton model, J_{Coul} elicits substantial changes in the optical response of molecular aggregates when intermolecular distances are on the order of a few to tens of Angstroms.[59] Physically, J_{Coul} generates delocalized excitonic states, or Frenkel excitons, where the energy eigenstate wavefunctions emerge as interferences of the local electronic wavefunctions.[59] Importantly, constructive interference yields an optically bright exciton, while destructive creates a dark exciton state. As detailed in Figure 1.7, the effect of appreciable Coulombic coupling is a shift in the optical electronic transition energy of the aggregate, with respect to that of an isolated monomer.[59] For aggregates with the molecules slip-stacked, J_{Coul} is negative in sign and results in the lower-energy exciton being optically bright. The case of $J_{Coul} < 0$ is commonly referred to as *J-aggregation*. In contrast, constructive interference in the case of *H-aggregation* ($J_{Coul} > 0$) forms an optically bright, higher-energy exciton, as shown by the blue-shifting of the absorption maximum in Figure 1.7 with increasingly positive values for J_{Coul}.
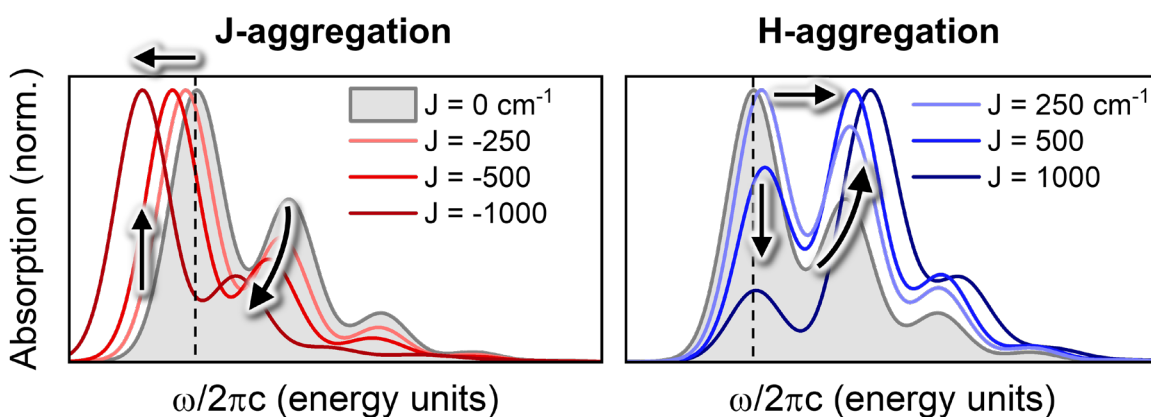
Figure 1.7. Illustration of how the steady-state absorption profile for an example molecular dimer is impacted by a range of Coulombic couplings.

In recent years, Spano and coworkers have built upon the Kasha exciton model by considering the effects of short-range electronic couplings, which are operative in systems with π-π stacking distances on the order of a few Angstroms.[59, 65, 66] This length scale is particularly important to solid-state materials chemistry as the typical π-π stacking distance in molecular crystals is around 3.5 Å. Spano and coworkers have shown that the Coulombic coupling in a crystal varies weakly as a function of slip-stacking along the short crystal axis and shows a sharp change in sign as the long-axis distance increases (transition from H- to J-aggregate). The short-range charge transfer coupling (J_{CT}) is directly proportional to the product of the electron and hole transfer integrals, t_e and t_h, respectively.[67] In contrast to the Coulombic coupling, this product varies dramatically as a function of both short- and long-crystal axes. Therefore, the interplay of long- and short-range electronic couplings in molecular aggregates may be extremely sensitive at short π-π stacking distances, which corresponds to an equally strong orientational dependence of the optical response exhibited by the aggregate.[67]

1.4.3 Coherence from interfering coupling pathways

As discussed in the preceding section, the electronic wavefunctions in molecular systems can couple and mix, which produces eigenstates with interference patterns evident in the spatial distribution of the wavefunction. The interplay of electronic couplings in molecular frameworks is intrinsically connected to the chemical reactivity and dynamics of such systems. Many past and ongoing efforts seek to leverage this notion to elicit coherence effects in electron transfer processes.[68] Consider, for example, a model electron transfer system constructed of a donor (**D**) and acceptor (**A**) moieties connected by two bridging units (**B₁** and **B₂**), as shown in Figure 1.8A. Both **D** and **A** are coupled to each bridging unit, indicated by V_{DBi} and V_{BiA}, respectively ($i=1,2$).

All coupling elements can be described as complex exponential functions with a phase factor, though for simplicity we represent only the **D**−**B$_i$** interactions in this form. Because of the symmetry between the site-basis **D**−**B$_1$**−**A** and **D**−**B$_2$**−**A** coupling pathways shown in Figure 1.8A, the eigenstates of the system Hamiltonian for this model four-member system exhibit interferences.

While each electron coupling pathway is an example of coherence in this toy molecular system, the interaction of these pathways gives rise to an additional instance of coherence that ultimately shapes the electronic structure of the system. The effects of this coherence are analogous to experimental measurements performed using interferometry.[69-71] Figure 1.8B illustrates a Michelson interferometer, which is commonly used to measure the frequency and phase of a coherent source of electromagnetic radiation (green box, gray and black traces in Figure 1.8D). The set-up employs a beam splitter, which serves to reflect a reference copy of the time-dependent electromagnetic field ($E(t)$) that transmits through the splitter. The transmitted beam traverses a path of fixed distance before reflecting and returning to the beam splitter, whereas the reflected copy beam proceeds through a path that has a variable distance (Δd) that is directly related to a variable delay time (Δt) by the speed of light. A square-law detector is used to measure the intensity of light emerging from the beam splitter after recombination of the original and reference fields, which is maximized and minimized in the cases of constructive and destructive interference, respectively. When Δt is varied, the signal measured by the detector changes due to destructive interference when the beam paths are neither equivalent in length nor displaced by an integer value of the wavelength. This interference in the signal detected from a Michelson interferometer is shown as a function of Δt by the red trace in Figure 1.8D. Translating this reasoning to interfering electronic coupling pathways in molecules, variations in the phase of the coupling elements between the unique

D−B−A paths (Figure 1.8C) should impart a similar interference pattern on the electron transmission from **D** to **A**. Indeed, the red trace in Figure 1.8C, which displays the expectation value of the projection operator onto A, oscillates as a function of phase difference between the two coupling pathways ($\Delta\varphi$).
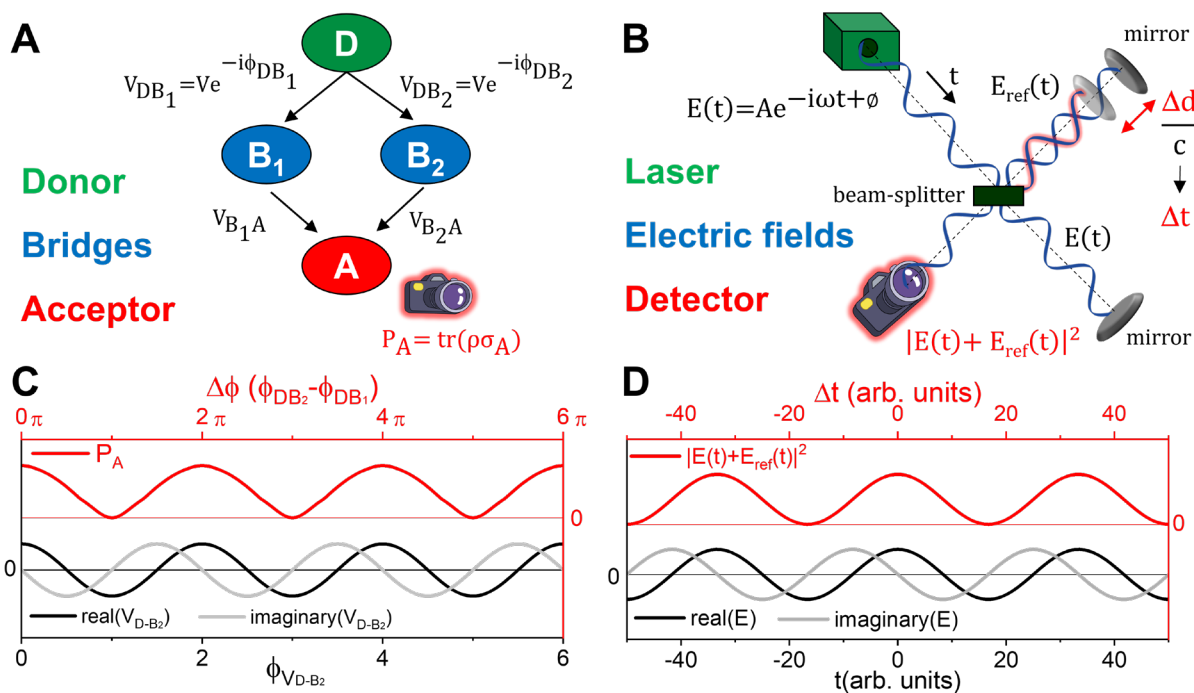
Figure 1.8. (A) The architecture and form of the quantum mechanical coupling for a symmetric **D−B₂−A** molecular interferometer. (B) A classical Michelson interferometer with a continuous-wave laser source. (C) Acceptor population (red) as a function of the phase difference between the symmetric **D−B−A** electronic coupling paths and the amplitude of the total **D−B₂** electronic coupling (black and gray) as a function of the phase angle. (D) Signal detected by a square-law camera (red) as a function of the time difference between the arms of the interferometer (Δt) and amplitude of the source electric field (black and gray) as a function of time.

Joachim and coworkers[72] first introduced the model molecular system shown in Figure 1.8A and demonstrated that asymmetries in the **D−B−A** coupling pathways can lead to destructive interference and suppression of the electron transfer rate between **D** and **A**. Skourtis and coworkers[71] showed that this coherence effect can (1) be erased by inelastic excitation of the bridge moieties and (2) relax orbital symmetry rules for electron transfer. The authors suggest that such properties of coherent pathway interference may enable feasible approaches to control electron transfer

pathways in large molecular systems. Goldsmith and coworkers[70] expanded this model to include local elastic dephasing and suggested possible experimental approaches, which in 2006 were rare,[73, 74] for observing this interference effect.

The implications of coherence between multiple electron transfer pathways are extraordinarily far reaching. Beyond electron transfer, numerous key intermolecular processes, such as Dexter energy transfer (DET) and singlet fission (SF), are well-known to rely on coupling pathways for charge transfer. Indeed, several theoretical studies have explored interference effects in DET[75, 76] and SF[77-79] that emerge from coherence between electronic coupling paths. Similar effects have been discussed in the context of molecular junctions for several decades.[80-83] We refer readers to several reviews[84, 85] concerning this topic.

It is important to note that interference between coupling pathways need not emerge solely from a network of covalently-bound molecules, but even from molecular orbitals (MOs) of a single molecule. As discussed by Nozaki and Toher in the case of benzene,[86] electron transmission through molecular wires bears resemblance to the double slit experiment. Gunasekaran and coworkers developed a convenient theoretical method for visualizing quantum interferences in molecular junctions using an energy-dependent transmission function.[87] Figure 1.9A illustrates the six MOs that comprise the benzene π-system, where both the HOMO and LUMO levels are doubly degenerate. Figure 1.9B shows the transmission function (along the Green's function approach and in the MO basis) for a system with benzene either para- or meta-connected to two electrodes. While the transmission function indicates constructive interference between the MOs of the benzene π-system, meta connection of the electrodes results in a completely destructive interference at the Fermi energy (E_F). In Figure 1.9C, Gunasekaran and coworkers define a *Q matrix* that distinguishes

the interfering and noninterfering components of the total transmission function. The off-diagonal elements of the Q matrix heat maps for the para- and meta-benzene connections indicate constructive (red) and destructive (blue) interference between MO pairs. Therefore, this matrix visualization approach directly illustrates that electron transmission through benzene is suppressed by destructive interference between the HOMO and LUMO when the electrodes are linked in a meta configuration. This coherent suppression of conjugation that emerges through meta benzene linkages has been experimentally revealed using electrochemical and spectro-electrochemical methods,[88], [89] as well as current-voltage measurements from mechanically controlled break-junction (MCB) experiments.[90]
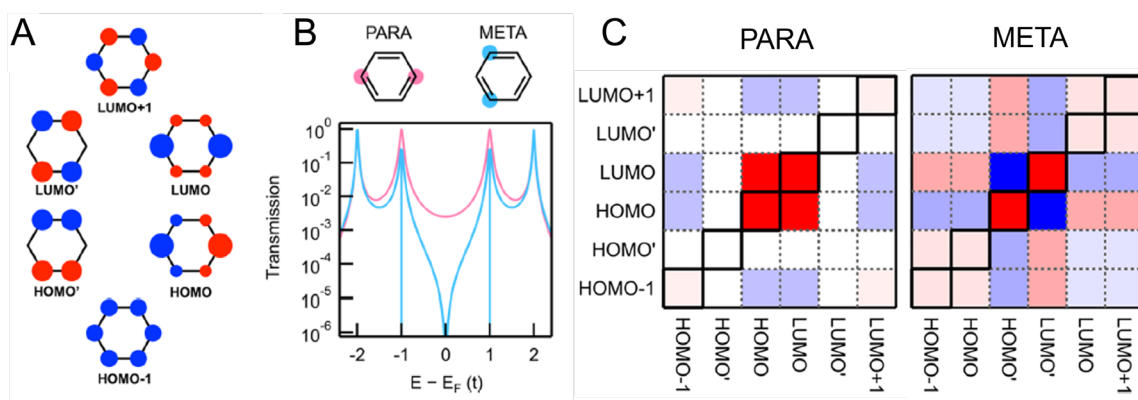
Figure 1.9. (A) π-based MOs of benzene. (B) (top) Electrical contact sites for molecular junctions of para- and meta-benzene. (bottom) Transmission functions for para- (pink) and meta-benzene (blue). (C) Quantum interference maps for (left) para- and (right) meta- benzene at the Fermi energy. The color scale for each map is normalized. Figure adapted from Gunasekaran, S.; Greenwald, J. E.; Venkataraman, L. *Nano Lett.* **2020**, *20*, 2843-2848.

Coherence between electronic coupling pathways in molecular wires is sometimes referred to as *crosstalk*,[81] which has been extensively theorized to enhance electron transport rates beyond classical limits.[69-71], [91-97] This prediction is experimentally challenging to prove since one needs not only a symmetric molecular system to exhibit the interference effect, but also an incoherent control

system that is not too different chemically (as to avoid influence from undesired factors).[98, 99] A breakthrough report in 2012 from Vazquez and coworkers overcame these hurdles and provided clear experimental evidence for enhancement of electron conductivity enabled by constructive interference between tunneling pathways.[100] The authors synthesized two single-molecule (**M**) circuits, one in series (**1**) and one in parallel (**2**) configuration, and individually connected each of these systems to pyramidal gold tips (**L**) for scanning tunnelling microscope (STM)-based break junction measurements. In the case of perfect symmetry between the two $\mathbf{L-M-L}$ paths, the electrodes couple solely to the bonding MO which results in a renormalized electrode-molecule coupling a factor of $\sqrt{2}$ larger than that of **1**. The result is that electron transmission in **2** is *four* times that of **1** (when the statistical, non-interfering limit instead predicts a factor of *two*). The factor of four that emerges from constructive interference between coupling pathways can be rationalized by Fermi's Golden Rule, as has been previously shown.[101] The experiments performed by Vazquez and coworkers show that the conductance ratio between **2** and **1** is 2.8, which directly illustrates that the quantum mechanical coherence, or crosstalk, between the two paths in **2** yields an enhanced conductivity beyond classical predictions. [100]

Experimental observations of interference between identical electronic coupling pathways to-date remain scarce. Richert et. al. used electron paramagnetic resonance spectroscopy (EPR) to find that quantum interference between parallel paths in a bis-copper six- porphyrin nanoring drives an enhancement of the electron exchange coupling by a factor of 4.5, as compared to a system with a single coupling path.[102] Recently, Phelan and coworkers have shown that similar interference effects emerge in ultrafast photodriven electron transfer between a single anthracene electron donor and two equivalent benzoquinone (BQ) acceptors.[99] At room temperature, they

observed a rate enhancement by a factor of 2.4 compared to the control compound with a single electron acceptor, which is only slightly larger than the classical 2x enhancement. In contrast, they observed that the rate enhancement increased as temperature decreased, where at liquid helium temperatures an enhancement factor near five was observed. This work demonstrated (1) that interference between electronic coupling pathways can significantly impact light-driven charge transfer and (2) that decoherence mediated by system-bath interactions acts to erase the interference effects on the electron transfer rate.

Phelan and coworkers also showed that quantum interference can impact charge shift reactions, where they observed that electron transfer from an initially charge separated species (between covalently bound p-(9-anthryl)-N,N-dimethylaniline (DMA) and anthracene groups) to two equivalent naphthalene-1,8:4,5-bis(dicarboximide) (NDI) electron acceptors exhibited a 2.6x rate enhancement compared to a control compound with a single NDI acceptor.[98] Again, this enhancement was only observed at cryogenic temperatures.

1.4.4 Coherence from coupling between electronic and nuclear degrees of freedom

In the most general form, electronic-vibrational (*vibronic*) coupling describes mixing between electronic and vibrational degrees of freedom. As Azumi and Matsuzaki pointed out in 1977,[103] a sentiment which still remains true to this day, the term *vibronic coupling* is quite ambiguous and, in turn, is often either used incorrectly or in a way that propagates misconceptions. This section outlines two important phenomena within the usages of vibronic coupling and how such couplings impact molecular behavior. Like quantum couplings in general, vibronic coupling establishes phase relationship(s) between wavefunctions or, in other words, coherence through quantum superpositions.

For molecules, the absorption spectrum originating from transitions between two electronic states, $|G\rangle$ and $|E\rangle$ (singly excited) for example, rarely appears as a single peak (ignoring broadening effects from system-bath interactions for simplicity). Instead, a progression of vibronic transitions) is observed (blue trace in Figure 1.10).[59] For the case that both $|G\rangle$ and $|E\rangle$ states are dressed with an identical and harmonic vibration (ν), vibronic transitions emerge when the equilibrium nuclear geometry for $|G\rangle$ and $|E\rangle$ differ. When a coordinate system is defined for this case, both electronic and vibrational degrees of freedom must be specified to fully describe a state within the system Hilbert space (requiring state vectors of the form $|G, \nu\rangle$ and $|E, \nu\rangle$). Note that this example is described in the adiabatic representation, which comes from the separable treatment of nuclear and electronic degrees of freedom as stated by the Born-Oppenheimer (BO) approximation. As we will cover later, the breakdown of the BO approximation is a specific case that falls within the larger umbrella of *vibronic coupling*. The adiabatic potential energy surface for the singly excited electronic state of molecules will generally have a global energy minimum at a different configuration of nuclear coordinates (commonly called 'geometry') compared to the geometry of the energy minimum for the ground electronic state. This case is diagrammed in the upper right of Figure 1.10, where the unitless λ parameter represents the displacement between the ground and singly excited electronic potentials. When light drives a resonant electronic transition in this case, the vibrational selection rules are relaxed and transitions between states with inequivalent vibrational quanta can be observed (for example, the transition from $|G, \nu = 0\rangle$ and $|E, \nu = 1\rangle$), as is seen by the blue trace at the bottom of Figure 1.10. Vibronic coupling in this context thus leads to optical transitions that are characterized by a change in both the electronic and nuclear quanta describing the state of the system. It is important to clarify here that the Franck-

Condon (FC) approximation states that these transitions do not invoke a change in the nuclear coordinate (i.e. the excitation is vertical between two adiabatic surfaces).[104] Another way to
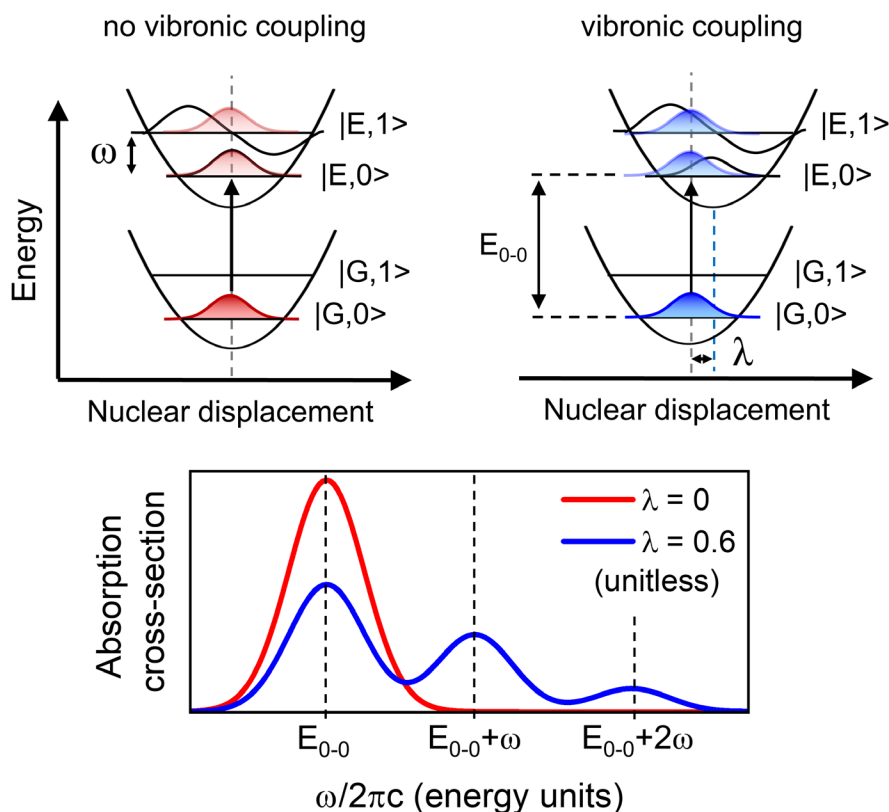
Figure 1.10. Graphical description of vibronic coupling in the context of a single molecule, which has both ground- and excited-electronic states (G and E, respectively) that are each dressed with a single vibrational quantum. In the case of zero nuclear displacement (λ) between G and E (upper left), the FC overlap between states with different vibrational quantum numbers is zero, which means only one peak is visible in the absorption spectrum (red trace in lower plot). When $\lambda > 0$, the FC overlap with higher vibrational quanta becomes nonzero, leading to a vibronic progression (blue trace) in the linear absorption spectrum. Note that the absorption spectra are simulated with more than one vibrational quanta on each electronic state, as opposed to the schematics at the top.

describe this approximation is that the transition dipole matrix (TDM) for the absorption event is independent of nuclear coordinate (commonly referred to as the Condon approximation).[105]

The discussion up until now has described vibronic coupling in the context of a model with two electronic states, one ground and one excited, each dressed with a single vibration. For systems where more than two electronic states are necessary to describe dynamics, vibronic coupling can not only impact dynamics on ground- and excited-electronic surfaces, but also the dynamics across

all of the electronically excited adiabatic surfaces. Vibronic coupling in the context of two or more excited electronic states most commonly refers to (1) breakdowns of the BO (adiabatic) approximation and (2) Herzberg–Teller (HT) (non-Condon) effects.[103] Here, we explore the differences between these two distinctions.

For well-separated adiabatic potential energy surfaces, vibronic couplings are often, justifiably, neglected.[104] Vibronic couplings become non-negligible at avoided crossings, where adiabatic surfaces approach each other in nuclear coordinate space, and singular at conical intersections, where the surfaces are degenerate. The non-adiabatic effects of these vibronic couplings represent a breakdown of the BO approximation. The particular case of resonance between an electronic energy gap and a molecular vibration has been explored fervently in the context of coherence in the primary events of natural photosynthesis.[106, 107] Studies have found that in this case, non-adiabatic coupling drives efficient electronic state mixing even in the absence of strong electronic coupling.[107] Figure 1.11 illustrates this mixing effect in three distinct scenarios for a molecular dimer. The left column considers two nested harmonic oscillators representing the diabatic singlet states, S_1 and S_2, from the two monomer units. Though the $v = 1$ state of S_1 is exactly resonant with the electronic gap between the S_1 and S_2 states (upper row), no mixing is observed (lower row) because there is zero electronic coupling between the monomers. However, the middle column shows that dramatic mixing between S_1 and S_2 is observed when weak ($<< \Delta E$) electronic coupling is switched on. In this case, the vibronic excited states of the dimer are highly delocalized and often said to be *vibronically coherent*. When the frequency of the vibration is lowered substantially and the resonance condition is lost, negligible mixing of S_1 and S_2 is observed (right column).
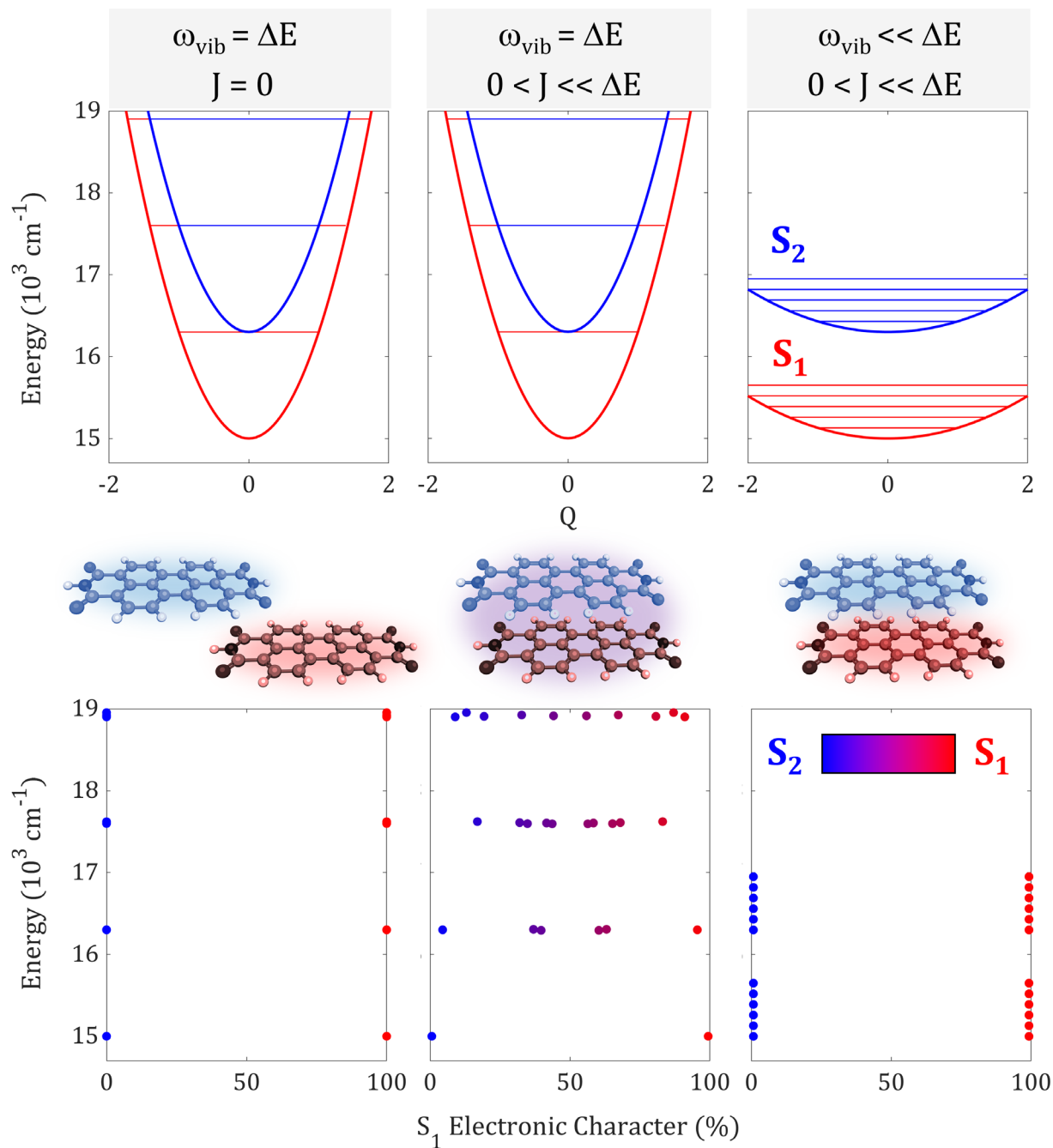
Figure 1.11. Toy model for a Frenkel exciton dimer with (left) a resonant vibration and zero electronic coupling, (middle) a resonant vibration and weak electronic coupling, and (right) an off-resonant vibration and weak electronic coupling. The top row illustrates the diabatic potentials for the S_1 (red) and S_2 (blue) monomer states. The middle row depicts possible scenarios for the dimer that could yield the parameters of each column (e.g., distant cofacial $\pi-\pi$ stacking yielding weak electronic coupling). The bottom row depicts the S_1 diabatic character of the lowest-energy eigenvalues, where the color of the dots corresponds to pure the S_1 (red) and S_2 (blue), and mixed (purple) character (color bar in bottom-right).)

It is vital to note that the Condon approximation is often not violated when vibronic coupling is used in reference to breakdown of the BO approximation. However, the nuclear dependence of dipole-dipole couplings is often also labeled as vibronic coupling.[103, 108] This case is known as Herzberg-Teller (HT) coupling. For example, consider the transition dipole moment (μ) with a dependence on normal mode coordinates k[109]

$$\mu(\boldsymbol{q}) \cong \mu^{(0)} + \sum_k \mu_k^{(1)} (\hat{q}_k - q_k^g) \qquad \text{Eq. 5}$$

where $\boldsymbol{q}$ is a vector containing k normal mode coordinates relative to the equilibrium geometry $\boldsymbol{q}^g$ of the ground electronic state, $\mu^{(0)}$ is the coordinate-independent portion of μ, and $\mu_k^{(1)}$ is the first derivative of μ with respect to coordinate q_k. The set of $\left\{\mu_k^{(1)}\right\}$ represents the HT vibronic coupling. Since the Coulombic coupling between chromophores arises from transition dipole couplings, J_{coul} also takes on a nuclear dependence. It is important to note that experimental confirmations of HT coupling are difficult as the resulting effects often manifest as "enhancements" to either peak intensities or dynamical features.[105, 110] However, the advent of new spectroscopic methods has led to some progress in this regard.[108, 111] It is important to note that although the majority of discussions in the literature invoke *either* the BO or the HT forms of vibronic coupling, *both* may be active in a given system since separating these coupling mechanisms experimentally remains challenging. Ongoing research in this regard is necessary to clarify physical models for vibronic phenomena in chemistry.

1.5. Optical methods for creating and probing coherence in chemistry

Spectroscopic experiments play a vital role across the scientific disciplines, often by providing rich structural and dynamical information about systems ranging from single atoms and

molecules[14, 112-115] to bulk materials. Moreover, spectroscopic techniques are ubiquitously used to study coherence effects in chemistry. In fact, spectroscopic signals themselves are completely dependent on light-matter interactions with well-defined phase relationships and, in many cases, coherence of the electromagnetic field(s).[12, 116, 117] Awarded the 1999 Nobel Prize in Chemistry for his contributions to the field of *femtochemistry*, Professor Ahmed Zewail noted that the coherence concept and the connections between coherence of classical light fields and that of molecular states forms the very foundation for time-resolved measurements of chemistry on the nano to femtosecond scales.[11] The use of coherence in spectroscopy ultimately serves to push a quantum mechanical system away from equilibrium to a highly localized configuration. By probing chemical dynamics that ensue from a localized initial state, one can effectively measure a distribution of single-molecule trajectories that would otherwise be obscured by the randomly phased ensemble.[11]

The intrinsic connections between spectroscopic experiments and numerous coherence contexts can generate confusion and ambiguity. As we discussed in Section 1.4.1, properties of both the laser light and the molecular systems are important to studies of coherence phenomena;[27] great care must be taken to convey the extent to which these ingredients are being referred to in communication of scientific results.[1] For example, a phrase such as "*electronic coherence between the ground and excited states of a light-harvesting complex*" may be interpreted as being counter-intuitive and groundbreaking, when in actuality, this phrase can describe the common process of linear absorption.

The sheer breadth of spectroscopy experimentation is not addressable in a single thesis. We instead cover some foundational concepts, such as the macroscopic polarization, and then

explore several important techniques to studies of coherence in chemical properties and dynamics. In this holistic approach to clarifying the connections between coherence phenomena and experimental methods, we refer often to previous review articles to supplement the rigorous technical details.

1.5.1 Coherence of the macroscopic polarization and molecular response

Most spectroscopic techniques operate in the perturbative limit, though non-perturbative processes are more important when the field strengths are intense.[117] Here, we restrict the discussion to techniques that probe chemical ensembles with strong (classical) perturbing fields.

Spectroscopic experiments fundamentally rely on the ability to launch, steer, and probe a *macroscopic polarization* within a sample.[117] Imagine a purely electronic ensemble of molecules that all have electron density residing in the ground state at thermal equilibrium (density matrix is diagonal in the energy eigenstate basis). Perturbation by light equates to an electromagnetic field coupling two eigenstates of the system Hamiltonian, where the energy separation of the states is resonant with the carrier frequency of the incident field. This coupling drives oscillation of electron density between the ground and excited electronic states for each molecule, or rather it launches a macroscopic polarization). Subsequent light matter interactions can perturb this polarization further from equilibrium. In the perturbative limit, the polarization ($P(t)$) driven by n electromagnetic fields ($E^n(t)$) is written as

$$P(t) = P_0 + \epsilon_0\left(\chi^{((1))}E(t) + \chi^{((2))}E^2(t) + \cdots\right) \qquad \text{Eq. 6}$$

$$= P_0 + P^1(t) + P^2(t) + \cdots \qquad \text{Eq. 7}$$

where P_0 is the polarization in the absence of the external electric field ($E(t)$) and $\chi^{(n)}$ is the nth-order optical susceptibility, which is a property of matter that describes amplitude of the

polarization within a material that is induced by incident electric fields.[117] Eqs. 6 and 7 assume that the medium is isotropic (an assumption that also guarantees that $\chi^{(n)}$ vanishes for even orders of n). As n increases, the amplitude of the polarization ($P^n(t)$) decreases, which makes the signals from optical processes increasingly difficult to measure as the number of participating electric fields (power of E) grows.[117] Linear optical processes, such as steady-state absorption, are therefore the least technically challenging to harness for measurement of chemical and material systems.

For a nth-order spectroscopic experiment, the light-driven quantum coherence evolves over n time periods, which occur between light-matter interactions that, in the impulsive limit, are often assumed as a delta function in the time domain. Using a perturbative expansion of the density matrix,[51] the general nth-order polarization is written as

$$P^{(n)}(t) = \int_0^\infty dt_n \int_0^\infty dt_{(n-1)} \cdots \int_0^\infty dt_1 \, E(t - t_n) E\big(t - t_n - t_{(n-1)}\big) \cdot \cdots$$

$$\cdot E\big(t - t_n - \cdots - t_{(1)}\big) \cdot R^n(t_n, \cdots, t_1)$$

Eq. 8

$$R^n(t_n, \cdots, t_1) = -\left(-\frac{i}{\hbar}\right)^n \langle \mu(t_n + t_{n-1} + \cdots + t_1)[\mu(t_{n-1} + \cdots$$

$$+ t_n), \cdots [\mu(0), \rho(-\infty)] \cdots] \rangle$$

Eq. 9

where $R^n(t)$ is the time-domain molecular response function describing free-evolution of the density matrix under the system Hamiltonian. After n perturbations and periods of free-evolution, $P^n(t)$ emits a signal field ($E_{sig}(t)$) at a time τ_{n+1} (equivalent to calculating the expectation value of

the transition dipole operator), which can then be detected an analyzed for amplitude and phase information.

We note that the macroscopic polarization itself is a coherence phenomenon in numerous contexts: It arises from the time-evolution of off-diagonal density matrix elements with reference to the phase of the driving field(s) and is probed through emission of a coherent signal field. Furthermore, the signals detected from the macroscopic polarization provide rich information about energy- and time-scales characteristic of the system and system-bath Hamiltonians. This information expands as the number and effect of free-evolution periods are resolved in the detected signal. These insights enable research capabilities such as the interpretation of chemical reaction mechanisms, characterization of functional molecular-scale interactions, identification of coherence effects in chemistry.[11] The hierarchy of coherence in spectroscopic experiments demonstrates that coherence is not only a property of electromagnetic waves, coupled molecules, dynamics, etc. that can be identified and quantified, but a tool by which experimenters can probe chemical physics at the molecular scale.

The network of ways that coherence manifests in spectroscopic experiments reiterates the importance of communicating as clearly and specifically as possible when discussing measurements of coherence. For example, off-diagonal density matrix elements are commonly trivial and requisite for generation of a measurable signal; they even underpin basic absorption experiments. Measuring the UV/visible absorption spectrum of a sample using an incoherent white light source, such as a lamp or the sun, entails the creation of off-diagonal density matrix elements between the electronic ground and excited states. Though the radiation source ($E(t)$) in this example is completely incoherent, the macroscopic polarization it generates evolves with a fixed

phase with respect to *E(t)*, such that the emitted field, *E$_{sig}$(t)*, destructively interferes with *E(t)* and indicates that the sample has absorbed photons.[51] Note that the detector in this example need not solely be a device, but could instead be a biological camera such as the human eye.

1.5.2 The interchangeability of the time and frequency domains

Spectroscopic methods can be equivalently described in either the time or frequency domain.[51, 116, 117] In general, experimental apparatuses are designed to detect signals as a function of whichever of these domains is most practical (e.g., expense, time, lab space, etc.). For example, linear technique of Fourier transform infrared (FTIR) absorption uses interferometry to measure spectra the time domain, which are subsequently Fourier transformed to the frequency domain to indicate absorption of light (by vibrational coherences launched by a single light-matter interaction) as a function of frequency. This is directly analogous to the free induction decay (FID) that is Fourier transformed to obtain nuclear magnetic resonance (NMR) spectra. As we cover various nonlinear techniques in the subsequent sections, recall that domains that the signals are represented and analyzed in are profoundly linked to the type of information that is sought and/or practically accessible.

1.5.3 Two-dimensional electronic spectroscopy

The order of a spectroscopic technique equates to the number of independent dimensions that are needed to fully resolve $R^n(t)$ in time/energy space. Therefore, the depth of information provided by a given technique tracks with the number of driving fields, *n*. Table 1.1 provides a comprehensive summary of linear and nonlinear spectroscopic techniques that are commonly used to study chemical properties and processes. Due to practical difficulties in measuring signals from *n*th-order techniques with $n > 5$, we focus on the those with $n \leq 5$. Though nonlinear techniques

involving the second (χ^2) and third-order susceptibilities (χ^3) are both utilized extensively in numerous disciplines of research, the fact that even orders of χ^n vanish in isotropic media makes third-order techniques the most common in studies of bulk media. The techniques summarized in Table 1.1 differ in numerous ways beyond number of the driving fields (e.g., carrier frequency and pulse shapes, instrumentation, samples of interest, experimental geometry, etc.).

Table 1.1. Phenomena arising from the optical susceptibility of orders n = 1, 2, 3, and 5. Representative references are included for each entry.

$\chi^{(n)}$	optical processes of order n
$\chi^{(1)}$	Absorption Refraction
$\chi^{(2)}$	second harmonic generation [117, 118] sum- and difference- frequency generation[117, 119] optical parametric amplification, generation, and oscillation [117]
$\chi^{(3)}$	**four-wave-mixing spectroscopy** transient absorption spectroscopy 2D electronic spectroscopy[120, 121] 2D infrared spectroscopy[51] 2D electronic-vibrational spectroscopy[108, 111, 122, 123] 2D vibrational-electronic spectroscopy[111, 124] femtosecond stimulated Raman spectroscopy[125, 126] transient grating spectroscopy[127] stimulated Raman scattering[128] third-harmonic generation[129] self-phase modulation optical kerr effect
$\chi^{(5)}$	two-dimensional impulsive stimulated Raman spectroscopy[130, 131] six-wave mixing femtosecond stimulated Raman[132, 133] 2D resonance Raman spectroscopy[134] gradient-assisted multidimensional electronic Raman spectroscopy[135]

In the study of coherent phenomena in chemistry, two-dimensional electronic spectroscopy (2DES) is a particularly notable third-order experiment. 2DES was pioneered by Jonas et. al. in the late 1990s and early 2000s,[121, 136] not too long after the first experimental demonstration of two-dimensional infrared (2DIR) spectroscopy.[137] The conceptual and technical development of

multidimensional optical spectroscopies (e.g., 2DES and 2DIR) proceeded along strong foundations formed by nuclear magnetic resonance (NMR) methods.[138] While 1D NMR reports predominantly on the properties of distinct nuclear spin species, 2D NMR reveals additional information about spin-spin couplings that are obscured within the 1D experiment. Similarly, 2DES provides the same information that the one-dimensional analogue, transient absorption (TA), affords, as well as additional insight clarified by resolution over the excitation frequency domain.[120, 138] Note that for 1D and 2D optical experiments with identical pulse spectra and characteristics, summation over the excitation axis of the 2D dataset will match exactly to the 1D data. The key element to note here is that while the 1D experiment theoretically contains all the same signal contributions as the 2D experiment, the interference of signals due to summation of the data over the excitation frequency axis obscures, and sometimes completely removes, information that may be clear with full resolution over the excitation and detection frequencies.

Numerous works cover the fundamentals of multidimensional optical spectroscopy methods,[120, 138] as well as 2DES specifically.[120, 139] Here, we briefly cover the concepts and nature of the results generated from 2DES experiments, especially with regard to how 2DES has emerged as a key probe of coherence in chemistry. Figure 1.12A and B show an example 2DES measurement in the time- and frequency domains, respectively. We note that these diagrams are produced in the energy eigenstate basis of the system Hamiltonian, and we have also assumed the impulsive limit. The bottom portion of Figure 1.12A illustrates a wave mixing energy level (WMEL) diagram for a four-level system (4LS), where the arrows each indicate a light-matter interaction and the time between each of these interactions represents a period of free-evolution of the system. The 4LS used here is a direct extension of the exciton Hamiltonian described in Figure

1.6 ([Section 1.4.2](#)). Here, the lowest energy state ($|G\rangle$) is the electronic ground state shared by the two excitonic excited states ($|E^+\rangle$ and $|E^-\rangle$). The $|F\rangle$ state is the doubly excited exciton state. For simplicity, we assume this toy model to capture an ensemble of molecular dimers held within an arbitrary bath that we capture phenomenologically.
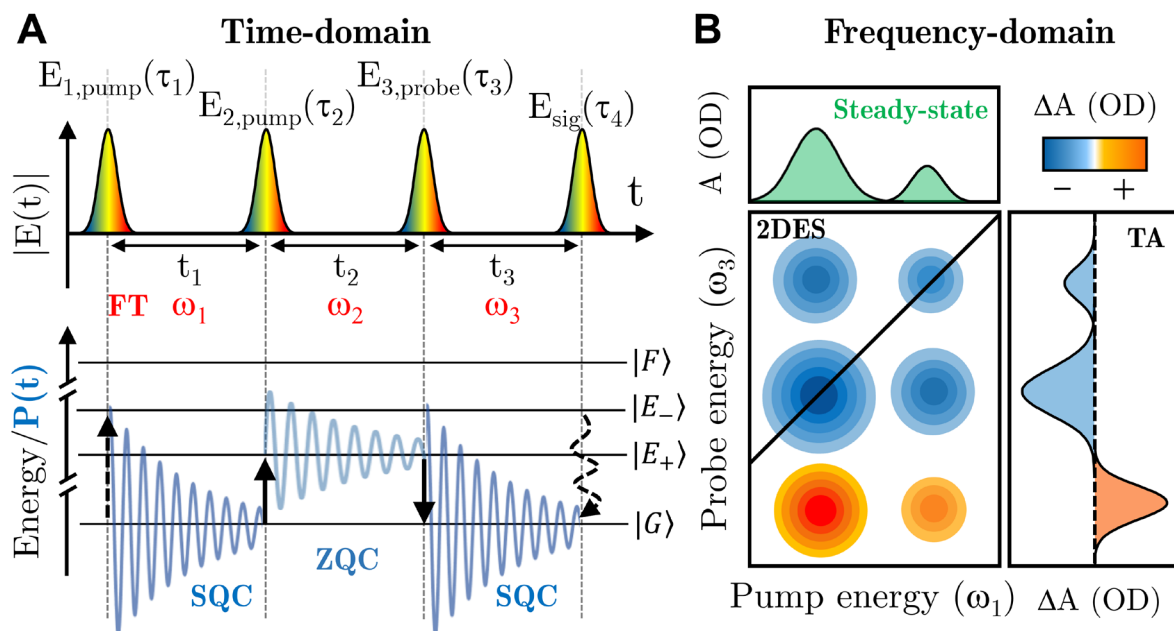
Figure 1.12. Time- and (B) frequency-domain representations of a two-dimensional electronic spectroscopy (2DES) measurement on an excitonic dimer system.

The time-domain 2DES measurement of this model system, as shown in Figure 1.12A, begins at time τ_1 with a resonant interaction between the pump electric field ($E_{1,pump}$) and the $\langle E^-|$ ← $\langle G|$ transition. This interaction generates an off-diagonal density matrix element between $|G\rangle$ and $\langle E^-|$, which is referred to as a single quantum coherence (SQC), as the superposition exists between two states with different electronic quantum numbers. The presence of the SQC is indicated by the damped oscillation (dark blue), which dephases due to system-bath interactions along the time delay between the two pump pulses (t_1) (often referred to as the coherence time). Note that the SQC present during t_1 is *identical* to that which is present during a linear absorption

measurement. We additionally note that the electronically excited portion of the SQC occurs on the *bra* side of the density matrix in this example, as indicated by the dashed vertical arrow in the bottom of Figure 1.12A.

For the purpose of latter discussions of coherence as measured by 2DES, the example signal generation pathway illustrated in Figure 1.12A (lower) exhibits coherences during each time delay. Note that this is but one example of the many possible Liouville pathways for this system. At τ_2, the second pump pulse ($E_{2,pump}$) pushes $|G\rangle$ to $|E^+\rangle$, after which point the system is described as a superposition between both excitonic states (which is referred to as a zero quantum coherence (ZQC) since the superposition exists between states that do not differ in electronic quantum number). The ZQC (light blue damped oscillation) evolves along the pump-probe time delay, or the waiting time (t_2). A third light-matter interaction at τ_3 from the probe pulse ($E_{3,probe}$) returns the system to a SQC between $|E^-\rangle$ and $\langle G|$, which evolves along the so-called rephasing time (t_3). Lastly, the macroscopic polarization *P(t)* emits a signal field at τ_4, which by convention always occurs on the bra side.[12]

Figure 1.12B illustrates frequency-domain spectra obtainable from linear absorption, 2DES, and TA measurements of the toy model in the lower part of Figure 1.12A. The shaded green trace at the top shows the linear absorption (*A*), with units of optical density (OD), as a function of pump energy (ω_1) and features two peaks, which originate from the two exciton transitions. The x-axis aligns with the pump energy (ω_1) x-axis of the absorptive 2DES spectrum because the x-dimension of *both* plots indicates the energy spectrum of the first SQC shown in Figure 1.12A. Both the 2DES and TA spectra in Figure 1.12B resolve the signal along the probe energy dimension (ω_3), which reports the energy content of the terminal SQC prior to emission of a signal

photon. Note that the ω_1 and ω_3 axes emerge from Fourier transformation (FT) of the t_1 and t_3 domains (see Section 2.5.2). In contrast to 2DES, TA does not resolve the ω_1 dimension. Hence, the 2DES spectrum at a constant t_2 value shows six differential absorption (ΔA) features whereas the TA trace reveals only three. The TA spectrum is equivalent to the summation of the 2DES spectrum along the pump axis, which will remain true as long as the pulse frequency spectra for both techniques remain identical. Note that the ΔA unit emerges as both techniques measure the difference in absorption detected with and without the pump pulse present.

Both 2DES and TA exhibit features of negative (blue) and positive (orange/red) value, which indicate the phase of the signal field emitted at τ_4. The non-rephasing, stimulated emission (SE) pathway shown in the WMEL diagram in Figure 1.12A radiates a signal field *in-phase* with $E_{3,probe}$ and therefore appear negative in ΔA space. Moreover, the energies of the first and last light-matter interactions (arrows) of Figure 1.12A indicates that this WMEL generates signal on the diagonal of the 2DES spectrum at ($\omega_1 = E_1$, $\omega_3 = E_1$). Both SE and ground-state bleach (GSB) yield negative ΔA features as the detector "sees" more light with the pump present compared to without. In contrast, excited-state absorption (ESA) signals are positive in sign and originate from FWM pathways involving higher-lying states that are not visible in the linear absorption measurement ($|F\rangle$ in this example).
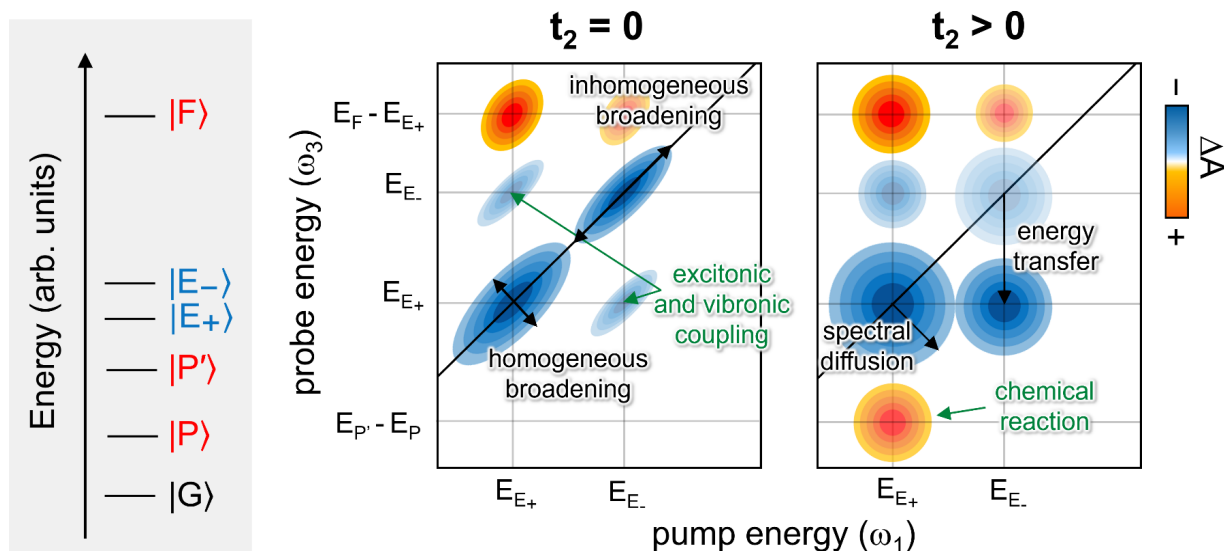
Figure 1.13. An energy level diagram (left) detailing electronic ground (G), singly (E_+ and E_-), and doubly (F) excited states, along with a photochemical product (P) and an associated high-lying excited state of the product (P'). At early waiting time delays ($t_2 \approx 0$), the 2D spectra for this model exhibit diagonally elongated peaks where the diagonal and anti-diagonal widths indicate the extent of inhomogeneous and homogeneous broadening, respectively. Cross-peaks at $t_2 \approx 0$ reveal couplings, such as the Coulombic coupling that yields the exciton states E_+ and E_-. With increased waiting times ($t_2 > 0$), the amplitudes and shapes of the spectral features evolve due to processes such as spectral diffusion and energy transfer. Evolution along a chemical reaction coordinate (production of P) can lead to new excited-state absorption pathways and the appearance of new positive-signed features.

The crosspeaks that occur between diagonal peaks in the 2DES spectrum in Figure 1.12B are the quintessential features that distinguishes TA and 2DES results.[54] For example, Figure 1.13 illustrates that at early waiting times ($t_2 \approx 0$), crosspeaks are evident between excitonic states $|E_+\rangle$ and $|E_-\rangle$ in the 2D spectrum (left).[54, 120] In contrast, as the system evolves over the waiting time (right spectrum), new peaks emerge that indicate chemical transformation. Growth of the crosspeak between $|E_+\rangle$ and $|E_-\rangle$ in the 2D spectrum in Figure 1.13 signifies downhill energy transfer between these states. Other crosspeaks may emerge, such as the positive peak below the diagonal that corresponds to ESA from the photochemical product $|P\rangle$ state, which could be a charge-transfer (CT) or excimer species, for example.[120, 139]

The waiting time dependence of 2DES spectra can also originate from spectral diffusion processes,[120, 139-141] which refers to the timescales over which the photoexcited wavepacket experiences sources of inhomogeneous broadening. At $t_2 = 0$ in Figure 1.13, the macroscopic polarization generated by the pump pulse has experienced zero evolution over the waiting time. Hence, while energy is pumped into the system according the spectral overlap of the pump and the inhomogeneously broadened sample absorption profile, the anti-diagonal linewidth is solely impacted by *homogeneous* broadening. The effect is that 2D spectra at early waiting times appear elongated along the diagonal direction (left spectrum in Figure 1.13). As the waiting time increases (right spectrum) and the polarization experiences sources of inhomogeneous broadening, the features of the 2DES spectra approach a circular shape (equal linewidth in both the diagonal and anti-diagonal directions).

1.5.4 Wavepackets and quantum beats

While 2DES is capable of measuring quantum coherence between adiabatic states through the presence of crosspeaks, the broad linewidths of electronic and vibronic transitions often hinder the visibility of crosspeaks, especially for room temperature measurements.[139] Fortunately, the evolution of 2DES spectra along the waiting time offers additional insight into coherence phenomena through the observation of *quantum beats*.[15] Quantum beats are intensity oscillations in spectroscopic signals that originate from superpositions of energy eigenstates, which are also often referred to as wavepackets.[22] Because the observation of quantum beats requires coherent preparation of wavepackets by a coherent light source,[11, 15] many have questioned the utility of such studies in learning about chemistry that occurs under incoherent illumination (e.g., photosynthesis).[1] The primary source of these tensions is the placement of too much emphasis on

the physical existence of quantum beats rather than the information that their artificial preparation and evolution affords. The ability to use coherent fields to prepare wavepackets of molecular states is the core discovery that launched the development of femtochemistry.[11] Zewail writes

> *"Molecular wave functions are spatially diffuse and exhibit no motion. Superposition of a number of separate wave functions of appropriately chosen phases can produce the spatially localized and moving coherent wave packet. The packet has a well-defined (group) velocity and position, which now makes it analogous to a moving classical marble, but at atomic resolution, and without violation of the uncertainty principle... Unless molecular and ensemble coherences are destroyed by intra- and/or intermolecular perturbations, the motion is that of a single molecule trajectory. This powerful concept of coherence lies at the core of femtochemistry and was a key advance in observing the dynamics."*

Quantum beats emerge in a variety of spectroscopic techniques and are extraordinarily powerful tools for probing physical properties of a system and revealing non-trivial coherence effects in chemical processes. The types of information provided by quantum beats depends on the nature of the wavepackets being prepared and the time and frequency scales over which they are probed. For example, vibronic wavepackets generated in TA and 2DES in the UV/visible/NIR wavelength regimes yield quantum beating signals containing information about vibrational frequencies,[15] Franck-Condon factors,[15, 142] energy gaps between vibronic states,[143, 144] and dynamic solvation timescales.[145, 146] Electron spin wavepackets produced in pulsed electron paramagnetic resonance (EPR) spectroscopy experiments manifest quantum beats in the signals that oscillate with a period proportional to the average distance between charges of a radical

pair.[147-149] Quantum beats in time-resolved femtosecond stimulated Raman spectroscopy (FSRS)[132] and two-dimensional impulsive stimulated Raman spectroscopy (2D-ISRS)[130, 131] stem from vibronic wavepackets and reveal quantum mechanical couplings between vibrational modes. For the sake of brevity, we limit our exploration of quantum beats in the following discussion to 2DES and TA measurements.

Figure 1.14 illustrates the distinctions between population (Figure 1.14A) and coherence (Figure 1.14B) dynamics in 2DES data.[150] The upper left portion of both Figure 1.14A and B illustrates WMEL diagrams for an arbitrary three level system, which correspond to the Feynman
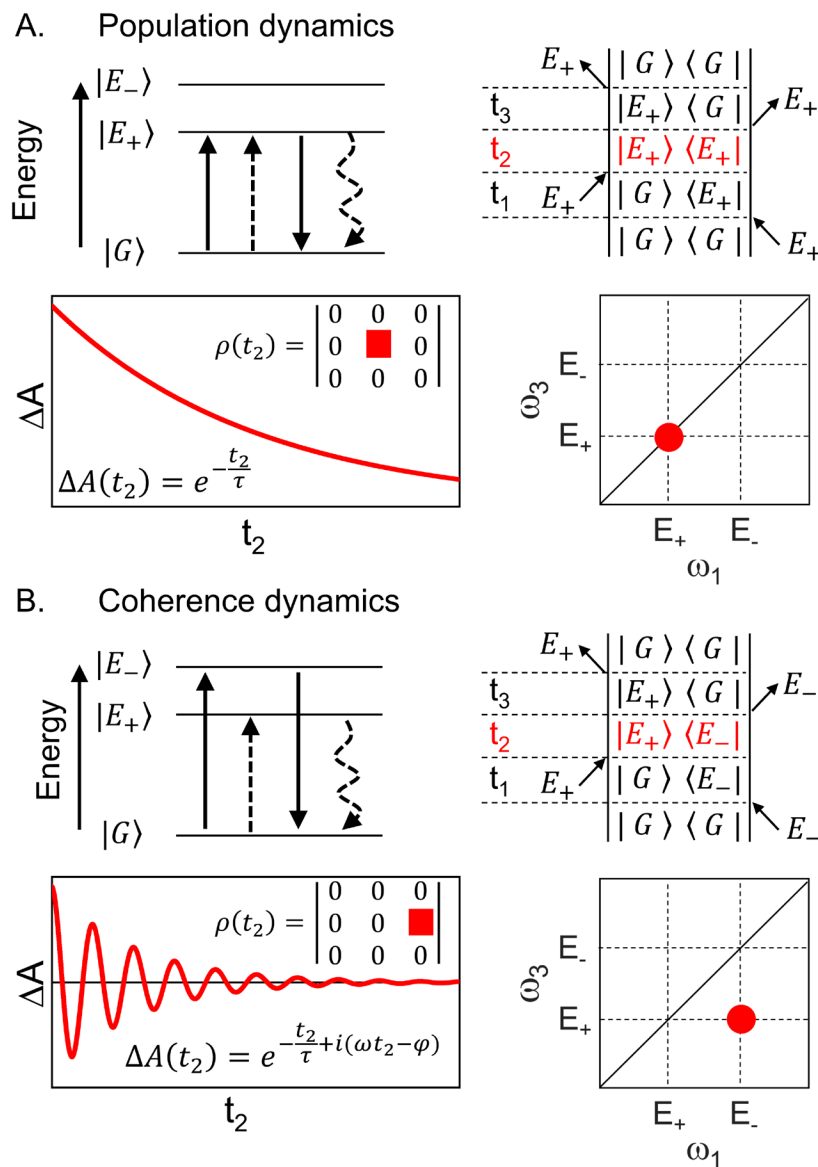
Figure 1.14. Example representations of (A) population and (B) coherence dynamics. Both (A) and (B) provide an example WMEL diagram (upper left), Feynman diagram (upper right), transient differential absorption signal (ΔA) (lower left), and the corresponding peak as measured by 2DES (lower right). The insets of the ΔA(t_2) plots indicate the functional form of the dynamics as well as the relevant entry of the density matrix. Each diagram is represented in the energy eigenstate basis. Portions of this figure were inspired by Collini and coworkers.[2]

diagrams shown to the right. Note that each Feynman diagram, which represents a single Liouville pathway of the system,[116] illustrates the evolution of the density matrix as a function of time (moving upward) and perturbation by impulsive light-matter interactions between each t_n interval. Population dynamics emerge from evolution of the diagonal elements (ρ_{nn}) of the density matrix

in the energy eigenstate basis. These track as non-oscillatory transients in the 2DES signal (lower left portion of Figure 1.14A) that are characterized by a lifetime parameter (τ). In contrast, the evolution of coherences (ρ_{nm}) manifests as a complex-valued exponential function (lower left of Figure 1.13B), which oscillates with a period related to the energy separation between eigenstates n and m and dephases on timescales dictated by population evolution and/or system-bath interactions (φ). The example population and coherence pathways illustrated by Figure 1.14 impact 2DES spectra in distinct locations, as shown by the lower right plots of both Figure 1.14A and B. Note that populations and coherences can impact both diagonal and off-diagonal signals; Figure 1.14 simply shows one possible case for both.

Quantum beats in 2DES signals alone have a wide range of distinguishing characteristics that provide different, yet complementary pieces of information about chemistry. For example, analysis of purely rephasing and/or non-rephasing 2DES signals, which are complex valued, yields the Fourier power of both negative and positive beat frequencies.[150-153] Song and coworkers[151] have shown the positive beat frequencies in the rephasing portion of the 2D signal can reveal beats from purely excited-state wavepacket evolution. Moreover, the amplitude distribution of quantum beats with respect to the excitation and emission frequencies in 2DES datasets is well-known to provide a wealth of information about upon the nature of the wavepackets driving the quantum beats.[15, 16, 154] A review from Dean and Scholes[15] demonstrates how the amplitude distribution of beats are examined by so-called *quantum beatmaps* after signals from population evolution are removed from 2DES data. Work from Butkus et al.[154] established that chemical systems well-described by the displaced harmonic oscillator Hamiltonian manifest markedly different quantum beatmaps than those from a purely electronic dimer. Schematics of these two models are shown in

the top row of Figure 1.15. The middle row of Figure 1.15 illustrates the general process of separating quantum beat signals from population dynamics, followed by Fourier transformation along t_2 to the ω_2 domain. In contrast to analyzing beats in the purely absorptive 2DES signals, focusing the analysis on the rephasing (photon-echo) and non-rephasing (free induction decay) signals enables unique insight to be gained from both positive and negative beat frequencies. The fundamental meanings and methods for separating rephasing and non-rephasing signals are discussed at length elsewhere,[120] as well as in Section 2.5.1 and Chapter 6. The utility of this characteristic is evident in the lower row of Figure 1.15, where the positive and negative frequency quantum beatmaps share several distinctions with each other and also between both molecular models (displaced harmonic oscillator and electronic dimer). Many have used these distinction in 2DES quantum beatmaps to assess the vibrational versus electronic (or mixed vibronic) character of quantum beats from natural[143, 155, 156] and artificial[144, 157-161] light-harvesting systems.
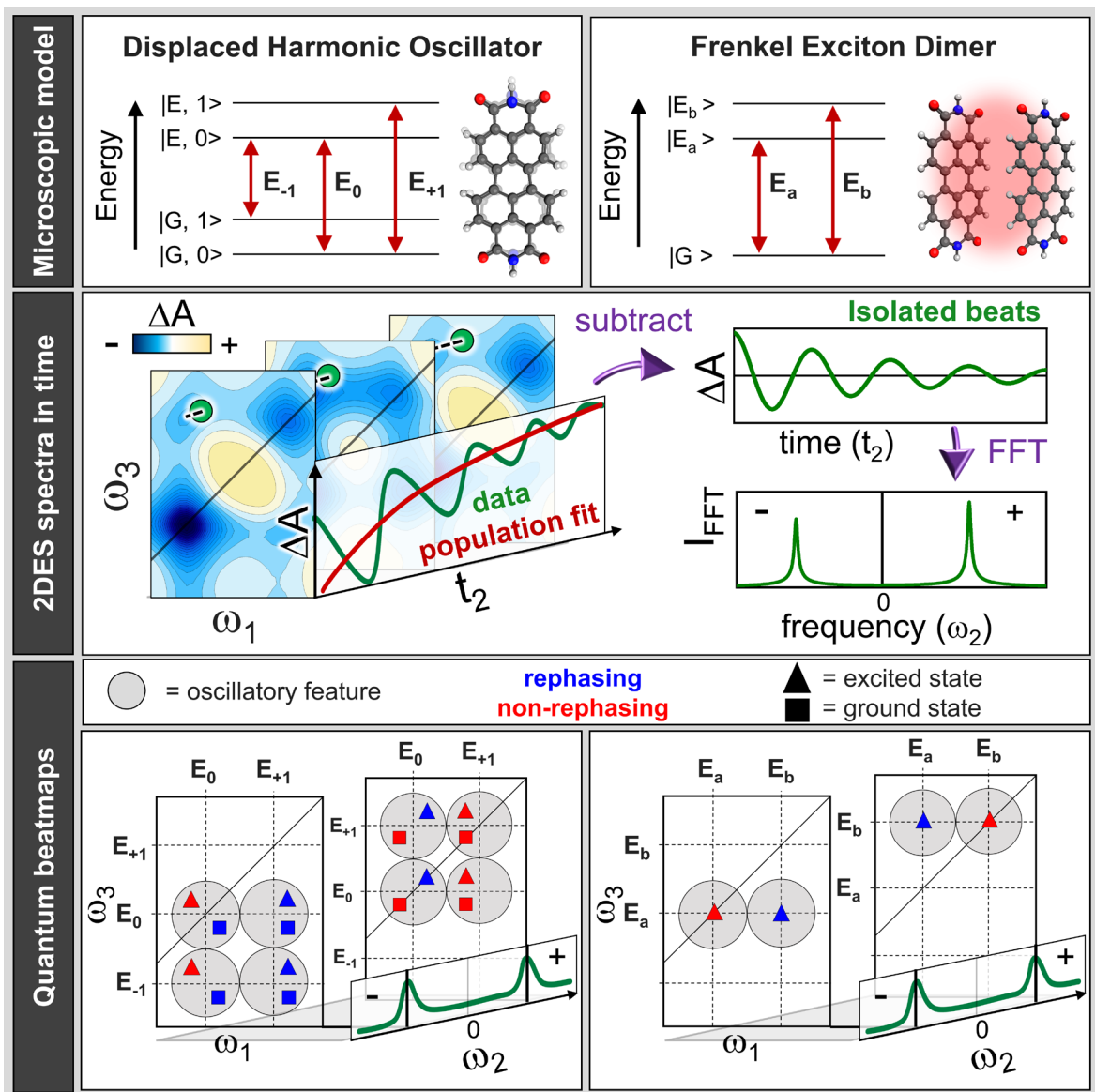
Figure 1.15. Energy level diagrams for the displaced harmonic oscillator (upper left) and electronic dimer (upper right), along with a schematic illustration of the procedure for separating and analyzing the Fourier power of quantum beats. The bottom row shows cartoon quantum beatmaps for both molecular models, as predicted with Liouville pathways. Details of the beatmap features are clarified by a key included at the top of the lower row.

Peaks in quantum beatmaps have also been used to observe coherence transfer processes,[153, 157, 162] which indicate movement of reactant wavepackets to product-regions of the

potential energy surface with maintained phase. These details can provide information about the mechanism of photochemical processes, such as key vibrational motions that lie at least partially along the reaction coordinate. On the other hand, numerous studies have observed instances of impulsive excitation of vibrational coherences by ultrafast charge transfer (CT) processes.[163-165] In other words, the extremely short rate for CT results in production of wavepackets on the product surface, similar to how an ultrashort laser pulse prepares reactant wavepackets. Evidence for coherence transfer and impulsive reaction events observed through either 2DES or TA are often corroborated by short-time Fourier transformation (STFT) and/or wavelet transform (WT) analyses to reveal the time-evolution of beat frequencies, which Volpato and coworkers have described at length.[166, 167] These analyses have been used to reveal timescales for inhomogeneous broadening,[168] chemical exchange,[165] and production of optically dark intermediates.[169]

A key takeaway of this section is that *quantum beats are dependent on parameters both from the molecular system as well as the measurement apparatus*. When viewed through the expectation value of the transition dipole operator of a molecular ensemble, a prerequisite for observing quantum beats is interaction between the system and a coherent source of light, such as a pulsed laser. This is because any unitary evolution driven by a purely incoherent light source evolves with random phase and therefore does not survive the calculation of an ensemble average. Hence, it is extremely unlikely (and some argue impossible) to observe quantum beats in signals emitted ensemble dynamics driven by sunlight, for example. Since quantum beats can only be measured when a system is placed in a non-equilibrium initial condition with a well-defined phase, quantum beats are dependent on coherence of the measurement apparatus itself, including the duration and spectral bandwidth of the laser pulses.

We reiterate that since coherent light sources are required to observe quantum beats,[22] the coherent wavepackets that underlie quantum beats are not present in photochemistry driven by incoherent radiation such as sunlight. *On the other hand*, quantum beats are intrinsically connected to the eigenstates of the chemical system under investigation, and therefore are a powerful tool for probing these molecular properties. As we discuss in the following section, tensions have historically surfaced when the spotlight is focused too much on the *physical existence* of quantum beats rather than the information that their artificial preparation and evolution affords.[19]

1.6. Coherence in natural photosynthesis

Natural photosynthesis is an exemplary example of the exquisite machinery that nature has constructed through billions of years of evolution. Understandably so, photosynthesis has fascinated scientists across many fields of study for numerous generations.[170] Decades of research have unveiled a detailed picture of the hierarchical structure (in time and space) of photosynthetic chromophore-protein complexes that serve as a conduit between the sun and key small-molecule nutrients on Earth. A vital design principle that photosynthetic organisms employ is bottom-up architecture. Here, interactions on the femtosecond timescale and nanometer length scale form the foundation of a network of antennas and reaction centers which enable the transport and repurposing of energy absorbed by the embedded chromophores. As this architecture is intrinsically dependent upon molecular-scale interactions, the role that quantum mechanics may play in guiding macroscopic photosynthetic light-harvesting is a long-standing question.[1, 171]

Molecular excitons (Section 1.4.2) play important roles in natural photosynthesis.[172, 173] In a purely electronic picture of a photosynthetic aggregate, each monomeric unit, typically a chlorin-based chromophores (e.g. chlorophyll, bacteriochlorophyll, pheophytin, etc.), is described by

ground and singly excited electronic quantum states. As described earlier, the system Hamiltonian for a collection of chromophores is diagonal in the site basis when the molecules are spaced infinitely apart. However, as chromophores are brought to close proximity, as is found within natural light-harvesting aggregates, coupling between the individual electronic wavefunctions can yield off-diagonal elements of the site-basis Hamiltonian. Diagonalization of this purely electronic Hamiltonian reveals that the system eigenstates are linear combinations of the site-basis electronic wavefunctions. These states, which are delocalized across multiple chromophores, are referred to as excitons and are a clear example of how quantum coherence is employed by photosynthetic organisms.[171]

In the 1990s, several reports of signal oscillations in time-resolved spectroscopy experiments raised new questions regarding the roles of coherence in photosynthesis.[174] These signal oscillations are generally referred to as *quantum beats* (Section 1.5.4) and arise from evolution of eigenstate superpositions, such as those generated by ultrashort (tens of femtoseconds) laser pulses.[15] For more information regarding quantum beats and spectroscopic probes of coherence, refer to Section 1.5. Note that while quantum beating signatures are a *property* of signals that emerge from the macroscopic polarization, they can reveal a wealth of information regarding coherence *intrinsic* to the Hamiltonian of a chemical system. As will become clear later in this section, the utility of quantum beating signatures is often obscured by the tendency of discussions to focus on the characteristics of the beats themselves rather than the system and/or system- bath couplings that they originate from.

In 1993, Vos et. al. provided evidence for excited-state evolution of nuclear wavepackets occurring on similar timescales as electron transfer (ET) in a purple bacterium, Rhodobacter

capsulatus, mutant.[175] The authors used near-infrared (NIR) pump-probe spectroscopy to launch electron transfer in the purple bacterium reaction center and found that several oscillations with varying frequencies (on the scale of 100 cm^1) were present in the transient signals. Prior to this work, Vos et. al. had reported similar oscillations,[176] but were unable to assign the dynamics to vibrational or electronic evolution. In their 1993 work, Vos et. al. leveraged the dependence of the beating amplitude on the probe wavelength to assign their origin to vibrational wavepackets on the electronic excited state of the bacterial reaction center. This type of analysis laid the groundwork for the more elaborate analyses of quantum beatmaps, which are discussed in Section 1.5.4.

Subsequent reports found oscillatory features in transients from a variety of additional photosynthetic systems.[177-181] We refer readers elsewhere[13, 16, 182] for more detailed coverage of this expansive area of research. One of the first assignments of electronic coherence emerged from Savikhin et al. in 1997, where they studied optical anisotropies of FMO trimers.[180] Though uncertainties regarding the roles of nuclear versus electronic coherence in photosynthesis already were evident in the 1990s, the majority of these works agree that the early-time dynamics within photosynthetic systems did not necessarily occur along completely thermalized population distributions, which the Förster description of photosynthesis relies upon.[13]

It is important to note that coherence of the photosynthesis *process* was not inferred in the 1990s by the observations of quantum beats. Instead, the focus largely remained on using the electronic structure information afforded by the quantum beats to examine the role of exciton localization in the primary events of photosynthesis.[180] Concurrent with the optical measurements, the early 1990s also featured several reports of quantum beats in transient electron paramagnetic resonance (EPR) experiments performed on photosynthetic reaction centers.[183-185] Together, these

works set the stage for decades-long debates concerning: (1) the underlying origin of these quantum beats as well as (2) the potential mechanistic role that quantum mechanical effects play in governing the function of both antenna and reaction center systems–the initial drivers of photosynthetic activity.

A 2007 Nature publication from Engel et. al.[186] proved extraordinarily influential to field of quantum biology and its popularization in the eyes of the general public. The authors examined the ultrafast dynamics of energy transfer within the FMO photosynthetic complex using 2DES (Section 1.5.3), from which they observed "long-lived signal oscillations." These persistent quantum beats were assigned to quantum coherence between electronic eigenstates.[186] This assignment marked a departure from previous studies, which ascribed similar signals to nuclear wavepackets, and sparked heated debates[1] over the origin[107, 187] and mechanistic function[23, 188] of the beating signals. As we will discuss below and throughout this dissertation, insights several years after the 2007 publication brought the vibrational underpinnings of the quantum beating signatures back to the forefront.

While the issue of origin for the quantum beats was overcome in the mid- to late-2010s, the mechanistic interpretation of the beats remains to this day.[1, 16] Engel et. al. postulated that the temporal persistence of the quantum beats indicates that nature evolved to protect and employ electronic coherence in FMO, possibly to boost the efficiency of harvesting incoherent sunlight. This train of thought implies the following physical insight: Superpositions of eigenstates underlie energy migration within photosynthetic complexes, *regardless of the initial state prepared by the photoexcitation event*. This claim was and remains quite controversial in the scientific community.[1, 16] While it is widely accepted that quantum coherent couplings are leveraged in

natural photosynthesis via phenomena such as excitons,[171, 172] the suggested functional importance of off-diagonal elements of the energy eigenstate density matrix faced significant skepticism.[1, 16] This is because in order for superpositions of eigenstates to be important in natural photosynthesis, they must exist independently from the nature of the excitation field.[58] Time-resolved spectroscopies employ coherent pulses of light, in contrast to the incoherent sunlight that fuels photosynthesis in nature. Moreover, since electronic states couple to each other and the surrounding bath via numerous mechanisms across a significant frequency range (i.e. broad spectral density), electronic eigenstate coherence is predicted to survive for less than 100 fs at room temperature,[156] which is corroborated by the broad homogeneous lineshapes one directly observes in time-domain 2DES spectra.[188] Some groups hypothesized that photosynthetic complexes evolved protein scaffolding to shield eigenstate superpositions from the rapid decoherence effects of the bath.[189-191] Despite several investigations into the encapsulating protein environment around Chl aggregates, [189-191] this hypothesis has yet to be supported by conclusive experimental evidence.[16] In contrast, several experimental studies between 2014 and 2022 have shown that purely electronic coherences do indeed dephase on the timescale of 10s of fs at physiological conditions.[156, 187, 192]

The report from Engel and coworkers[186] in 2007 sparked a frenzy of research thrusts centering on examining quantum effects within complex, condensed-phase systems. Numerous reports of similar observations from additional photosynthetic complexes solidified interest in how quantum beats emerge from both photosynthetic antennas and reaction centers, as discussed elsewhere.[13, 193] In 2011, Womick and Moran posited in a that *coupling between nuclear and electronic degrees of freedom* could explain the robust and efficient energy transport capabilities

of biological light harvesting frameworks (i.e., the origin of the quantum beating signatures is vibronic rather than purely electronic or vibrational).[194] The authors elaborated that while heterogeneity in the local environments of individual chromophores in photosynthetic aggregates acts to hinder the survival of electronic coherence, this heterogeneity actually promotes vibronic coupling, a phenomenon which is discussed at length in Section 1.4.4. Two famous approximations in quantum mechanics, the Born-Oppenheimer (BO) and Condon approximations, rely on the assumption that electronic and nuclear degrees of freedom can be solved separately due to the drastic difference in the timescales for electronic versus nuclear evolution. These approximations are used ubiquitously to calculate the adiabatic potential energy surface. Nonetheless, Tiwari and coworkers[107] found that the BO approximation can breakdown in the event of a near-resonance between the frequency of an anti-correlated pigment vibration and an electronic energy gap between two or more chromophores. The resulting non-adiabatic coupling acts to form highly delocalized states that are vibronic in nature. A key piece of evidence supporting their theory was the prediction of an off-diagonal quantum beating signature in experimental 2DES results that had not been accounted for with the prior, purely electronic frameworks.[107] Compared to the case of purely electronic excitons, the spatial delocalization afforded by vibronic coupling (in combination with system-bath interaction strengths on a similar energetic scale) can open additional transport channels by which the excitation can navigate to the reaction center.[13] Therefore, coherence driven by vibronic coupling is theorized to explain enhancements of energy transport rates and efficiencies compared to purely incoherent transport.[58, 106, 195]

A better understanding of the vibronic exciton model and its effects on 2DES signals was fervently pursued after 2011.[154, 160, 161] Butkus et. al. showed that quantum beatmaps (Section 1.5.4)

from a 2DES measurement should be markedly different depending on whether a displaced Harmonic oscillator or an electronic dimer are being probed.[154] Refer to Figure 1.15 of Section 1.5.4 and the associated text for further information. Readers can also visit several recent review articles[15, 16, 139] that discuss quantum beatmaps. The separability of vibrational versus electronic molecular models based on their quantum beating patterns has been heavily relied upon, including in this dissertation (Chapters 5 and 6), in efforts to pin down the physical origin of quantum beats from natural and artificial photosynthetic systems. For example, Dean and coworkers[143] revealed the presence of vibronic interactions in the light-harvesting complex phycocyanin 645 (PC645) by examining quantum beatmaps from the rephasing and non-rephasing portions of the third-order signal. Compared to the evolution of purely vibrational wavepackets, vibronic coherences increasingly modulate the off-diagonal and on-diagonal portions of the rephasing and non-rephasing signals, respectively.[143, 144, 154] Dean and coworkers observed this trend in the quantum beatmaps for PC645, which they reproduced in spectral simulations using the vibronic exciton model.[143]

Theoretical tools for interpreting complex quantum beating signatures continue to be indispensable in efforts to understand coherence phenomena in natural and artificial light harvesting. Tempelaar and coworkers[187] performed simulations using a Holstein-type Hamiltonian and found that the beatings observed in seminal 2DES experiments[186] were primarily vibrational, rather than electronic, in nature. Since the simulation calculates all portions of the third-order response function separately, Tempelaar et al. were able to compare quantum beating signatures emerging from purely ground- (vibrational) and excited-state (vibronic or electronic) coherences. They observed that purely electronic coherences between excitonic states of FMO generate beats

with significantly less intensity and faster dephasing than beating from ground-state vibrational wavepackets. Using a similar theoretical framework, a joint theoretical/experimental study by Halpin et al.[160] provided the first experimental evidence that vibronic coupling increases coherence lifetimes in comparison to purely electronic coherence. They also demonstrated that synergy between synthetic design and theory can enable experimental extraction of 2DES signals that *selectively* identify beating from vibronic states.[160] Hauer and coworkers reported similar findings for coherences observed from quantum beats in the optical response of self-assembled j-aggregates.[161, 196] While the emerging consensus overwhelmingly suggested the vibronic origin of many of the observed signals, these conclusions rely completely on interpretation of spectra, as opposed to comparisons between rates or efficiencies of energy transfer. The role of quantum mechanical effects in photosynthesis continues to be an area of vigorous research.

As a final comment, it is often not clear that the connections between vibronic coupling and natural photosynthesis emerged long before the controversy following Engel and coworkers' 2007 paper.[186] For example, Skourtis and coworkers[197] wrote in 1992 regarding the primary charge separation in photosynthetic bacteria:

"We propose that this reaction may lie in a regime that is different from the traditional nonadiabatic (golden rule) regime... we propose that vibrational relaxation in the charge-separated state might well compete with the rate of initial electron transfer. To describe such a regime, we abandon the nonadiabatic theory and suggest that in the case of this reaction, the vibronic mixings between initial and final vibronic states are of the same order of magnitude as the vibronic widths of the final states. When this is true, the transfer rate competes with relaxation in the final vibronic manifold."

Despite its clear relevance to widespread research thrusts over the subsequent three decades, this report has gone largely unrecognized in the 21st century (only *six* of 50 citations come after the year 2000, excluding self-citations, according to Google Scholar).

1.7. Dissertation motivation

Research motivated by coherence effects in biological photosynthesis has provided ample evidence that off-diagonal density matrix elements between excitonic states *do not* play a significant function in photochemistry driven under physiological conditions.[16, 58, 156] Moreover, the predictions of transport rate enhancement[106, 155] from vibronic coupling have yet to be experimentally validated, much less integrated into artificial light harvesters. Nonetheless, the field of quantum biology has sparked a re-examination of vibronic excitons and their influence on photochemical processes in synthetic systems. In comparison to biological architectures, the tunability and broad range of exotic photophysics exhibited by synthetic materials offer unprecedented opportunities to better understand and exploit vibronic coherence in molecular technologies. For example, by leveraging chemical synthesis alongside advanced experimental probes and theoretical models, Halpin and coworkers[160] reported the first direct characterization of vibronic coherence, a feat that was not achieved in the context of biological samples until nearly four years later and with the help of meticulous experimental upgrades.[156] This single example highlights the ability of synthetic, experimental, and theoretical collaborations to hasten studies of quantum coherence without relying completely on additional technological development.

Despite the substantial progress that has been made in recent years toward understanding coherence effects in synthetic architectures, many questions surrounding the salient functions and governing factors of quantum coherence still remain. For example, organic photovoltaic

technologies rely on solid-state architectures, where excitations are prone to a broad distribution of intermolecular interactions and orientations. How and to what extent do key molecular-scale variables impact mixing between electronic and vibrational dynamics? Moreover, though vibronic coupling has been explored extensively in EET contexts, the function of this coupling in other useful photophysical processes, *particularly those leveraged in synthetic photovoltaic technologies*, remains comparatively opaque. A growing body of research suggests that both BO and HT vibronic couplings play non-trivial roles in a wide range of photophysical processes beyond energy transfer, such as singlet fission,[158, 198-209] charge transfer,[164, 210-218] and structural phase transformations.[37, 219] This is an exciting area of research as several of these processes underlie the efficiency of emerging photovoltaic technologies. For example, symmetry-breaking charge separation (SB-CS) is a promising photochemical reaction to OPV devices, as SB-CS generates free charges with low driving force for charge separation (translating to less energy dissipated as heat).[220, 221] As the driving force approaches the energy scale of vibrational frequencies,[220] considerable effects from vibronic coupling may offer ways to control and optimize SB-CS dynamics. Understanding the generalized function(s) and tunable parameter space(s) of vibronic coupling in synthetic contexts is *vital* for designing next-generation photovoltaic and optoelectronic devices.[19, 222]

Vibronic coupling, and excited-state coherences in general, are fragile. Experimental factors such as pulse compression, signal-to-noise ratio, stability of the laser and samples, and background signal from the electronic ground state all impede efforts to understand vibronic coherence. These factors are amplified by complexity at the molecular scale (e.g., energetic and conformational disorder, distributed kinetics, etc.), of which biological light harvesters and self-

assembled macromolecular systems exhibit no shortage. The disconnect between the major developments in understanding vibronic coherence and actualization of its benefits owes in part to the lack of studies focusing on small molecular systems with high control over interchromophoric interactions. Thus, there is a need for investigations of well-defined, precisely tunable structures that feature small numbers of chromophores, such as dimers and trimers, from which design principles regarding larger light harvesting arrays can be developed. The present dissertation follows this bottom-up approach through investigations of vibronic coherence in model synthetic systems.

1.8 Dissertation outline

This dissertation aims to build upon current understandings of (1) factors that influence vibronic coupling in multichromophoric systems and (2) the roles of vibronic couplings in the photophysics of model organic assemblies. Chapters 2 and 3 describe in detail the experimental and theoretical tools, respectively, that we employed in the research covered by subsequent chapters. The translation of signals from multidimensional spectroscopy (both experimental and theoretical) into chemical insight requires extensive data processing and presentation. Chapters 2 and 3 therefore serve as roadmaps for understanding the data and figures throughout this dissertation. While some readers may find nonlinear spectroscopy methods to be abstract, they provide a unique manner of investigating the microscopic couplings that govern the eventual outcomes of energy deposited into a material.

Chapter 4 investigates the nature of vibronic coherences in rigid cyclophane architectures that each hold two perylenediimide (PDI) monomers in a close-packed, cofacial geometry. We discuss the possible influence on quantum beats from distortions mediated by Van der Waals

forces between the π-stacked PDIs, as opposed to vibronic enhancement of beating signals. The observations drawn from 2DES measurements in this work are supplemented by FSRS experiments and DFT computations, which is a combination used again in both Chapters 5 and 6.

Chapter 5 assesses the mechanism of ultrafast (< 100 fs) singlet fission in a linear terrylenediimide (TDI) dimer, which appears to be influenced by multi-mode vibronic couplings. Interpretation of the 2DES results, in the context of a massive, multi-vibration Hamiltonian that treats both singlet and correlated triplet diabatic states, clarifies the nature of the state-mixing and ultrafast dynamics in this TDI system.

Chapter 6 provides a thorough analysis, backed by theory and experiment, of how coupling between purely harmonic oscillators manifests directly in the quantum beating signatures from 2DES measurements. We show that this coupling, which has been largely overlooked in prior experimental 2DES studies, can lead to the breakdown of a common assumption that is used to analyze excited-state coherence signatures. Experimental validation of this framework is based on measurements from several molecular dyes, including TDI and the non-fullerene acceptor ITIC.

We conclude with Chapter 7, which offers a brief recap of the dissertation, along with a discussion of the outlook for future studies of vibronic coupling and coherence in organic molecular aggregates.

Chapter 2: Experimental instrumentation and methodology

2.1 Introduction

Spectroscopy is an indispensable experimental tool that scientists use to better understand the properties and behaviors of chemicals. This section overviews key detail of the equipment and analyses that enabled the molecular understanding discussed throughout this dissertation. As mentioned in the Acknowledgements, Drs. Eileen Foszcz and Aritra Mandal established the 2DES instrumentation in the Wasielewski lab and laid the foundation for the work presented in this dissertation. With unwavering help from Dr. Taeyeon Kim, James O'Connor, and Karen Ji, this instrumentation has advanced substantially over the years.

2.2 Sample Preparation

All measurements in this work were performed on solution-phase samples. Each analyte was dissolved in a solvent such that the maximum optical density of the solution in a glass cuvette (1 mm pathlength) was between 0.2 and 0.8. While depositing solution into a glass cuvette, we filtered the sample using 0.2 μm PTFE syringe filters to remove any macroscopic particulates (which tend to cause issues through scattering light).

2.3 Steady-state spectroscopy

Steady-state UV/Visible absorption spectra for room temperature solutions of each compound were collected by a Shimadzu UV-1800 spectrophotometer.

2.4 Pulsed-spectroscopy

2.4.1 Pulse characterization

A commercial second-harmonic generation frequency resolved optical gating (SHG-FROG) instrument (Mesa Photonics Inc.) was used to visualize transient absorption (TA) and two-dimensional electronic spectroscopy (2DES) pump pulses in the time domain. We used this

information to determine chirp correction parameters (see Section 2.4.2) that engendered the shortest pulse duration obtainable. Figure 2.1 illustrates a representative SHG-FROG trace where the measured pulse width was approximately 10 fs.
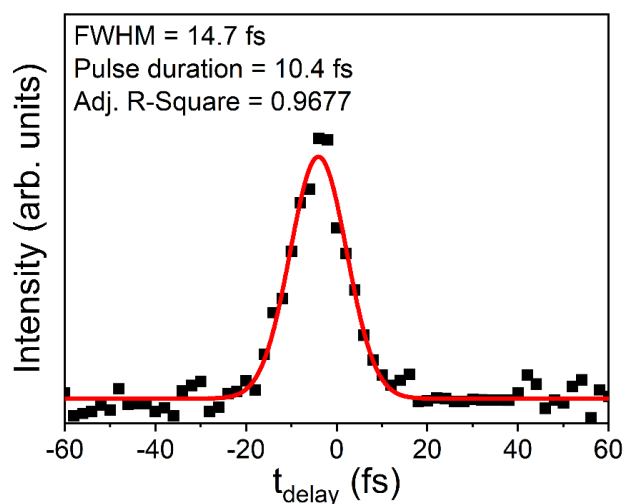
Figure 2.1. An example SHG-FROG trace at 313 nm for the pump pulse overlaid with a Gaussian fit (FWHM = 14.7 fs), indicating a pulse duration of approximately 10 fs.

Polarization-gated frequency resolved optical gating (PG-FROG) measurements were performed to determine the frequency-dependent instrument response function between the pump and probe pulses under similar experimental conditions to those used in analyte measurements. These measurements were conducted with the dispersion-corrected pump pulse as the gate and the white-light supercontinuum as the probe (same beam geometry utilized for 2DES experiments, Section 2.4.2). We used a polarizer to minimize the probe intensity on the spectrometer and rotated the polarization of the pump pulse 45° relative to that of the probe. Both beams were spatially and temporally overlapped in a 1 mm cuvette filled with neat solvent. Figure 2.2 shows representative PG-FROG signal (pre-time zero signal subtracted) obtained for two spectral regions of interest to the measurements discussed in Chapter 4.
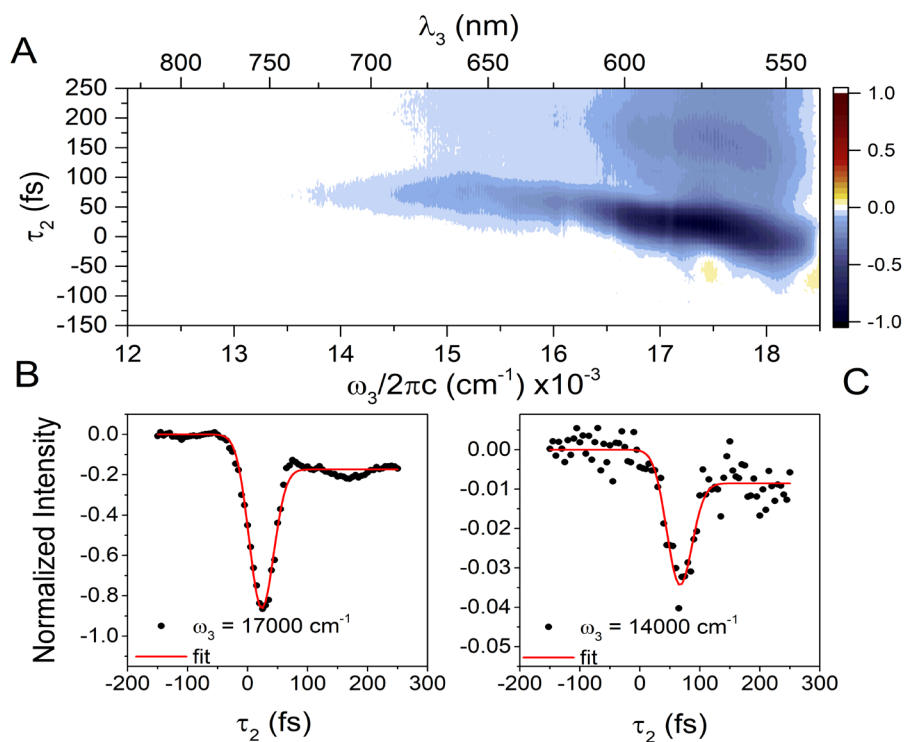
Figure 2.2. (A) OKE signal and example time-domain slices at (B) $\omega_3 \sim 17000$ cm^{-1} and (C) $\omega_3 \sim 14000$ cm^{-1} of the OKE trace overlaid with a Gaussian-shelf convolution fit (FWHM ~48 and 49 fs respectively).

2.4.2 Two-dimensional electronic spectroscopy

For two-dimensional electronic spectroscopy (2DES) experiments, the 1040 nm fundamental output of a Yb:KGW regenerative amplifier system at 100 kHz (Spirit 1040-4, Spectra Physics, Inc.) to generate femtosecond pulses in a noncollinear optical parametric amplifier (Spirit-NOPA, Light Conversion Inc.) to be used for the pump. These pulses were frequency dispersed into a tellurium dioxide (Chapter 4) or quartz (Chapters 5 and 6) acousto-optic modulator (AOM)-based pulse shaper to create two time-ordered pulses from each input pulse and to correct for dispersion.[52] In some experiments, masks to compensate for the frequency-dependent Bragg angle[223] were employed to help compress the pulse. The two time-ordered pump pulses generated by the pulse shaper with coherence time delay (t_1) were focused at the sample position with dispersion-corrected white light (WL) probe pulses spanning approximately 500-1000 nm.

2DES experiments were conducted in the pump-probe geometry using a commercial 2D spectrometer (2DQuickVIS, Phasetech Spectroscopy, Inc.). This apparatus is interfaced with Phastech's QuickControl (QC) software. Unless otherwise stated, the pump and probe were parallel in polarization and the pump energy at the sample was approximately 10 nJ/pulse. Data were collected in the rotating frame and sampled along t_1 with either a 3 or 4 fs step size (depending on the bandwidth of the pump pulse). The data with respect to t_1 were Fourier transformed in post-processing (see Section 2.5) to produce the ω_1 axis of the 2D spectrum, which thereby reflects energies provided to the chemical system via the pump pulses. For each t_1, spectra that reflect the third order signal heterodyned with the probe are collected to create the ω_3 dimension. The delay between the second pump and the probe pulses (the waiting time t_2) is controlled by a digital delay stage.
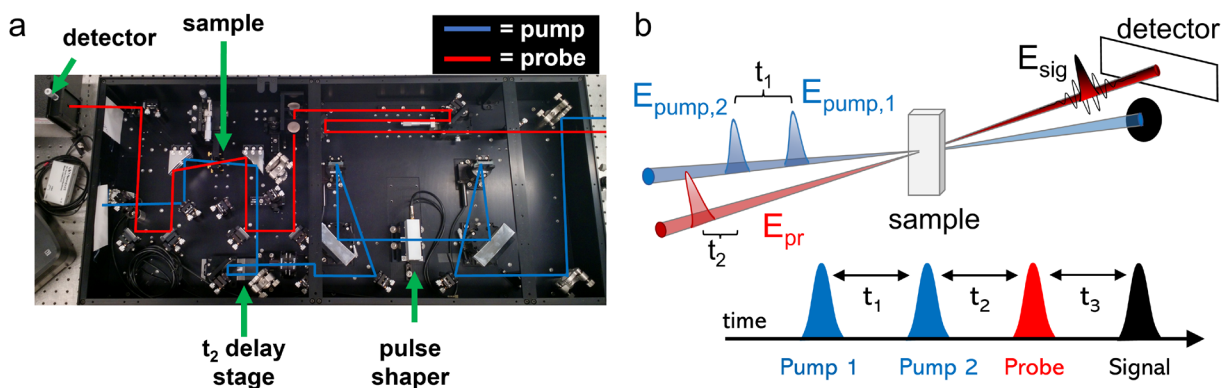
Figure 2.3. (a) Diagram of commercial 2D spectrometer (2DQuickVIS, Phasetech Spectroscopy, Inc.) and (b) a schematic for 2DES in the pump-probe geometry with time delays identified.

We used four-frame phase cycling to remove transient absorption and pump scatter background signals from the 2DES data. We collected data using each of the following relative pump phases ($\phi_{i=1,2}$), where S indicates the raw signal on the CCD array:

$$S_1(\phi_1 = 0, \phi_2 = 0); \; S_2(\phi_1 = 0, \phi_2 = \pi); \; S_3(\phi_1 = \pi, \phi_2 = \pi); \; S_4(\phi_1 = \pi, \phi_2 = 0) \qquad \text{Eq. 10}$$

$$S_1(\phi_1 = 0, \phi_2 = 0); \; S_2(\phi_1 = 0, \phi_2 = \pi); \; S_3\left(\phi_1 = 0, \phi_2 = \frac{\pi}{2}\right); \; S_4(\phi_1 = 0, \phi_2 = \frac{3\pi}{2}) \qquad \text{Eq. 11}$$

Measurements with Eq. 10 yield absorptive 3rd-order signals *de facto*.[50] In contrast, for measurements using Eq. 11, we used established methods to extract the absorptive, rephasing, and non-rephasing signals.[50, 224]

We averaged between 1000 and 10000 laser cycles for each 2D spectrum depending on the sample optical density. To evaluate quantum beating signatures, series of spectra were collected as a function of t_2. This delay was scanned from -100 to between 1500 and 2500 fs with a fixed timestep (between 5 and 10 fs depending on the project). Elements of data analysis for 2DES experiments are covered in Section 2.5.

2.4.3 Femtosecond stimulated Raman spectroscopy

FSRS measurements operate using the 800 nm, 35 fs fundamental output of a regeneratively amplified 1 kHz Ti:Sapphire laser system (Spitfire Pro XP, Spectra Physics, Inc.). The Raman pump is generated via a second harmonic bandwidth compressor pumping an optical parametric amplifier (SHBC/TOPAS-400, Light Conversion, LLC). The broadband WL Raman probe is produced by focusing the fundamental 800 nm light into an H_2O/D_2O mixture. The Raman pump was adjusted to approximately 2 μJ/pulse at the sample and parallel in polarization with the probe for the measurements described in this dissertation. Data were processed into Raman gain by dividing the heterodyned signal and probe spectrum with the Raman pump incident by the probe spectrum without the pump present. For excited-state experiments, a tunable actinic pump (ca. 1 μJ/pulse) is generated via an optical parametric amplifier (TOPAS-C, Light Conversion, LLC). The polarization of the actinic pump was set at 54.7° (magic angle) relative to the Raman pump/probe to negate rotational effects. The timing between the actinic pump and Raman

pump/probe pair is controlled with a motorized delay stage. Samples for these experiments were prepared as described in Section 2.2, but with slightly higher concentrations (less than 200 μM) and in cuvettes with a 2 mm pathlength.

2.5 Methods for analyzing 2DES data

All data processing methodologies described here pertain to an original MATLAB package, MDS_EXP, located at our cited GitHub repository.[225] The codes and sample data are available to all for use, modification, etc. Note that the documentation within the repository contains further information and more specific details for each piece of the code. Readers are implored to contact the author with any questions and/or issues with utilizing the toolbox.

2.5.1 Generation of absorptive, rephasing, and non-rephasing signals

We process data output from QC using an original MATLAB toolbox.[225] For 2DES measurements, QC output files of the type .SCAN, which reported intensities (S) as a function of CCD array pixel and phase cycling frame. We calculated absorptive differential absorption, $\Delta A(t_1, t_2, \omega_3)$, from the phase cycling scheme in Eq. 10 using Eq. 12:

$$\Delta A(t_1, t_2, \omega_3) = -log\left(\frac{S_1}{S_2} * \frac{S_3}{S_4}\right) \qquad \text{Eq. 12}$$

where S_i is the raw CCD intensity for frame i. For the phase cycling scheme in Eq. 11, consider the value $\Delta\phi_{1,2}$, which represents the absolute value of the phase difference between the two pump pulses used in a single signal frame ($S_{i=1,2,3,4}$). Eq. 11 indicates that $\Delta\phi_{1,2}$ for frames S_1, S_2, S_3, and S_4 are 0, π, $\frac{\pi}{2}$, and $\frac{3\pi}{2}$, respectively. This is markedly different than for the scheme in Eq. 10, where $\Delta\phi_{1,2}$ for frames S_1, S_2, S_3, and S_4 are 0, π, 0, and π respectively. For both the schemes in Eqs. 10 and 11, the difference between $\Delta\phi_{1,2}$ for S_1 and S_2 (denoted as ϕ_{12}) is π, which is also true for S_3

and S_4 ($\phi_{34} = \pi$). The key difference is that S_3 and S_4 are 90° offset from S_1 and S_2, respectively,

for Eq. 11 (ϕ_{13} and $\phi_{24} = \frac{\pi}{2}$), whereas there is zero offset between these frame pairings in Eq. 10

(ϕ_{13} and $\phi_{24} = 0$). This difference enables the calculation two phase-offset differential absorption

signals:

$$\Delta A_0(t_1, t_2, \omega_3) = -log\left(\frac{S_1}{S_2}\right)$$ Eq. 13

$$\Delta A_{\frac{\pi}{2}}(t_1, t_2, \omega_3) = -log\left(\frac{S_3}{S_4}\right)$$ Eq. 14

Note that the $\Delta A(t_1, t_2, \omega_3)$ values at this stage are real-valued. We then perform an inverse Fourier

transformation on the ΔA data of the form shown by Eqs. 13 and 14 along the ω_3 dimension, which

yields $\Delta A(t_1, t_2, t_3)$. By setting all values for $t_3 < 0$ fs equal to zero, we enforce causality and obtain

the rephasing (R) and non-rephasing (NR) portions of the 3rd-order signal using Eq. 15[50, 51, 224]

$$\Delta A_{\frac{R}{NR}}(t_1, t_2, t_3) = \Delta A_0(t_1, t_2, t_3) \pm i * \Delta A_{\frac{\pi}{2}}(t_1, t_2, t_3)$$ Eq. 15

Note that the combination of the factor of i and the intrinsic 90° offset between the two ΔA terms

in Eq. 15 leads to the expected 180° phase difference between the rephasing and non-rephasing

signals. Fourier transformation of the causal rephasing and non-rephasing signals along ω_3 yields

complex-valued $\Delta A(t_1, t_2, \omega_3)$ data that encode additional phase information not available by phase

cycling with Eq. 10.[50] We use this additional information in Chapter 6.

2.5.2 Obtaining pump-energy resolution

2DES spectra are most-commonly presented as a function of pump and probe *energy*,

which requires Fourier transformation of $\Delta A(t_1, t_2, \omega_3)$ with respect to t_1. This procedure involves

multiplication of the data by a windowing function (Hanning in this work) to bring the end of each

trace smoothly to zero.[51] Without this step, the Fourier transformed data can display oscillatory artifacts. The data are then zero padded[51] to a vector length of 2^8 prior to fast Fourier transformation (FFT) in MATLAB. For an example analyte, Figure 2.4 illustrates steady-state absorption (upper right), 3rd-order signals as collected in the time-domain (left column), and the final $\Delta A(\omega_1, t_2, \omega_3)$ signal (lower right).
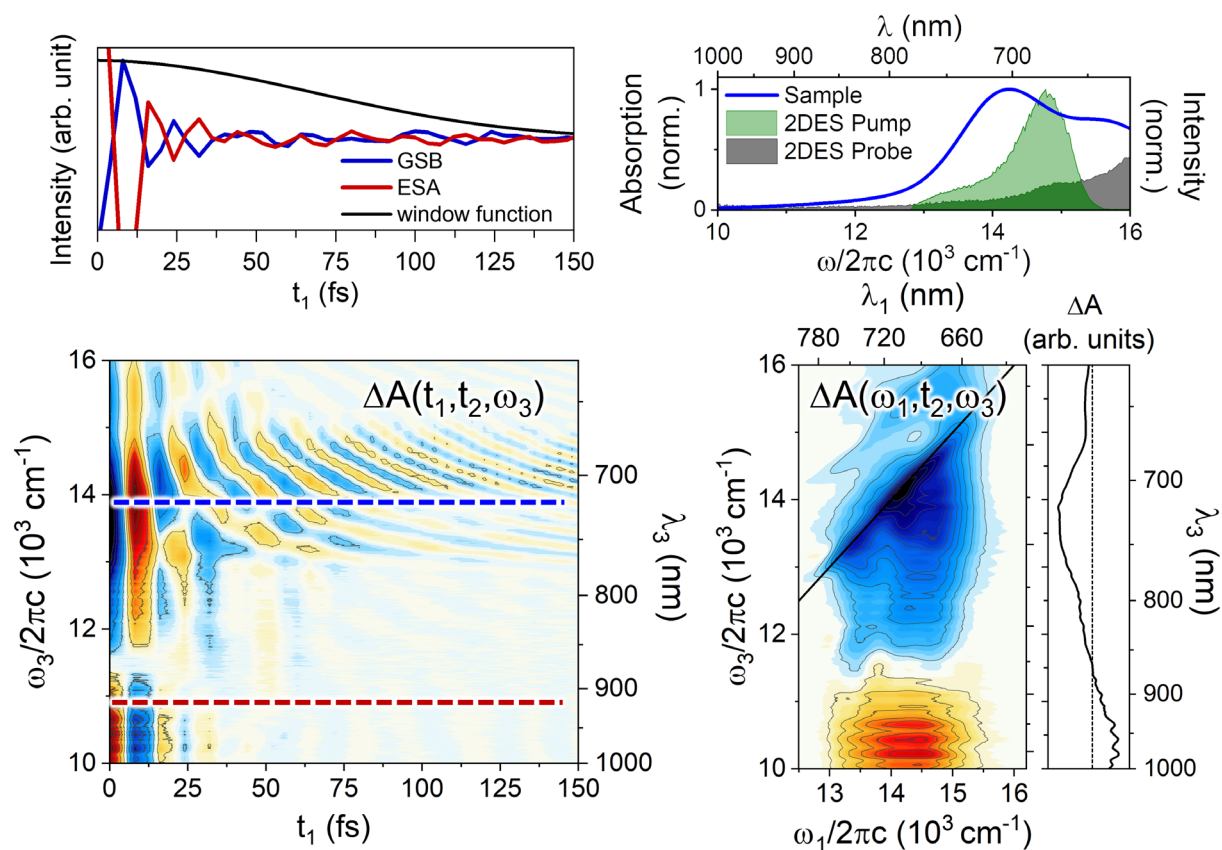
Figure 2.4. Example experimental data at various stages of analysis. The sample steady-state absorption and pulse profiles are shown in the upper right, while the left column displaces the form of the 3rd-order signals as collected. The final 2DES signals as a function of pump and probe energy are shown in the lower right.

The frequency resolution ($\Delta\omega$) along the pump domain is calculated using Eq. 16

$$\Delta\omega = (c * \Delta t * n)^{-1}$$ Eq. 16

where c is the speed of light, Δt is the timestep, and n is the number of datapoints in the time-domain vector (including any entries from zero padding).

2.5.3 Separation of populations and coherences

To isolate coherent dynamics in these studies, we fit population dynamics at each (ω_1, ω_3) coordinate to isolate the purely oscillatory residuals (Figure 1.8). This fitting is performed using one of two approaches: either with (1) offset exponential functions or (2) an existing package developed elsewhere to extract oscillation-associated spectra (OAS) in the context of acoustic phonons.[226] Approach (1) follows the form:

$$\Delta A(\omega_1, \omega_3, t_2) = \Delta A_0 + \sum a_i e^{-t_2/\tau_i}$$ Eq. 17

where ΔA_0 is the vertical offset, and a_i and τ_i are the amplitude and time constant of component i, respectively. Waiting times contaminated by cross-phase modulation (typically those prior to 100 fs) were not considered. We used between two and three exponential functions in Eq. 17 for fits of this form. One rapidly decaying exponential (< 300 fs) was necessary to capture population evolution from inertial solvent motion[145, 146] as well as inter-exciton relaxation in the case of H-aggregated dimers (Chapter 4).[227] The second exponential function removed population evolution along a ca. 1 to 2 ps time component, which generally can be attributed to vibrational cooling and solvent reorganization. Fits to Eq. 17 were achieved by minimizing the sum of the square residuals with MATLAB's *fminsearch* function.

The OAS package used by approach (2) is described in detail elsewhere.[226] Notably, the OAS code fits both non-oscillatory and oscillatory kinetics. To combat the occasional tendency

of rapid population dynamics to be fit as quickly dephasing, low-frequency oscillations, we included oscillatory components below a threshold frequency of 150 cm^{-1} within our population fits (in addition to the non-oscillatory components). We found approach (2) to be approximately an order of magnitude faster than approach (1), which is rate-limited by *fminsearch*.

For purely absorptive signals, population subtraction only requires a single pass of processing (i.e., the data are real-valued). In contrast, analyzing quantum beats in the rephasing and non-rephasing signals each requires two subtraction passes, one each for the real and imaginary portions of the data. We separated these components, processed them both as real-values, and then recombined the isolated beats into complex vectors by multiplying the imaginary residuals by *i* and adding them to the real-valued residuals.

After isolation from population kinetics, Fourier analysis of quantum beating traces with respect to the population time follows a similar procedure for that of the coherence time delay. However, these data are zero-padded to a length of 2^{10}. Since data between 0 and near-100 fs are truncated (to avoid cross-phase modulation artifacts), we input zeros as corresponding placeholders to ensure no systematic frequency shifts occur between scans.

2.5.4 Power spectral analysis of quantum beats

We assess quantum beats routinely through *Frobenius norms* and *quantum beatmaps*. Frobenius norms (Y) are calculated using Eq. 18, where the *i* and *j* indices correspond to indices of the probe and pump energy axes, respectively, as defined by a specified energy range in each dimension.

$$Y = \sqrt{\sum_i \sum_j |X_{ij}|^2} \qquad \text{Eq. 18}$$

Frobienus norms serve to display the Fourier power of quantum beats as a function of ω_2 for a window of pump and probe energies. As opposed to visualizing beats at single (ω_1, ω_3) coordinates, Frobenius norms minimize bias in the representation of beating signatures and improve the signal-to-noise ratio.

Absorptive 2DES data are real-valued, so power spectra extracted from absorptive signals are *symmetric* about the zero-frequency. In other words, the positive and negative beat frequency regions contain identical information. In contrast, the complex rephasing and non-rephasing $\Delta A(\omega_1,t_2,\omega_3)$ signals yield power spectra with distinct information in the positive and negative frequency domains. This characteristic has been shown to be highly beneficial in the interpretation of wavepacket evolution on the ground- versus excited-electronic states.[151] We expand on this utility in Chapter 6.

2.5.5 Quantum beatmaps

Plots of the quantum beat amplitude for a single frequency as a function of the pump and probe energy axes are known as *quantum beatmaps* (Figure 1.14, Section 1.5.4). We calculate and analyze these beatmaps at length in Chapters 4 through 6. Each quantum beatmap is calculated by defining a single ω_2 center value and averaging the beating signal along the ω_2 axis over a small window (ca. 10 cm^{-1}) around the center frequency. This approach accounts for slight frequency shifts in Fourier peaks that can occur between different measurements.

2.5.6 Diagrammatic summary

Figure 2.5 organizes the workflow described in Section 2.5 into a comprehensive diagram. Note that all procedures, notation, etc. correspond to our published software available at the cited

GitHub repository.[225] Readers are also implored to contact the author with any questions and/or issues with utilizing the toolbox.
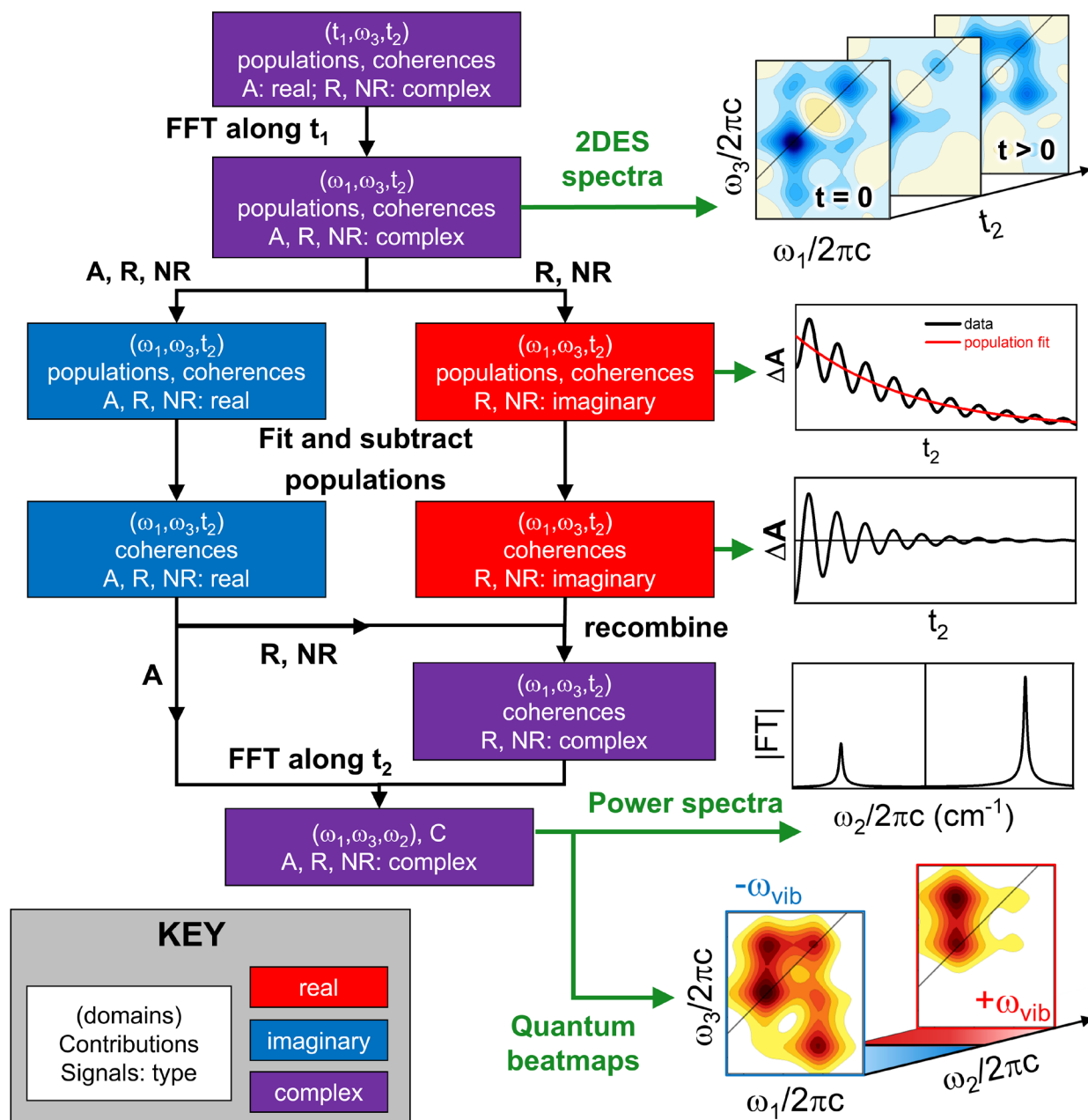
Figure 2.5. Diagrammatic summary of the workflow for processing 2DES data, as described in Sections 2.5.1 through 2.5.4. A key in the bottom left indicates the meaning of text within each box, as well as the color of the boxes. Images on the right side of the figure portray how simulated data look at each stage of the processing (the associated steps are shown with a green arrow).

Chapter 3: Theoretical methodology

3.1 Introduction

Synergy between experimental and theoretical chemistry is powerful, especially in the context of nonlinear spectroscopy. This section overviews the foundations of theoretical and computational tools that we use throughout Chapters 4 to 6. This chapter describes the original MATLAB toolbox[157, 228] that we developed to generate a Holstein-like Hamiltonian[67, 205] with an arbitrary number of vibrations and subsequently time-propagate the system in response to electromagnetic perturbations. We developed this toolbox by drawing upon several previously described methodologies[158, 160, 229] and thank Professor Roel Tempelaar for numerous helpful discussions and insights.

The MATLAB codes discussed in this chapter are organized into a package named *Optical REspOnse Simulator*, or OREOS, which is available to all readers via a dedicated GitHub repository.[230] OREOS contains further documentation detailing specific aspects of the underlying codes. Readers are implored to contact the author with any questions and/or issues with utilizing the toolbox.

3.2 General formulation

Figure 3.1 illustrates the generalized workflow for simulating optical spectra with OREOS. A vital prerequisite to spectra is calculation of the nth-order molecular response function, depending on whether the user desires linear absorption spectra or 2DES spectra. Working backwards through Figure 3.1, we see that the molecular response is fundamentally linked to the system Hamiltonian. OREOS is therefore constructed to allow for facile tunability at the levels underlying the system Hamiltonian (i.e., operators and basis sets).
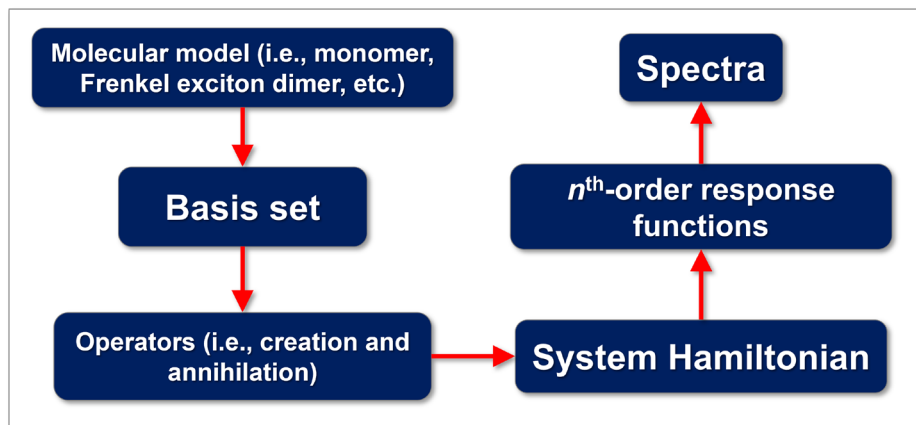
Figure 3.1. Diagrammatic workflow for the OREOS software package used to simulate spectroscopic signals.

We formulate basis sets and operators for all Hamiltonians using the occupation number representation, which means that different types of molecular systems can be modeled by adjusting the basis set formulation, generating quantum mechanical operators by reading the new basis set, and combining these operators as defined by a Hamiltonian equation. For example, the equation for a monomeric displaced harmonic oscillator (left side of Figure 3.2) is written as

$$H_{sys} = \varepsilon c^\dagger c + \omega b^\dagger b + \omega c^\dagger c [\lambda(b^\dagger + b) + \varepsilon \lambda^\dagger] \qquad \text{Eq. 19}$$

where ε represents the singlet electronic transition energy, $c^\dagger(c)$ creates (annihilates) electronic quanta, $b^\dagger(b)$ creates (annihilates) vibrational quanta with frequency ω and Huang-Rhys factor λ^2. The basis kets for this system are written as $|E, \nu\rangle$, E and ν represent the electronic and vibrational quanta, respectively. To the right of the energy level diagram, Figure 3.2 illustrates the matrix form of the basis set for a displaced harmonic oscillator with two vibrational quanta on each electronic state. OREOS can then read this basis set to generate the electronic and vibrational ladder operators, which can then translate Eq. 19 into matrix form. Figure 3.2 illustrates these matrices, where red squares indicate matrix entries with non-zero values. This general approach applies to

the formulation of all other Hamiltonians discussed in <u>Section 3.3</u>, which are all available within

the OREOS software.
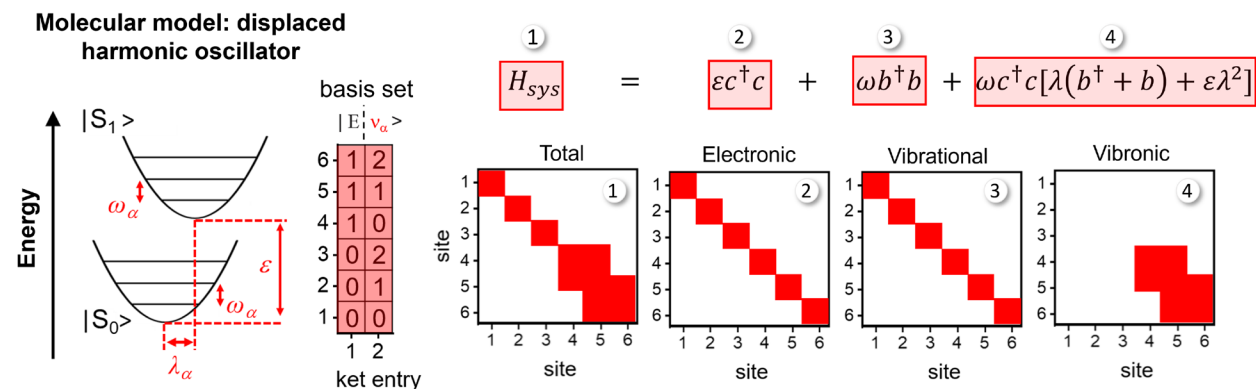
Figure 3.2. An example energy level schematic (left), basis set (middle), and matrix forms of each term within the system Hamiltonian for a displaced harmonic oscillator.

3.3 System Hamiltonians

3.3.1 Multimode displaced harmonic oscillator (monomer)

To account for multiple Franck-Condon (FC) active vibrations and higher-lying electronic

states, we extend the Hamiltonian in Eq. 19 to include an arbitrary number of vibrations and a third

electronic state. The time-independent system Hamiltonian is formulated as follows:

$$H_{sys} = \sum_i \left[\varepsilon_i c_i^\dagger c_i + \omega_m \sum_m \left[b_m^\dagger b_m + c_i^\dagger c_i [\lambda_{m,i}(b_m^\dagger + b_m) + \varepsilon_i \lambda_{m,i}^2] \right] \right] \qquad \text{Eq. 20}$$

where ε represents the singlet electronic transition energy, $c_i^\dagger(c_i)$ creates (annihilates) electronic

quanta for the manifold i (g = ground singlet, e = first excited singlet, and f = n^{th} excited singlet

states, respectively), $b_i^\dagger(b_i)$ creates (annihilates) vibrational quanta for vibration m, with

frequency ω_m and Huang-Rhys factor $\lambda_{m,i}^2$. We set ε_g and $\lambda_{m,g}$ equal to zero to serve as reference

points for the e and f electronic states. For all considered vibrations, we assume that the site-basis

vibrational frequency is independent of the electronic configuration and that $\lambda_{m,f}^2 = 2\lambda_{m,e}^2$. As

specified within each chapter, we use either five or ten vibrational quanta for all vibrations included in the system Hamiltonian. These values were selected to ease computational effort while still capturing the optical response of higher-lying vibronic states (as evident in the experimental results).

3.3.2 Frenkel-exciton (FE) dimer

Eq. 21 extends the Hamiltonian in Eq. 20 to a molecular dimer with electronic coupling:

$$H_{sys} = \varepsilon \sum_n c_n^\dagger c_n + J \sum_{n \neq n'} c_n^\dagger c_{n'}$$

$$+ \sum_{m,n} \omega_{m,n} b_{m,n}^\dagger b_{m,n} + \omega_{m,n} c_n^\dagger c_n [\lambda_{m,n}(b_{m,n}^\dagger + b_{m,n}) + \varepsilon \lambda_{m,n}^2]$$

Eq. 21

where ε represents the singlet electronic transition energy of the isoenergetic monomers (homodimer), $c_n^\dagger (c_n)$ creates (annihilates) electronic quanta on molecule n ($n = 1, 2$), $b_{m,n}^\dagger (b_{m,n})$ creates (annihilates) vibrational quanta for vibration m on molecule n, and J tailors the overall electronic coupling strength the chromophores (assumed to be purely Coulombic in this work).

3.3.3 Coupled FE and correlated triplet dimer

To explain experimental results in Chapter 5, we employ a modified Holstein Hamiltonian[158, 160, 205] that accounts for diabatic singlet ground (S_0S_0) and excited states $^1(S_0S_1) \leftrightarrow$ $^1(S_1S_0)$, as well as the correlated triplet configuration $^1(T_1T_1)$. The total Hamiltonian can be written as a combination of electronic and nuclear Hamiltonians:

$$H_{sys} = H_{el} + H_{vib}$$

Eq. 22

The electronic Hamiltonian is written as:

$$H_{el} = H_{S_1} + H_{TT} + H_{S_1-TT}$$

Eq. 23

where H_{S_1} and H_{TT} are the singlet and correlated triplet components, while H_{S_1-TT} describes the Hamiltonian elements that couple the singlet and triplet manifolds. We invoke the superexchange approximation where the charge-transfer (CT) state is not explicitly treated with an individual block in the Hamiltonian, but rather as a mediator of the coupling between the singlet and triplet manifolds.[158, 231-234] The singlet Frenkel Exciton Hamiltonian is formulated using Eq. 21.

The correlated triplet species is described in the site basis as:

$$H_{TT} = \varepsilon_{TT} \sum_{n \neq n'} g_n^\dagger g_n + \sum_{m,n} \omega_{m,n} b_{m,n}^\dagger b_{m,n} + \omega_{m,n} g_n^\dagger g_n [\lambda_{TT,m,n}(b_{m,n}^\dagger + \qquad \text{Eq. 24}$$
$$b_{m,n}) + \varepsilon_{TT} \lambda_{TT,m,n}^2]$$

where ε_{TT} represents the electronic energy gap between the ground and correlated triplet states (assumed to be twice the energy of T_1 as computed by DFT), $g_n^\dagger(g_n)$ creates (annihilates) triplet electronic quanta on molecule n ($n = 1, 2$), and $\lambda_{TT,m,n}^2$ is the Huang-Rhys factor for vibration m on the correlated triplet species. Because the correlated triplet is delocalized in the site basis, we drop the summation over n to avoid double-counting.[205]

To couple the Frenkel exciton and correlated triplet states, we invoke the following interaction Hamiltonian:

$$H_{S_1-TT} = \sum_{n=1,2} J_{eff}(c_n^\dagger g + g^\dagger c_n) \qquad \text{Eq. 25}$$

where J_{eff} describes the effective coupling. As discussed further in Chapter 5, we estimate this parameter based on an expression derived for the superexchange regime.[232] Since DFT is known to predict systematic shifts in electronic transition energies relative to experiments, we used the calculated energy difference between the S_1 and $^1(T_1T_1)$ states to predict the energy of the latter with respect to the experimental the S_1 energy. We used previously determined redox potentials

and ionic radii estimated from the DFT structures to calculate the energy of the CT state using the

Weller equation.[235] Lastly, we treat the $^1(T_1T_1)$ state as optically dark from the ground-singlet state.

3.4 Time-domain simulations of the molecular response function

We performed all simulations discussed here within the Condon approximation. We use

the sum-over-states approach, in which the total molecular response function emerges from the

combination of all accessible Liouville pathways.[130] To simulate light-matter interactions, we

formulate the transition dipole operator between two electronic states as:

$$\mu(\tau_i) = c^\dagger + c \qquad \text{Eq. 26}$$

where τ_i reflects the instantaneous time of the light-matter interaction i.[160] Assuming the system

begins in the ground vibrational state ($\omega_0 >> k_bT$), the time-domain linear response, $R(\tau)$,

involving two impulsive optical field interactions at times ($\tau_i = 1, 2$) is expressed as:[160]

$$R(\tau) = \langle 0|\mu(\tau_2)U(\tau_2, \tau_1)\mu(\tau_1)|0\rangle \qquad \text{Eq. 27}$$

where free propagation under the system Hamiltonian during the time delay $t(\tau_j, \tau_k)$ between two

sequential light-matter interactions j and k is captured by the operator U:

$$U\left(t(\tau_j, \tau_k)\right) = \exp(-iH_{sys}t(\tau_j, \tau_k)) \qquad \text{Eq. 28}$$

Given that we force τ_j and τ_k to represent sequential interaction times ($j = k+1$), we simplify the

notation by setting $t(\tau_j, \tau_k) = t_k$, which recovers the commonly referred to coherence (t_1), waiting

(t_2), and rephasing (t_3) time delays in 2DES. Furthermore, we lower the computational effort for

propagation through time by partitioning the transition dipole and time evolution matrices into

blocks based on the relevant electronic states in each expression. In this notation, U_{jk} and μ_{jk} refer

to the blocks corresponding to the electronic state(s) j and k (g = ground singlet, e = first excited

singlet, and f = nth excited singlet states, respectively). We account for six possible signal pathways in our simulations of 2DES signals, namely the rephasing and non-rephasing ground-state bleach (GSB), stimulated emission (SE), and excited-state absorption (ESA) pathways. Noting that we assume the transition dipole moment to be impulsive and thus time-independent, these six response functions ($R_{\#; phase, pathway}$) are individually calculated using the following expressions:[229]

$$R_{1; NR,GSB}(t_1, t_2, t_3) = \langle 0 | \mu_{eg} U_{ee}(t_3) \mu_{ge} U_{gg}(t_2) \mu_{eg} U_{ee}(t_1) \mu_{ge} | 0 \rangle \qquad \text{Eq. 29}$$

$$R_{2; R,SE}(t_1, t_2, t_3) = \langle 0 | \mu_{ge} U_{ee}^\dagger(t_1) U_{ee}^\dagger(t_2) \mu_{eg} \mu_{eg} U_{ee}(t_3) U_{ee}(t_2) \mu_{ge} | 0 \rangle \qquad \text{Eq. 30}$$

$$R_{3; R,GSB}(t_1, t_2, t_3) = \langle 0 | \mu_{ge} U_{ee}^\dagger(t_1) \mu_{eg} U_{gg}^\dagger(t_2) \mu_{eg} U_{ee}(t_3) \mu_{ge} | 0 \rangle \qquad \text{Eq. 31}$$

$$R_{4; NR,SE}(t_1, t_2, t_3) = \langle 0 | \mu_{ge} U_{ee}^\dagger(t_2) \mu_{eg} U_{gg}^\dagger(t_3) \mu_{eg} U_{ee}(t_3) U_{ee}(t_2) U_{ee}(t_1) \mu_{ge} | 0 \rangle \qquad \text{Eq. 32}$$

$$R_{5; R,ESA}(t_1, t_2, t_3) = \langle 0 | \mu_{ge} U_{ee}^\dagger(t_1) U_{ee}^\dagger(t_2) U_{ee}^\dagger(t_3) \mu_{fe} U_{ff}(t_3) \mu_{ef} U_{ee}(t_2) \mu_{ge} | 0 \rangle \qquad \text{Eq. 33}$$

$$R_{6; NR,ESA}(t_1, t_2, t_3) = \langle 0 | \mu_{ge} U_{ee}^\dagger(t_2) U_{ee}^\dagger(t_3) \mu_{fe} U_{ff}(t_3) \mu_{ef} U_{ee}(t_2) U_{ee}(t_1) \mu_{ge} | 0 \rangle \qquad \text{Eq. 34}$$

where the *(i,j)* subscripts on each operator indicate the particular *(row, column)* matrix block, and *R* and *NR* denote rephasing and non-rephasing signals, respectively.

We simulate all spectra in the rotating frame by removing either one or two electronic quanta from the diagonal entries of the S_1 and S_n blocks, respectively; this is corrected at the end of the simulation by shifting the Fourier frequency axis by one electronic quantum. In simulating the linear response, we propagated the system over a time range of $t_{1,2}$ = 0 to 256 fs with a 1 fs step size. For simulations of 2DES spectra in Chapter 6, we used a 3 fs step size and the following time ranges to reduce computation time: t_1 = t_3 = 0 to 186 fs, t_2 = 0 to 1000 fs. Spectral linewidths in the simulations were captured using the following lineshape function:[236]

$$g(t) = \Delta^2 t_c^2 e^{-\frac{t}{t_c} + (\frac{t}{t_c} - 1)}$$ Eq. 35

where Δ captures the energy gap fluctuations induced by the system-bath interaction and t_c is the correlation time for these fluctuations. The lineshape function g is incorporated into the simulation by multiplying the undamped response function in the time domain by $e^{-g(t)}$ to yield the total simulated response function. Lineshape parameters were chosen to yield reasonable agreement in comparison to the experimentally observed features in the quantum beatmaps. We processed the simulated 2DES data and analyzed quantum beating signatures using procedures outlined in the experimental data analysis sections (Section 2.5).

3.5 Density functional theory computations

DFT calculations were performed using either the Q-Chem 5.0, 5.1, or ADF software packages. Functionals and basis sets are specified within the associated sections of Chapters 4 through 6. We confirmed optimized geometries for compounds by ensuring that no negative frequencies were present in the final frequency output. If present, we removed imaginary frequencies by scaling the system geometry by an arbitrary percentage (typically 75%) of the nuclear displacements associated with the negative frequency mode, re-conducting the geometry optimization and frequency analysis, and iterating this process until no negative frequencies remained.

Chapter 4: Vibronic Coherences in Perylenediimide Cyclophanes

4.1. Introduction

The function of quantum coherence in excitation energy transfer has been a topic of interest to biologists, chemists, and physicists for decades.[155, 180, 186] Recent developments in multidimensional optical spectroscopy[121] have highlighted the importance of vibronic coherence, i.e. phase-related superpositions with mixed nuclear and electronic character, in natural photosynthetic complexes. Studies suggest these coherences may enhance both the rate and efficiency of energy and charge transfer in multichromophoric systems.[13, 106, 107, 155, 160, 161, 194, 195, 237] While coherence phenomena have been examined in several chromophores,[19, 144, 214-216, 238-241] relatively few studies have focused on well-defined structures having a small number of chromophores, such as dimers and trimers, from which design principles regarding larger light harvesting arrays can be developed.[144, 239]

Small chromophore assemblies having synthetically tunable structures allow for extracting maximal insight into the factors that influence vibronic coherences.[144, 160, 161, 168, 239] Through this bottom-up approach, researchers have elucidated the role of energy level ordering[144, 161] and conformational disorder[144, 168] in controlling the degree of electronic-vibrational coupling. An additional important factor to address is van der Waals forces between neighboring chromophores. Depending on the orientation and packing of the chromophores, structural distortions resulting from steric interactions may strongly impact vibronic couplings through changes in Franck-Condon (FC) factors and/or broken molecular symmetry.[59] In order to rationalize these effects in light-harvesting arrays, we must first build a better fundamental understanding by exploring model systems with precise control over interchromophoric interactions.
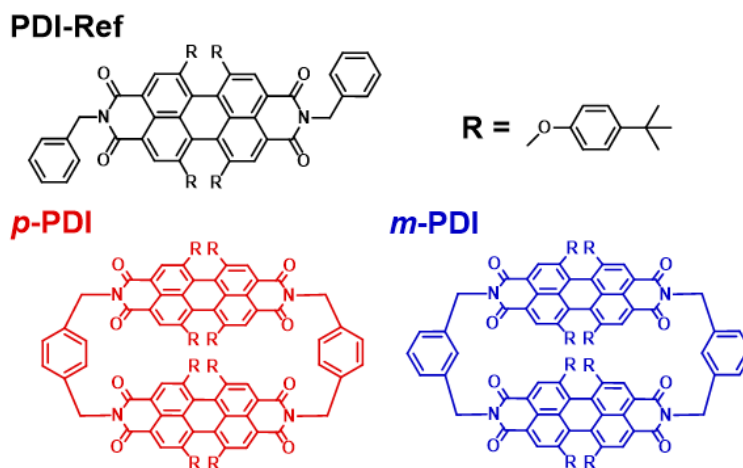
Figure 4.1. Molecular structures for the compounds in this study. PDI-Ref, p-PDI, and m-PDI represent the PDI monomer, para-connected, and meta-connected cyclophanes, respectively.

Perylenediimide (PDI) is a particularly interesting organic chromophore from this perspective[242] because it is synthetically tunable,[243] which facilitates its tailoring to a wide variety of applications such as highly efficient fluorescence,[244, 245] photoinduced energy[246] and electron transfer,[247] and singlet fission.[248] PDI derivatives have been utilized in organic electronics,[249, 250] artificial photosynthesis,[251] and organic photovoltaic devices.[252] We wish to use the covalent control afforded by PDI cyclophane dimers[253] (Scheme 1) to investigate how van der Waals forces influence vibronic coherences. In particular, cyclophanes incorporating 1,6,7,12-tetrakis(4-*t*-butylphenoxy)perylene-3,4:9,10-bis-(dicarboximide) chromophores allow us to precisely fix the interchromophoric distance using different linking groups. Inclusion of such bulky bay-substituents has been shown to induce twisting in the monomeric PDI core.[253-255] Different degrees of steric interactions between the 4-*t*-butylphenoxy groups in the cyclophanes may alter the extent of twisting in the PDI cores, which allows us to examine how substituent interactions and resultant differences in core structure affect vibronic and/or vibrational coherences. In this chapter, we report significant differences in the amplitude of signal modulations stemming from excited- and

ground-state wavepackets in the cyclophane dimers versus the corresponding monomer reference. These coherences may play an important role in symmetry-breaking charge separation[247] and singlet fission[248] involving PDI cyclophanes, processes that are both important for photo-driven charge separation leading to energy storage.

4.2. Experimental details

2DES experiments were conducted using an apparatus described in Section 2.4.2. These experiments utilized a tellurium dioxide crystal as the AOM medium, with exception to the data shown in Figure S4.15 (Appendix A), which were acquired with a quartz AOM. The experiments conducted for this work employed pump pulses centered near 17550 cm^{-1} (~570 nm, Figure S4.1) and ca. 28 fs in duration, as characterized by SHG-FROG (Figure S4.2). The pump energy at the sample was ~12 nJ/pulse. Data were collected in the rotating frame with a rotation frequency of 15500 cm^{-1} and sampled from 0 to 300 fs with a 4-fs step size. To evaluate quantum beating signatures, a series of spectra were collected as a function of t_2. This delay was scanned from -100 to 1500 fs with a timestep of 10 fs, which yields a frequency resolution of ~24 cm^{-1} (Section 2.5.2). Numerous experiments were conducted on different days with different solvent aliquots to ensure the results were not correlated to laser fluctuations or solvent impurities (Figures S4.8-S4.10). Solutions of each analyte in tetrahydrofuran (THF, dried using a Glass Contour solvent system) were prepared in 1 mm glass cuvettes with maximum optical densities of ~0.25, ~0.45, and ~0.28 for **PDI-Ref**, *p*-**PDI**, and *m*-**PDI**, respectively.

4.3. Results and Discussion

4.3.1. Steady-State Characterization

The cyclophanes reported here are composed of monomeric 4-*t*-butylphenoxy (bay) substituted PDI units covalently bound via para (***p*-PDI**) or meta (***m*-PDI**) connections to benzyl group linkers. Molecular structures for ***p*-PDI**, ***m*-PDI**, and the reference compound, **PDI-Ref**, are provided in Figure 4.1. The synthesis details and characterization of the intermediates and final products are provided in the Supporting Information (Appendix A). Normalized visible electronic absorption spectra for **PDI-Ref**, ***p*-PDI**, and ***m*-PDI** dissolved in THF at room temperature are shown in Figure 4.2. **PDI-Ref** exhibits a prominent vibronic progression of ~1280 cm^{-1} with absorption maxima near 17600 and 18890 cm^{-1} (568 and 530 nm, respectively). The absorption spectra of ***p*-PDI** and ***m*-PDI** exhibit similar vibronic progressions, but with an increasing absorption near the 0-1 vibronic band relative to that of the 0-0 transition. This altered ratio of the vibronic bands is well described by positive dipolar coupling between the cofacial PDI moieties (*H*-aggregation),[59, 66] which is further reflected by the blueshift of the absorption maxima in ***m*-PDI** relative to **PDI-Ref**. Simulation of the linear absorption spectra with the Holstein Hamiltonian (Figure S4.4) yields dipolar couplings of ~180 and ~270 cm^{-1} for ***p*-PDI** and ***m*-PDI**, respectively, in agreement with previous work on similar systems.[253] This is thus the energy regime we are interested in investigating for vibronic coupling phenomena.
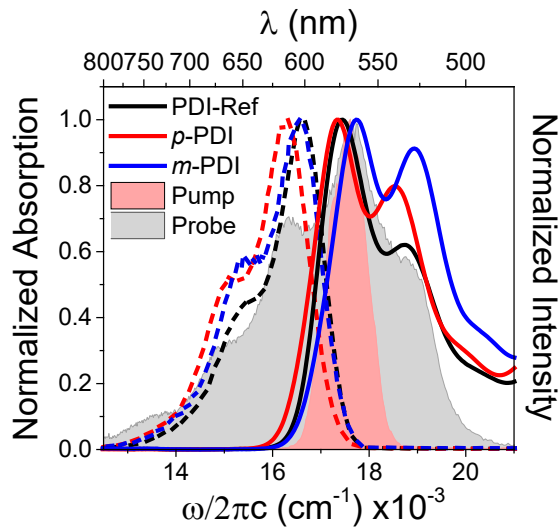
Figure 4.2. Normalized steady-state absorption (solid) and emission (dashed) spectra of PDI-Ref, p-PDI, and m-PDI obtained in THF at room temperature. Pump and probe pulses for the 2DES measurements are superimposed.

4.3.2. Nonlinear spectroscopy

We characterize the coherences in these systems with a combination of two-dimensional electronic spectroscopy (2DES) and femtosecond stimulated Raman spectroscopy (FSRS) to disentangle vibronic from vibrational coherences. 2DES is a powerful third-order nonlinear spectroscopic technique which produces optical spectra with frequency resolution in both the pump and probe pulse dimensions.[120, 121, 138] A rich understanding of the Franck-Condon envelope of a molecule can be obtained through this technique because the short time duration pump pulses can generate coherent wavepackets composed of FC-active vibrations on both the ground and excited states.[15, 155, 160, 186] Such wavepackets manifest themselves as amplitude oscillations of relevant spectral features as a function of the time between the second pump pulse and the probe.[15] In contrast to 2DES, by using a narrowband resonant Raman pump, FSRS is capable of generating and probing purely vibrational coherences on the molecular ground or excited state surface, depending on the resonance of the Raman pump.[125, 256] FSRS therefore provides a complementary

method of unraveling the contributions of electronic and vibrational character to the coherences observed via 2DES.
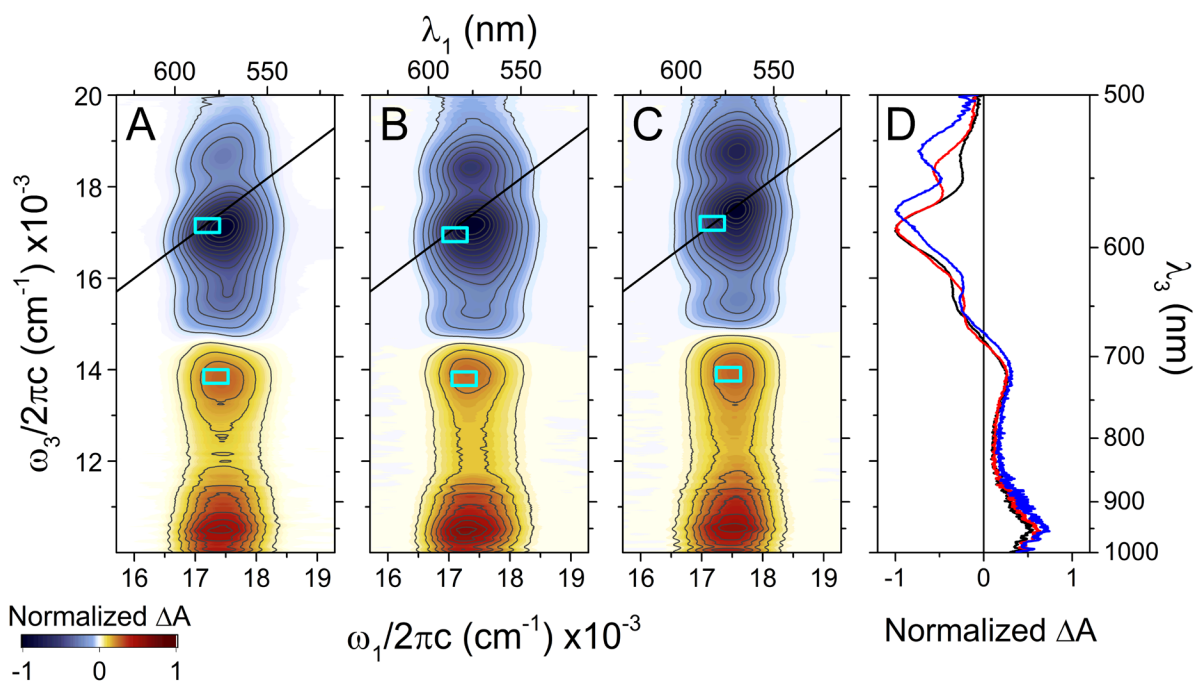
Figure 4.3. Absorptive 2DES spectra at a waiting time of 150 fs for (A) **PDI-Ref**, (B) *p*-**PDI**, and (C) *m*-**PDI** obtained in THF at room temperature. Each spectrum is normalized to the maximum absolute change in absorption. Cyan rectangles indicate the approximate regions over which the coherence analysis was performed. (D) Corresponding transient absorption spectra for **PDI-Ref** (black), *p*-**PDI** (red), and *m*-**PDI** (blue).

2DES spectra were collected following $S_1 \leftarrow S_0$ excitation of **PDI-Ref**, *p*-**PDI**, and *m*-**PDI**. Experimental details are provided in the SI. Spectra of the three compounds at a waiting time delay of 150 fs are shown in Figure 4.3. Each system displays negative ground-state bleach (GSB) features near ω_{pump} (ω_1) = ω_{probe} (ω_3) = 17500 cm^{-1} with a higher-energy vibronic transition ~1300 cm^{-1} above the diagonal in the probe dimension. A negative stimulated emission (SE) band can be observed ~1300 cm^{-1} below the diagonal. Positive excited-state absorption (ESA) features are observed near (ω_1 = 17500 cm^{-1}, ω_3 = 14000 cm^{-1}) and (ω_1 = 17500 cm^{-1}, ω_3 = 10500 cm^{-1}), which correspond to $S_n \leftarrow S_1$ transitions.
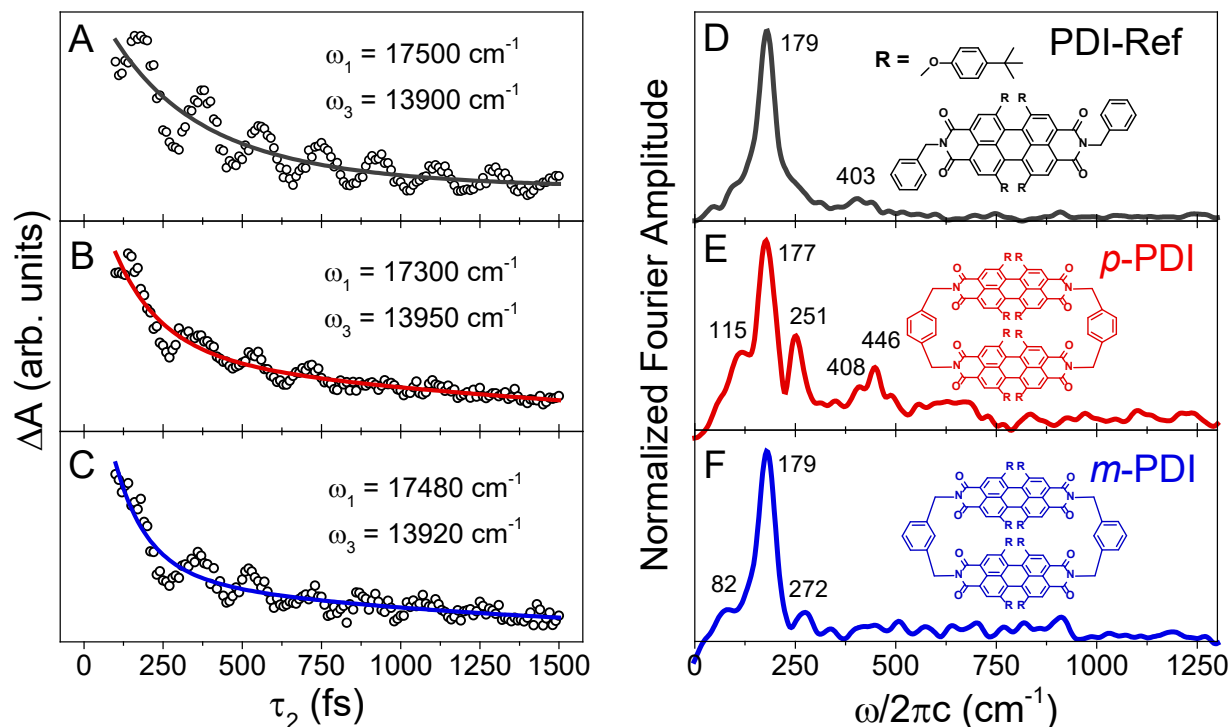
Figure 4.4. Time-domain data (hollow circles) from the real part of the optical 2DES signal and exponential fits (solid lines) integrated over a 30 x 30 cm^{-1} region near the specified coordinates for (A) **PDI-Ref**, (B) *p*-PDI, and (C) *m*-PDI. Frobenius norms calculated in the frequency domain across a 300 x 400 cm^{-1} region on the higher energy $S_n \leftarrow S_1$ ESA feature for (D) **PDI-Ref**, (E) *p*-PDI, and (F) *m*-PDI. Replicate and control traces are available in the SI.

The nature of the coherences observed in 2DES experiments has been widely debated.[107, 155, 160, 186] The spectral region accessible by our pump is particularly relevant to investigate considering these frequencies are on the energetic order of the exciton coupling in the dimer systems. Thus, vibrations in this frequency region may mix strongly with the electronic degrees of freedom.[107] To address the effects of interchromophoric steric interactions on the nature of such coherences in these PDI systems, we separated the oscillatory signals from population dynamics in the 2DES data by fitting the population kinetics at each (ω_1, ω_3) coordinate as a function of the waiting time. Representative time traces and corresponding population fits for **PDI-Ref**, *p*-PDI, and *m*-PDI are shown in Figure 4.4A-C.

We examined the Fast Fourier Transform (FFT) of the isolated traces at each (ω_1, ω_3) position to extract frequency-domain information regarding the oscillations present in the **PDI-Ref**, **p-PDI**, and **m-PDI** 2DES data. Frobenius norms of the frequency-domain signals across a limited spectral region were used to improve the signal-to-noise ratio and better sample the oscillations associated with the specific optical transition; these norms were chosen to be centered near the maximum of the oscillatory beating amplitude (cyan rectangles in Figure 4.3 and Figure S4.13). We first turn our attention to excited-state oscillatory signatures in these data, as these are most relevant to application in coherent energy transport.[13] While such signals can be deconvoluted from those associated with coherences on the ground state in the GSB region of the 2D spectrum,[154, 257] the wide spectral coverage in the probe dimension here permits resolution of purely ESA features, which can only exhibit excited-state coherences. Power spectra of the oscillations integrated across the higher-energy ESA feature for **PDI-Ref**, **p-PDI**, and **m-PDI** are shown in Figure 4.4D-F. In the excited-state power spectrum for **PDI-Ref**, we observe peaks at 179 and 403 cm^{-1}. In contrast, the spectrum of **p-PDI** contains additional peaks at 115, 177, 251, and 446 cm^{-1}, and a clear increase in the relative intensity of the 408 cm^{-1} mode. The oscillations below 300 cm^{-1} observed in **p-PDI** remain prominent in **m-PDI**, where the interchromophoric distance is decreased, but at significantly lower intensities relative to the strongest peak near 179 cm^{-1}. A peak near 400 cm^{-1} is observed in some **m-PDI** experiments (Figures S4.10 and S4.15F), but also at lower relative intensity compared to that in the **p-PDI** power spectrum.

Several factors can contribute to the differences between the power spectra for **PDI-Ref**, **p-PDI**, and **m-PDI**. The presence of an additional coherence in a dimer system compared to the monomer could imply the oscillation originates from a superposition of two excitonic states

induced by dipolar coupling.[160] However, such purely electronic coherences are reported to dephase on the order of tens of femtoseconds.[156, 160, 188] Considering these measurements were conducted in room temperature solutions and data prior to 100 fs are neglected, the features observed in *p*-**PDI** and *m*-**PDI** are most likely not purely excitonic in origin. While the coherences are purely vibrational in **PDI-Ref**, those observed in the dimers are likely vibronic in nature since both the linear absorption and 2DES spectra indicate the presence of Frenkel excitons. Thus, one explanation for the differences between Figure 4.4D-F could be varying degrees of transition dipole coupling in the dimers, which will alter the degree of interaction between excitons and underdamped vibrational modes.[107, 160, 258] Studies have predicted[107, 258] and shown[144] amplitude enhancement of vibronic coherences when excitonic splitting yields bright vibronic states not present in the monomer.

While this enhancement has received much attention in recent literature,[107, 144, 258] it is important to note that structural deformations of the monomer units in the cyclophanes could also account for the observed differences in the power spectra. As discussed above, it is known that bay substituents in PDI molecules can induce twisting in the core.[255] Steric interactions between the substituents in the dimers here could result in changes to the degree of core twisting in relation to the isolated monomer; this effect could be exacerbated at smaller chromophore spacings. Such structural deformations may alter the displacement between the ground- and excited-state potential energy minima and thus yield different sets of FC factors for each system, thereby leading to different signal amplitudes from vibronic coherences.
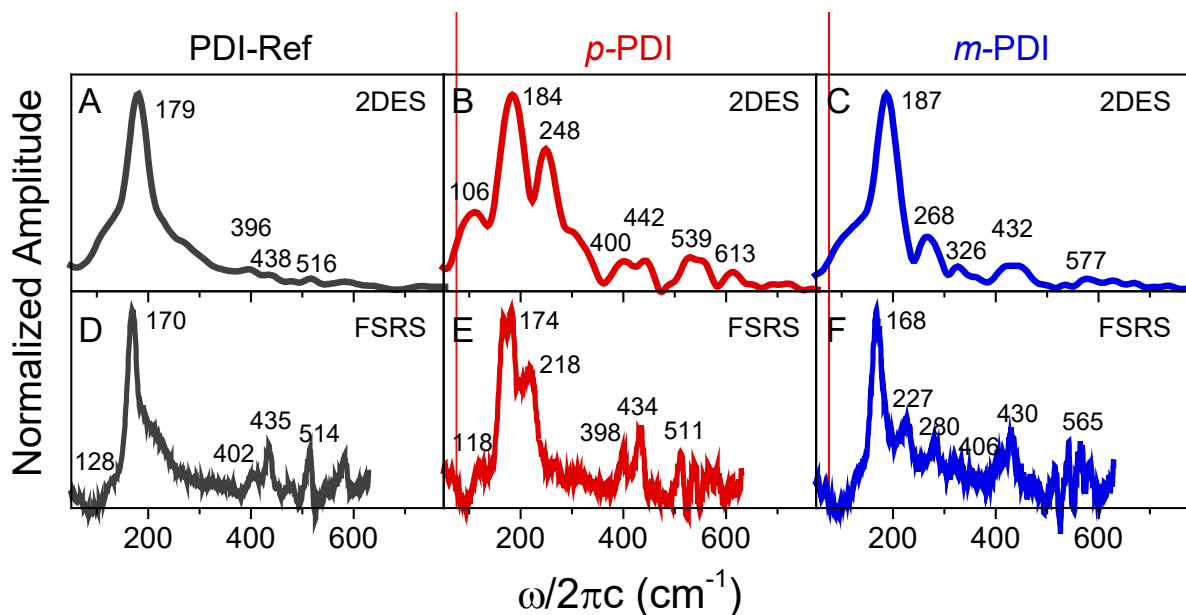
Figure 4.5. Normalized ground-state 2DES and FSRS spectra for (A and D) **PDI-Ref**, (B and E) **p-PDI**, and (C and F) **m-PDI**, respectively, in THF at room temperature. Replicate and control traces are available in the SI.

Deconvoluting the influence of excitonic splitting versus steric hindrance in these results requires evaluation of the origin state (ground or excited) of the coherence. Isolating purely ground-state signals from those on the excited state surface is known to be difficult in room-temperature 2DES.[154, 257] However, the ultrafast Stokes shift observed in these systems (Figure S4.18D) results in transient separation of the these signals in the probe frequency dimension, with ground- and excited-state oscillations occurring primarily near and below the diagonal in the 2D maps, respectively. Figure 4.5A-C shows power spectra integrated at frequencies near the diagonal, thus reflecting primarily ground-state coherences for **PDI-Ref**, **p-PDI**, and **m-PDI**. However, some excited-state contribution from SE pathways cannot be explicitly ruled out. Similar to the purely excited-state results, a dominant oscillation frequency ($\sim$179 cm^{-1}) with potential shoulders is observed for **PDI-Ref**. In comparison, peaks near 106, 248, 400, 442, 539,

and 613 cm^{-1} grow in relative intensity in the **p-PDI** power spectrum. Most of these modes are apparent in the spectrum for **m-PDI**, but with significant reduction in relative intensity.

It is important to note here that some ground-state vibrational coherence signals will also be altered substantially by vibronic coupling due to intensity borrowing.[107, 258] Conversely, signals which do not involve resonance with both excitonic states will not undergo this signal amplification mechanism and will be primarily sensitive to alterations in FC factors between the compounds.[107] The tendency for excited- and ground-state oscillatory signals to overlap in 2DES complicates exploitation of this notion, but femtosecond stimulated Raman spectroscopy (FSRS) offers a complementary method of isolating such a signal. Thus, we examined pure ground-state coherence signatures from **PDI-Ref**, **p-PDI**, and **m-PDI** using FSRS. By using a Raman pump pre-resonant with the $S_1 \leftarrow S_0$ absorption band, we only observe those coherences resonantly enhanced by the lower-energy exciton state in the dimers.

Figure 4.5D-F shows Stokes FSRS spectra for the PDI compounds. **PDI-Ref** exhibits a strong mode at 170 cm^{-1} and numerous peaks between 400 and 600 cm^{-1}. The 170 cm^{-1} peak is accompanied by weak shoulders. In comparison, the FSRS spectrum of **p-PDI** shows two additional intense peaks at 118 and 218 cm^{-1} and slightly increased relative intensity of the peaks at 398 and 434 cm^{-1}. We also observe other peaks between 500 and 600 cm^{-1}, but they do not show increased relative intensity compared to those observed for **PDI-Ref**. The spectrum for **m-PDI** exhibits similar peaks at 227, 406, and 430 cm^{-1}. The relative amplitude of the former is significantly reduced when compared to the corresponding peak in the **p-PDI** spectrum, while the relative intensities of the latter two modes are only slightly reduced.

The ground-state FSRS results corroborate many of the peak trends noted both from Figure 4.4D-F and Figure 4.5A-C. As discussed above, the primary pathway leading to FSRS gain in a ground-state experiment should be minimally affected by the vibronic enhancement mechanism that has been discussed in the context of time-domain oscillations in 2DES.[107, 258] Thus, the Raman data imply the amplitude differences in the ground-state 2DES power spectra between **PDI-Ref**, ***p*-PDI**, and ***m*-PDI** can be described predominantly by changes to FC factors and not intensity borrowing from coherent interaction between dimer exciton states and near-resonant vibrational states. Though peak amplitudes in the excited-state power spectra in Figure 4.4D-F additionally rely on FC factors between the S_1 and a higher-lying excited state, the similarity between the excited- and ground-state 2DES trends suggests that the excited-state coherences are also impacted primarily by changes to FC factors apart from vibronic enhancement. These claims are further supported by an additional 2DES experiment we conducted with the pump center moved ~500 cm^{-1} higher in energy, where the results show nearly identical trends to the ones we presented here despite having different resonance conditions with the low frequency vibrational and/or vibronic states (Figure S4.15, Appendix A). Furthermore, excited-state FSRS spectra for each compound corroborate our conclusions with similar trends present to those of the ground-state (Figure S4.20).

While the prominent vibrations exhibited by unsubstituted PDI variants in previous literature[259, 260] are characterized by in-plane ring distortion, inclusion of the 4-*t*-butylphenoxy substituents in the systems here leads to significant twisting of the PDI core,[253-255, 261] thus heavily altering the nature of the vibrations in the low frequency region of the Raman spectrum. Both dimerization and decreasing interchromophoric spacing by changing the benzyl linkage introduces extra steric hindrance between the substituents and thus likely alters the degree of core twisting.

Considering that the low frequency vibrations in these systems primarily involve motions of the PDI core nuclei, as revealed by DFT normal mode analysis on **PDI-Ref** (Figure S4.21), this structural strain may result in a combination of altered FC factors and the presence of new normal modes. Such an effect accounts for the differences observed in both the 2DES power and FSRS spectra for **PDI-Ref**, ***p*-PDI**, and ***m*-PDI** without invoking the vibronic enhancement mechanism. Furthermore, it is worth noting that similar trends in the relative intensity of Raman-active modes in cyclophane dimers as a function of decreasing $\pi-\pi$ distance have been observed previously,[262] which suggests this result may be general to systems of closely-spaced chromophores.

4.4. Conclusions

Here we have shown a significant dependence of the vibronic and vibrational coherences in PDI cyclophanes upon interchromophoric interactions. Through comparison of the power spectra obtained via time-domain 2DES signal modulations to FSRS measurements and DFT calculations, we determined this dependence is of structural origin. While vibronic enhancement is potentially present in some of the observed oscillations, our results suggest this mechanism cannot fully account for the trends. For PDI systems specifically, our results indicate particular chromophore arrangements may be ideal for strong prevalence of certain coherences. Furthermore, these results illustrate the sensitivity of vibronic and vibrational coherences to van der Waals forces between neighboring chromophores. Such knowledge is critical for understanding how vibronic coherences may be exploited for efficient energy transfer in synthetic light-harvesting arrays.

Chapter 5: Influence of Vibronic Couplings on Ultrafast Singlet Fission

5.1. Introduction

Over the past decade, the potential importance of coherent mixing between electronic and nuclear degrees of freedom in natural photosynthesis has been widely researched.[13, 19, 107, 143, 156, 160, 188, 194, 258, 263-274] Understanding these coherence phenomena may also prove important in designing new molecular opto-electronic devices, such as photovoltaics.[19, 215, 218, 238, 266] While most of this research has centered on energy[13, 143, 186, 268, 269] and electron transfer,[68, 98, 99, 214, 263, 272] it is also clear that electronic-vibrational (vibronic) coherence may play a role in a wider range of photophysical mechanisms, such as singlet fission (SF). SF is the photo-driven conversion of a single, high-energy singlet exciton to two independent, lower-energy triplet excitons in systems involving two neighboring organic chromophores.[275] SF is predicted to boost photovoltaic efficiencies, making a fundamental understanding of this complex process of paramount importance.[276] The initial SF event involves the spin-allowed conversion of the singlet state $^1(S_0S_1) \leftrightarrow {}^1(S_1S_0)$, which we will abbreviate as S_1, into a spin-correlated triplet pair state $^1(T_1T_1)$, which may undergo further spin evolution before separating into two uncorrelated triplet states.[277] To date, research has elucidated two mechanisms for this conversion: direct and indirect/mediated.[278] Direct SF relies on coupling between the S_1 and $^1(T_1T_1)$ diabatic states, making SF a concerted two-electron process.[231, 233, 234, 278, 279] In contrast, the indirect/mediated mechanism suggests that the link between the S_1 and $^1(T_1T_1)$ states is bridged by their individual coupling elements with the CT state.[231, 233, 234] These two pictures have been further divided into incoherent and coherent counterparts. The incoherent picture of indirect SF involves two sequential charge hopping events, where the CT state acts as an intermediate. Indirect SF becomes coherent when the effective coupling between the S_1 and $^1(T_1T_1)$ states becomes large relative to

the system-bath coupling.[231] For example, it has been demonstrated that virtual CT states can drive efficient SF via coherent superexchange coupling mediated by high-lying CT states.[233, 234, 278] More recently, coherent SF has been suggested to rely on vibronic coherence, where the S_1 and $^1(T_1T_1)$ states are directly mixed via nonadiabatic interactions.[46, 158, 198, 199, 203-206, 208, 280, 281] This could be achieved under both the direct and indirect mechanisms; in the latter case, the system eigenstates are described as mixtures of all three S_1, $^1(T_1T_1)$, and CT basis states. While the role of nuclear motions in driving coherent SF has recently been recognized, details of the influence of particular vibrations on the reaction coordinate of coherent SF remain largely unexplored.

Synthetic covalent dimers offer a direct route to study the role of nuclear motions in SF with high levels of control and detail. The synthetic versatility and photostability,[282] tunable energetics,[209, 283-285] and spectral characteristics[209] of terrylene-3,4:11,12-bis(dicarboximide) (TDI) make it an excellent system for probing vibronically coherent SF. We have shown previously that SF in slip-stacked cofacial TDI dimers involves S_1 - $^1(T_1T_1)$ mixing;[209, 284, 285] however, the mechanism for this mixing was not identified. Here, we use two-dimensional electronic spectroscopy (2DES) to examine the interplay of electronic and nuclear degrees of freedom during ultrafast SF in a covalently linked, linear TDI dimer with perpendicular TDI π systems. 2DES is a nonlinear spectroscopic technique that provides detailed information about energy flow within a molecular system and any redistribution of energy that occurs,[120, 121] such as through SF. Moreover, 2DES allows us to generate and probe vibronic coherences to investigate how any underlying vibronic coupling impacts ultrafast SF.[144, 156, 158, 160, 161, 263] We also use femtosecond stimulated Raman spectroscopy (FSRS) and resonance Raman DFT computations to characterize the key nuclear motions we observe via 2DES. By directly comparing the results we obtain from

the dimeric system to a monomeric TDI control compound, we find signatures of vibronic wavepackets traversing the S_1 surface to the $^1(T_1T_1)$ product state during SF in the dimer. Within the context of a modified Holstein Hamiltonian, our results suggest that low-frequency normal modes of the S_1 surface enhance vibronic coupling with high-frequency motions on the $^1(T_1T_1)$ state surface, enabling rapid SF within our < 50 fs time resolution. These results provide a mechanistic understanding of how coupling between electronic and nuclear degrees of freedom can impact SF.

5.2. Experimental details

The molecular structure of the monomer (**TDI₁**) and the dimer (**TDI₂**) are provided in Figure 5.1a. Both compounds were prepared according to literature procedures.[286, 287] For steady-state and time-resolved measurements, solutions of **TDI₁** and **TDI₂** in chlorobenzene solvent were prepared with optical densities of ranging from 0.2 to 0.5 OD in glass cuvettes with a 1 mm pathlength.

The 2DES apparatus used for this work is detailed in Section 2.4.2. We employed pump pulses centered around 16650 cm^{-1} (600 nm), spanning nearly 4000 cm^{-1} baseline-to-baseline (Figure S5.1, Appendix B) and compressed to 21 fs in duration. We collected a series of 2DES spectra in the pump-probe geometry as a function of the delay between the second pump and the probe pulses (the waiting time t₂) to analyze signatures of quantum coherence. For the results shown in the main text and a replicate trial, this delay was scanned from -98 to 2504 fs with 8 fs time steps, which yielded a frequency resolution of 14 cm^{-1} after cutting early timepoints containing coherence artifacts. We additionally performed experiments with different waiting time step sizes to identify laboratory noise signatures, as shown in the Supporting Information (Appendix B) for this chapter.

All replicate experiments were conducted independently on different days with different solvent aliquots to ensure the results were not correlated to laser fluctuations or solvent impurities (Figures S5.9-5.13). Further details describing the apparatus, pulse characterization, post-processing, and replicate trials can be found in Appendix B.

We performed FSRS with a narrowband (approximately 15 cm^{-1}) Raman pump centered at 14900 cm^{-1} (670 nm), which we tuned to be resonant with the primary 0-0 vibronic transition visible in the steady-state linear absorption (Figure 5.1b). Samples for these experiments were prepared as described above, but in cuvettes with a 2 mm pathlength.

5.3. Computational details

DFT calculations were performed using the Amsterdam Density Functional (ADF) software package. We employed the BP86 functional in conjunction with a DZP basis set to compute optimized geometries, normal modes, and resonance Raman spectra for both compounds *in vacuo*. Frequencies were scaled to account for anharmonicity using parameters reported in a previous study.[288] To estimate the effective coupling for SF, we calculated the energies of the S_1, $^1(T_1T_1)$, and CT states relative to the electronic ground state at the level of ωB97XD/DZP. We account for the chlorobenzene solvent environment by including an implicit solvation model in these calculations. This level of theory was additionally used to calculate electron and hole transfer integrals for **TDI$_2$**. Refer to Appendix B for further computational details.

5.4. Theoretical modeling

To rationalize the experimental signatures of coherence that we observe, we employed a modified Holstein Hamiltonian (Section 3.3) to predict the composition of the vibronic manifolds involved in SF in **TDI$_2$**. This Hamiltonian has been used to evaluate the impact of vibronic

coupling on initially pure basis states.[158, 205] Here we explicitly include the basis singlet excited states $^1(S_1S_0)$ and $^1(S_0S_1)$ and the correlated triplet $^1(T_1T_1)$ state in the model. We approximate the coupling between these states by assuming that CT states link the S_1 and $^1(T_1T_1)$ states via superexchange.[231, 289] We dress each electronic basis state with three independent Franck-Condon (FC)-active vibrations, based on our experimental observations. A maximum of ten vibrational quanta were included for each vibration in the simulation. We compare the simulated linear responses of these compounds directly to the experimental absorption spectra to parameterize the Hamiltonian. See Chapter 3 and the Appendix B for more details regarding the simulations.
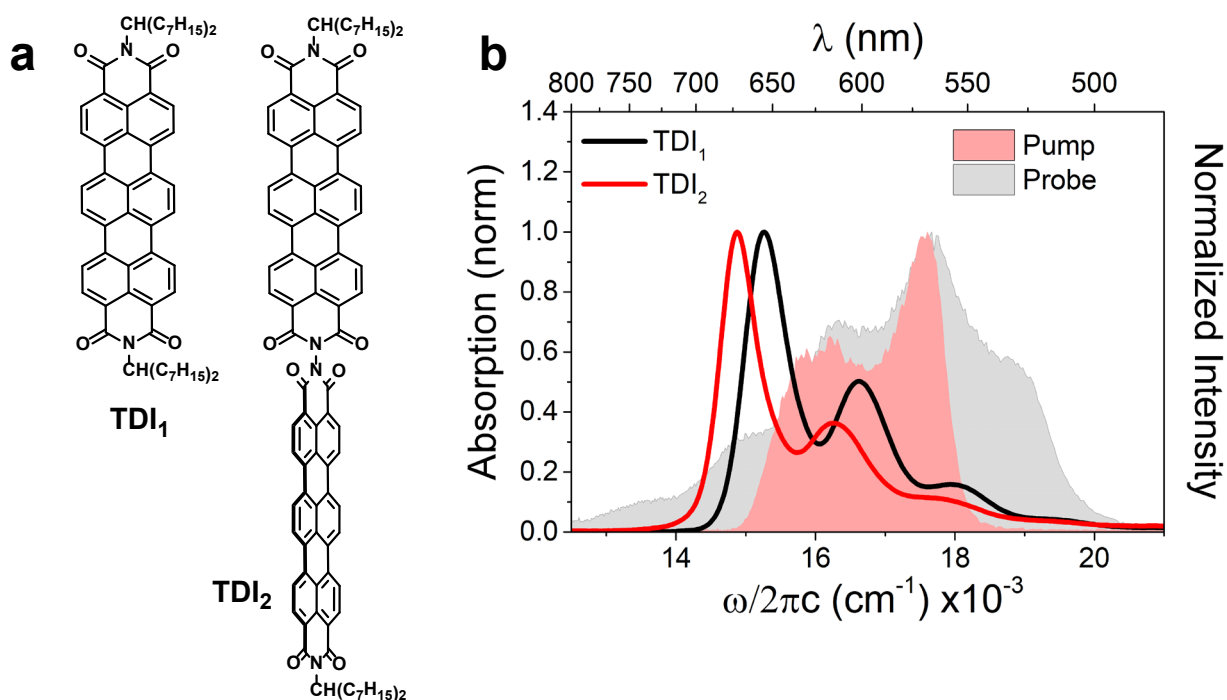
Figure 5.1. (a) Structures of **TDI₁ and TDI₂**. (b) Normalized steady-state absorption spectra for **TDI₁** and **TDI₂** obtained in chlorobenzene at room temperature. Pump and probe spectra for the 2DES measurements are superimposed.

5.5. Results

5.5.1. Electronic spectroscopy

Normalized absorption spectra for **TDI₁** and **TDI₂** dissolved in chlorobenzene at room temperature are shown in Figure 5.1b. The spectrum of **TDI₁** features a vibronic progression of about 1300 cm^{-1} with absorption maxima near 15400, 16700, and 18000 cm^{-1} (650, 600, and 555 nm, respectively). The vibronic progression in the absorption spectrum of **TDI₂** is similarly spaced, but the relative absorption of the 0-0 FC transition is increased. This result is well described by negative dipolar coupling (*J*-aggregation) between the collinear TDI $S_1 \leftarrow S_0$ transition dipoles and indicates the presence of vibronic exciton states in **TDI₂**.
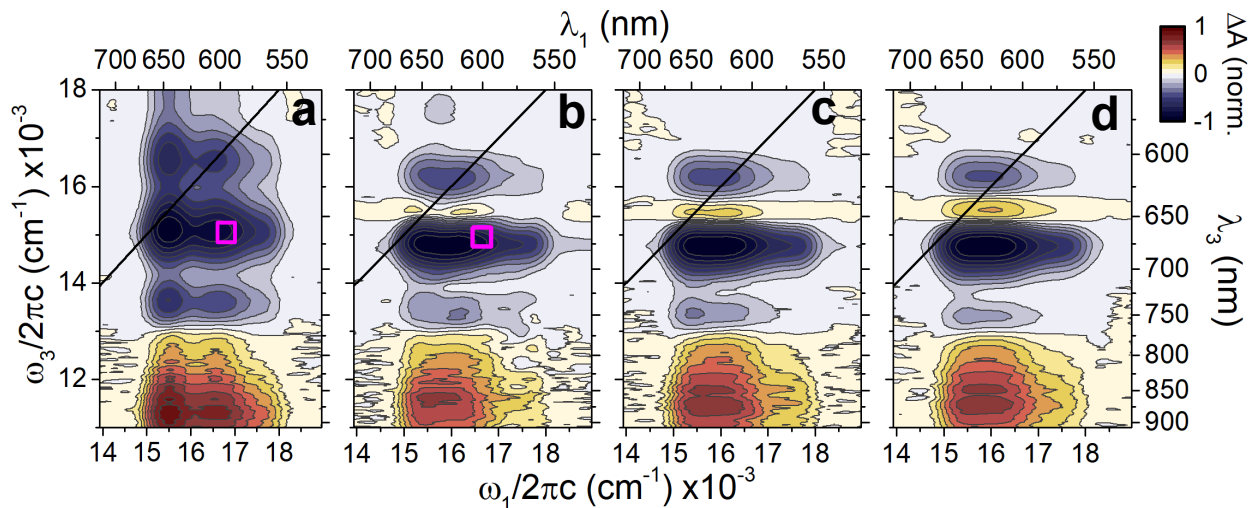
Figure 5.2. Absorptive 2DES spectra for (a) **TDI₁** at $t_2 = 1.5$ ps, and **TDI₂** in chlorobenzene at (b) $t_2 = 90$ fs, (c) $t_2 = 1.5$ ps, and (d) $t_2 = 155$ ps. All spectra are normalized to their respective maximum absolute change in absorption. Magenta rectangles indicate the approximate regions over which the coherence power spectrum analysis was performed for each sample.

Figure 5.2a shows the 2DES spectrum of **TDI₁** in chlorobenzene at a waiting time of 1.5 ps. The *x*- and *y*-axes of the 2D plot denote the pump (ω_1) and probe (ω_3) energies, respectively. Several clear features manifest themselves in Figure 5.2a. Namely, a grid of negative (blue) peaks straddle the diagonal line ($\omega_3 = \omega_1$). These peaks represent a combination of ground-state bleach

(GSB) and stimulated emission (SE) signals. Due to the well-resolved vibronic peaks shown in the steady-state spectrum, the peaks in the 2DES spectrum are spaced in both the pump and probe dimensions by approximately the energy of the FC-active C=C stretch. Near the diagonal, GSB and SE cannot be easily distinguished. However, the features above the diagonal in the probe dimension (ω_3 = 16500 cm^{-1} and ω_3 = 17800 cm^{-1}) are predominantly composed of GSB signal. Conversely, features near ω_3 = 13500 cm^{-1} are dominated by SE. Two positive (red) peaks appear at ω_3 = 11500 cm^{-1} and are assigned to excited-state absorption (ESA) from the S_1 to a higher-lying S_n state. Figure S5.5 shows that from t_2 = 0 to 155 ps, no transient features beyond those visible in Figure 5.2a appear in 2DES spectrum of **TDI$_1$**.

Figures 5.2b-d show 2DES spectra for **TDI$_2$** at waiting times of 90 fs, 1.5 ps, and 155 ps, respectively. The general grid structure of the GSB/SE features remains for **TDI$_2$**, and in contrast to **TDI$_1$**, the 2DES spectrum for **TDI$_2$** immediately after photoexcitation shows positive ESA features centered near a probe frequency of ω_3 = 15500 cm^{-1}. These features grow in amplitude and merge as the waiting time increases, as seen in Figures 5.2c and 5.2d. We attribute these features to ESA of the $^1(T_1T_1)$ state. Notably, the ESA appears within the ~42 fs instrument response function. Moreover, SE from the S_1 state remains prevalent even as the $^1(T_1T_1)$ ESA increases. These observations align with previous investigations of this system, and other SF compounds, in that the pure S_1 and $^1(T_1T_1)$ basis states do not reflect the eigenstates of **TDI$_2$**.[158, 205, 209, 283, 284, 286, 290] Rather, the electronic structure of this compound is composed of optically bright mixed S_1-$^1(T_1T_1)$ states. While the initial photoexcited state in **TDI$_2$** has partial $^1(T_1T_1)$ character, we observe that the final state within the waiting times accessible to our experiment (160 ps) has significantly greater $^1(T_1T_1)$ character.[285]

5.5.2. Quantum beats

Beating signatures from quantum coherences report on mixing between diabatic states and manifest themselves as oscillations in the signal amplitude of relevant spectral features as a function of t_2.[15] Quantum beats arise from the production of superpositions of eigenstates lying within the pump pulse bandwidth. To isolate signals reporting on coherences, we subtracted the population dynamics at each (ω_1, ω_3) coordinate and Fourier transformed the residual traces to examine the frequency (ω_2) and power of any oscillatory signals (see Appendix B for further information).
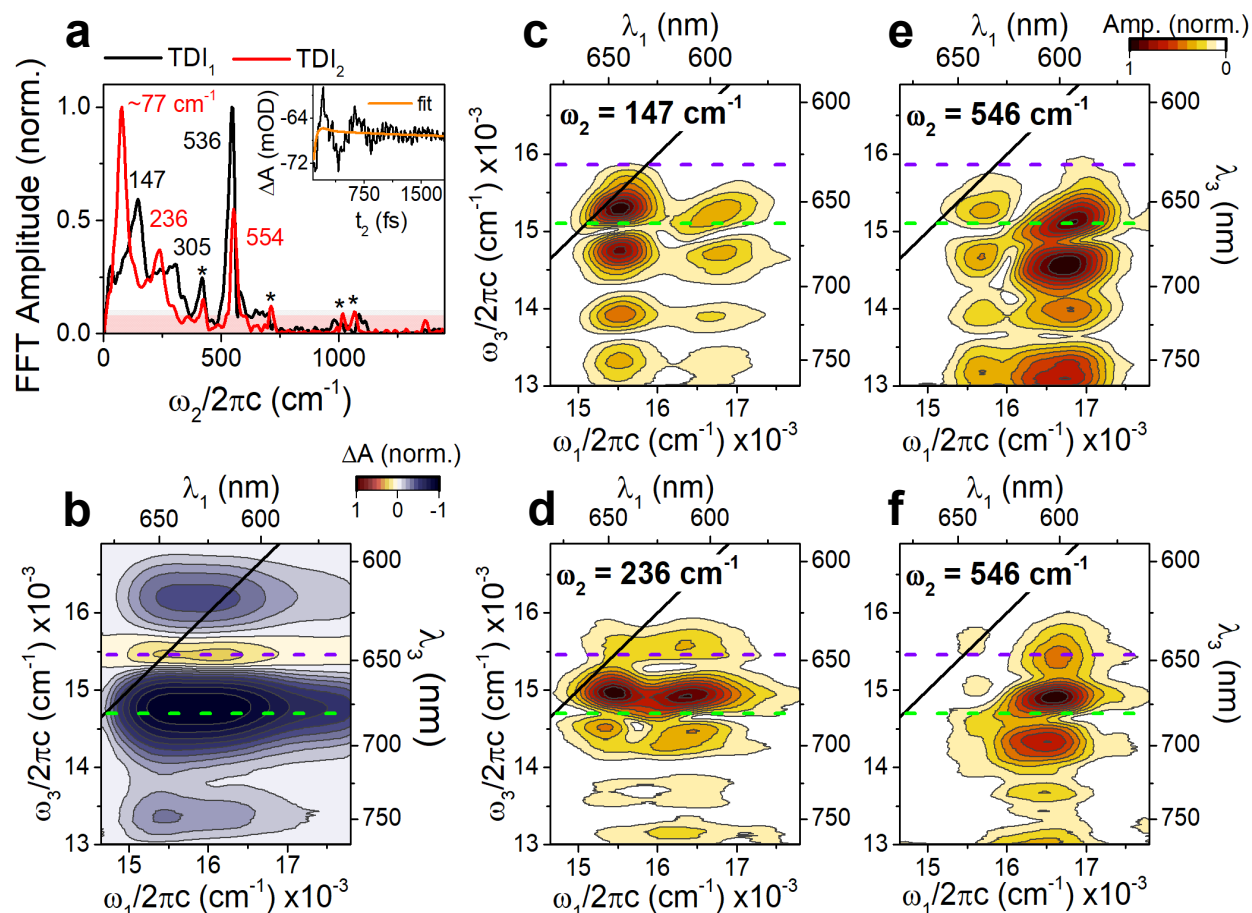
Figure 5.3. (a) Power spectra calculated in the frequency domain across a 400×400 cm^{-1} region of the (ω_1,ω_3) data for **TDI$_1$** (black) and **TDI$_2$** (red) in chlorobenzene. The shaded areas indicate the noise floor, defined as the average value for the respective spectrum. Inset: representative time-domain data and fit for **TDI$_1$**. (b) Time-domain 2DES spectrum of **TDI$_2$** at $t_2 = 1.5$ ps (expanded Figure 2c) indicating the region over which beatmaps were created. Beatmaps for the specified ω_2 values for (c and e) **TDI$_1$** and (d and f) **TDI$_2$**. Green and purple dashed lines indicate the probe frequencies that correspond to the (0-0) S$_1 \leftarrow$ S$_0$ and $^1(T_nT_1) \leftarrow$ $^1(T_1T_1)$ transition energies, respectively.

Figure 5.3a shows power spectra for **TDI$_1$** and **TDI$_2$** in chlorobenzene calculated as a Frobenius norm over a small window near the 0-1 vibronic crosspeak (magenta rectangles in Figure 5.2). The time-domain data shown in the inset to Figure 5.3a exhibits prominent intensity oscillations, which upon Fourier transformation result in a number of intense peaks in the frequency-domain spectra. We attribute the three major peaks that arise in the **TDI$_1$** power spectrum near 147, 305, and 546 cm^{-1} to intramolecular vibrational coherences. We cannot yet

distinguish between vibrational coherences on the ground vs excited state surfaces from these data alone (*vide infra*). Weak features are present at 800 and 1400 cm^{-1}, but their amplitude falls below our defined noise floor (shaded region). For **TDI$_2$**, we observe two new peaks at 77 and 236 cm^{-1}, a slight blueshift of the 550 cm^{-1} peak, and loss of the 305 cm^{-1} feature. While these new peaks could result from coherence between excitonic states, this explanation is unlikely considering that the linewidth of the peaks is significantly narrower than anticipated for electronic coherences at room temperature.[156, 192] The presence of coulombic coupling in **TDI$_2$** does suggest the coherences may be vibronic in nature.[160] Similar to the **TDI$_1$** data, the peaks observed for the dimer could originate from coherences on either the ground or excited state surfaces, or a combination of both. For clarity, we will refer to the excited- and ground-state coherences of **TDI$_2$** as vibronic and vibrational, respectively.

The amplitudes of these quantum beats with respect to the pump and probe frequencies can aid in the differentiating between ground- and excited-state signatures.[154] Following population subtraction on every (ω_1, ω_3) coordinate, we took slices of the purely frequency-domain data at a constant ω_2 value to create beatmaps. Figure 5.3b shows a time-domain trace of the **TDI$_2$** data at $t_2 = 1.5$ ps highlighting the entire region of this analysis. Figures 5.3c-f show the corresponding beatmaps over this region for select beat frequencies observed in the **TDI$_1$** and **TDI$_2$** data. To aid comparison of features in the beatmaps between the two compounds, we include green and purple dashed lines to indicate the probe frequencies that correspond to the (0-0) $S_1 \leftarrow S_0$ and $^1(T_nT_1) \leftarrow {}^1(T_1T_1)$ transition energies, respectively. While both of these energies were obtained experimentally for **TDI$_2$**, the value of ω_3 for the purple dashed line in the **TDI$_1$** beatmaps was determined by adding the difference in these transition energies in **TDI$_2$** to the S_1 energy of **TDI$_1$**.

Figure 5.3c shows the 147 cm^{-1} beat frequency appears strong in eight different pump-probe regions. We attribute the peaks occurring below $\omega_3 = 14000$ cm^{-1} to excited-state vibrational coherences since this region is dominated by SE and S_1 ESA and is several beat energy quanta below the diagonal. The peaks in the beatmap closer to the diagonal are likely due to a combination of ground- and excited-state coherences, although the node present near $\omega_3 = 15000$ cm^{-1} suggests a significant excited-state contribution.[146] Features in the beatmap centered at pump frequencies greater than $\omega_1 = 16200$ cm^{-1} likely originate from non-trivial interplay of the strongly FC-active 1300 cm^{-1} vibration and the weaker low-frequency modes in generating quantum beats.

The beatmap for the low-frequency ($\omega_2 = 236$ cm^{-1}) oscillation in the **TDI$_2$** data, Figure 5.3d, indicates this quantum beat modulates the 2DES signals in similar regions as the 147 cm^{-1} oscillation in the **TDI$_1$** data. However, quantum beating is observed near $\omega_3 = 15550$ cm^{-1}, which lies close in energy to the dashed purple line that indicates the center ESA transition energy from the $^1(T_1T_1)$ state. This is not the case for the 147 cm^{-1} oscillation in the **TDI$_1$** data. Similar observations can also be made in Figures 5.3e and 5.3f, where the overall prevalence of the $\omega_2 = 546$ cm^{-1} frequency is similar for both molecules, but the beatmap for **TDI$_2$** indicates beating at the location of the $^1(T_1T_1)$ ESA near $\omega_3 = 15500$ cm^{-1}.

Our observation of low-frequency quantum beating near the $^1(T_1T_1)$ ESA feature, which is not observed in the **TDI$_1$** data, indicates that these signal modulations may originate from wavepackets on a region of the potential energy surface (PES) that is predominantly $^1(T_1T_1)$ in character. This contrasts with initial expectations given that the resonance between the pump spectrum and the $S_1 \leftarrow S_0$ transition energy leads to coherences between states of mostly S_1 character. One possibility is that vibronic coupling generates a pathway for photoexcited wavepackets to transfer to the

$^1(T_1T_1)$ state. Alternatively, a portion of these beating signals may originate from the higher-energy, optically dark Frenkel exciton state; however, this contribution should be small due to the rapid time scale of exciton relaxation.[227] Further characterization is needed to understand the potential influence of nonadiabatic mixing between the S_1 and $^1(T_1T_1)$ states on the SF reaction coordinate in **TDI₂**.

5.5.3. Raman spectroscopy and calculations

We performed femtosecond stimulated Raman spectroscopy (FSRS) on each compound in chlorobenzene to examine the nuclear component of the coherences probed via 2DES. In contrast to 2DES, ground- and excited-state coherences can be independently studied with FSRS solely through the chosen resonance conditions.[125, 126] Though excited-state coherences can be monitored through use of an actinic pump pulse, observations obtained in this fashion will report on the coupling of vibrations to $S_n \leftarrow S_1$ transitions, which are not involved in the aforementioned quantum beating signatures. In order to elucidate any vibronic coupling between the S_1 and $^1(T_1T_1)$ states, we employ FSRS to probe purely vibrational coherences on the molecular ground state. This experimental implementation provides a direct look into the nuclear displacements between the S_1 manifold and the initial state relevant to 2DES, S_0.[228]

Figure 5.4a shows the baseline-subtracted FSRS spectra for each compound with the solvent peaks obscured. The low frequency (<600 cm⁻¹) regions of the FSRS and the 2DES power spectra are in good agreement. Notably, we observe Raman frequencies near 155, 300, and 550 cm⁻¹ for **TDI₁** and 80, 250, and 540 cm⁻¹ for **TDI₂**. The high-frequency side of the FSRS spectra features intense peaks near 1290 and 1400 cm⁻¹ for each compound, while the 2DES power spectra

do not. This is likely due to the differing resonance conditions between the experiments and the dependence of quantum beats in 2DES on the duration and profile of the pump pulse.
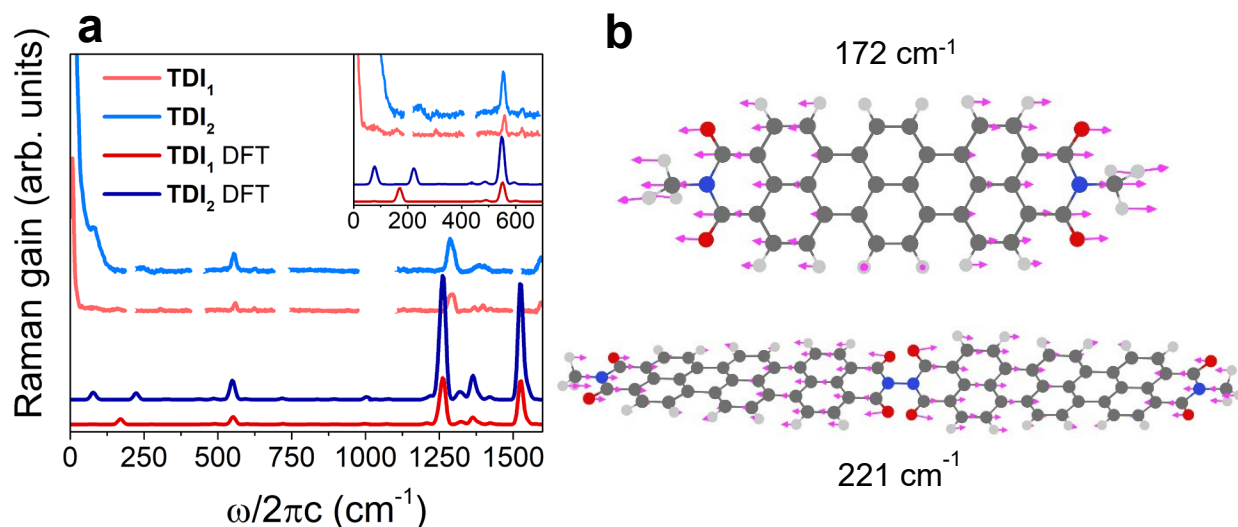
Figure 5.4. (a) FSRS and calculated resonance-Raman spectra for the **TDI₁** and **TDI₂** electronic ground states. FSRS spectra were collected with each compound dissolved in chlorobenzene. Solvent normal modes are removed for clarity. The RR spectra were computed with the compounds *in vacuo*. (b) Nuclear motions associated with the 172 cm⁻¹ and 221 cm⁻¹ normal modes computed for **TDI₁** and **TDI₂**, respectively.

We used DFT to calculate the resonance Raman spectra for each compound to compare the vibrational frequencies with the experimental results. We set the resonance condition equal to the lowest-energy bright electronic transition, thus mirroring the resonance condition present in the FSRS experiment. The calculated spectra are shown in Figure 5.4a. In the low-frequency region, we see two strong peaks for **TDI₁** at 172 and 552 cm⁻¹, similar to the experimental spectrum. Figure 5.4b shows that the calculated 172 cm⁻¹ mode for **TDI₁** is a symmetric, in-plane stretch of the TDI core directed in the long molecular axis. For **TDI₂**, we observe three intense peaks in the low-frequency resonance Raman spectrum, located at 78, 221, and 548 cm⁻¹. This mirrors the peaks observed for **TDI₂** via FSRS. These modes correspond approximately to linear combinations of the calculated monomeric modes. While the 550 cm⁻¹ mode does not shift dramatically between

TDI$_1$ and **TDI$_2$**, the 221 cm^{-1} vibration originates from the 172 cm^{-1} monomeric mode, as diagrammed in Figure 5.4b. See Figure S5.15 ([Appendix B](#)) for additional **TDI$_2$** normal mode assignments.

5.5.4. Theoretical modeling

Our DFT results indicate the $^1(T_1T_1)$ state lies 1450 cm^{-1} below the S$_1$ state in energy, which agrees with previously reported computations.[285] Moreover, the computed electron and hole transfer integrals suggest that weak effective coupling (< 10 cm^{-1}) exists between these two basis states. This is expected due to the minimal π-π overlap allowed by the perpendicular geometry and the orbital nodes at the imide positions of each TDI unit. While only weak electronic coupling may be present, vibronic coupling could explain the ultrafast SF observed in **TDI$_2$**. Near-resonance between a low-energy vibrational state in the S$_1$ manifold and a high-frequency $^1(T_1T_1)$ vibration may mix these states, similar to what has been observed in photosynthetic light-harvesting proteins[107, 263] and synthetic aggregates.[144, 160, 161, 291] Such mixing has been found to impact SF in multichromophoric systems of hexacene,[199] pentacene,[158, 208] rubrene,[198] and tetracene.[46, 280] However, our observation of wavepacket transfer between the S$_1$ and $^1(T_1T_1)$ states suggests that an interplay of low-frequency S$_1$ motions and a high frequency $^1(T_1T_1)$ mode(s) yields the energetic resonance(s) needed for vibronic coupling. We thus explored a modified Holstein Hamiltonian describing coupled singlet and correlated triplet manifolds, each dressed with low- and high-frequency vibrations. We specifically included the ~240, ~550 cm^{-1} vibrations that appear prominently on the $^1(T_1T_1)$ ESA (Figure 5.3), as well as the dominant FC-active ~1300 cm^{-1} motion visible in the absorption and FSRS spectra. We scaled the relative displacements between the ground and excited electronic states for each vibration using the relative intensity of the features

observed via FSRS. Parameterizing the dimeric Hamiltonian with outputs from the **TDI$_1$** control simulation (Figure S5.16a) and computations, we simulated the linear response of **TDI$_2$**. Refer to Appendix B for more theoretical details and control simulations that examine a range of input parameters (Figures S5.17 and S5.18).
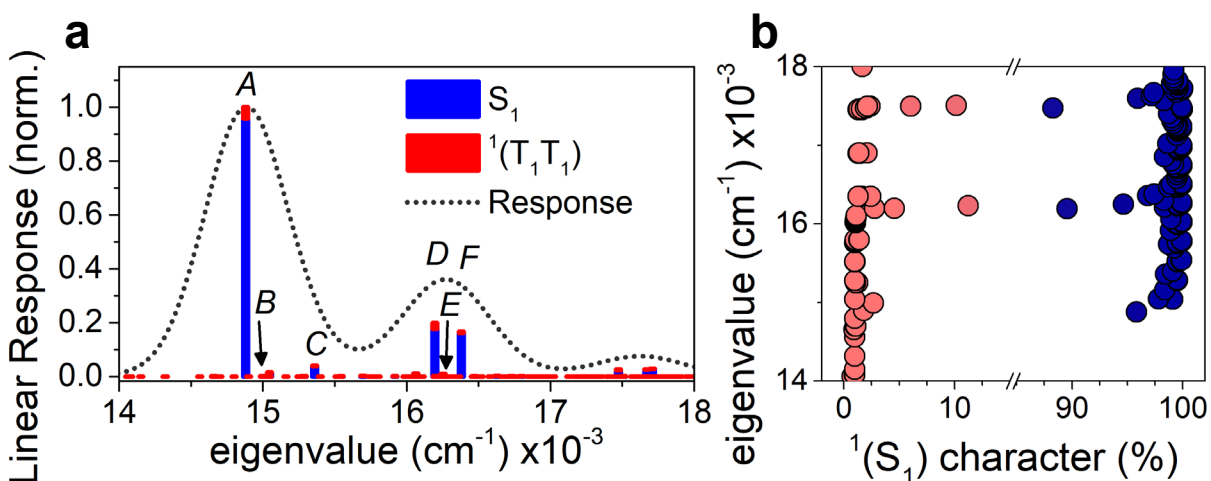
Figure 5.5. (a) Simulated linear response with the underlying stick spectrum superimposed. The oscillator strength for each transition is represented in terms of S$_1$ state composition. (b) Eigenvalues plotted versus corresponding eigenvector state compositions calculated from the modified Holstein Hamiltonian for **TDI$_2$**.

Figure 5.5a illustrates the calculated linear response of **TDI$_2$** with the oscillator strength of each transition decomposed into S$_1$ and ^{1}(T$_1$T$_1$) contributions. Several bright optical transitions emerge from the model, namely near 14880, 15360, 16195, and 16380 cm^{-1} (672, 651, 617, and 611 nm, respectively). For simplicity, we will refer to the final eigenstates of these transitions as *states A*, *C*, *D*, and *F*. States *A* and *C* correspond to the 0-0 FC transitions for the 1300 and 550 cm^{-1} vibrations on the bright S$_1$ exciton surface, while *D* and *F* are 0-1 vibronic features for the 1300 cm^{-1} mode of the two excitons present from the *J*-type interaction between the transition dipole moments. We additionally highlight the transitions to *states B* and *E* near 14995 and 16235 cm^{-1} (667 and 616 nm), respectively, for the subsequent analysis.

Notably, none of the transitions in Figure 5.5a are of pure S_1 origin, despite our prediction of weak electronic coupling between the S_1 and $^1(T_1T_1)$ states. In fact, we see the bright transition to state *A* is composed of approximately 96% S_1 and 4% $^1(T_1T_1)$ character. Such mixing is not observed when linear vibronic coupling is excluded from the simulation (Figure S5.17b). Figure 5.5b shows each system eigenvalue with respect to the S_1 character. Diabatic mixing is again observed here, with several states trending toward the center of the plot, primarily near the bright transition energies mentioned above. Based on the energetic spacing between the states with the most mixing, we suggest that near-resonances between vibrational levels of the 1300 cm^{-1} motion on the $^1(T_1T_1)$ and S_1 surfaces cause this departure from pure basis states. However, several additional states exhibit small, but non-negligible mixing, implying contribution beyond the 1300 cm^{-1} vibration.
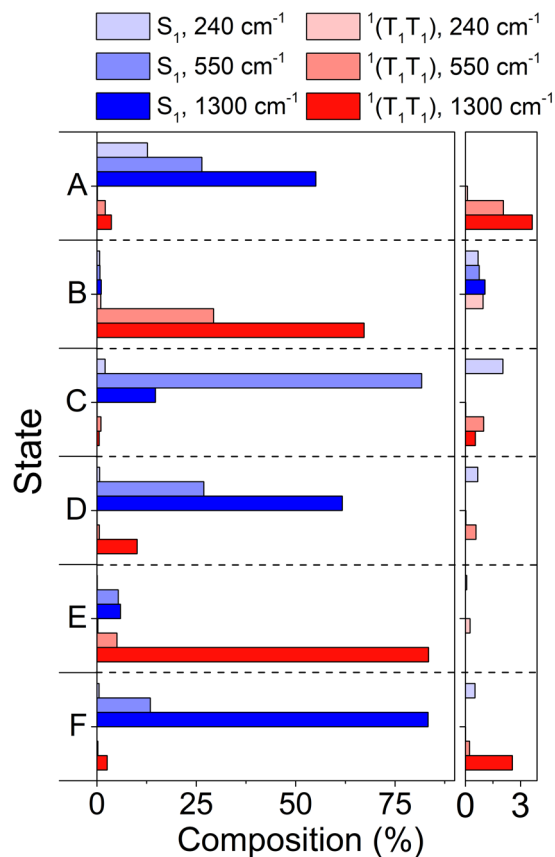
Figure 5.6. The specified eigenstates decomposed into percent contributions from all normal modes in the site basis. The right graph expands the small bars and suppresses the large bars in the left graph.

Figure 5.6 illustrates the composition of the indicated states (Figure 5.5a) in terms of each pure site-basis vibration. We note that this compositional analysis accounts for interactions from all states associated with a particular vibration, independent of occupation number. While the optically bright states A, D, and F originate predominantly from the 1300 cm^{-1} S_1 vibration, we see significant contribution from the 550 cm^{-1} S_1 vibration and, in the case of state A, the 240 cm^{-1} S_1 mode. State C highlights an example of diabatic state mixing driven not predominantly by the high frequency mode, but rather by the 550 cm^{-1} vibration. From the perspective of eigenstates more localized in the $^1(T_1T_1)$ manifold, the non-trivial contribution from the low-frequency motions is

again observed. All three motions on the S_1 surface contribute almost equally to state B, and state E cannot be described without the 550 cm^{-1} S_1 mode.

5.6. Discussion

We observe that mixed diabatic states underlie sub-50 fs SF in **TDI$_2$**, as evidenced by the simultaneous presence of both singlet and correlated triplet features in the time-domain 2DES spectra (Figures 5.2b-d). Based on the resonance condition, all coherent superpositions created by the 2DES pump pulses are initially located within the diabatic S_1 manifold. Nonetheless, we observe low-frequency oscillations of the $^1(T_1T_1)$ ESA signals. This suggests the reaction coordinate for SF most likely depends on a particular set of nuclear degrees of freedom. Simulations accounting for several vibrational motions with non-negligible Huang-Rhys factors indicate that vibronic coupling between S_1 and $^1(T_1T_1)$ produces states of mixed electronic character, even in the presence of weak electronic coupling. Moreover, this mixing is not driven solely by the high-frequency motion that bridges the S_1 and $^1(T_1T_1)$ electronic energy gap but, in addition, is aided by low-frequency motions on both electronic states.

The presence of vibrational coherences acting as "spectators" to ultrafast photophysics has been highlighted in previous literature[68] and could explain the behavior we observe in our experimental results. However, methods of confidently assigning integral versus spectator motions remain to be established. In contrast to models of SF wherein the reaction coordinate is described as a single vibration, a recent study describes the complex function that high-frequency intermolecular and low-frequency intramolecular motions may play in ultrafast SF.[208] Our analysis suggests the sub-50 fs SF observed here in **TDI$_2$** falls within this framework. The SF reaction coordinate in **TDI$_2$** is illustrated by the schematic multidimensional PES in Figure 5.7. SF proceeds

predominantly along the 1300 cm^{-1} vibration on the site-basis $^1(T_1T_1)$ state, since the first vibronic level for this vibration is near-resonant with the bottom of the S_1 energy well. In other words, motion along this vibration leads to an approach of the pure S_1 and $^1(T_1T_1)$ PESs, where vibronic coupling becomes significant. Higher-energy resonances between the 1300 cm^{-1} vibration on both diabatic states contribute additional instances of mixing, but drive SF less efficiently due to ultrafast relaxation effects.[285] Low-frequency motions originating on the S_1 surface aid mixing with the $^1(T_1T_1)$ manifold, yielding eigenstates of complex mixed nuclear and electronic character, such as states *A* through *F*. The effect of these nonadiabatic interactions is portrayed in Figure 7 by the smooth surface between the mixed states. The eigenstates as calculated by our theoretical model represent different nuclear configurations within the PES in Figure 5.7, highlighting the significance of molecular geometry to SF in **TDI₂**.

Our experimental observation of low-frequency coherences modulating $^1(T_1T_1)$ ESA signals supports this SF reaction coordinate. The low-frequency vibronic coherences that we create using ultrashort pump pulses have non-negligible $^1(T_1T_1)$ character immediately upon photoexcitation. These coherences could be between eigenstates *A*, *B*, and/or *C*, for example. The geometry of the molecule, and energy deposited along key nuclear motions, allows the collective wavepacket to traverse into the region of the PES dominated by $^1(T_1T_1)$ configurations and modulate the corresponding ESA signals.
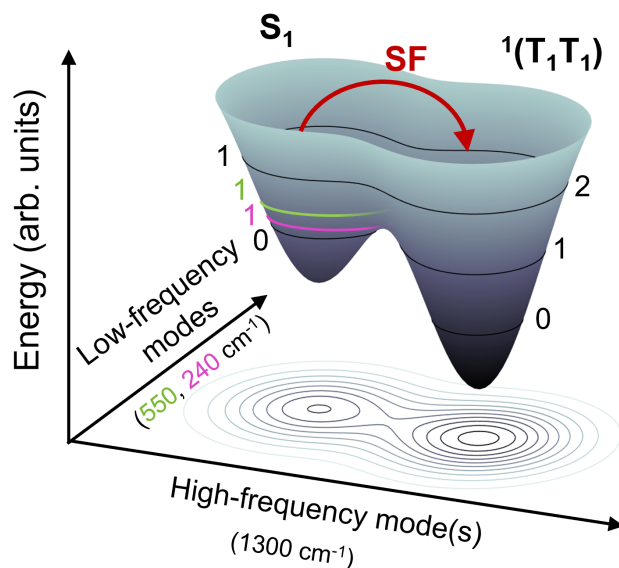
Figure 5.7. A potential energy surface, in the eigenbasis, described by high and low-frequency regimes of nuclear motion. Vibrational occupation numbers from the diabatic basis, included for qualitative interpretation, are provided for the 550 (green) and 240 (magenta) cm^{-1} S$_1$ vibrations, as well as the 1300 (black) cm^{-1} vibration on both the S$_1$ and ^{1}(T$_1$T$_1$) states. Contours projected on the floor plane illustrate (not to scale) the relative efficiency of each frequency regime in mixing the diabatic states.

This framework captures our experimental observation of sub-50 fs SF and predicts the states driving SF in **TDI$_2$** are *de facto* coherently mixed via nonadiabatic interactions along several nuclear coordinates. This is consistent with the description of eigenstates relevant to SF as points within a vector space defined by the linear combinations of the S$_1$, ^{1}(T$_1$T$_1$), and CT diabatic states. The relative weighting of these diabatic states in the final system eigenstates will be defined by the strength of their nonadiabatic interactions. Previous 2DES studies of a slip-stacked TDI dimer revealed a dependence of ultrafast SF and symmetry-breaking charge transfer photophysics on the pump wavelength.[209] Such excitation wavelength dependence is a manifestation of this vector space formalism driven by vibronic coupling. In general, this model predicts that the energy level distribution of the S$_1$, ^{1}(T$_1$T$_1$), and CT states will dictate the degree of mixing that occurs between them due to vibronic coupling. In the work presented here, the CT state likely lies too high in

energy to mix effectively with the other basis states, although it most likely couples the S_1 and $^1(T_1T_1)$ states via superexchange.[289] Even in benzonitrile, having a dielectric constant of 25.2, we do not observe strong coherent mixing with the CT state (Figure S5.14). Therefore, we do not see kinetic pathways with varying state compositions dependent on the pump energy. In contrast, the energetic proximity of the CT state to the S_1 and $^1(T_1T_1)$ states in the slip-stacked TDI dimer results in eigenstates comprising all three basis states. Slight energetic offsets between the $^1(T_1T_1)$ and CT states may result in different vibrations providing efficient mixing with the S_1 state. Thus, the dependence of the photophysics on the pump wavelength in the slip-stacked TDI dimer arises from the reaction pathways of the predominantly $^1(T_1T_1)$ and CT eigenstates being described by differing nuclear degrees of freedom.

In comparison to frameworks describing coherent SF along a single vibrational coordinate, we anticipate that the inclusion of multiple key vibrations will complicate the role of the bath in SF. Since intramolecular low-frequency motions couple efficiently to the environment,[292] SF relying on these vibrations may be more susceptible to relaxation processes. However, as we observe in this work and in our previous studies,[285, 286] state mixing remains prevalent near the equilibrium geometry of the photoexcited state in **TDI₂**. This can be explained by our finding that including additional, low-frequency modes in the SF reaction coordinate yields an increased density of vibronic states around the resonances between high-frequency S_1 and $^1(T_1T_1)$ motions. This effect remains true at the zeroth vibrational level for the high-frequency S_1 motion, therefore affording additional SF pathways closer in energy to the local PES minimum of the photoexcited state (Figure 5.7). In general, this formalism implies that coherent SF may be achieved in systems where

the molecular geometry allows the S_1, $^1(T_1T_1)$, and possibly CT states to share similar and accessible nuclear configurations, thus taking advantage of the resulting vibronic coupling.

5.7. Conclusions

Here, we observe that mixed singlet and correlated triplet pair states underlie sub-50 fs SF in a covalently linked, perpendicular TDI dimer. The transfer of low-frequency coherent wavepackets between the S_1 and $^1(T_1T_1)$ states was captured via 2DES experiments and suggests the SF reaction coordinate is defined by nonadiabatic interactions between these diabatic states. We employed FSRS to characterize the nature of key vibrations and the strength of their couplings to the bright $S_1 \leftarrow S_0$ electronic transition. In contrast to models of vibronic coupling that condense the photophysics to a single nuclear coordinate, we interpreted our results using a modified Holstein Hamiltonian with both S_1 and $^1(T_1T_1)$ states dressed with several vibrations. We found that multiple vibrations are necessary to account for the observed mixing between the S_1 and $^1(T_1T_1)$ states. This formalism suggests that the coherent mechanism of SF may necessitate consideration of the potential energy landscape in multiple nuclear dimensions. Moreover, these results highlight the potential function and intricacies of interactions between electronic configurations and nuclear geometries within the ultrafast SF process. Such characteristics offer tangible design principles in developing systems that employ coherent SF.

Chapter 6: Harmonic vibrational couplings in quantum beat spectra

6.1. Introduction

The interplay of nuclear and electronic coordinates in driving photochemical reactions offers a platform for external control of chemical dynamics on the molecular scale.[19, 222, 293] Coupled electronic-vibrational (vibronic) degrees of freedom have been shown to underlie several important photochemical reactions such as energy[54, 143, 194, 241, 294-296] and charge transfer,[68, 155, 164, 214-218, 297-300] singlet fission,[46, 157-159, 208, 301, 302] excimer formation,[303, 304] phase transitions,[37, 219] and solvation dynamics.[145] While many techniques allow insight into the vibronic configurations of multichromophoric systems, disentangling the key contributors to reaction coordinates remains challenging.[68, 305] The extensive frequency- and time-domain information afforded by two-dimensional electronic spectroscopy (2DES) has been particularly insightful for uncovering vibronic couplings and their connections to electronic dynamics.[19, 143, 155, 157, 158, 160, 161, 206, 218, 258, 294] In addition, the growing accessibility[53, 54] and range of experimental 2DES implementations[120] make it a powerful tool for bridging disciplinary gaps that have historically hampered progress toward engineering vibronic coherence within rationally designed molecular systems.[1, 222]

Owing to the temporally short and spectrally broad pulses that are required for 2DES, this nonlinear spectroscopic technique is able to launch and track the evolution of both populations and coherences among the quantum mechanical states of a molecular ensemble.[120, 306] While 2DES spectra are often analyzed with respect to excitation (ω_1) and emission (ω_3) dimensions at specified waiting time delays (t_2), as portrayed in the top panel of Figure 6.1, information explicitly about coherence phenomena can be extracted by fitting and subtracting population dynamics in the t_2 domain (middle panel of Figure 6.1) and subsequently performing a Fourier transformation of the residuals over t_2.[15] In the product purely frequency-domain ($\omega_1, \omega_2, \omega_3$) representation, as shown in

the lower panel of Figure 6.1, slices in the dataspace taken at constant ω_2 values indicate the amplitude of specific coherent signal oscillations, or quantum beats, as a function of excitation and emission energies. These so-called quantum beatmaps offer rich topological insight into the potential energy landscape of a molecular system and have been used to probe vibronically coherent energy transfer in photosynthetic complexes,[156, 192] reveal nuclear motions that enable important photochemical transformations in organic photovoltaic systems,[157, 158, 208, 214, 215, 218, 241] and explore the possibility of harnessing vibronic coupling as a design parameter in chemical technologies.[19, 37, 144, 196, 219, 238, 307]
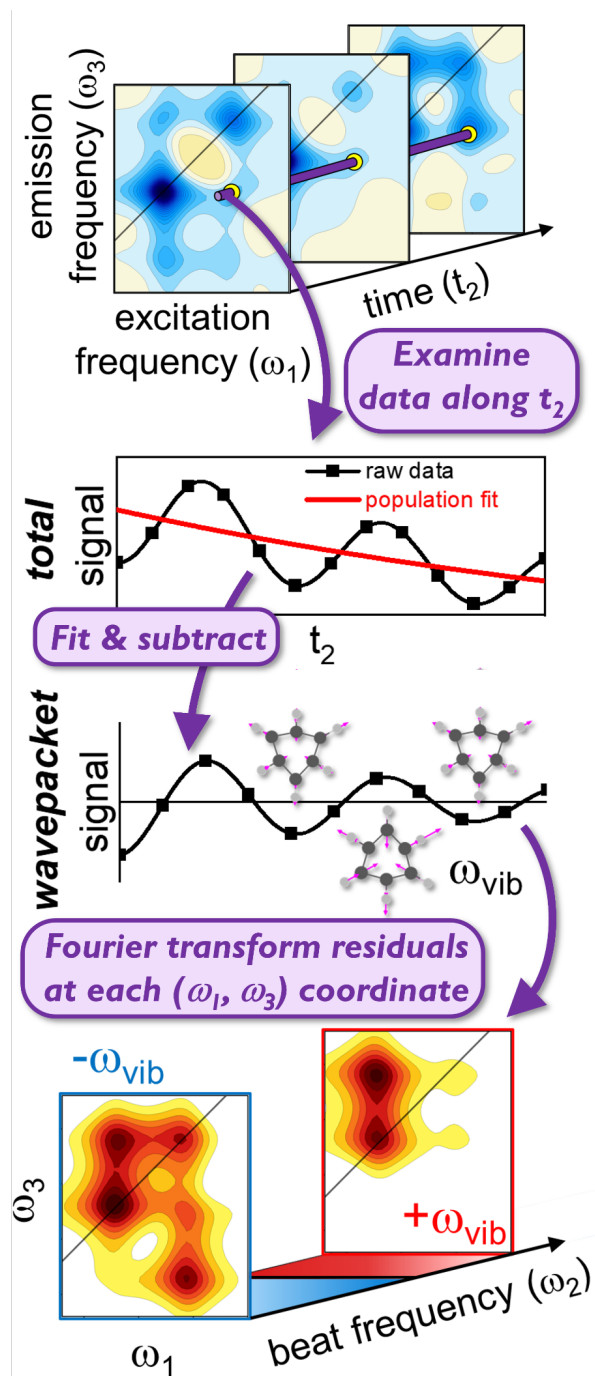
Figure 6.1. 2DES produces signals as a function of excitation (pump) and emission (probe) frequencies and the waiting time (t_2). The signal intensity along t_2 reveals population (non-oscillatory) and coherence (oscillatory) dynamics. Fitting and subtracting the former yields isolated wavepacket signals. Quantum beatmaps are obtained by repeating this process at all (ω_1, ω_3) coordinates and Fourier transforming the residuals. The features in each ω_2 beatmap are directly linked to the underlying nature of the system.

While 2DES beatmaps help to parse the fundamental parameter space of complex chemical ensembles, translating these maps into meaningful conclusions is by no means trivial. The single displaced harmonic oscillator (DHO) model is often assumed for simplicity when rationalizing patterns within beatmaps while accounting for both electronic and nuclear degrees of freedom.[154, 308, 309] The validity of this assumption, however, is brought into question by an increasing number of works that highlight the need to account for multiple vibrational coordinates in the mechanisms of a variety of ultrafast photochemical phenomena.[159, 164, 169, 208, 294, 310-313] While measuring couplings between nuclear motions is a central focus of many experimental techniques, such as multidimensional infrared,[314, 315] electronic-vibrational,[108, 123, 265, 316-318] vibrational-electronic,[316, 317, 319] and impulsive stimulated Raman spectroscopies,[130] the effects of such coupling are largely ignored in the analysis of 2DES beatmaps. Recent theoretical[320] and experimental studies[310, 312] have attributed marked deviations from the single-DHO model of 2DES beatmaps to wavepacket motion along coupled nuclear coordinates. Nevertheless, the shortage of direct comparisons between theoretical and experimental results limits the accuracy and general applicability of models that account for vibrational coupling in calculating 2DES beatmaps. As the connections between 2DES and the rational design of quantum technologies continue to expand,[222, 307] the effects and prevalence of coupled vibrational coordinates must be clarified.

Here, we use a joint experimental-theoretical approach to test the ability of the single-DHO versus multiple-DHO formalisms to reproduce experimental 2DES results from an array of chromophores, namely terrylenediimide (TDI), ITIC, methylene blue (MB), and Nile blue A (NB). Both TDI and ITIC have applications in organic photovoltaics as singlet fission sensitizers[283, 321] and non-fullerene electron acceptors,[322, 323] respectively, while MB and NB are important dyes to

the biomedical community.[142, 324] We first focus on comparisons between simulated quantum beatmaps for TDI, using both single- and multiple-DHO Hamiltonians, and experimental 2DES results. We show unambiguously that accounting for multiple unique vibrations significantly increases the accuracy of the simulation in capturing patterns within the experimental beatmaps. We attribute this agreement, which is achieved *without* treatment of anharmonicity, to vibronic coupling between multiple linearly displaced harmonic oscillators. Additional experiments indicate that deviations from the single-DHO formalism are also prevalent in the beatmaps for ITIC, MB, and NB, which illustrates the broad influence of harmonically coupled vibrations on 2DES results. Furthermore, we demonstrate that the multiple-DHO model increases the amplitude of ground-state vibrational signatures in the positive-frequency rephasing beatmaps in comparison to those predicted by the single-DHO formalism. Thus, harmonic coupling between vibrations may significantly complicate established procedures for separating signals from ground- and excited-state vibrational coherence, which highlights the importance of considering multiple nuclear coordinates when drawing conclusions from 2DES beatmaps, especially when multiple Franck-Condon (FC)-active modes are present. Taken together, these results demonstrate that 2DES simulations treating multiple vibrations on the same footing can increase the extent to which features in experimental quantum beatmaps can be linked to the fine vibronic structure of the molecular Hamiltonian, even for complex, solution-phase ensembles.
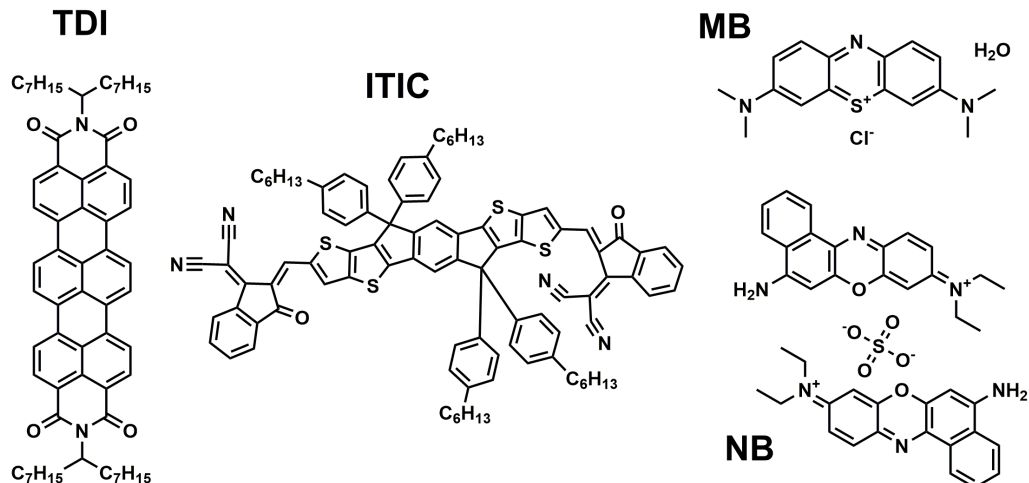
Figure 6.2. Structures for the chromophores investigated in this report.

6.2. Methods

Terrylene-3,4:11,12-bis(dicarboximide) (TDI) was prepared according to literature procedures.[283] 3,7-Bis(dimethylamino)phenazathionium chloride (MB) and the non-fullerene acceptor 2,2′-[[6,6,12,12-Tetrakis(4-hexylphenyl)-6,12-dihydrodithieno[2,3-d:2′,3′-d′]-s-indaceno[1,2-b:5,6-b′]dithiophene-2,8-diyl]bis[methylidyne(3-oxo-1H-indene-2,1(3H)-diylidene)]]bis[propanedinitrile] (ITIC) were purchased from Sigma-Aldrich and used without any further purification. 5-Amino-9-(diethylamino)-benzo[a]phenoxazin-7-ium perchlorate (NB) was purchased from Exciton and used without further purification. Figure 6.2 illustrates molecular structures for all compounds included in this study.

6.2.1. Optical spectroscopy

Steady-state UV/Vis absorption spectra for room temperature solutions of each dye molecule were collected using a Shimadzu UV-1800 spectrophotometer. Solutions were prepared with optical densities of ranging from 0.2 to 0.8 OD in glass cuvettes with a 1 mm pathlength for the following solute/solvent pairs: TDI/tetrahydrofuran (THF), MB/water (deionized), NB/ethanol,

and ITIC/dichloromethane (DCM). Both THF and DCM were dried using a Glass Contour solvent system.

2DES experiments were conducted using an apparatus detailed in Section 2.4.2 and employed pump pulses centered near 16650 cm^{-1} (Figure 2), which spanned 3390 cm^{-1} baseline-to-baseline (defined as 5% of the maximum intensity). We compressed these pulses to between 10 and 15 fs in duration (Figure S6.1) and focused them on the sample position with dispersion-corrected white light (WL) probe pulses spanning approximately 500-1000 nm. We collected a series of 2DES spectra in the pump-probe geometry as a function of the delay between the second pump and the probe pulses (the waiting time, t_2) to analyze wavepacket dynamics. This delay was scanned from approximately -100 to 1600 fs across several trials with either 5- or 8-fs step sizes. To extract the absorptive, rephasing, and non-rephasing contributions to the pump-probe geometry 2DES signals, we employed well-documented phase cycling procedures.[50, 224] Quantum beatmaps were extracted from the data per our protocols described in Section 2.5. Samples for transient experiments were prepared as described above. Refer to the Supporting Information (Appendix C) for further details regarding the apparatus, pulse characterization, experimental parameters and replicate results (Figures S6.4, S6.6, S6.12, and S6.13), post-processing, and additional experiments (Figures S6.7, S6.8, S6.10).

We performed femtosecond stimulated Raman scattering (FSRS) experiments with a previously described laser system.[325] The narrowband (approximately 15 cm^{-1}) Raman pump was tuned to be pre-resonant with the 0-0 vibronic transition visible in the steady-state linear absorption for TDI (Figure 6.3a). Samples for these experiments were prepared as described above, but in cuvettes with a 2 mm pathlength.

6.2.2. Theoretical modeling.

We employed an original MATLAB toolbox[157, 228] to generate a Holstein-form Hamiltonian (Equation 20, Section 3.3.1) with an arbitrary number of vibrations and propagate the system through real time in response to electromagnetic perturbations. See Chapter 3 for a complete description of the toolbox. We treated system-bath interactions with a stochastic fluctuation lineshape model[236] and fixed the phenomenological parameters for all simulations (Equation 35), which means that the microscopic mechanism(s) for variations between our simulations are solely based on the structure of the system Hamiltonian. In this work, we examine the effects of including either one or two DHOs within the system Hamiltonian on the resulting 2DES quantum beatmaps. Importantly, all DHOs are treated on equal footing. Based on our previous study of TDI,[157] we explored the 550 and 1350 cm^{-1} vibrations that are evident in the 2DES power spectra and linear response of TDI, respectively. We parametrized these vibronic Hamiltonians based on the degree to which the simulations reproduce the steady-state absorption (Figure S6.2) and 2DES spectra at constant waiting times for TDI, as summarized in Table S6.1. By enforcing time-ordering, we simulated each component of the four-wave-mixing signal separately. These components are the rephasing and non-rephasing contributions to the ground-state bleach (GSB), stimulated emission (SE), and excited-state absorption (ESA) signal generation pathways (Equations 29-34, Section 3.4). Refer to Appendix C for additional details regarding the theoretical model and data processing methods.

6.2.3 Computational details.

DFT calculations were performed using the Amsterdam Density Functional (ADF) software package. We employed the BP86 functional in conjunction with a DZP basis set to compute

optimized geometries, normal modes, and resonance Raman spectra of TDI in silico. Frequencies

were scaled to account for anharmonicity using parameters reported in a previous study.[288]

6.3 Results and Discussion

6.3.1 Experimental and theoretical TDI response comparisons.

We first investigated the linear response of TDI. Figure 6.3a shows the experimental TDI

steady-state absorption spectrum, in addition to the spectra of the pulses used to perform 2DES

measurements. The TDI absorption spectrum features a progression of vibronic peaks with an

average spacing of 1360 cm^{-1} (15260, 16600, and 17980 cm^{-1}). While we have previously shown

that numerous vibrations are coupled to the $S_1 \leftarrow S_0$ electronic transition of TDI,[157] we dressed

the multiple-DHO Hamiltonian with 550 and 1350 cm^{-1} vibrations to simulate the linear response
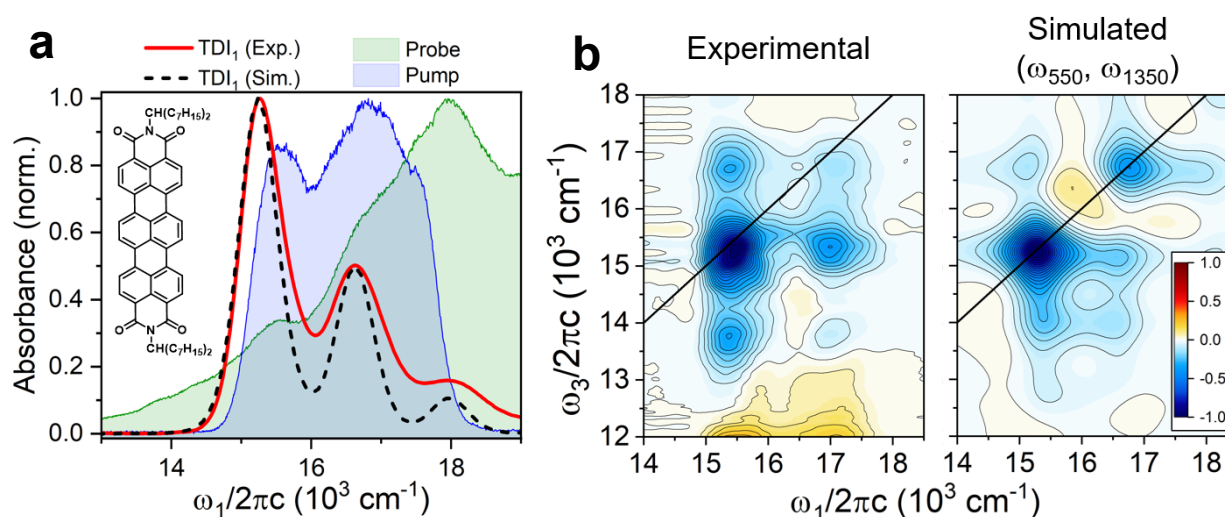
Figure 6.3. (a) Normalized experimental (Exp.) and simulated (Sim.) steady-state absorption spectra for TDI (structure inset) with 2DES pump and probe spectra superimposed. (b) Experimental and simulated 2DES spectra near $t_2 = 100$ fs. Contours are plotted at 5% intervals with 10% contour lines darkened. Experimental spectra were collected with the sample dissolved in THF at room temperature.

(Figure S6.2). This allowed us to maintain reasonable computational time while still representing

both low- and high-frequency regimes within the simulations. We found that the Huang-Rhys (HR)

factor (λ^2) for the 1350 cm^{-1} vibration ($\lambda^2 = 0.42$) is more than three times larger than that of the 550 cm^{-1} vibration ($\lambda^2 = 0.13$), which is a common outcome when comparing the HR factors for high- and low-frequency vibrations of organic chromophores.[326] Refer to Table S6.1 in Appendix C for a full compilation of parameters used in these simulations.

Using the parameters obtained through reproducing the experimental linear response with the multiple-DHO simulation, we extended our model to calculate the third-order response. The left panel of Figure 6.3b illustrates an experimental 2DES spectrum collected at t_2 = 100 fs (S_1 lifetime = 2.5 ns in CH_2Cl_2),[283] which agrees with our previous 2DES studies of TDI-based compounds.[157, 209] Briefly, a grid of intense, negative-signed peaks surrounds the diagonal $\omega_3 = \omega_1$ line. The peaks near the diagonal (ω_1, ω_3) = (15440, 15240 cm^{-1}) and (17070, 16730 cm^{-1}) arise from both ground state (S_0) bleach (GSB) and excited-state (S_1) stimulated emission (SE) from the 0-0 and 0-1 vibronic transitions of the 1350 cm^{-1} mode, respectively. We attribute the 300 cm^{-1} increase in the spacing between these peaks in the pump dimension relative to the 1350 cm^{-1} vibration to the spectral bandwidth of the pump pulse. As anticipated, these transitions also exhibit crosspeaks near (15390, 16750 cm^{-1}) and (17000, 15330 cm^{-1}). SE crosspeaks from the 1350 cm^{-1} mode are also observed near (15370, 13740 cm^{-1}) and (17030, 13820 cm^{-1}). In addition, the tails of two positive ESA peaks are visible at the bottom edge of the ω_3 axis and are attributed to an S_n ← S_1 transition. While we include this transition in our simulations (Figures S6.4 and S6.17), we draw our primary conclusions from the pump-probe frequency regime portrayed by the spectra in Figure 6.3b. See Appendix C for further details. As shown by right panel of Figure 6.3b, our simulation yields excellent agreement with the experimental 2D spectrum, with exception of the finite bandwidth in the latter. While the experimental spectrum represents a convolution of the

third-order response and the pump spectrum, we maintain generality in our simulations by centering discussions around the unconvoluted response. We note however that this convolution is more important to consider when the pump-bandwidth spans only a fraction of the steady-state absorption spectrum of the solute.[327]

6.3.2 Signatures of wavepacket motion from TDI.

As shown by the blue trace in Figure 6.4a, we observe clear wavepacket motion from TDI manifested as numerous quantum beats in the 2DES data near frequencies ω_2 = 160, 550, 800, 1300, and 1550 cm^{-1}. Since GSB and SE signals overlap substantially near the diagonal line in a 2DES dataset, these beats likely originate from a combination of both ground- (S_0) and excited-state (S_1) vibrational coherences.[154] The ground-state contribution is supported by the excellent agreement between most features and the spectra obtained from FSRS and resonance-Raman DFT. Two key differences are noteworthy, however. First, the ω_2 = 800 cm^{-1} peak in the 2DES power spectrum (observed between 800 and 860 cm^{-1} in additional independent measurements (Figures S6.7 and S6.8)) is completely absent in both the FSRS and DFT spectra. This discrepancy indicates that this mode stems predominantly from excited-state wavepacket evolution. This feature could be rationalized by a significant Duschinsky rotation[328] or as a combination band due to anharmonic coupling. However, we note that both of these phenomena have been observed to manifest in experimental FSRS spectra.[329] The second difference between the spectra in Figure 6.4a is the relative amplitude of the low- and high-frequency motions, which is seen most clearly by comparing the ratio of the 550 and 1300 cm^{-1} modes in each spectrum. While FSRS and the DFT computations indicate that the 1300 cm^{-1} vibration couples more strongly to the $S_1 \leftarrow S_0$ transition than the 550 cm^{-1} mode, the 2DES power spectrum suggests the opposite. Since we know this is

incorrect considering the 1300 cm^{-1} vibration is likely responsible for the prominent 1350 cm^{-1} vibronic progression in the linear absorption spectrum (Figure 6.3a), we attribute this discrepancy to effects of the finite pulse duration in launching and probing wavepacket motion.[330]

Although we observe that more than four TDI vibrations have significant FC activity, we restrict our multiple-DHO simulations to the inclusion of 1350 and 550 cm^{-1} vibrations for several reasons. First, the former mode is dominant in the FSRS, DFT, and linear absorption spectra, whereas the latter modulates the 2DES signals with the strongest intensity. Second, previous works report that the effects of interference between wavepacket motions are most evident when a significant difference exists between their carrier frequencies.[310, 320] Thus, our choice of both low-(<1000 cm^{-1}) and high-frequency (>1000 cm^{-1}) vibrations allows us to examine the generality of this finding.
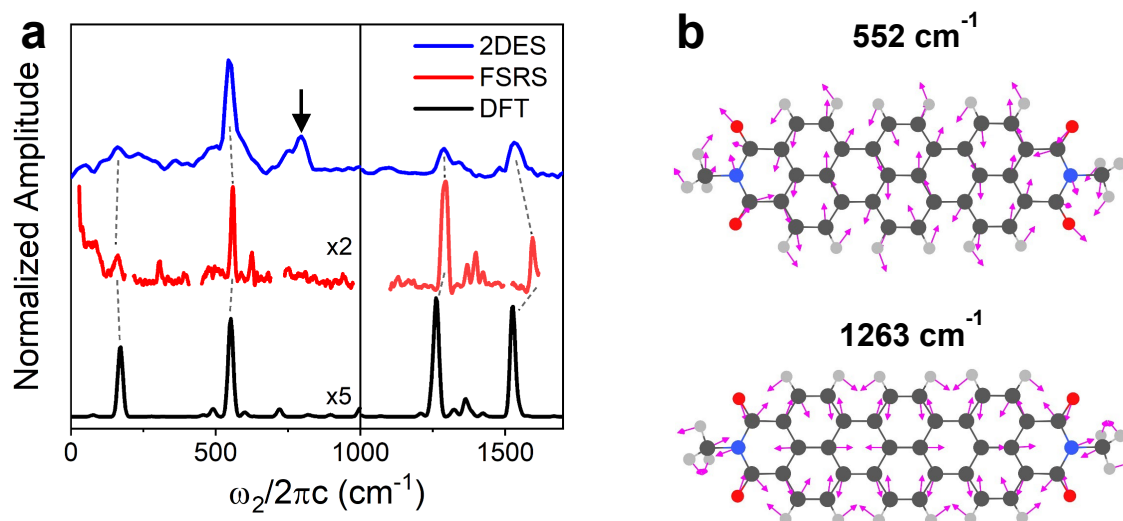
Figure 6.4. Comparison of (a) power spectra obtained via 2DES, FSRS, and resonance-Raman DFT calculations and (b) the calculated nuclear motions that are represented within the multiple-DHO model for TDI. The solid vertical line in (a) indicates the region (left) over which the indications of magnification are applicable. The dotted lines in (a) connect features that are commonly observed through all three methods, accounting for minor frequency shifts.

6.3.3. Comparisons of experimental and theoretical TDI quantum beatmaps.

A significant advantage of using 2DES to study wavepacket dynamics is the ability to analyze both rephasing and non-rephasing contributions to the third-order signal, which serves to isolate overlapping oscillatory signals that may otherwise interfere with each other.[16, 331] Isolating these signals also allows additional information to be obtained by examining both the positive- and negative-signed beat frequencies.[16, 150, 151, 332] We therefore focus our analysis on the rephasing portions of the experimental and theoretical signals, while the non-rephasing (Figures S6.12) and absorptive (Figures S6.10) counterparts are provided in Appendix C.

Significant effort has been placed on linking quantum beatmaps to particular molecular models, both for the 1D[164, 241, 269, 308, 331, 333] and 2D implementations of ultrafast electronic spectroscopy.[107, 142-144, 151, 154, 156, 158, 161, 320, 332] In the simplest case of an isolated chromophore, the single-DHO model predicts features in the positive and negative frequency rephasing 2DES beatmaps spaced by the frequency of the harmonic oscillator,[154] as shown in Figure 6.5a for both the 550 and 1350 cm^{-1} vibrations (assuming their wavepacket motions are completely independent). In contrast to our simulations, which include five quanta for each electronic state, these depictions consider only a single quantum of the nuclear motion on both the ground- and excited-electronic states. The experimental rephasing beatmaps for the $\omega_2 = +543$ (top) and -543 cm^{-1} (bottom) are shown in Figure 6.5b, where deviations from the schematics in Figure 4a are immediately evident. Namely, we observe several peaks in the beatmap located greater than one energy quantum away from the diagonal line. While it is tempting to assign these features to signal pathways involving higher vibrational states of the 550 cm^{-1} vibration ($v > 1$), our simulations using the single-DHO Hamiltonian do not predict such behavior (Figure 6.5c). Since the 0-v_n FC factor decreases rapidly as v_n increases, quantum beats originating from a single vibrational motion

dramatically decrease in amplitude as the distance from the 0-0 vertical transition energy in pump-

probe frequency space increases.
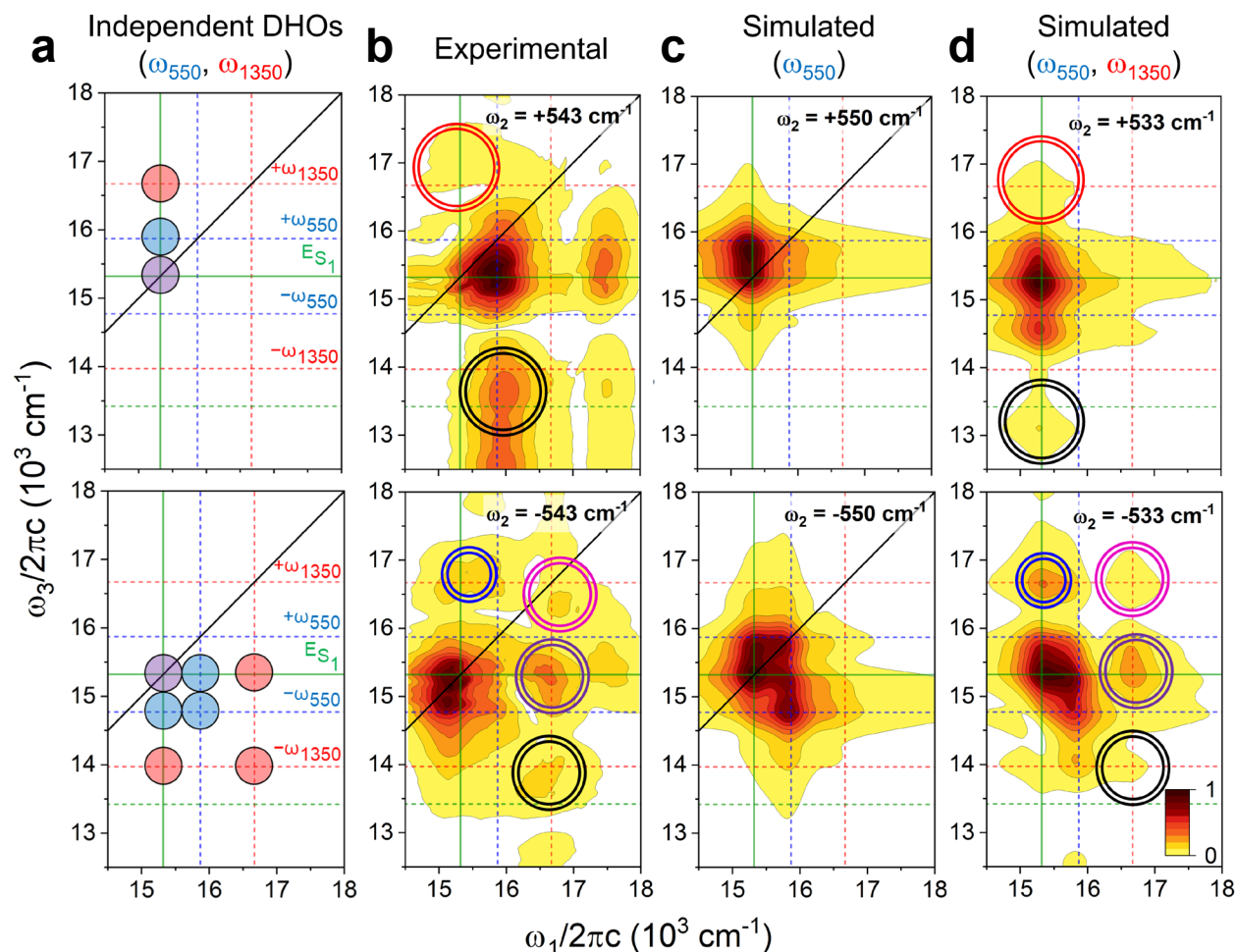
Figure 6.5. Rephasing quantum beatmaps for the positive (top) and negative (bottom) 550 cm^{-1} beat frequencies obtained from (a) a schematic picture of individual 550 and 1350 cm-1 vibrations, (b) experimental 2DES data, and third-order signals simulated with the (c) single-DHO simulations and (d) multiple-DHO Hamiltonians. The solid green lines indicate the 0-0 singlet electronic transition energies for all vibrations. Dotted lines indicate energies that represent either one or two frequency quanta away from the 0-0 singlet transition energy in either the pump (vertical lines) or probe (horizontal lines) axis for the 550 (blue), 1350 (red), and combination (green) bands. Solid circles in (a) indicate regions with non-zero beating amplitude (color coded according to origin vibration: ω_{550} = blue, ω_{1350} = red, overlap of ω_{550} and ω_{1350} = purple) while hollow circles in (b) and (d) highlight features that are not accounted for within the single-DHO approximation.

In stark contrast to the theoretical single-DHO results, the rephasing beatmaps obtained from

the multiple-DHO simulation (Figure 6.5d) exhibit remarkable agreement with the experimental

beatmaps, as highlighted by the colored circles in both Figures 6.5b and 6.5d. Comparing Figures 6.5b and 6.5d to the schematic in Figure 6.5a suggests that the 550 cm^{-1} beatmap draws amplitude from both the 550 and 1350 cm^{-1} modes. Based on recent theoretical predictions,[320] this observation suggests that interference between the 550 and 1350 cm^{-1} modes is responsible for the marked deviations from the expectations from the traditional single-DHO model. Comparisons between our experimental and simulated absorptive beatmaps (Figure S6.10, Appendix C) corroborate the insight drawn by Farfan and Turner from simulations of absorptive 2DES spectra in the presence of interfering vibronic modes.[320] Building upon this work, we observe that the mapping of the high frequency 1350 cm^{-1} mode onto the beatmap of the low-frequency 550 cm^{-1} vibration persists and is significantly more evident in the rephasing beatmaps. Moreover, the shift in the fundamental vibrational frequencies from 550 to 533 cm^{-1} and 1350 to 1367 cm^{-1} in the single- and multiple-DHO simulations, respectively, supports the presence of an interaction between the 550 and 1350 cm^{-1} modes.

In addition to modulating the shape of quantum beatmaps, interference between vibrational wavepackets is also predicted to generate combination bands in the power spectra of the quantum beats in 2DES.[320] As noted from Figures 6.4a and S6.7, the peak near 800 cm^{-1} in the power spectrum for TDI is not accounted for in the FSRS experiment and computed resonance-Raman spectrum. Figure 6.6a compares the experimental power spectrum to those obtained from both the single- and multiple-DHO simulations. As expected, both simulations predict beating signatures at the fundamental frequencies of the DHO(s) included. However, only the multiple-DHO simulation produces a feature near 850 cm^{-1}, which matches well with the experiment and is assigned to a difference-frequency band originating from coupling between the 550 and 1350 cm^{-}
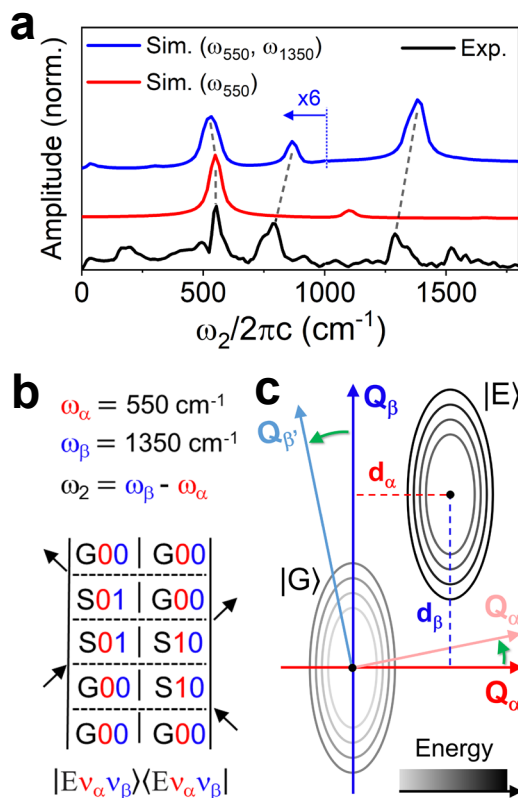
Figure 6.6. (a) Comparisons of experimental and simulated power spectra using both the single- and multiple-DHO Hamiltonians, (b) an example double-sided Feynman diagram that yields difference-frequency beating during t_2, and (c) a schematic illustrating the ground- (G) and excited-state (E) potential energy surfaces for the multiple-DHO model with vibrations α and β. The diagrams in (b) and (c) are color coded with red and blue signifying the 550 and 1350 cm^{-1} vibrational coordinates, respectively. Q_β (Q_α) and d_β (d_α) in (c) represent the site-basis nuclear coordinate and displacement for the β (α) vibrations, respectively, while $Q_{\beta'}$ and $Q_{\alpha'}$ indicate nuclear coordinates in the eigenstate basis. Green arrows portray the basis rotation.

[1] wavepackets. Moreover, we find reasonable agreement between the experimental and simulated beatmaps for this difference-frequency band, as shown in Figure S6.18. Figure 6.6b illustrates an example double-sided Feynman diagram that can explain quantum beats with a frequency equivalent to the frequency difference between two arbitrary vibrations α and β, in this case 550 and 1350 cm^{-1}, respectively. Importantly, such a beat frequency can only be generated by electronic excited-state evolution of the density matrix. While vibrational coherence on an excited electronic state can manifest in FSRS spectra by means of vertical-FSRS pathways,[334, 335] the lack

of the 800 cm^{-1} feature in our measured FSR spectrum (Figure 6.4a) suggests that the ground-state

FSRS signals are dominant. FSRS measurements with an actinic pump may provide further

information as combination bands have been observed in this manner previously.[329]

For the signal pathway illustrated in Figure 6.6b to be observable via 2DES, vibrations α

and β must not be orthogonal in the eigenstate basis. This non-orthogonality is also required to

explain how the 1350 cm^{-1} motion impacts the beatmaps for the 550 cm^{-1} vibration. The direct

experimental and theoretical comparisons put forth in Figures 6.5 and 6.6 illustrate the accuracy

of the multiple-DHO model in predicting the behavior of experimental quantum beating signatures

from TDI. We can therefore use this model to rationalize the physical origin of the coupling

between the 550 and 1350 cm^{-1} vibrations. Specifically, because we formulate our model with

vibrations treated within the system Hamiltonian, we can pinpoint the origin of the coupling to

system-specific interactions. Both anharmonic coupling and the Duschinsky rotation (where the

normal modes of the ground and excited electronic states are different yet related by linear

combination) can induce mixing between vibrational modes.[130, 308, 336, 337]   These effects are

expensive to treat in comparison to simple parallel harmonic potentials. In contrast to recent

experimental reports of deviations from single-DHO beatmap predictions due to anharmonic

coupling between vibrational wavepackets,[310] we find that the experimental TDI beatmaps are

excellently reproduced within the harmonic approximation. Moreover, since we do not explicitly

couple the vibrations in our multiple-DHO Hamiltonian, our model achieves this accuracy without

accounting for a possible Duschinsky rotation. Instead, we suggest that the vibrational coupling

evidenced by the TDI quantum beating signatures originates from purely harmonic coupling,

similar to that used recently in the calculation of crosspeaks in two-dimensional impulsively stimulated resonant Raman spectra.[130]

Figure 6.6c illustrates a top-down view of the potential energy surface (PES) captured by our model in the *site basis*. Importantly, the harmonic potentials for the ground- (G) and excited- (E) electronic surfaces are shaped by two orthogonal nuclear coordinates Q_α and Q_β. For TDI, where $\omega_\alpha = 550$ cm^{-1} and $\omega_\beta = 1350$ cm^{-1}, the potentials have an elliptical curvature since $\omega_\alpha \neq \omega_\beta$. However, the theory and its predictions are still applicable to the case where $\omega_\alpha = \omega_\beta$. Though no coupling is explicitly defined between the normal modes α and β, the PES is displaced along *both* nuclear coordinates by their respective HR factors. Diagonalizing the Hamiltonian to *the system eigenstate basis* effectively rotates the axes in Figure 6.6c, as shown by the green arrows, thereby yielding vibrations α' and β', which are linear combinations of vibrations α and β. Qualitatively, this means that treatment of multiple DHOs within the same system Hamiltonian results in purely harmonic coupling between the orthogonal vibrations, α and β in this example, which is then manifested in experimental measurements of the system eigenstates (quantum beatmaps and Fourier power spectra). We note that this interpretation has broad implications for the studies of a wide range of materials since the harmonic coupling is sensitive to the Huang-Rhys factors of all displaced oscillators within the system. Since FC activity is the only prerequisite, the effects of this harmonic coupling may manifest in 2DES experiments of individual molecules and as well as multichromophoric systems, where the complexity of the effects will scale with both the size of the individual molecules as well as the extent of interactions within a molecular ensemble. We hypothesize that the effects of this harmonic coupling are distinct from those that would arise from direct treatment of anharmonic coupling or a Duschinsky rotation in our multiple-DHO model.

While anharmonicity may play a role in shaping features in 2DES beatmaps,[310] the agreement between our simulated and experimental TDI beatmaps (Figures 6.5 and S6.10) suggests that harmonic vibrational coupling is predominantly responsible for the deviations from the predictions of the single-DHO approximation.

6.3.4. Generality and implications of coupled vibrational wavepackets.

Taking recent studies of multi-component vibrational wavepackets[310, 312, 320, 338, 339] in conjunction with the agreements that we observe between the multiple-DHO simulations and experimental TDI data, we posit that the single-DHO approximation breaks down more often than is commonly anticipated. Indeed, examination of the quantum beatmaps obtained in our previous study of perylenediimide-based monomers and dimers reveals that signatures of coupled vibrational and/or vibronic wavepackets are evident.[228] To further test the generality of the multiple-DHO formalism, we performed additional 2DES experiments on NB and MB, which are dye molecules applied in numerous biomedical contexts,[142] as well as ITIC, an efficient non-fullerene electron acceptor commonly employed in organic photovoltaic research.[322]

Figure 6.7 illustrates rephasing quantum beatmaps for the oscillations near 440, 461, and 600 cm^{-1} for MB, ITIC, and NB, respectively. We analyze the positive-signed beat frequency for each compound since, under the standard single-DHO approximation, only excited-state vibrational wavepackets modulate the positive-signed regime of the rephasing beating signals (*vide infra*).[151] This portion of the 2DES signal is therefore of significant importance when diagnosing quantum beating signatures in complex chemical systems.
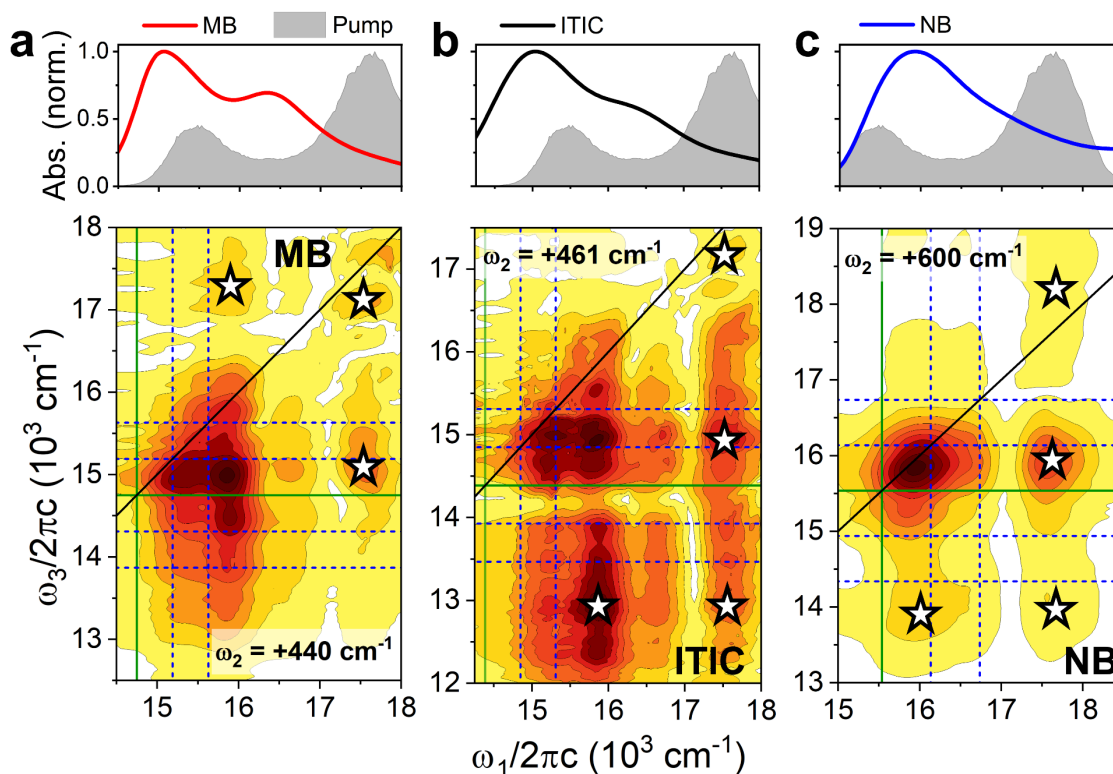
Figure 6.7. Positive frequency rephasing beatmaps for the strongest oscillatory feature observed from (a) MB (b) ITIC, and (c) NB. Linear absorption spectra (solid lines) for each compound are shown in the top row with the pump spectrum (shaded gray) superimposed. The solid green lines indicate the approximate 0-0 singlet electronic transition energies, while dashed lines show energies that represent either one or two frequency quanta away from the 0-0 electronic transition energy in either the pump (vertical lines) or probe (horizontal lines) axis. Stars highlight particularly strong features that are captured well when accounting for coupling of the fundamental vibration to one or more high-frequency oscillators.

The frequencies of these beating signatures match well with existing literature for MB,[142] ITIC,[323, 340] and NB,[341, 342] and in each case are among the strongest low-frequency vibrations coupled to their respective $S_1 \leftarrow S_0$ transitions. In each compound, the most intense quantum beating occurs within the region near the diagonal characteristic of a purely vibrational coherence,[154] accounting for systematic blueshifts from the $S_1 \leftarrow S_0$ transition energies[324, 342, 343] due to the overlap of the molecular absorption and pump spectra. However, as denoted by the stars, numerous features in each beatmap have clear deviations from the single-DHO model (top of Figure 6.5b), several of which are predicted by our multiple-DHO TDI simulations (top of Figure

6.5c) after taking the differences in beat frequencies into consideration. We expect that thorough accounting for the number, frequencies, and HR factors of the FC-active modes in each of these compounds would yield better agreement between simulation and experiment. These findings illustrate the general applicability of the multiple-DHO model and the importance of accounting for multiple nuclear coordinates when rationalizing quantum beating signatures in 2DES data.

In numerous previous works, positive-frequency quantum beats in the rephasing 2DES signal have been utilized to study purely excited-state wavepacket evolution, often for the purpose of connecting a particular vibrational mode to a reaction coordinate.[151, 156, 158] Figure 6.8a shows a simulated TDI beatmap from the rephasing GSB response function (Equation 29, Section 3.4) using the single- DHO Hamiltonian. The maximum amplitude in the simulated ω_2 = -550 cm^{-1} beatmap, located in the diagonal feature near $\omega_1 = \omega_3$ =15300 cm^{-1}, is nearly 90 times stronger than that of the ω_2 = +550 cm^{-1} beatmap. This result matches the expectation that ground-state wavepackets minimally modulate rephasing beatmaps for positive ω_2 values. However, we find that the multiple-DHO model, including both 550 and 1350 cm^{-1} vibrations, reveals a fallacy in this assumption, as shown in Figure 6.8b. In this case, the maximum amplitude of the ω_2 = +533 cm^{-1} oscillation relative to that of the ω_2 = -533 cm^{-1} frequency increases 350% in comparison to the corresponding relative maximum amplitude from the single-DHO simulation. Moreover, coupling between the low- and high-frequency wavepackets is particularly evident as a new diagonal feature and corresponding crosspeaks aligned with vertical transition energies corresponding to the 1350 cm^{-1} mode appear.

Figure 6.8 illustrates that including more than one DHO when examining vibrational wavepackets with 2DES and quantum beatmaps may lead to the breakdown of common
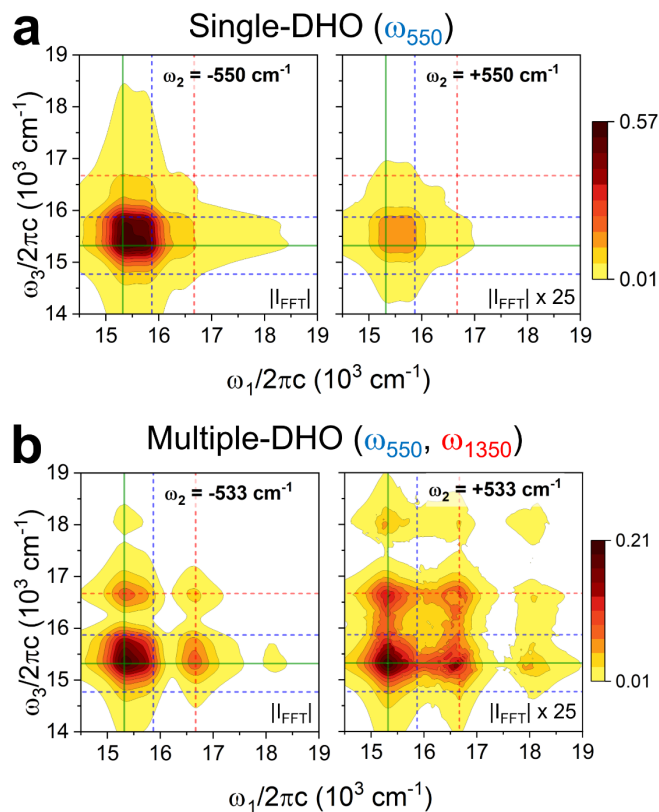
Figure 6.8. Simulated rephasing-GSB quantum beatmaps for the (a) single-DHO and (b) multiple-DHO models parameterized for TDI. The quantum beating signatures are partitioned into positive and negative ω_2 amplitudes.

assumptions, such as neglecting the ground-state background in positively signed rephasing beatmaps. More generally, dressing Holstein-like Hamiltonians with additional vibrations will invoke non-trivial interference between the conventional beatmaps predicted under the single-DHO approximation. We anticipate the effects of coupled harmonic wavepacket evolution will be even more pronounced and complex in studies of interacting, multichromophoric systems. This would imply that established approaches for disentangling signatures of vibrational, vibronic, and/or electronic coherence from the quantum beatmaps of molecular aggregates may be perturbed when the FC envelope consists of numerous vibrations. However, we believe this framework may help elucidate the nature of photochemical reactions that are driven by an interplay of vibrations

and, in turn, increase the accuracy of molecular design rules that are informed by 2DES experiments. Future work aims to expand these multiple-DHO simulations to molecular aggregates and critically assess these hypotheses. Though addressing numerous nuclear dimensions intensifies the required computational resources, the multiple-DHO model that we employed here requires relatively little input and can be applied in advance of 2DES experimentation. For example, experimental or computed steady-state absorption and resonance Raman spectra for a monomeric chromophore is sufficient to parameterize the multiple-DHO Hamiltonian and guide further experimental design.

6.4. Conclusions

We examined coupling between vibrational wavepackets in both theoretical and experimental contexts. Direct comparison of simulations using the single- and multiple-DHO Hamiltonians shows clear evidence for the substantial effects of such coupling in the experimental 2DES quantum beating signatures collected from TDI, ITIC, MB, and NB. We predicted and experimentally demonstrated that harmonic coupling between vibrational wavepackets results in mixing of their respective quantum beatmaps. We attribute this effect to the fact that both DHOs in our multiple-DHO simulations are treated simultaneously and on equal footing, which results in vibronic coupling between the originally orthogonal site-basis vibrations, even in the absence of anharmonic interactions. We note that this situation is applicable to any molecular system with two or more FC-active vibrations. We showed that the multiple-DHO model reveals the breakdown of the assumption that positive rephasing beat frequencies correspond to vibrational wavepacket motion solely in the electronically excited manifold of an isolated chromophore. This represents a clear instance in which the single-DHO model may misdirect the translation of

quantum beatmaps into meaningful chemical insight, particularly in studies of complex, multichromophoric systems. Considering that 2DES beatmaps are a current and vital tool for interrogating the potential energy landscape of key photodriven reactions, we stress the importance of accounting for the possible observables that can originate from coupled nuclear degrees of freedom in these experiments.

Chapter 7: Outlook for understanding and leveraging vibronic coherence

7.1. A brief recap of the dissertation

We wish to conclude with a recap of this dissertation, followed by a discussion of research outlooks for vibronic coupling and quantum coherence phenomena in chemistry. In Chapter 1, we explored the connections between coherence and several chemical contexts. We additionally overviewed how these connections have evolved in research foci over the past several decades. Importantly, we highlighted distinctions between two key pieces of most quantum coherence research: coherence of the *molecular system* and coherence of the *laser field(s)* (or, more generally, the means of measuring the observable). These pieces form an intrinsic connection between ongoing ambitions to understand emergent coherence phenomena in photophysical processes (e.g., photosynthesis, artificial light harvesting, etc.) and endeavors for controlling chemical dynamics with coherence.

In Chapter 2, we built upon the introductions to nonlinear optical spectroscopy in Chapter 1 by delving deeper into the instruments and methodologies used to perform the experimental research encompassed by Chapters 4 through 6. We have made our data processing codes publicly available[225] with the hope that readers may *use* the work discussed here as a starting point for their own research. Likewise, in Chapter 3 we explored the details of the theoretical simulations that corroborate various aspects of the experimental results in Chapters 4 through 6. These simulations can also be performed by readers using our OREOS software package (located at the cited GitHub repository[230]).

In Chapter 4, we leveraged two-dimensional electronic spectroscopy and femtosecond stimulated Raman spectroscopy to investigate the role of steric hindrance between chromophores in driving changes to vibronic and vibrational coherences in a series of substituted perylenediimide

(PDI) cyclophane dimers. We report significant differences in the frequency power spectra from the cyclophane dimers versus the corresponding monomer reference. We attribute these differences to distortion of the PDI cores from steric interactions between the substituents. These results highlight the importance of considering structural changes when rationalizing signatures of vibronic coupling in multichromophoric systems.

In Chapter 5, we report our observation of mixed singlet and correlated triplet pair states giving rise to sub-50 fs singlet fission (SF) in a linear terrylene-3,4:11,12-bis(dicarboximide) (TDI) dimer with perpendicular π systems. We observed the transfer of low-frequency coherent wavepackets between the initial predominantly singlet states to the product triplet-dominated states, which suggests that nonadiabatic couplings are involved with SF in this dimer. We interpret our experimental results in the framework of a modified Holstein Hamiltonian (Section 3.3.3), which predicts that vibronic interactions between low-frequency singlet modes and high-frequency correlated triplet pair motions lead to mixing of the diabatic electronic states. This work highlights how vibronic coupling can shape the complex potential energy landscape underlying ultrafast SF.

In Chapter 6, we focused on the information content of 2DES quantum beatmaps, which are well-known to provide direct insight into the intra- and interchromophoric couplings within a chemical system. We built upon traditional beatmap interpretations, which frequently consider only one nuclear coordinate, by simulating 2DES spectra and beatmaps with vibronic Hamiltonians dressed with multiple vibrational modes. By comparing the simulations directly to experimental 2DES results from two organic semiconductors and biomedical dyes, we show that coupling between purely harmonic vibrational wavepackets can have significant and prevalent effects on experimental 2DES results. Moreover, we demonstrated that users of standard

assumptions to separate ground- and excited-state vibrational coherence signatures from 2DES data should be wary of the complications that interactions between harmonic wavepackets can create.

The work discussed in this dissertation contributes understanding of the factors that can impact vibronic coupling in multichromophoric systems and the influence that vibronic coupling may have on photophysical dynamics in organic molecular assemblies. Moreover, the analytical and theoretical tools that we developed here serve as quality starting points for researchers that are utilizing nonlinear spectroscopy to investigate coherence phenomena in chemistry.

7.2. Outlook

While nature boasts mechanisms for capturing solar energy that have been evolutionarily optimized over billions of years, humans have the unique opportunity to borrow intuition from nature to improve artificial light harvesting. Used in combination with the knowledge gained from studies of quantum coherence in natural photosynthesis (Section 1.6), the limitless tunability of synthetic materials offers unprecedented opportunities to *understand* and *exploit* vibronic coupling in molecular electronics and devices.

The subset of findings described by this thesis and the references therein are but a fraction of the progress that has been made. Ongoing developments of third-order techniques, such as two-dimensional electronic-vibrational (2DEV)[108, 111, 123, 265, 316, 317, 344, 345] and two-dimensional vibrational-electronic (2DVE)[111, 124] spectroscopies, as well as fifth-order techniques such as two-dimensional impulsive stimulated Raman spectroscopy (2D-ISRS),[130, 131, 311] are opening doors to increasingly detailed pictures of vibronic phenomena. Pulse shaping technologies have been shown to dramatically expand the accessibility of advanced spectroscopic techniques,[51-53, 57, 224,]

[346-348] such as multidimensional infrared and electronic spectroscopies, therefore enabling a broader range of labs to address questions surrounding vibronic coupling.

The arenas of synthetic and materials chemistry are also progressing research of coherence phenomena. Several recent studies have demonstrated handles for modulating excitonic and/or vibronic couplings. For example, Alvertis and coworkers provided extensive evidence for solvent-enabled control over the transition between coherent and incoherent singlet fission exhibited by a tetracene dimer.[46] Wang et al. developed a molecular heterodimer platform to "switch on" vibronic coupling by tuning the electronic energy gap between the monomer moieties and restricting intramolecular rotations.[144] Hart and coworkers demonstrated independent control over excitonic couplings and system-bath interactions using a DNA-based platform integrated with cyanine chromophores.[307]

Recently, exciting developments have been made in using machine learning to *process* and *decipher* complex spectroscopic signals. For instance, Ren et al. taught a convolutional neural network to recognize protein secondary structures with high accuracy using simulated two-dimensional UV spectra as inputs.[349] Work in this direction may enable more accurate and efficient interpretation of experimental nonlinear spectra.

The example studies discussed in this section bode well for those who are interested in harnessing vibronic coupling and/or other coherence phenomena to steer chemistry. As research continues to become increasingly interdisciplinary, collaborations that effectively span experiment, synthesis, and theory will hold the greatest promise for progress in leveraging molecular characteristics for desirable macroscopic outcomes. It is important to acknowledge, however, that fields of research surrounding coherence effects in chemistry have faced a non-

negligible amount of controversy over the past two decades.[1, 16, 188, 350-352] Recent review articles[1, 16] have assigned some responsibility for this controversy to issues with interdisciplinary communication (among other issues that are beyond the scope of the present discussion). We reiterate the importance of bearing in mind the societal factors that impact the funding and execution of STEM research. In light of hurdles that these fields have faced, the collective knowledge, tools, and collaborations that have emerged from studies of coherence phenomena in chemistry hopefully have set the stage for substantial progress in years to come.

References

1. Mančal, T. A decade with quantum coherence: How our past became classical and the future turned quantum. *Chem. Phys.* **2020**, *532*, 110663.

2. Kippelen, B.; Bredas, J. L. Organic photovoltaics. *Energy Environ. Sci.* **2009**, *2* (3), 251-261.

3. Shockley, W.; Queisser, H. J. Detailed balance limit of efficiency of p-n junction solar cells. *J. Appl. Phys.* **1961**, *32*, 510-519.

4. Cui, Y.; Yao, H. F.; Hong, L.; Zhang, T.; Tang, Y. B.; Lin, B. J.; Xian, K. H.; Gao, B. W.; An, C. B.; Bi, P. Q.; et al. Organic photovoltaic cell with 17% efficiency and superior processability. *Natl. Sci. Rev.* **2020**, *7* (7), 1239.

5. Liu, X.; Rand, B. P.; Forrest, S. R. Engineering Charge-Transfer States for Efficient, Low-Energy-Loss Organic Photovoltaics. *Trends Chem.* **2019**, *1* (9), 815.

6. Lopez, S. A.; Sanchez-Lengeling, B.; de Goes Soares, J.; Aspuru-Guzik, A. Design Principles and Top Non-Fullerene Acceptor Candidates for Organic Photovoltaics. *Joule* **2017**, *1* (4), 857.

7. Clarke, T. M.; Durrant, J. R. Charge Photogeneration in Organic Solar Cells. *Chem. Rev.* **2010**, *110* (11), 6736-6767.

8. Jackson, N. E.; Savoie, B. M.; Marks, T. J.; Chen, L. X.; Ratner, M. A. The next breakthrough for organic photovoltaics? *J. Phys. Chem. Lett.* **2015**, *6*, 77.

9. Bredas, J.-L.; Norton, J. E.; Cornil, J.; Coropceanu, V. Molecular Understanding of Organic Solar Cells: The Challenges. *Acc. Chem. Res.* **2009**, *42* (11), 1691-1699.

10. Rao, A.; Friend, R. H. Harnessing singlet exciton fission to break the Shockley–Queisser limit. *Nat. Rev. Mat.* **2017**, *2*, 17063.

11. Zewail, A. H. Femtochemistry: Atomic-Scale Dynamics of the Chemical Bond. *J. Phys. Chem. A* **2000**, *104*, 5660.

12. Tokmakoff, A. *Time-dependent quantum mechanics and spectroscopy*; 2014.

13. Chenu, A.; Scholes, G. D. Coherence in Energy Transfer and Photosynthesis. *Annu. Rev. Phys. Chem.* **2015**, *66* (1), 69-96.

14. Yampolsky, S.; Fishman, D. A.; Dey, S.; Hulkko, E.; Banik, M.; Potma, E. O.; Apkarian, V. A. Seeing a single molecule vibrate through time-resolved coherent anti-Stokes Raman scattering. *Nat. Photon.* **2014**, *8* (8), 650-656.

15. Dean, J. C.; Scholes, G. D. Coherence Spectroscopy in the Condensed Phase: Insights into Molecular Structure, Environment, and Interactions. *Acc. Chem. Res.* **2017**, *50* (11), 2746-2755.

16. Cao, J.; Cogdell, R. J.; Coker, D. F.; Duan, H.-G.; Hauer, J.; Kleinekathöfer, U.; Jansen, T. L. C.; Mančal, T.; Miller, R. J. D.; Ogilvie, J. P.; et al. Quantum biology revisited. *Sci. Adv.* **2020**, *6* (14), eaaz4888.

17. de la Torre, A.; Kennes, D. M.; Claassen, M.; Gerber, S.; McIver, J. W.; Sentef, M. A. Colloquium: Nonthermal pathways to ultrafast control in quantum materials. *Rev. Mod. Phys.* **2021**, *93* (4), 041002.

18. Wasielewski, M. R.; Forbes, M. D.; Frank, N. L.; Kowalski, K.; Scholes, G. D.; Yuen-Zhou, J.; Baldo, M. A.; Freedman, D. E.; Goldsmith, R. H.; Goodson, T. Exploiting chemistry and molecular systems for quantum information science. *Nat. Rev. Chem.* **2020**, *4*, 490.

19. Scholes, G. D.; Fleming, G. R.; Chen, L. X.; Aspuru-Guzik, A.; Buchleitner, A.; Coker, D. F.; Engel, G. S.; van Grondelle, R.; Ishizaki, A.; Jonas, D. M.; et al. Using coherence to enhance function in chemical and biophysical systems. *Nature* **2017**, *543* (7647), 647-656.

20. Kavokin, A. V.; Baumberg, J. J.; Malpuech, G.; Laussy, F. P. Glossary. In *Microcavities*, Oxford University Press, 2017; p 0.

21. Dirac, P. A. M.; Fowler, R. H. On the theory of quantum mechanics. *Proc. R. Soc. Lond. A* **1926**, *112* (762), 661-677.

22. Blum, K. *Density matrix theory and applications*; Springer Science & Business Media, 2012.

23. Kassal, I.; Yuen-Zhou, J.; Rahimi-Keshari, S. Does coherence enhance transport in photosynthesis? *J. Phys. Chem. Lett.* **2013**, *4* (3), 362-367.

24. Bartlett, S. D.; Rudolph, T.; Spekkens, R. W. Reference frames, superselection rules, and quantum information. *Rev. Mod. Phys.* **2007**, *79* (2), 555.

25. Rabi, I. I.; Zacharias, J. R.; Millman, S.; Kusch, P. A new method of measuring nuclear magnetic moment. *Phys. Rev.* **1938**, *53* (4), 318.

26. Rabi, I. I. Space quantization in a gyrating magnetic field. *Phys. Rev.* **1937**, *51* (8), 652.

27. Gordon, R. J.; Zhu, L.; Seideman, T. Coherent control of chemical reactions. *Acc. Chem. Res.* **1999**, *32* (12), 1007-1016.

28. Shapiro, M.; Brumer, P. *Principles of the quantum control of molecular processes*; 2003.

29. Shapiro, M.; Brumer, P. Coherent control of molecular dynamics. *Rep. Prog. Phys.* **2003**, *66* (6), 859.

30. Brumer, P.; Shapiro, M. Coherence chemistry: controlling chemical reactions with lasers. *Acc. Chem. Res.* **1989**, *22* (12), 407-413.

31. Brumer, P.; Shapiro, M. Control of unimolecular reactions using coherent light. *Chem. Phys. Lett.* **1986**, *126* (6), 541-546.

32. Warren, W. S.; Rabitz, H.; Dahleh, M. Coherent control of quantum dynamics: the dream is alive. *Science* **1993**, *259* (5101), 1581-1589.

33. Gordon, R. J.; Rice, S. A. Active control of the dynamics of atoms and molecules. *Annu. Rev. Phys. Chem.* **1997**, *48* (1), 601-641.

34. Dantus, M.; Lozovoy, V. V. Experimental coherent laser control of physicochemical processes. *Chem. Rev.* **2004**, *104* (4), 1813-1860.

35. Nuernberger, P.; Vogt, G.; Brixner, T.; Gerber, G. Femtosecond quantum control of molecular dynamics in the condensed phase. *Phys. Chem. Chem. Phys.* **2007**, *9* (20), 2470-2497.

36. Zewail, A. H. Laser selective chemistry—is it possible? *Phys. Today* **1980**, *33* (11), 27-33.

37. Horstmann, J. G.; Böckmann, H.; Wit, B.; Kurtz, F.; Storeck, G.; Ropers, C. Coherent control of a surface structural phase transition. *Nature* **2020**, *583* (7815), 232-236.

38. Zenesini, A.; Lignier, H.; Ciampini, D.; Morsch, O.; Arimondo, E. Coherent control of dressed matter waves. *Phys. Rev. Lett.* **2009**, *102* (10), 100403.

39. Potter, E. D.; Herek, J. L.; Pedersen, S.; Liu, Q.; Zewail, A. H. Femtosecond laser control of a chemical reaction. *Nature* **1992**, *355* (6355), 66-68.

40. Oka, T.; Kitamura, S. Floquet engineering of quantum materials. *Annu. Rev. Condens. Matter Phys.* **2019**, *10*, 387-408.

41. Paul, K.; Sengupta, P.; Ark, E. D.; Tu, H.; Zhao, Y.; Boppart, S. A. Coherent control of an opsin in living brain tissue. *Nature physics* **2017**, *13* (11), 1111-1116.

42. Prokhorenko, V. I.; Nagy, A. M.; Waschuk, S. A.; Brown, L. S.; Birge, R. R.; Miller, R. J. D. Coherent control of retinal isomerization in bacteriorhodopsin. *Science* **2006**, *313* (5791), 1257-1261.

43. Prokhorenko, V. I.; Nagy, A. M.; Brown, L. S.; Miller, R. J. D. On the mechanism of weak-field coherent control of retinal isomerization in bacteriorhodopsin. *Chem. Phys.* **2007**, *341* (1-3), 296-309.

44. Prokhorenko, V. I.; Halpin, A.; Johnson, P. J. M.; Miller, R. J. D.; Brown, L. S. Coherent control of the isomerization of retinal in bacteriorhodopsin in the high intensity regime. *J. Chem. Phys.* **2011**, *134* (8), 02B630.

45. Tomasi, S.; Baghbanzadeh, S.; Rahimi-Keshari, S.; Kassal, I. Coherent and controllable enhancement of light-harvesting efficiency. *Phys. Rev. A* **2019**, *100* (4), 043411.

46. Alvertis, A. M.; Lukman, S.; Hele, T. J. H.; Fuemmeler, E. G.; Feng, J.; Wu, J.; Greenham, N. C.; Chin, A. W.; Musser, A. J. Switching between Coherent and Incoherent Singlet Fission via Solvent-Induced Symmetry Breaking. *J. Am. Chem. Soc.* **2019**, *141* (44), 17558-17570.

47. Paulus, B. C.; Adelman, S. L.; Jamula, L. L.; McCusker, J. K. Leveraging excited-state coherence for synthetic control of ultrafast dynamics. *Nature* **2020**, *582* (7811), 214-218.

48. Pan, H.; Liu, K. Fermi-phase-induced interference in the reaction between Cl and vibrationally excited CH3D. *Nat. Chem.* **2022**, 1-5.

49. Lozovoy, V. V.; Pastirk, I.; Dantus, M. Multiphoton intrapulse interference. IV. Ultrashort laser pulse spectral phase characterization and compensation. *Opt. Lett.* **2004**, *29* (7), 775-777.

50. Zhang, Z.; Wells, K. L.; Hyland, E. W. J.; Tan, H.-S. Phase-cycling schemes for pump–probe beam geometry two-dimensional electronic spectroscopy. *Chem. Phys. Lett.* **2012**, *550*, 156-161.

51. Hamm, P.; Zanni, M. *Concepts and methods of 2D infrared spectroscopy*; 2011.

52. Middleton, C. T.; Woys, A. M.; Mukherjee, S. S.; Zanni, M. T. Residue-specific structural kinetics of proteins through the union of isotope labeling, mid-IR pulse shaping, and coherent 2D IR spectroscopy. *Methods* **2010**, *52* (1), 12-22.

53. Shim, S.-H.; Zanni, M. T. How to turn your pump–probe instrument into a multidimensional spectrometer: 2D IR and Vis spectroscopiesvia pulse shaping. *Phys. Chem. Chem. Phys.* **2009**, *11* (5), 748-761.

54. Lewis, K. L. M.; Ogilvie, J. P. Probing Photosynthetic Energy and Charge Transfer with Two-Dimensional Electronic Spectroscopy. *J. Phys. Chem. Lett.* **2012**, *3* (4), 503-510.

55. Weiner, A. M. Femtosecond pulse shaping using spatial light modulators. *Rev. Sci. Instrum.* **2000**, *71* (5), 1929-1960.

56. Kawashima, H.; Wefers, M. M.; Nelson, K. A. Femtosecond pulse shaping, multiple-pulse spectroscopy, and optical control. *Annu. Rev. Phys. Chem.* **1995**, *46* (1), 627-656.

57. Weiner, A. M. Ultrafast optical pulse shaping: A tutorial review. *Opt. Commun.* **2011**, *284* (15), 3669-3692.

58. Tomasi, S.; Kassal, I. Classification of coherent enhancements of light-harvesting processes. *J. Phys. Chem. Lett.* **2020**, *11* (6), 2348-2355.

59. Hestand, N. J.; Spano, F. C. Expanded Theory of H- and J-Molecular Aggregates: The Effects of Vibronic Coupling and Intermolecular Charge Transfer. *Chem. Rev.* **2018**, *118* (15), 7069-7163.

60. Kasha, M.; Rawls, H. R.; Ashraf El-Bayoumi, M. The Exciton Model in Molecular Spectroscopy. *Pure Appl. Chem.* **1965**, *11*, 371-392.

61. Kasha, M. Energy transfer mechanisms and the molecular exciton model for molecular aggregates. *Radiat. Res.* **1963**, *20* (1), 55-70.

62. Sekar, R. B.; Periasamy, A. Fluorescence resonance energy transfer (FRET) microscopy imaging of live cell protein localizations. *J. Cell Biol.* **2003**, *160* (5), 629.

63. Foster, T. Intermolecular energy migration and fluorescence. *Ann Phys* **1948**, *2* (13), 55.

64. Forster, T. Mechanisms of energy transfer. In *Comprehensive biochemistry*, Vol. 22; 1967; pp 61-80.

65. Hestand, N. J.; Spano, F. C. Molecular Aggregate Photophysics beyond the Kasha Model: Novel Design Principles for Organic Materials. *Acc. Chem. Res.* **2017**, *50*, 341.

66. Spano, F. C. Spectral signatures of Frenkel polarons in H and J aggregates. *Acc. Chem. Res.* **2010**, *43*, 429-439.

67. Hestand, N. J.; Spano, F. C. Interference between Coulombic and CT-mediated couplings in molecular aggregates: H-to J-aggregate transformation in perylene-based π-stacks. *J. Chem. Phys.* **2015**, *143* (24), 244707.

68. Rafiq, S.; Scholes, G. D. From fundamental theories to quantum coherences in electron transfer. *J. Am. Chem. Soc.* **2018**, *141* (2), 708-722.

69. Xiao, D.; Skourtis, S. S.; Rubtsov, I. V.; Beratan, D. N. Turning charge transfer on and off in a molecular interferometer with vibronic pathways. *Nano Lett.* **2009**, *9* (5), 1818-1823.

70. Goldsmith, R. H.; Wasielewski, M. R.; Ratner, M. A. Electron Transfer in Multiply Bridged Donor-Acceptor Molecules: Dephasing and Quantum Coherence. *J. Phys. Chem. B* **2006**, *110* (41), 20258-20262.

71. Skourtis, S. S.; Waldeck, D. H.; Beratan, D. N. Inelastic Electron Tunneling Erases Coupling-Pathway Interferences. *J. Phys. Chem. B* **2004**, *108* (40), 15511-15518.

72. Marvaud, V.; Launay, J. P.; Joachim, C. Electron-Transfer through 2,7,9,10-Tetraazaphenanthrene - a Quantum Interference Effect. *Chem. Phys.* **1993**, *177* (1), 23-30.

73. Skourtis, S. S.; Lin, J.; Beratan, D. N. The effects of bridge motion on electron transfer reactions mediated by tunneling. In *Modern Methods for Theoretical Physical Chemistry of Biopolymers*, 2006; pp 357-382.

74. Zeng, Y.; Zimmt, M. B. Symmetry Effects on Electron-Transfer Reactions - Temperature-Dependence as a Diagnostic-Tool. *J. Phys. Chem.* **1992**, *96* (21), 8395-8403.

75. Bai, S.; Zhang, P.; Antoniou, P.; Skourtis, S. S.; Beratan, D. N. Quantum interferences among Dexter energy transfer pathways. *Faraday Discuss.* **2019**, *216*, 301-318.

76. Skourtis, S. S.; Liu, C.; Antoniou, P.; Virshup, A. M.; Beratan, D. N. Dexter energy transfer pathways. *Proc. Natl. Acad. Sci. U.S.A.* **2016**, *113* (29), 8115-8120.

77. Greyson, E. C.; Stepp, B. R.; Chen, X.; Schwerin, A. F.; Paci, I.; Smith, M. B.; Akdag, A.; Johnson, J. C.; Nozik, A. J.; Michl, J.; et al. Singlet Exciton Fission for Solar Cell Applications: Energy Aspects of Interchromophore Coupling. *J. Phys. Chem. B* **2010**, *114* (45), 14223-14232.

78. Greyson, E. C.; Vura-Weis, J.; Michl, J.; Ratner, M. A. Maximizing Singlet Fission in Organic Dimers: Theoretical Investigation of Triplet Yield in the Regime of Localized Excitation and Fast Coherent Electron Transfer. *J. Phys. Chem. B* **2010**, *114* (45), 14168-14177.

79. Zang, H.; Zhao, Y.; Liang, W. Quantum interference in singlet fission: J-and H-aggregate behavior. *J. Phys. Chem. Lett.* **2017**, *8* (20), 5105-5112.

80. Solomon, G. C.; Andrews, D. Q.; Hansen, T.; Goldsmith, R. H.; Wasielewski, M. R.; Van Duyne, R. P.; Ratner, M. A. Understanding quantum interference in coherent molecular conduction. *J. Chem. Phys.* **2008**, *129* (5), 054701.

81. Solomon, G. C.; Andrews, D. Q.; Van Duyne, R. P.; Ratner, M. A. When Things Are Not as They Seem: Quantum Interference Turns Molecular Electron Transfer "Rules" Upside Down. *J. Am. Chem. Soc.* **2008**, *130* (25), 7788-7789.

82. Polakovsky, A.; Showman, J.; Valdiviezo, J.; Palma, J. L. Quantum interference enhances rectification behavior of molecular devices. *Phys. Chem. Chem. Phys.* **2021**, *23* (2), 1550-1557.

83. Valdiviezo, J.; Rocha, P.; Polakovsky, A.; Palma, J. L. Nonexponential Length Dependence of Molecular Conductance in Acene-Based Molecular Wires. *ACS Sens.* **2021**, *6* (2), 477-484.

84. Liu, J.; Huang, X.; Wang, F.; Hong, W. Quantum interference effects in charge transport through single-molecule junctions: detection, manipulation, and application. *Acc. Chem. Res.* **2018**, *52* (1), 151-160.

85. Lambert, C. J. Basic concepts of quantum interference and electron transport in single-molecule electronics. *Chem. Soc. Rev.* **2015**, *44* (4), 875-888.

86. Nozaki, D.; Toher, C. Is the antiresonance in meta-contacted benzene due to the destructive superposition of waves traveling two different routes around the benzene ring? *J. Phys. Chem. C* **2017**, *121* (21), 11739-11746.

87. Gunasekaran, S.; Greenwald, J. E.; Venkataraman, L. Visualizing quantum interference in molecular junctions. *Nano Lett.* **2020**, *20* (4), 2843-2848.

88. Patoux, C.; Coudret, C.; Launay, J. P.; Joachim, C.; Gourdon, A. Topological effects on intramolecular electron transfer via quantum interference. *Inorg. Chem.* **1997**, *36* (22), 5037-5049.

89. Mayor, M.; Bschel, M.; Fromm, K. M.; Lehn, J. M.; Daub, J. Electron transfer through bridging molecular structures. *Ann. N. Y. Acad. Sci.* **2002**, *960* (1), 16-28.

90. Mayor, M.; Weber, H. B.; Reichert, J.; Elbing, M.; Von Hnisch, C.; Beckmann, D.; Fischer, M. Electric current through a molecular rod—relevance of the position of the anchor groups. *Angew. Chem. Int. Ed.* **2003**, *42* (47), 5834-5838.

91. Onuchic, J. N.; Beratan, D. N. Molecular Bridge Effects on Distant Charge Tunneling. *J. Am. Chem. Soc.* **1987**, *109* (22), 6771-6778.

92. Beratan, D. N.; Hopfield, J. J. Calculation of electron tunneling matrix elements in rigid systems: mixed-valence dithiaspirocyclobutane molecules. *J. Am. Chem. Soc.* **1984**, *106*, 1584-1594.

93. Goldsmith, R. H.; Wasielewski, M. R.; Ratner, M. A. Scaling laws for charge transfer in multiply bridged donor/acceptor molecules in a dissipative environment. *J. Am. Chem. Soc.* **2007**, *129* (43), 13066-13071.

94. Curtiss, L. A.; Naleway, C. A.; Miller, J. R. Superexchange pathway calculation of electronic coupling through cyclohexane spacers. *J. Phys. Chem.* **1995**, *99* (4), 1182-1193.

95. Renaud, N.; Powell, D.; Zarea, M.; Movaghar, B.; Wasielewski, M. R.; Ratner, M. A. Quantum interferences and electron transfer in photosystem I. *J. Phys. Chem. A* **2013**, *117* (29), 5899-5908.

96. Zarea, M.; Powell, D.; Renaud, N.; Wasielewski, M. R.; Ratner, M. A. Decoherence and quantum interference in a four-site model system: Mechanisms and turnovers. *J. Phys. Chem. B* **2013**, *117* (4), 1010-1020.

97. Kumar, K.; Kurnikov, I. V.; Beratan, D. N.; Waldeck, D. H.; Zimmt, M. B. Use of modern electron transfer theories to determine electronic coupling matrix elements in intramolecular systems. *J. Phys. Chem. A* **1998**, *102*, 5529-5541.

98. Phelan, B. T.; Schultz, J. D.; Zhang, J.; Huang, G.-J.; Young, Ryan M.; Wasielewski, M. R. Quantum coherence in ultrafast photo-driven charge separation. *Faraday Discuss.* **2019**, *216* (0), 319-338.

99. Phelan, B. T.; Zhang, J.; Huang, G.-J.; Wu, Y.-L.; Zarea, M.; Young, R. M.; Wasielewski, M. R. Quantum Coherence Enhances Electron Transfer Rates to Two Equivalent Electron Acceptors. *J. Am. Chem. Soc.* **2019**, *141* (31), 12236-12239.

100. Vazquez, H.; Skouta, R.; Schneebeli, S.; Kamenetska, M.; Breslow, R.; Venkataraman, L.; Hybertsen, M. S. Probing the conductance superposition law in single-molecule circuits with parallel paths. *Nat. Nanotech.* **2012**, *7* (10), 663-667.

101. Magoga, M.; Joachim, C. Conductance of molecular wires connected or bonded in parallel. *Phys. Rev. B.* **1999**, *59* (24), 16011-16021.

102. Richert, S.; Cremers, J.; Kuprov, I.; Peeks, M. D.; Anderson, H. L.; Timmel, C. R. Constructive quantum interference in a bis-copper six-porphyrin nanoring. *Nat. Commun.* **2017**, *8* (1), 1-5.

103. Azumi, T.; Matsuzaki, K. What does the term "vibronic coupling" mean? *Photochem. Photobiol.* **1977**, *25* (3), 315-326.

104. Jonas, D. M. Vibrational and nonadiabatic coherence in 2D electronic spectroscopy, the Jahn-Teller effect, and energy transfer. *Annu. Rev. Phys. Chem.* **2018**, *69*, 327-352.

105. Zhang, H.-D.; Qiao, Q.; Xu, R.-X.; Yan, Y. Effects of Herzberg-Teller vibronic coupling on coherent excitation energy transfer. *J. Chem. Phys.* **2016**, *145* (20), 204109.

106. Tiwari, V.; Peters, W. K.; Jonas, D. M. Electronic energy transfer through non-adiabatic vibrational-electronic resonance. I. Theory for a dimer. *J. Chem. Phys.* **2017**, *147* (15), 154308.

107. Tiwari, V.; Peters, W. K.; Jonas, D. M. Electronic resonance with anticorrelated pigment vibrations drives photosynthetic energy transfer outside the adiabatic framework. *Proc. Natl. Acad. Sci. U.S.A.* **2013**, *110* (4), 1203-1208.

108. Arsenault, E. A.; Schile, A. J.; Limmer, D. T.; Fleming, G. R. Vibronic coupling in energy transfer dynamics and two-dimensional electronic–vibrational spectra. *J. Chem. Phys.* **2021**, *155* (5), 054201.

109. Kundu, S.; Roy, P. P.; Fleming, G. R.; Makri, N. Franck–Condon and Herzberg–Teller Signatures in Molecular Absorption and Emission Spectra. *J. Phys. Chem. B* **2022**, *126* (15), 2899-2911.

110. Bizimana, L. A.; Carbery, W. P.; Gellen, T. A.; Turner, D. B. Signatures of Herzberg-Teller coupling in three-dimensional electronic spectroscopy. *J. Chem. Phys.* **2017**, *146* (8), 084311.

111. Gaynor, J. D.; Khalil, M. Signatures of vibronic coupling in two-dimensional electronic-vibrational and vibrational-electronic spectroscopies. *J. Chem. Phys.* **2017**, *147* (9), 094202.

112. Moerner, W. E.; Fromm, D. P. Methods of single-molecule fluorescence spectroscopy and microscopy. *Rev. Sci. Instrum.* **2003**, *74* (8), 3597-3619.

113. Moerner, W. E. A dozen years of single-molecule spectroscopy in physics, chemistry, and biophysics. In *The Journal of Physical Chemistry B*, 2002; Vol. 106, pp 910-927.

114. Moya, R.; Norris, A. C.; Kondo, T.; Schlau-Cohen, G. S. Observation of robust energy transfer in the photosynthetic protein allophycocyanin using single-molecule pump-probe spectroscopy. *Nat. Chem.* **2022**, 1-7.

115. Barkai, E.; Jung, Y.; Silbey, R. Theory of single-molecule spectroscopy: beyond the ensemble average. *Annu. Rev. Phys. Chem.* **2004**, *55*, 457-507.

116. Mukamel, S. *Principles of Nonlinear Optical Spectroscopy*; Oxford University Press, 1995.

117. Boyd, R. W. *Nonlinear Optics*; 2020.

118. Kleinman, D. A. Theory of second harmonic generation of light. *Phys. Rev.* **1962**, *128* (4), 1761.

119. Shen, Y. R. Surface properties probed by second-harmonic and sum-frequency generation. *Nature* **1989**, *337* (6207), 519-525.

120. Fuller, F. D.; Ogilvie, J. P. Experimental implementations of two-dimensional fourier transform electronic spectroscopy. *Annu. Rev. Phys. Chem.* **2015**, *66*, 667-690.

121. Jonas, D. M. Two-dimensional femtosecond spectroscopy. *Annu. Rev. Phys. Chem.* **2003**, *54*, 425-463.

122. Gaynor, J. D.; Courtney, T. L.; Balasubramanian, M.; Khalil, M. Fourier transform two-dimensional electronic-vibrational spectroscopy using an octave-spanning mid-IR probe. *Opt. Lett.* **2016**, *41* (12), 2895.

123. Arsenault, E. A.; Bhattacharyya, P.; Yoneda, Y.; Fleming, G. R. Two-dimensional electronic–vibrational spectroscopy: Exploring the interplay of electrons and nuclei in excited state molecular dynamics. *J. Chem. Phys.* **2021**, *155* (2), 020901.

124. Courtney, T. L.; Fox, Z. W.; Slenkamp, K. M.; Khalil, M. Two-dimensional vibrational-electronic spectroscopy. *J. Chem. Phys.* **2015**, *143*, 154201.

125. Kukura, P.; McCamant, D. W.; Mathies, R. A. Femtosecond Stimulated Raman Spectroscopy. *Annu. Rev. Phys. Chem.* **2007**, *58* (1), 461-488.

126. Frontiera, R. R.; Mathies, R. A. Femtosecond stimulated Raman spectroscopy. *Laser & Photonics Reviews* **2011**, *5* (1), 102-113.

127. Heilweil, E. J.; Hochstrasser, R. M. Nonlinear spectroscopy and picosecond transient grating study of colloidal gold. *J. Chem. Phys.* **1985**, *82* (11), 4762-4770.

128. Hellwarth, R. W. Theory of stimulated Raman scattering. *Phys. Rev.* **1963**, *130* (5), 1850.

129. New, G. H. C.; Ward, J. F. Optical third-harmonic generation in gases. *Phys. Rev. Lett.* **1967**, *19* (10), 556.

130. Fumero, G.; Schnedermann, C.; Batignani, G.; Wende, T.; Liebel, M.; Bassolino, G.; Ferrante, C.; Mukamel, S.; Kukura, P.; Scopigno, T. Two-Dimensional Impulsively Stimulated Resonant Raman Spectroscopy of Molecular Excited States. *Phys. Rev. X* **2020**, *10* (1), 011051.

131. Kuramochi, H.; Takeuchi, S.; Kamikubo, H.; Kataoka, M.; Tahara, T. Fifth-order time-domain Raman spectroscopy of photoactive yellow protein for visualizing vibrational coupling in its excited state. *Sci. Adv.* **2019**, *5* (6), eaau4490.

132. Silva, W. R.; Frontiera, R. R. Excited state structural evolution during charge-transfer reactions in betaine-30. *Phys. Chem. Chem. Phys.* **2016**, *18* (30), 20290-20297.

133. Molesky, B. P.; Guo, Z.; Moran, A. M. Femtosecond stimulated Raman spectroscopy by six-wave mixing. *J. Chem. Phys.* **2015**, *142* (21), 212405.

134. Molesky, B. P.; Guo, Z.; Cheshire, T. P.; Moran, A. M. Perspective: Two-dimensional resonance Raman spectroscopy. *J. Chem. Phys.* **2016**, *145* (18), 180901.

135. Spencer, A. P.; Hutson, W. O.; Harel, E. Quantum coherence selective 2D Raman-2D electronic spectroscopy. *Nat. Commun.* **2017**, *8* (1), 1-8.

136. Hybl, J. D.; Albrecht, A. W.; Faeder, S. M. G.; Jonas, D. M. Two-dimensional electronic spectroscopy. *Chem. Phys. Lett.* **1998**, *297* (3-4), 307-313.

137. Asplund, M. C.; Zanni, M. T.; Hochstrasser, R. M. Two-dimensional infrared spectroscopy of peptides by phase-controlled femtosecond vibrational photon echoes. *Proc. Natl. Acad. Sci. U.S.A.* **2000**, *97* (15), 8219-8224.

138. Cho, M. Coherent Two-Dimensional Optical Spectroscopy. *Chem. Rev.* **2008**, *108* (4), 1331-1418.

139. Biswas, S.; Kim, J.; Zhang, X.; Scholes, G. D. Coherent Two-Dimensional and Broadband Electronic Spectroscopies. *Chem. Rev.* **2022**, *122* (3), 4257-4321.

140. Do, T. N.; Khyasudeen, M. F.; Nowakowski, P. J.; Zhang, Z.; Tan, H.-S. Measuring Ultrafast Spectral Diffusion and Correlation Dynamics by Two-Dimensional Electronic Spectroscopy. *Chem. Asian J.* **2019**, *14* (22), 3992-4000.

141. Wells, K. L.; Zhang, Z.; Rouxel, J. R.; Tan, H.-S. Measuring the spectral diffusion of chlorophyll a using two-dimensional electronic spectroscopy. *J. Phys. Chem. B* **2013**, *117* (8), 2294-2299.

142. Dean, J. C.; Rafiq, S.; Oblinsky, D. G.; Cassette, E.; Jumper, C. C.; Scholes, G. D. Broadband Transient Absorption and Two-Dimensional Electronic Spectroscopy of Methylene Blue. *J. Phys. Chem. A* **2015**, *119* (34), 9098-9108.

143. Dean, J. C.; Mirkovic, T.; Toa, Z. S. D.; Oblinsky, D. G.; Scholes, G. D. Vibronic Enhancement of Algae Light Harvesting. *Chem* **2016**, *1* (6), 858-872.

144. Wang, L.; Griffin, G. B.; Zhang, A.; Zhai, F.; Williams, N. E.; Jordan, R. F.; Engel, G. S. Controlling quantum-beating signals in 2D electronic spectra by packing synthetic heterodimers on single-walled carbon nanotubes. *Nat. Chem.* **2017**, *9* (3), 219-225.

145. Jumper, C. C.; Arpin, P. C.; Turner, D. B.; McClure, S. D.; Rafiq, S.; Dean, J. C.; Cina, J. A.; Kovac, P. A.; Mirkovic, T.; Scholes, G. D. Broad-Band Pump–Probe Spectroscopy Quantifies Ultrafast Solvation Dynamics of Proteins and Molecules. *J. Phys. Chem. Lett.* **2016**, *7* (22), 4722-4731.

146. Cina, J. A.; Kovac, P. A.; Jumper, C. C.; Dean, J. C.; Scholes, G. D. Ultrafast transient absorption revisited: Phase-flips, spectral fingers, and other dynamical features. *J. Chem. Phys.* **2016**, *144* (17), 175102.

147. Bittl, R.; Weber, S. Transient radical pairs studied by time-resolved EPR. *Biochim. Biophys. Acta - Bioenerg.* **2005**, *1707* (1), 117-126.

148. Santabarbara, S.; Kuprov, I.; Hore, P. J.; Casal, A.; Heathcote, P.; Evans, M. C. W. Analysis of the Spin-Polarized Electron Spin Echo of the [P700+A1-] Radical Pair of Photosystem I Indicates That Both Reaction Center Subunits Are Competent in Electron Transfer in Cyanobacteria, Green Algae, and Higher Plants. *Biochemistry* **2006**, *45* (23), 7389-7403.

149. Olshansky, J. H.; Krzyaniak, M. D.; Young, R. M.; Wasielewski, M. R. Photogenerated spin-entangled qubit (radical) pairs in DNA hairpins: Observation of spin delocalization and coherence. *J. Am. Chem. Soc.* **2019**, *141* (5), 2152-2160.

150. Volpato, A.; Bolzonello, L.; Meneghin, E.; Collini, E. Global Analysis of Coherence and Population Dynamics in 2d Electronic Spectroscopy. *Opt. Express* **2016**, *24*, 24773.

151. Song, Y.; Hellmann, C.; Stingelin, N.; Scholes, G. D. The separation of vibrational coherence from ground- and excited-electronic states in P3HT film. *J. Chem. Phys.* **2015**, *142* (21), 212410.

152. Schultz, J. D.; Kim, T.; O'Connor, J. P.; Young, R. M.; Wasielewski, M. R. Coupling between Harmonic Vibrations Influences Quantum Beating Signatures in Two-Dimensional Electronic Spectra. *J. Phys. Chem. C.* **2022**, *126* (1), 120-131.

153. Policht, V. R.; Niedringhaus, A.; Willow, R.; Laible, P. D.; Bocian, D. F.; Kirmaier, C.; Holten, D.; Manal, T.; Ogilvie, J. P. Hidden vibronic and excitonic structure and vibronic coherence transfer in the bacterial reaction center. *Sci. Adv.* **2022**, *8* (1), eabk0953.

154. Butkus, V.; Zigmantas, D.; Valkunas, L.; Abramavicius, D. Vibrational vs Electronic Coherences in 2DES. *Chem. Phys. Lett.* **2012**, *545*, 40-43.

155. Fuller, F. D.; Pan, J.; Gelzinis, A.; Butkus, V.; Senlik, S. S.; Wilcox, D. E.; Yocum, C. F.; Valkunas, L.; Abramavicius, D.; Ogilvie, J. P. Vibronic coherence in oxygenic photosynthesis. *Nat. Chem.* **2014**, *6*, 706-711.

156. Thyrhaug, E.; Tempelaar, R.; Alcocer, M. J. P.; Zidek, K.; Bina, D.; Knoester, J.; Jansen, T. L. C.; Zigmantas, D. Identification and characterization of diverse coherences in the Fenna-Matthews-Olson complex. *Nat. Chem.* **2018**, *10* (7), 780-786.

157. Schultz, J. D.; Shin, J. Y.; Chen, M.; O'Connor, J. P.; Young, R. M.; Ratner, M. A.; Wasielewski, M. R. Influence of Vibronic Coupling on Ultrafast Singlet Fission in a Linear Terrylenediimide Dimer. *J. Am. Chem. Soc.* **2021**, *143* (4), 2049-2058.

158. Bakulin, A. A.; Morgan, S. E.; Kehoe, T. B.; Wilson, M. W. B.; Chin, A. W.; Zigmantas, D.; Egorova, D.; Rao, A. Real-time observation of multiexcitonic states in ultrafast singlet fission using coherent 2D electronic spectroscopy. *Nat. Chem.* **2016**, *8* (1), 16-23.

159. Wang, G.; Zhang, C.; Liu, Z.; Wang, R.; Ma, H.; Wang, X.; Xiao, M. Singlet Fission Dynamics in Tetracene Single Crystals Probed by Polarization-Dependent Two-Dimensional Electronic Spectroscopy. *J. Phys. Chem. A* **2020**, *124* (50), 10447-10456.

160. Halpin, A.; Johnson, P. J.; Tempelaar, R.; Murphy, R. S.; Knoester, J.; Jansen, T. L.; Miller, R. J. Two-dimensional spectroscopy of a molecular dimer unveils the effects of vibronic coupling on exciton coherences. *Nat. Chem.* **2014**, *6* (3), 196-201.

161. Lim, J.; Palecek, D.; Caycedo-Soler, F.; Lincoln, C. N.; Prior, J.; von Berlepsch, H.; Huelga, S. F.; Plenio, M. B.; Zigmantas, D.; Hauer, J. Vibronic origin of long-lived coherence in an artificial molecular light harvester. *Nat. Commun.* **2015**, *6*, 7755.

162. Higgins, J. S.; Allodi, M. A.; Lloyd, L. T.; Otto, J. P.; Sohail, S. H.; Saer, R. G.; Wood, R. E.; Massey, S. C.; Ting, P.-C.; Blankenship, R. E.; et al. Redox conditions correlated with vibronic coupling modulate quantum beats in photosynthetic pigment-protein complexes. *Proc. Natl. Acad. Sci. U.S.A.* **2021**, *118* (49), e2112817118.

163. Aster, A.; Bornhof, A.-B.; Sakai, N.; Matile, S.; Vauthey, E. Lifetime Broadening and Impulsive Generation of Vibrational Coherence Triggered by Ultrafast Electron Transfer. *J. Phys. Chem. Lett.* **2021**, *12* (3), 1052-1057.

164. Rafiq, S.; Fu, B.; Kudisch, B.; Scholes, G. D. Interplay of vibrational wavepackets during an ultrafast electron transfer reaction. *Nat. Chem.* **2021**, *13* (1), 70-76.

165. Lin, C.; Kim, T.; Schultz, J. D.; Young, R. M.; Wasielewski, M. R. Accelerating symmetry-breaking charge separation in a perylenediimide trimer through a vibronically coherent dimer intermediate. *Nat. Chem.* **2022**.

166. Volpato, A.; Collini, E. Time-frequency methods for coherent spectroscopy. *Opt. Express* **2015**, *23*, 20040.

167. Volpato, A.; Collini, E. Optimization and selection of time-frequency transforms for wave-packet analysis in ultrafast spectroscopy. *Opt. Express* **2019**, *27*, 2975.

168. Volpato, A.; Zerbetto, M.; Bolzonello, L.; Meneghin, E.; Fresch, B.; Benelli, T.; Giorgini, L.; Collini, E. Effect of Different Conformational Distributions on the Ultrafast Coherence Dynamics in Porphyrin-Based Polymers. *J. Phys. Chem. C* **2019**, *123* (16), 10212-10224.

169. Hart, S. M.; Banal, J. L.; Bathe, M.; Schlau-Cohen, G. S. Identification of Nonradiative Decay Pathways in Cy3. *J. Phys. Chem. Lett.* **2020**, *11* (13), 5000-5007.

170. Knox, R. S. Storage of Light Energy and Photosynthesis. *Nature* **1969**, *221* (5177), 263-&.

171. Sumi, H. Bacterial photosynthesis begins with quantum-mechanical coherence. *Chem. Rec.* **2001**, *1* (6), 480-493.

172. Blankenship, R. E. *Molecular mechanisms of photosynthesis*; 2021.

173. Rhee, K. H.; Morriss, E. P.; Barber, J.; Kuhlbrandt, W. Three-dimensional structure of the plant photosystem II reaction centre at 8 angstrom resolution. *Nature* **1998**, *396* (6708), 283-286.

174. Weber, S.; Ohmes, E.; Thurnauer, M. C.; Norris, J. R.; Kothe, G. Quantum beats as probes of the primary events in bacterial photosynthesis. *Reaction Center of Photosynthetic*

Bacteria: Structure and Dynamics, Proceedings of the Workshop on the Reaction Center of Photosynthetic Bacteria: Structure and Dynamics, Feldafing, Germany, Mar. 1-4, 1995 **1996**, 341-351.

175. Vos, M. H.; Rappaport, F.; Lambry, J. C.; Breton, J.; Martin, J. L. Visualization of Coherent Nuclear Motion in a Membrane-Protein by Femtosecond Spectroscopy. *Nature* **1993**, *363*, 320–325

176. Vos, M. H.; Lambry, J.-C.; Robles, S. J.; Youvan, D. C.; Breton, J.; Martin, J.-L. Direct observation of vibrational coherence in bacterial reaction centers using femtosecond absorption spectroscopy. *Proc. Natl. Acad. Sci. U.S.A.* **1991**, *88* (20), 8885-8889.

177. Vos, M. H.; Jones, M. R.; Hunter, C. N.; Breton, J.; Lambry, J.; Martin, J. Coherent Dynamics during the Primary Electron-Transfer Reaction in Membrane-Bound Reaction Centers of Rhodobacter sphaeroides. *Biochemistry* **1994**, *33*, 6750.

178. Vos, M. H.; Jones, M. R.; McGlynn, P.; Hunter, C. N.; Breton, J.; Martin, J.-L. Influence of the membrane environment on vibrational motions in reaction centres of Rhodobacter sphaeroides. *Biochim. Biophys. Acta - Bioenerg.* **1994**, *1186* (1-2), 117-122.

179. Chachisvilis, M.; Pullerits, T.; Jones, M. R.; Hunter, C. N.; Sundstrm, V. Vibrational dynamics in the light-harvesting complexes of the photosynthetic bacterium Rhodobacter sphaeroides. *Chem. Phys. Lett.* **1994**, *224* (3-4), 345-354.

180. Savikhin, S.; Buck, D. R.; Struve, W. S. Oscillating anisotropies in a bacteriochlorophyll protein: Evidence for quantum beating between exciton levels. *Chem. Phys.* **1997**, *223* (2), 303-312.

181. Savikhin, S.; Struve, W. S. Low-temperature energy transfer in FMO trimers from the green photosynthetic bacterium Chlorobium tepidum. *Photosynth. Res.* **1996**, *48* (1), 271-276.

182. Cheng, Y.-C.; Fleming, G. R. Dynamics of light harvesting in photosynthesis. *Annu. Rev. Phys. Chem.* **2009**, *60*, 241-262.

183. Kothe, G.; Weber, S.; Bittl, R.; Ohmes, E.; Thurnauer, M. C.; Norris, J. R. Transient EPR of light-induced radical pairs in plant photosystem I: observation of quantum beats. *Chem. Phys. Lett.* **1991**, *186* (6), 474-480.

184. Bittl, R.; Kothe, G. Transient EPR of radical pairs in photosynthetic reaction centers: Prediction of quantum beats. *Chem. Phys. Lett.* **1991**, *177*, 547-553.

185. Gierer, M.; van der Est, A.; Stehlik, D. Transient EPR of weakly coupled spin-correlated radical pairs in photosynthetic reaction centres: increase spectral resolution from nutation analysis. *Chem. Phys. Lett.* **1991**, *186* (2-3), 238-247.

186. Engel, G. S.; Calhoun, T. R.; Read, E. L.; Ahn, T. K.; Mancal, T.; Cheng, Y. C.; Blankenship, R. E.; Fleming, G. R. Evidence for wavelike energy transfer through quantum coherence in photosynthetic systems. *Nature* **2007**, *446* (7137), 782-786.

187. Tempelaar, R.; Jansen, T. L. C.; Knoester, J. Vibrational beatings conceal evidence of electronic coherence in the FMO light-harvesting complex. *J. Phys. Chem. B* **2014**, *118* (45), 12865-12872.

188. Duan, H. G.; Prokhorenko, V. I.; Cogdell, R. J.; Ashraf, K.; Stevens, A. L.; Thorwart, M.; Miller, R. J. D. Nature does not rely on long-lived electronic quantum coherence for photosynthetic energy transfer. *Proc. Natl. Acad. Sci. U.S.A.* **2017**, *114* (32), 8493-8498.

189. Lee, H.; Cheng, Y. C.; Fleming, G. R. Coherence dynamics in photosynthesis: Protein protection of excitonic coherence. *Science* **2007**, *316* (5830), 1462-1465.

190. Ishizaki, A.; Calhoun, T. R.; Schlau-Cohen, G. S.; Fleming, G. R. Quantum Coherence and Its Interplay with Protein Environments in Photosynthetic Electronic Energy Transfer. *Phys. Chem. Chem. Phys.* **2010**, *12*, 7319.

191. Rolczynski, B. S.; Zheng, H.; Singh, V. P.; Navotnaya, P.; Ginzburg, A. R.; Caram, J. R.; Ashraf, K.; Gardiner, A. T.; Yeh, S.-H.; Kais, S.; et al. Correlated protein environments drive quantum coherence lifetimes in photosynthetic pigment-protein complexes. *Chem* **2018**, *4* (1), 138-149.

192. Irgen-Gioro, S.; Gururangan, K.; Saer, R. G.; Blankenship, R. E.; Harel, E. Electronic coherence lifetimes of the Fenna–Matthews–Olson complex and light harvesting complex II. *Chem. Sci.* **2019**, *10* (45), 10503-10509.

193. Cheng, Y. C.; Fleming, G. R. Dynamics of light harvesting in photosynthesis. *Annu. Rev. Phys. Chem.* **2009**, *60*, 241.

194. Womick, J. M.; Moran, A. M. Vibronic Enhancement of Exciton Sizes and Energy Transport in Photosynthetic Complexes. *J. Phys. Chem. B* **2011**, *115* (6), 1347-1356.

195. Tiwari, V.; Jonas, D. M. Electronic energy transfer through non-adiabatic vibrational-electronic resonance. II. 1D spectra for a dimer. *J. Chem. Phys.* **2018**, *148* (8), 084308.

196. Milota, F.; Prokhorenko, V. I.; Mancal, T.; Von Berlepsch, H.; Bixner, O.; Kauffmann, H. F.; Hauer, J. Vibronic and Vibrational Coherences in Two-Dimensional Electronic Spectra of Supramolecular J-Aggregates. *J. Phys. Chem. A.* **2013**, *117* (29), 6007-6014.

197. Skourtis, S. S.; Da Silva, A. J. R.; Bialek, W.; Onuchic, J. N. New look at the primary charge separation in bacterial photosynthesis. *J. Phys. Chem.* **1992**, *96* (20), 8034-8041.

198. Miyata, K.; Kurashige, Y.; Watanabe, K.; Sugimoto, T.; Takahashi, S.; Tanaka, S.; Takeya, J.; Yanai, T.; Matsumoto, Y. Coherent singlet fission activated by symmetry breaking. *Nat. Chem.* **2017**, *9* (10), 983.

199. Monahan, N. R.; Sun, D.; Tamura, H.; Williams, K. W.; Xu, B.; Zhong, Y.; Kumar, B.; Nuckolls, C.; Harutyunyan, A. R.; Chen, G.; et al. Dynamics of the triplet-pair state reveals the likely coexistence of coherent and incoherent singlet fission in crystalline hexacene. *Nat. Chem.* **2017**, *9* (4), 341.

200. Kim, W.; Musser, A. J. Tracking ultrafast reactions in organic materials through vibrational coherence: vibronic coupling mechanisms in singlet fission. *Adv. Phys.: X* **2021**, *6* (1), 1918022.

201. Schnedermann, C.; Alvertis, A. M.; Wende, T.; Lukman, S.; Feng, J.; Schröder, F. A. Y. N.; Turban, D. H. P.; Wu, J.; Hine, N. D. M.; Greenham, N. C.; et al. A Molecular Movie of Ultrafast Singlet Fission. *Nat. Commun.* **2019**, *10* (1), 4207.

202. Alvertis, A. M.; Lukman, S.; Hele, T. J. H.; Fuemmeler, E. G.; Feng, J.; Wu, J.; Greenham, N. C.; Chin, A. W.; Musser, A. J. Switching between Coherent and Incoherent Singlet Fission via Solvent-Induced Symmetry Breaking Dimer. *J. Am. Chem. Soc.* **2019**, *141*, 17558.

203. Musser, A. J.; Liebel, M.; Schnedermann, C.; Wende, T.; Kehoe, T. B.; Rao, A.; Kukura, P. Evidence for conical intersection dynamics mediating ultrafast singlet exciton fission. *Nat. Phys.* **2015**, *11*, 352.

204. Tempelaar, R.; Reichman, D. R. Vibronic exciton theory of singlet fission. III. How vibronic coupling and thermodynamics promote rapid triplet generation in pentacene crystals. *J. Chem. Phys.* **2018**, *148* (24), 244701.

205. Tempelaar, R.; Reichman, D. R. Vibronic exciton theory of singlet fission. I. Linear absorption and the anatomy of the correlated triplet pair state. *J. Chem. Phys.* **2017**, *146* (17), 174703.

206. Tempelaar, R.; Reichman, D. R. Vibronic exciton theory of singlet fission. II. Two-dimensional spectroscopic detection of the correlated triplet pair state. *J. Chem. Phys.* **2017**, *146* (17), 174704.

207. Breen, I.; Tempelaar, R.; Bizimana, L. A.; Kloss, B.; Reichman, D. R.; Turner, D. B. Triplet separation drives singlet fission after femtosecond correlated triplet pair production in rubrene. *J. Am. Chem. Soc.* **2017**, *139* (34), 11745-11751.

208. Duan, H.-G.; Jha, A.; Li, X.; Tiwari, V.; Ye, H.; Nayak, P. K.; Zhu, X.-L.; Li, Z.; Martinez, T. J.; Thorwart, M.; et al. Intermolecular vibrations mediate ultrafast singlet fission. *Sci. Adv.* **2020**, *6* (38), eabb0052.

209. Mandal, A.; Chen, M.; Foszcz, E.; Schultz, J. D.; Kearns, N. M.; Young, R. M.; Zanni, M. T.; Wasielewski, M. R. Two-Dimensional Electronic Spectroscopy Reveals Excitation Energy-Dependent State Mixing during Singlet Fission in a Terrylenediimide Dimer. *J. Am. Chem. Soc.* **2018**, 17907–17914.

210. Rafiq, S.; Dean, J. C.; Scholes, G. D. Observing Vibrational Wavepackets during an Ultrafast Electron Transfer Reaction. *J. Phys. Chem. A* **2015**, *119* (49), 11837-11846.

211. Wynne, K.; Reid, G. D.; Hochstrasser, R. M. Vibrational coherence in electron transfer: The tetracyanoethylene–pyrene complex. *J. Chem. Phys.* **1996**, *105* (6), 2287-2297.

212. Wolfseder, B.; Seidner, L.; Domcke, W.; Stock, G.; Seel, M.; Engleitner, S.; Zinth, W. Vibrational coherence in ultrafast electron-transfer dynamics of oxazine 1 in N,N-dimethylaniline: simulation of a femtosecond pump-probe experiment. *Chem. Phys* **1998**, *233* (2), 323-334.

213. Schweighöfer, F.; Dworak, L.; Braun, M.; Zastrow, M.; Wahl, J.; Burghardt, I.; Rück-Braun, K.; Wachtveitl, J. Vibrational coherence transfer in an electronically decoupled molecular dyad. *Sci. Rep.* **2015**, *5*, 9368.

214. Song, Y.; Clafton, S. N.; Pensack, R. D.; Kee, T. W.; Scholes, G. D. Vibrational coherence probes the mechanism of ultrafast electron transfer in polymer-fullerene blends. *Nat. Commun.* **2014**, *5*, 4933.

215. Falke, S. M.; Rozzi, C. A.; Brida, D.; Lienau, C. Coherent ultrafast charge transfer in an organic photovoltaic blend. *Science* **2014**, *344*, 1001-1005.

216. Rozzi, C. A.; Falke, S. M.; Spallanzani, N.; Rubio, A.; Molinari, E.; Brida, D.; Maiuri, M.; Cerullo, G.; Schramm, H.; Christoffers, J.; et al. Quantum coherence controls the charge separation in a prototypical artificial light-harvesting system. *Nat. Commun.* **2013**, *4*, 1602.

217. Rafiq, S.; Scholes, G. D. Is back-electron transfer process in Betaine-30 coherent? *Chem. Phys. Lett.* **2017**, *683*, 500-506.

218. De Sio, A.; Lienau, C. Vibronic coupling in organic semiconductors for photovoltaics. *Phys. Chem. Chem. Phys.* **2017**, *19* (29), 18813-18830.

219. Christopher, R.; Renee, F. Coherent Phonon Catalysts: Lattice Vibrations Drive a Photoinduced Phase Transition in a Molecular Crystal. *ChemRxiv* **2020**.

220. Kellogg, M.; Akil, A.; Muthiah Ravinson, D. S.; Estergreen, L.; Bradforth, S. E.; Thompson, M. E. Symmetry breaking charge transfer as a means to study electron transfer with no driving force. *Faraday Discuss.* **2019**, *216*, 379.

221. Vauthey, E. Photoinduced symmetry-breaking charge separation. *ChemPhysChem* **2012**, *13*, 2001.

222. Collini, E. 2D Electronic Spectroscopic Techniques for Quantum Technology Applications. *J. Phys. Chem. C* **2021**, *125* (24), 13096-13108.

223. Jones, A. C.; Kunz, M. B.; Tigges-Green, I.; Zanni, M. T. Dual spectral phase and diffraction angle compensation of a broadband AOM 4-f pulse-shaper for ultrafast spectroscopy. *Opt. Express* **2019**, *27* (26), 37236-37247.

224. Myers, J. A.; Lewis, K. L. M.; Tekavec, P. F.; Ogilvie, J. P. Two-color two-dimensional Fourier transform electronic spectroscopy with a pulse-shaper. *Opt. Express* **2008**, *16* (22), 17420-17428.

225. *MDS_EXP*; 2022. doi.org/10.5281/zenodo.6758004.

226. Kirschner, M. S.; Jeong, Y.; Spencer, A. P.; Watkins, N. E.; Lin, X.-M.; Schatz, G. C.; Chen, L. X.; Schaller, R. D. Phonon-induced plasmon-exciton coupling changes probed via oscillation-associated spectra. *Appl. Phys. Lett.* **2019**, *115* (11), 111903.

227. Jumper, C. C.; Anna, J. M.; Stradomska, A.; Schins, J.; Myahkostupov, M.; Prusakova, V.; Oblinsky, D. G.; Castellano, F. N.; Knoester, J.; Scholes, G. D. Intramolecular radiationless transitions dominate exciton relaxation dynamics. *Chem. Phys. Lett.* **2014**, *599*, 23-33.

228. Schultz, J. D.; Coleman, A. F.; Mandal, A.; Shin, J. Y.; Ratner, M. A.; Young, R. M.; Wasielewski, M. R. Steric Interactions Impact Vibronic and Vibrational Coherences in Perylenediimide Cyclophanes. *J. Phys. Chem. Lett.* **2019**, *10* (23), 7498-7504.

229. Jansen, T. l. C.; Knoester, J. Nonadiabatic Effects in the Two-Dimensional Infrared Spectra of Peptides: Application to Alanine Dipeptide. *J. Phys. Chem. B* **2006**, *110* (45), 22910-22916.

230. *OREOS*; 2022. doi.org/10.5281/zenodo.6757664.

231. Monahan, N.; Zhu, X. Y. Charge Transfer–Mediated Singlet Fission. *Annu. Rev. Phys. Chem.* **2015**, *66* (1), 601-618.

232. Miller, C. E.; Wasielewski, M. R.; Schatz, G. C. Modeling Singlet Fission in Rylene and Diketopyrrolopyrrole Derivatives: The Role of the Charge Transfer State in Superexchange and Excimer Formation. *J. Phys. Chem. C* **2017**, *121*, 10345–10350.

233. Berkelbach, T. C.; Hybertsen, M. S.; Reichman, D. R. Microscopic theory of singlet exciton fission. II. Application to pentacene dimers and the role of superexchange. *J. Chem. Phys.* **2013**, *138* (11), 114103.

234. Berkelbach, T. C.; Hybertsen, M. S.; Reichman, D. R. Microscopic theory of singlet exciton fission. I. General formulation. *J. Chem. Phys.* **2013**, *138* (11), 114102.

235. Weller, A. Photoinduced electron transfer in solution: exciplex and radical ion pair formation free enthalpies and their solvent dependence. *Z. Phys. Chem* . **1982**, *133* (1), 93-98.

236. Kubo, R. *Fluctuation, Relaxation, and Resonance in Magnetic Systems*; Oliver and Boyd, 1962.

237. Romero, E.; Novoderezhkin, V. I.; van Grondelle, R. Quantum design of photosynthesis for bio-inspired solar-energy conversion. *Nature* **2017**, *543*, 355.

238. Bredas, J. L.; Sargent, E. H.; Scholes, G. D. Photovoltaic concepts inspired by coherence effects in photosynthetic systems. *Nat. Mater.* **2016**, *16* (1), 35-44.

239. Hayes, D.; Griffin, G. B.; Engel, G. S. Engineering coherence among excited states in synthetic heterodimer systems. *Science* **2013**, *340* (6139), 1431-1434.

240. Caram, J. R.; Zheng, H.; Dahlberg, P. D.; Rolczynski, B. S.; Griffin, G. B.; Fidler, A. F.; Dolzhnikov, D. S.; Talapin, D. V.; Engel, G. S. Persistent Inter-Excitonic Quantum Coherence in CdSe Quantum Dots. *J. Phys. Chem. Lett.* **2014**, *5* (1), 196-204.

241. Pandya, R.; Chen, R. Y. S.; Cheminal, A.; Thomas, T.; Thampi, A.; Tanoh, A.; Richter, J.; Shivanna, R.; Deschler, F.; Schnedermann, C.; et al. Observation of Vibronic-Coupling-Mediated Energy Transfer in Light-Harvesting Nanotubes Stabilized in a Solid-State Matrix. *J Phys Chem Lett* **2018**, *9* (18), 5604-5611.

242. Würthner, F.; Saha-Möller, C. R.; Fimmel, B.; Ogi, S.; Leowanawat, P.; Schmidt, D. Perylene Bisimide Dye Assemblies as Archetype Functional Supramolecular Materials. *Chem. Rev.* **2016**, *116* (3), 962-1052.

243. Huang, C.; Barlow, S.; Marder, S. R. Perylene-3,4,9,10-tetracarboxylic Acid Diimides: Synthesis, Physical Properties, and Use in Organic Electronics. *J. Org. Chem.* **2011**, *76* (8), 2386-2407.

244. Lang, E.; Würthner, F.; Köhler, J. Photophysical Properties of a Tetraphenoxy-Substituted Perylene Bisimide Derivative Characterized by Single-Molecule Spectroscopy. *ChemPhysChem* **2005**, *6* (5), 935-941.

245. Weil, T.; Vosch, T.; Hofkens, J.; Peneva, K.; Müllen, K. The Rylene Colorant Family—Tailored Nanoemitters for Photonics Research and Applications. *Angew. Chem.* **2010**, *49* (48), 9068-9093.

246. Serin, J. M.; Brousmiche, D. W.; Fréchet, J. M. J. Cascade energy transfer in a conformationally mobile multichromophoric dendrimer. *Chem. Comm.* **2002**, (22), 2605-2607.

247. Spenst, P.; Young, R. M.; Wasielewski, M. R.; Wuerthner, F. Guest and solvent modulated photo-driven charge separation and triplet generation in a perylene bisimide cyclophane. *Chem. Sci.* **2016**, *7* (8), 5428-5434.

248. Eaton, S. W.; Shoer, L. E.; Karlen, S. D.; Dyar, S. M.; Margulies, E. A.; Veldkamp, B. S.; Ramanan, C.; Hartzler, D. A.; Savikhin, S.; Marks, T. J.; et al. Singlet Exciton Fission in Polycrystalline Thin Films of a Slip-Stacked Perylenediimide. *J. Am. Chem. Soc.* **2013**, *135* (39), 14701-14712.

249. Angadi, M. A.; Gosztola, D.; Wasielewski, M. R. Organic light emitting diodes using poly(phenylenevinylene) doped with perylenediimide electron acceptors. *Mater. Sci. Eng. B* **1999**, *63* (3), 191-194.

250. Zhan, X.; Facchetti, A.; Barlow, S.; Marks, T. J.; Ratner, M. A.; Wasielewski, M. R.; Marder, S. R. Rylene and Related Diimides for Organic Electronics. *Adv. Mater.* **2011**, *23* (2), 268-284.

251. Rybtchinski, B.; Sinks, L. E.; Wasielewski, M. R. Combining Light-Harvesting and Charge Separation in a Self-Assembled Artificial Photosynthetic System Based on Perylenediimide Chromophores. *J. Am. Chem. Soc.* **2004**, *126* (39), 12268-12269.

252. Zhang, J.; Li, Y.; Huang, J.; Hu, H.; Zhang, G.; Ma, T.; Chow, P. C. Y.; Ade, H.; Pan, D.; Yan, H. Ring-Fusion of Perylene Diimide Acceptor Enabling Efficient Nonfullerene Organic Solar Cells with a Small Voltage Loss. *J. Am. Chem. Soc.* **2017**, *139* (45), 16092-16095.

253. Bialas, D.; Bruning, C.; Schlosser, F.; Fimmel, B.; Thein, J.; Engel, V.; Wurthner, F. Exciton-Vibrational Couplings in Homo- and Heterodimer Stacks of Perylene Bisimide Dyes within Cyclophanes: Studies on Absorption Properties and Theoretical Analysis. *Chem. Eur. J.* **2016**, *22* (42), 15011-15018.

254. Wu, Y.; Young, R. M.; Frasconi, M.; Schneebeli, S. T.; Spenst, P.; Gardner, D. M.; Brown, K. E.; Wurthner, F.; Stoddart, J. F.; Wasielewski, M. R. Ultrafast Photoinduced Symmetry-Breaking Charge Separation and Electron Sharing in Perylenediimide Molecular Triangles. *J. Am. Chem. Soc.* **2015**, *137* (41), 13236-13239.

255. Spenst, P.; Young, R. M.; Phelan, B. T.; Keller, M.; Dostal, J.; Brixner, T.; Wasielewski, M. R.; Wurthner, F. Solvent-Templated Folding of Perylene Bisimide Macrocycles into Coiled Double-String Ropes with Solvent-Sensitive Optical Signatures. *J. Am. Chem. Soc.* **2017**, *139* (5), 2014-2021.

256. Frontiera, R. R.; Shim, S.; Mathies, R. A. Origin of negative and dispersive features in anti-Stokes and resonance femtosecond stimulated Raman spectroscopy. *J. Chem. Phys.* **2008**, *129* (6), 064507.

257. Turner, D. B.; Wilk, K. E.; Curmi, P. M. G.; Scholes, G. D. Comparison of Electronic and Vibrational Coherence Measured by Two-Dimensional Electronic Spectroscopy. *J. Phys. Chem. Lett.* **2011**, *2* (15), 1904-1911.

258. Chenu, A.; Christensson, N.; Kauffmann, H. F.; Mancal, T. Enhancement of vibronic and ground-state vibrational coherences in 2D spectra of photosynthetic complexes. *Sci. Rep.* **2013**, *3*, 2029.

259. Son, M.; Park, K. H.; Yoon, M. C.; Kim, P.; Kim, D. Excited-State Vibrational Coherence in Perylene Bisimide Probed by Femtosecond Broadband Pump-Probe Spectroscopy. *J. Phys. Chem. A* **2015**, *119* (24), 6275-6282.

260. Tekavec, P. F.; Myers, J. A.; Lewis, K. L. M.; Ogilvie, J. P. Two-dimensional electronic spectroscopy with a continuum probe. *Opt. Lett.* **2009**, *34*, 1390-1392.

261. Hippius, C.; van Stokkum, I. H. M.; Zangrando, E.; Williams, R. M.; Wykes, M.; Beljonne, D.; Würthner, F. Ground- and Excited-State Pinched Cone Equilibria in Calix[4]arenes Bearing Two Perylene Bisimide Dyes. *J. Phys. Chem. C* **2008**, *112* (37), 14626-14638.

262. Wu, Y.; Zhou, J.; Phelan, B. T.; Mauck, C. M.; Stoddart, J. F.; Young, R. M.; Wasielewski, M. R. Probing Distance Dependent Charge-Transfer Character in Excimers of Extended Viologen Cyclophanes Using Femtosecond Vibrational Spectroscopy. *J. Am. Chem. Soc.* **2017**, *139* (40), 14265-14276.

263. Fuller, F. D.; Pan, J.; Gelzinis, A.; Butkus, V.; Senlik, S. S.; Wilcox, D. E.; Yocum, C. F.; Valkunas, L.; Abramavicius, D.; Ogilvie, J. P. Vibronic coherence in oxygenic photosynthesis. *Natre Chemistry* **2014**, *6*, 706-711.

264. Schlau-Cohen, G. S.; Ishizaki, A.; Fleming, G. R. Two-Dimensional Electronic Spectroscopy and Photosynthesis: Fundamentals and Applications to Photosynthetic Light-Harvesting. *Chem. Phys.* **2011**, *386*, 1.

265. Arsenault, E. A.; Yoneda, Y.; Iwai, M.; Niyogi, K. K.; Fleming, G. R. Vibronic mixing enables ultrafast energy flow in light-harvesting complex II. *Nat. Commun.* **2020**, *11* (1), 1460.

266. Romero, E.; Augulis, R.; Novoderezhkin, V. I.; Ferretti, M.; Thieme, J.; Zigmantas, D.; van Grondelle, R. Quantum Coherence in Photosynthesis for Efficient Solar-Energy Conversion. *Nat. Phys.* **2014**, *10*, 676-682.

267. Meneghin, E.; Leonardo, C.; Volpato, A.; Bolzonello, L.; Collini, E. Mechanistic insight into internal conversion process within Q-bands of chlorophyll a. *Sci. Rep.* **2017**, *7* (1), 11389.

268. Collini, E.; Wong, C. Y.; Wilk, K. E.; Curmi, P. M. G.; Brumer, P.; Scholes, G. D. Coherently wired light-harvesting in photosynthetic marine algae at ambient temperature. *Nature* **2010**, *463* (7281), 644-U669.

269. Paleček, D.; Edlund, P.; Westenhoff, S.; Zigmantas, D. Quantum coherence as a witness of vibronically hot energy transfer in bacterial reaction center. *Sci. Adv.* **2017**, *3* (9), e1603141.

270. Thyrhaug, E.; Lincoln, C. N.; Branchi, F.; Cerullo, G.; Perlík, V.; Šanda, F.; Lokstein, H.; Hauer, J. Carotenoid-to-bacteriochlorophyll energy transfer through vibronic coupling in LH2 from Phaeosprillum molischianum. *Photosynth. Res.* **2018**, *135* (1), 45-54.

271. Richards, G. H.; Wilk, K. E.; Curmi, P. M. G.; Quiney, H. M.; Davis, J. A. Coherent Vibronic Coupling in Light-Harvesting Complexes from Photosynthetic Marine Algae. *J. Phys. Chem. Lett.* **2012**, *3* (2), 272-277.

272. Ma, F.; Romero, E.; Jones, M. R.; Novoderezhkin, V. I.; van Grondelle, R. Vibronic Coherence in the Charge Separation Process of the Rhodobacter sphaeroides Reaction Center. *Journal of Physical Chemistry Letters* **2018**, *9* (8), 1827-1832.

273. Son, M.; Pinnola, A.; Bassi, R.; Schlau-Cohen, G. S. The Electronic Structure of Lutein 2 Is Optimized for Light Harvesting in Plants. *Chem* **2019**, *5* (3), 575-584.

274. Stones, R.; Olaya-Castro, A. Vibronic Coupling as a Design Principle to Optimize Photosynthetic Energy Transfer. *Chem* **2016**, *1* (6), 822-824.

275. Smith, M. B.; Michl, J. Recent Advances in Singlet Fission. *Annu. Rev. Phys. Chem.* **2013**, *64* (1), 361.

276. Hanna, M. C.; Nozik, A. J. Solar conversion efficiency of photovoltaic and photoelectrolysis cells with carrier multiplication absorbers. *J. Appl. Phys.* **2006**, *100* (7), 074510/074511-074510/074518.

277. Smith, M. B.; Michl, J. Singlet Fission. *Chem. Rev.* **2010**, *110* (11), 6891-6936.

278. Chan, W. L.; Berkelbach, T. C.; Provorse, M. R.; Monahan, N. R.; Tritsch, J. R.; Hybertsen, M. S.; Reichman, D. R.; Gao, J.; Zhu, X. Y. The quantum coherent mechanism for singlet fission: Experiment and theory. *Acc. Chem. Res.* **2013**, *46* (6), 1321.

279. Fuemmeler, E. G.; Sanders, S. N.; Pun, A. B.; Kumarasamy, E.; Zeng, T.; Miyata, K.; Steigerwald, M. L.; Zhu, X. Y.; Sfeir, M. Y.; Campos, L. M.; et al. A direct mechanism of ultrafast intramolecular singlet fission in pentacene dimers. *ACS Cent. Sci.* **2016**, *2* (5), 316.

280. Stern, H. L.; Cheminal, A.; Yost, S. R.; Broch, K.; Bayliss, S. L.; Chen, K.; Tabachnyk, M.; Thorley, K.; Greenham, N.; Hodgkiss, J. M.; et al. Vibronically coherent ultrafast triplet-pair formation and subsequent thermally activated dissociation control efficient endothermic singlet fission. *Nat. Chem.* **2017**, *9* (12), 1205.

281. Young, R. M.; Wasielewski, M. R. Mixed Electronic States in Molecular Dimers: Connecting Singlet Fission, Excimer Formation, and Symmetry-Breaking Charge Transfer. *Acc. Chem. Res.* **2020**.

282. Nolde, F.; Qu, J. Q.; Kohl, C.; Pschirer, N. G.; Reuther, E.; Mullen, K. Synthesis and modification of terrylenediimides as high-performance fluorescent dyes. *Eur. J. Chem.* **2005**, *11* (13), 3959-3967.

283. Margulies, E. A.; Miller, C. E.; Wu, Y.; Ma, L.; Schatz, G. C.; Young, R. M.; Wasielewski, M. R. Enabling singlet fission by controlling intramolecular charge transfer in π-stacked covalent terrylenediimide dimers. *Nat. Chem.* **2016**, *8* (12), 1120.

284. Chen, M.; Bae, Y. J.; Mauck, C. M.; Mandal, A.; Young, R. M.; Wasielewski, M. R. Singlet Fission in Covalent Terrylenediimide Dimers: Probing the Nature of the Multiexciton State Using Femtosecond Mid-Infrared Spectroscopy. *J. Am. Chem. Soc.* **2018**, *140* (29), 9184-9192.

285. Chen, M.; Shin, J. Y.; Young, R. M.; Wasielewski, M. R. Tuning the charge transfer character of the multiexciton state in singlet fission. *J. Chem. Phys.* **2020**, *153* (9), 094302.

286. Chen, M.; Krzyaniak, M. D.; Nelson, J. N.; Bae, Y. J.; Harvey, S. M.; Schaller, R. D.; Young, R. M.; Wasielewski, M. R. Quintet-triplet mixing determines the fate of the multiexciton state produced by singlet fission in a terrylenediimide dimer at room temperature. *Proc. Natl. Acad. Sci. U.S.A.* **2019**, *116* (17), 8178-8183.

287. Pisula, W.; Kastler, M.; Wasserfallen, D.; Robertson, J. W. F.; Nolde, F.; Kohl, C.; Muellen, K. Pronounced Supramolecular Order in Discotic Donor-Acceptor Mixtures. *Angew. Chem. Int. Ed.* **2006**, *45*, 819-823.

288. Laury, M. L.; Carlson, M. J.; Wilson, A. K. Vibrational frequency scale factors for density functional theory and the polarization consistent basis sets. *J. Comput. Chem.* **2012**, *33* (30), 2380-2387.

289. Berkelbach, T. C.; Hybertsen, M. S.; Reichman, D. R. Microscopic theory of singlet exciton fission. II. Application to pentacene dimers and the role of superexchange. *J. Chem. Phys.* **2013**, *138* (11), 114103.

290. Young, R. M.; Wasielewski, M. R. Mixed Electronic States in Molecular Dimers: Connecting Singlet Fission, Excimer Formation, and Symmetry-Breaking Charge Transfer. *Acc. Chem. Res.* **2020**, *53* (9), 1957-1968.

291. Pandya, R.; Chen, R. Y. S.; Cheminal, A.; Thomas, T.; Thampi, A.; Tanoh, A.; Richter, J.; Shivanna, R.; Deschler, F.; Schnedermann, C.; et al. Observation of Vibronic-Coupling-Mediated Energy Transfer in Light-Harvesting Nanotubes Stabilized in a Solid-State Matrix. *J. Phys. Chem. Lett.* **2018**, *9* (18), 5604-5611.

292. Cheatum, C. M.; Heckscher, M. M.; Bingemann, D.; Crim, F. F. CH2I2 fundamental vibrational relaxation in solution studied by transient electronic absorption spectroscopy. *J. Chem. Phys.* **2001**, *115* (15), 7086-7093.

293. Collini, E.; Gattuso, H.; Bolzonello, L.; Casotto, A.; Volpato, A.; Dibenedetto, C. N.; Fanizza, E.; Striccoli, M.; Remacle, F. Quantum Phenomena in Nanomaterials: Coherent Superpositions of Fine Structure States in CdSe Nanocrystals at Room Temperature. *J. Phys. Chem. C* **2019**, *123* (51), 31286-31293.

294. Kim, J.; Nguyen-Phan, T. C.; Gardiner, A. T.; Cogdell, R. J.; Scholes, G. D.; Cho, M. Low-Frequency Vibronic Mixing Modulates the Excitation Energy Flow in Bacterial Light-Harvesting Complex II. *J. Phys. Chem. Lett.* **2021**, *12* (27), 6292-6298.

295. Perlík, V.; Seibt, J.; Cranston, L. J.; Cogdell, R. J.; Lincoln, C. N.; Savolainen, J.; Šanda, F.; Mančal, T.; Hauer, J. Vibronic coupling explains the ultrafast carotenoid-to-bacteriochlorophyll energy transfer in natural and artificial light harvesters. *J. Chem. Phys.* **2015**, *142* (21), 212434.

296. Irgen-Gioro, S.; Gururangan, K.; Spencer, A. P.; Harel, E. Non-Uniform Excited State Electronic-Vibrational Coupling of Pigment–Protein Complexes. *J. Phys. Chem. Lett.* **2020**, *11* (24), 10388-10395.

297. Kim, P.; Valentine, A. J. S.; Roy, S.; Mills, A. W.; Chakraborty, A.; Castellano, F. N.; Li, X.; Chen, L. X. Ultrafast Excited-State Dynamics of Photoluminescent Pt(II) Dimers Probed by a Coherent Vibrational Wavepacket. *J. Phys. Chem. Lett.* **2021**, *12* (29), 6794-6803.

298. Kim, T.; Kim, W.; Vakuliuk, O.; Gryko, D. T.; Kim, D. Two-Step Charge Separation Passing Through the Partial Charge-Transfer State in a Molecular Dyad. *J. Am. Chem. Soc.* **2020**, *142* (3), 1564-1573.

299. Kim, W.; Kim, T.; Kang, S.; Hong, Y.; Würthner, F.; Kim, D. Tracking structural evolution during symmetry-breaking charge separation in quadrupolar perylene bisimide with time-resolved impulsive stimulated Raman spectroscopy. *Angew. Chem., Int. Ed.* **2020**, *59*, 8571.

300. Yoneda, Y.; Mora, S. J.; Shee, J.; Wadsworth, B. L.; Arsenault, E. A.; Hait, D.; Kodis, G.; Gust, D.; Moore, G. F.; Moore, A. L.; et al. Electron–Nuclear Dynamics Accompanying Proton-Coupled Electron Transfer. *J. Am. Chem. Soc.* **2021**, *143* (8), 3104-3112.

301. Monahan, N. R.; Sun, D.; Tamura, H.; Williams, K. W.; Xu, B.; Zhong, Y.; Kumar, B.; Nuckolls, C.; Harutyunyan, A. R.; Chen, G.; et al. Dynamics of the triplet-pair state reveals the likely coexistence of coherent and incoherent singlet fission in crystalline hexacene. *Nat. Chem.* **2017**, *9* (4), 341-346.

302. Miyata, K.; Kurashige, Y.; Watanabe, K.; Sugimoto, T.; Takahashi, S.; Tanaka, S.; Takeya, J.; Yanai, T.; Matsumoto, Y. Coherent singlet fission activated by symmetry breaking. *Nat. Chem.* **2017**, *9* (10), 983-989.

303. Kang, S.; Kim, T.; Hong, Y.; Würthner, F.; Kim, D. Charge-Delocalized State and Coherent Vibrational Dynamics in Rigid PBI H-Aggregates. *J. Am. Chem. Soc.* **2021**, *143* (26), 9825-9833.

304. Kim, T.; Kang, S.; Kirchner, E.; Bialas, D.; Kim, W.; Würthner, F.; Kim, D. Switching resonance character within merocyanine stacks and its impact on excited-state dynamics. *Chem* **2021**, *7* (3), 715-725.

305. Patra, S.; Sahu, A.; Tiwari, V. Effective normal modes identify vibrational motions which maximally promote vibronic mixing in excitonically coupled aggregates. *J. Chem. Phys.* **2021**, *154* (11), 111106.

306. Hybl, J. D.; Ferro, A. A.; Jonas, D. M. Two-Dimensional Fourier Transform Electronic Spectroscopy. *J. Chem. Phys.* **2001**, *115*, 6606.

307. Hart, S. M.; Chen, W. J.; Banal, J. L.; Bricker, W. P.; Dodin, A.; Markova, L.; Vyborna, Y.; Willard, A. P.; Häner, R.; Bathe, M.; et al. Engineering couplings for exciton transport using synthetic DNA scaffolds. *Chem* **2021**, *7* (3), 752-773.

308. Arpin, P. C.; Turner, D. B. Signatures of Vibrational and Electronic Quantum Beats in Femtosecond Coherence Spectra. *J. Phys. Chem. A* **2021**, *125* (12), 2425-2435.

309. Le, D. V.; Leng, X.; Tan, H.-S. Regarding expressions of the oscillatory patterns in the 2D spectra of a displaced oscillator model. *Chem. Phys.* **2021**, *546*, 111142.

310. Zhu, R.; Zou, J.; Wang, Z.; Chen, H.; Weng, Y. Electronic State-Resolved Multimode-Coupled Vibrational Wavepackets in Oxazine 720 by Two-Dimensional Electronic Spectroscopy. *J. Phys. Chem. A* **2020**, *124* (45), 9333-9342.

311. Kuramochi, H.; Tahara, T. Tracking Ultrafast Structural Dynamics by Time-Domain Raman Spectroscopy. *J. Am. Chem. Soc.* **2021**.

312. Yue, S.; Wang, Z.; Leng, X.; Zhu, R. D.; Chen, H. L.; Weng, Y. X. Coupling of Multi-Vibrational Modes in Bacteriochlorophyll a in Solution Observed with 2d Electronic Spectroscopy. *Chem. Phys. Lett.* **2017**, *683*, 591-597.

313. Le, D. V.; De La Perrelle, J. M.; Do, T. N.; Leng, X.; Tapping, P. C.; Scholes, G. D.; Kee, T. W.; Tan, H.-S. Characterization of the ultrafast spectral diffusion and vibronic coherence of TIPS-pentacene using 2D electronic spectroscopy. *J. Chem. Phys.* **2021**, *155* (1), 014302.

314. Hamm, P.; Lim, M.; Hochstrasser, R. M. Structure of the Amide I Band of Peptides Measured by Femtosecond Nonlinear-Infrared Spectroscopy. *J. Phys. Chem. B* **1998**, *102* (31), 6123-6138.

315. Zanni, M. T.; Hochstrasser, R. M. Two-dimensional infrared spectroscopy: a promising new method for the time resolution of structures. *Curr. Opin. Struct. Biol.* **2001**, *11* (5), 516-522.

316. Gaynor, J. D.; Weakly, R. B.; Khalil, M. Multimode two-dimensional vibronic spectroscopy. I. Orientational response and polarization-selectivity. *J. Chem. Phys.* **2021**, *154* (18), 184201.

317. Weakly, R. B.; Gaynor, J. D.; Khalil, M. Multimode two-dimensional vibronic spectroscopy. II. Simulating and extracting vibronic coupling parameters from polarization-selective spectra. *J. Chem. Phys.* **2021**, *154* (18), 184202.

318. Gaynor, J. D.; Sandwisch, J.; Khalil, M. Vibronic coherence evolution in multidimensional ultrafast photochemical processes. *Nat. Commun.* **2019**, *10* (1), 5621.

319. Fox, Z. W.; Blair, T. J.; Khalil, M. Determining the Orientation and Vibronic Couplings between Electronic and Vibrational Coordinates with Polarization-Selective Two-Dimensional Vibrational-Electronic Spectroscopy. *J. Phys. Chem. Lett.* **2020**, *11* (4), 1558-1563.

320. Farfan, C. A.; Turner, D. B. Interference among Multiple Vibronic Modes in Two-Dimensional Electronic Spectroscopy. *Mathematics* **2020**, *8* (2), 157.

321. Zhan, X.; Facchetti, A.; Barlow, S.; Marks, T. J.; Ratner, M. A.; Wasielewski, M. R.; Marder, S. R. Rylene and Related Diimides for Organic Electronics. *Advanced Materials* **2011**, *23* (2), 268-284.

322. Eastham, N. D.; Logsdon, J. L.; Manley, E. F.; Aldrich, T. J.; Leonardi, M. J.; Wang, G.; Powers-Riggs, N. E.; Young, R. M.; Chen, L. X.; Wasielewski, M. R.; et al. Hole-Transfer Dependence on Blend Morphology and Energy Level Alignment in Polymer: ITIC Photovoltaic Materials. *Adv. Mater.* **2018**, *30* (3), 1704263.

323. Song, Y.; Liu, X.; Li, Y.; Nguyen, H. H.; Duan, R.; Kubarych, K. J.; Forrest, S. R.; Ogilvie, J. P. Mechanistic Study of Charge Separation in a Nonfullerene Organic Donor–Acceptor Blend Using Multispectral Multidimensional Spectroscopy. *J. Phys. Chem. Lett.* **2021**, *12* (13), 3410-3416.

324. Dean, J. C.; Oblinsky, D. G.; Rafiq, S.; Scholes, G. D. Methylene Blue Exciton States Steer Nonradiative Relaxation: Ultrafast Spectroscopy of Methylene Blue Dimer. *J. Phys. Chem. B* **2016**, *120* (3), 440-454.

325. Brown, K. E.; Veldkamp, B. S.; Co, D. T.; Wasielewski, M. R. Vibrational Dynamics of a Perylene-Perylenediimide Donor-Acceptor Dyad Probed with Femtosecond Stimulated Raman Spectroscopy. *J. Phys. Chem. Lett.* **2012**, *3* (17), 2362-2366.

326. Gelin, M. F.; Chen, L.; Borrelli, R.; Thyrhaug, E. Generalized Huang-Rhys factors for molecular aggregates. *Chem. Phys.* **2020**, *528*, 110495.

327. de A. Camargo, F. V.; Grimmelsmann, L.; Anderson, H. L.; Meech, S. R.; Heisler, I. A. Resolving Vibrational from Electronic Coherences in Two-Dimensional Electronic Spectroscopy: The Role of the Laser Spectrum. *Phys. Rev. Lett.* **2017**, *118* (3), 033001.

328. Duschinsky, F. The importance of the electron spectrum in multi atomic molecules. concerning the Franck-Condon principle. *Acta Physicochim. U.R.S.S.* **1937** *7*(4), 551-566.

329. Ellis, S. R.; Hoffman, D. P.; Park, M.; Mathies, R. A. Difference Bands in Time-Resolved Femtosecond Stimulated Raman Spectra of Photoexcited Intermolecular Electron Transfer from Chloronaphthalene to Tetracyanoethylene. *J. Phys. Chem. A* **2018**, *122* (14), 3594-3605.

330. Jonas, D. M.; Bradforth, S. E.; Passino, S. A.; Fleming, G. R. Femtosecond Wavepacket Spectroscopy: Influence of Temperature, Wavelength, and Pulse Duration. *J. Phys. Chem.* **1995**, *99* (9), 2594-2608.

331. Fitzpatrick, C.; Odhner, J. H.; Levis, R. J. Spectral Signatures of Ground- and Excited-State Wavepacket Interference after Impulsive Excitation. *J. Phys. Chem. A* **2020**, *124* (34), 6856-6866.

332. Perlík, V.; Lincoln, C.; Šanda, F.; Hauer, J. Distinguishing Electronic and Vibronic Coherence in 2D Spectra by Their Temperature Dependence. *J. Phys. Chem. Lett.* **2014**, *5* (3), 404-407.

333. Turner, D. B.; Arpin, P. C. Basis set truncation further clarifies vibrational coherence spectra. *Chem. Phys.* **2020**, *539*, 110948.

334. Quick, M.; Dobryakov, A. L.; Kovalenko, S. A.; Ernsting, N. P. Resonance Femtosecond-Stimulated Raman Spectroscopy without Actinic Excitation Showing Low-Frequency Vibrational Activity in the S2 State of All-Trans β-Carotene. *J. Phys. Chem. Lett.* **2015**, *6* (7), 1216-1220.

335. Dobryakov, A. L.; Quick, M.; Ioffe, I. N.; Granovsky, A. A.; Ernsting, N. P.; Kovalenko, S. A. Excited-state Raman spectroscopy with and without actinic excitation: S1 Raman spectra of trans-azobenzene. *J. Chem. Phys.* **2014**, *140* (18), 184310.

336. Fidler, A. F.; Engel, G. S. Nonlinear Spectroscopic Theory of Displaced Harmonic Oscillators with Differing Curvatures: A Correlation Function Approach. *J. Phys. Chem. A* **2013**, *117* (39), 9444-9453.

337. Zuehlsdorff, T. J.; Hong, H.; Shi, L.; Isborn, C. M. Nonlinear spectroscopy in the condensed phase: The role of Duschinsky rotations and third order cumulant contributions. *J. Chem. Phys.* **2020**, *153* (4), 044127.

338. Weng, Y. X. Detection of Electronic Coherence Via Two-Dimensional Electronic Spectroscopy in Condensed Phase. *Chin. J. Chem. Phys.* **2018**, *31*, 135−151.

339. Weng, X. Y. W., Z.; Chen, H.-L.; Leng, X.; Zhu, R.-D. Quantum Coherence Measurement with Femtosecond Time-Resolve Two-Dimensional Electronic Spectroscopy: Principles, Applications and Outlook. *Acta Phys. Sin.* **2018**, *67*, 127801.

340. Wang, R.; Zhang, C.; Zhang, Z.; Li, Y.; Wang, X.; Xiao, M. Ultrafast Coherent Hole Transfer in Non-Fullerene OPV Blends. In *Conference on Lasers and Electro-Optics*, San Jose, California, 2018/05/13, 2018; Optical Society of America: p JTh2A.151. DOI: 10.1364/CLEO_AT.2018.JTh2A.151.

341. Son, M.; Mosquera-Vázquez, S.; Schlau-Cohen, G. S. Ultrabroadband 2D electronic spectroscopy with high-speed, shot-to-shot detection. *Opt. Express* **2017**, *25* (16), 18950-18962.

342. Mewes, L.; Ingle, R. A.; Al Haddad, A.; Chergui, M. Broadband visible two-dimensional spectroscopy of molecular dyes. *J. Chem. Phys.* **2021**, *155* (3), 034201.

343. Cai, Y.; Wei, Z.; Song, C.; Tang, C.; Huang, X.; Hu, Q.; Dong, X.; Han, W. Novel acceptor–donor–acceptor structured small molecule-based nanoparticles for highly efficient photothermal therapy. *Chem. Comm.* **2019**, *55* (61), 8967-8970.

344. Arsenault, E. A.; Schile, A. J.; Limmer, D. T.; Fleming, G. R. Vibronic coupling in light-harvesting complex II revisited. *J. Chem. Phys.* **2021**, *155* (9), 096101.

345. Gaynor, J. D.; Sandwisch, J.; Khalil, M. Vibronic coherence evolution in multidimensional ultrafast photochemical processes. *Nat. Comm.* **2019**, *10* (1).

346. Kearns, N. M.; Jones, A. C.; Kunz, M. B.; Allen, R. T.; Flach, J. T.; Zanni, M. T. Two-dimensional white-light spectroscopy using supercontinuum from an all-normal dispersion photonic crystal fiber pumped by a 70 MHz Yb fiber oscillator. *J. Phys. Chem. A* **2019**, *123*, 3046.

347. Kearns, N. M.; Mehlenbacher, R. D.; Jones, A. C.; Zanni, M. T. Broadband 2D electronic spectrometer using white light and pulse shaping: noise and signal evaluation at 1 and 100 kHz. *Opt. Express* **2017**, *25* (7), 7869-7883.

348. Fuller, F. D.; Wilcox, D. E.; Ogilvie, J. P. Pulse shaping based two-dimensional electronic spectroscopy in a background free geometry. *Opt. Express* **2014**, *22*, 1018.

349. Ren, H.; Zhang, Q.; Wang, Z.; Zhang, G.; Liu, H.; Guo, W.; Mukamel, S.; Jiang, J. Machine learning recognition of protein secondary structures based on two-dimensional spectroscopic descriptors. *Proc. Natl. Acad. Sci. U.S.A.* **2022**, *119* (18), e2202713119.

350. Mukamel, S. Comment on "Coherence and uncertainty in nanostructured organic photovoltaics". *J. Phys. Chem. A* **2013**, *117* (40), 10563-10564.

351. Halpin, A.; Johnson, P. J. M.; Miller, R. J. D. Comment on "Engineering coherence among excited states in synthetic heterodimer systems". *Science* **2014**, *344* (6188), 1099-1099.

352. Harush, E. Z.; Dubi, Y. Do photosynthetic complexes use quantum coherence to increase their efficiency? Probably not. *Sci. Adv.* **2021**, *7* (8), eabc4631.

353. Spenst, P.; Würthner, F. A Perylene Bisimide Cyclophane as a "Turn-On" and "Turn-Off" Fluorescence Probe. *Angew. Chem.* **2015**, *54* (35), 10165-10168.

354. Pollard, W. T.; Dexheimer, S. L.; Wang, Q.; Peteanu, L. A.; Shank, C. V.; Mathies, R. A. Theory of dynamic absorption spectroscopy of nonstationary states. 4. Application to 12-fs resonant impulsive Raman spectroscopy of bacteriorhodopsin. *J. Phys. Chem.* **1992**, *96* (15), 6147-6158.

355. McClure, S. D.; Turner, D. B.; Arpin, P. C.; Mirkovic, T.; Scholes, G. D. Coherent Oscillations in the PC577 Cryptophyte Antenna Occur in the Excited Electronic State. *J. Phys. Chem. B* **2014**, *118* (5), 1296-1308.

356. Irgen-Gioro, S.; Roy, P.; Padgaonkar, S.; Harel, E. Low energy excited state vibrations revealed in conjugated copolymer PCDTBT. *J. Chem. Phys.* **2020**, *152* (4), 044201.

357. Patra, S.; Tiwari, V. Vibronic resonance along effective modes mediates selective energy transfer in excitonically coupled aggregates. *J. Chem. Phys.* **2022**, *156* (18), 184115.

358. Gaynor, J. D.; Petrone, A.; Li, X.; Khalil, M. Mapping vibronic couplings in a solar cell dye with polarization-selective two-dimensional electronic-vibrational spectroscopy. *J. Phys. Chem. Lett.* **2018**, *9* (21), 6289-6295.

359. Arsenault, E. A.; Bhattacharyya, P.; Yoneda, Y.; Fleming, G. R. Two-dimensional electronic-vibrational spectroscopy: Exploring the interplay of electrons and nuclei in excited state molecular dynamics. *J. Chem. Phys.* **2021**, *155* (2), 020901.

360. Fujisawa, T.; Kuramochi, H.; Hosoi, H.; Takeuchi, S.; Tahara, T. Role of Coherent Low-Frequency Motion in Excited-State Proton Transfer of Green Fluorescent Protein Studied by Time-Resolved Impulsive Stimulated Raman Spectroscopy. *J. Am. Chem. Soc.* **2016**, *138* (12), 3942-3945.

361. Takeuchi, S.; Ruhman, S.; Tsuneda, T.; Chiba, M.; Taketsugu, T.; Tahara, T. Spectroscopic Tracking of Structural Evolution in Ultrafast Stilbene Photoisomerization. *Science* **2008**, *322* (5904), 1073-1077.

362. Fujiyoshi, S.; Takeuchi, S.; Tahara, T. Time-Resolved Impulsive Stimulated Raman Scattering from Excited-State Polyatomic Molecules in Solution. *J. Phys. Chem. A* **2003**, *107* (4), 494-500.

363. Fujiyoshi, S.; Ishibashi, T.-a.; Onishi, H. Fifth-order Raman spectroscopy of excited-state molecules. *J. Phys. Chem. A* **2004**, *108* (51), 11165-11171.

364. Johansson, J. R.; Nation, P. D.; Nori, F. QuTiP: An open-source Python framework for the dynamics of open quantum systems. *Comput. Phys. Commun.* **2012**, *183* (8), 1760-1772.

365. Chosrowjan, H.; Taniguchi, S.; Mataga, N.; Unno, M.; Yamauchi, S.; Hamada, N.; Kumauchi, M.; Tokunaga, F. Low-Frequency Vibrations and Their Role in Ultrafast Photoisomerization Reaction Dynamics of Photoactive Yellow Protein. *J. Phys. Chem. B.* **2004**, *108* (8), 2686-2698.

366. Barclay, M. S.; Huff, J. S.; Pensack, R. D.; Davis, P. H.; Knowlton, W. B.; Yurke, B.; Dean, J. C.; Arpin, P. C.; Turner, D. B. Characterizing Mode Anharmonicity and Huang–Rhys Factors Using Models of Femtosecond Coherence Spectra. *J. Phys. Chem. Lett.* **2022**, 5413-5423.

Appendix A: Supplementary Information for Chapter 4

A.1 Synthesis and characterization

Synthetic procedures for the 4-*t*-butyltetraphenoxy bay-substituted perylenediimide para-cyclophane (**p-PDI**) and the monomeric reference (**PDI-Ref**) compound can be found in previous literature.[247, 353]

Synthesis of meta-cyclophane (m-PDI):

1,6,7,12-tetra(4-*t*-butylphenoxy)perylene-3,4:9,10-tetracarboxylic acid dianhydride (100mg, 0.1mmol), 1,3-bis(aminomethyl)benzene (1.4 mL of a solution of 0.1mL diamine in 10mL toluene, 0.1mmol), imidazole (1 g, 15 mmol), pyridine (10 mL, 124 mmol), and toluene (200 mL) were mixed. The mixture was heated to 115°C for 18 hours. After cooling to room temperature, 250 mL of 2M HCl was added. The organic layer was collected and washed with water. The remaining aqueous layer was extracted with DCM, and the organic layer was collected. The solvent was removed from the combined organic layers under reduced pressure. The crude product was purified via column chromatography (DCM, silica) and HPLC to yield 23 mg of **m-PDI** (6%). ^{1}H NMR was collected at 363K on a Bruker Avance III 600 MHz system. Mass spectrometry was performed on a Bruker IMPACT II to generate high-resolution HR-APPI-MS spectra at the Integrated Molecular Structure Education and Research Center (IMSERC) at Northwestern University. All solvents and reagents were purchased from commercial suppliers and used without purification. Column chromatography was performed using silica gel from Macherey-Nagel and HPLC was performed on a Shimadzu HPLC.

^{1}H-NMR (600 MHz, 363K, C2D2Cl4): δ = 8.08 (s, 8H), 7.45 (d, J=7.74 Hz, 4H), 7.32 (t, J=7.74 Hz, 2H), 7.28 (bs, 2H), 7.23 (d, J=8.22 Hz, 16H), 6.73 (bs, 16H), 5.24 (s, 8H), 1.33 (s, 72H) ppm.

HRMS (APPI, positive mode, DCM): m/z: calculated for $C_{144}H_{129}N_4O_{16}$: 2169.9398 [M+H] [+],

found: 2169.9349.

A.2. Laser pulse characterization
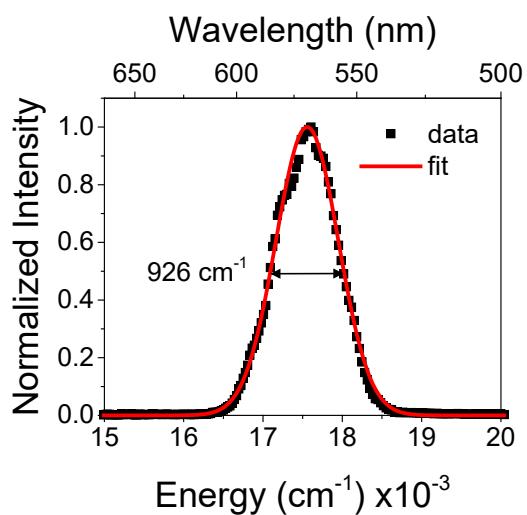
Figure S4.1. A typical pump pulse spectrum. Fitting
to a single Gaussian yields a FWHM of 926 cm^{-1}.

Figure S4.1 shows a typical chirp-corrected pulse spectrum, centered at 17540 cm^{-1} (570

nm), spanning 16500 to 18600 cm^{-1} with a ~926 cm^{-1} full-width at half-maximum (FWHM). Group

velocity and third-order dispersions were compensated for using the pulse shaper. Example SHG-

FROG traces are provided in Figure S4.2A and B. The measured pulse width of the 2DES pump

pulse was ~28 fs.
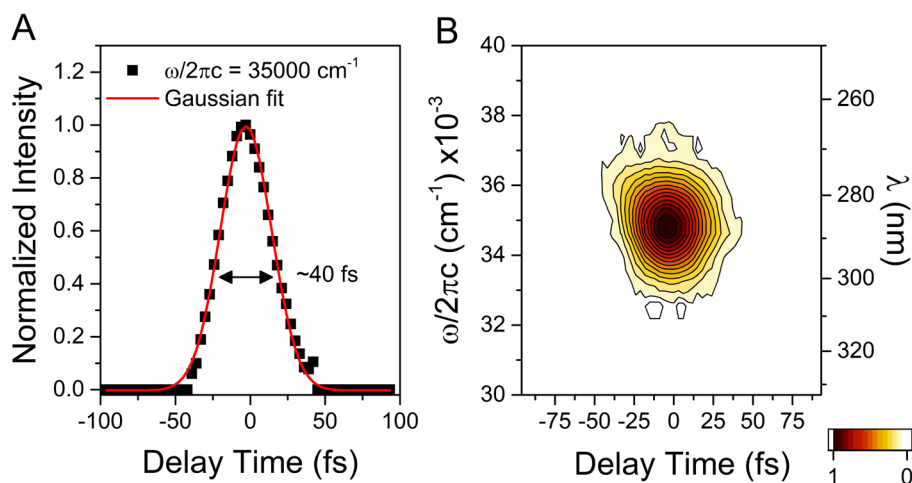
Figure S4.2. (A) SHG-FROG trace of the typical pump pulse employed in these experiments and (B) a single time-domain slice of the FROG trace overlaid with a Gaussian fit (FWHM = ~40 fs). The average pulse duration determined via six FROG traces was ~28 fs.

A.3 Femtosecond Stimulated Raman Spectroscopy (FSRS)

For experiments probing the ground state, the Raman pump was centered near 600 nm and focused at the sample with 2 μJ/pulse and parallel polarization to the probe for the measurements. For excited-state experiments, the actinic pump (573 nm, 1 μJ/pulse) was used in conjunction with a 710 nm Raman pump. Polarization of the actinic pump was set at 54.7° (magic angle) relative to the Raman pump/probe to negate rotational effects.

A.4 Computational details

All DFT calculations were performed using the Q-Chem 5.0 software package at the level of B3LYP/6-31G* *in vacuo*. To lower the computational cost, the tert-butyl groups of the phenoxy substituents were substituted with methyl groups. The fully optimized geometry of **PDI-Ref** was confirmed by ensuring no imaginary frequencies were present in the final frequency output.

A.5 2DES Population analysis

To isolate coherent dynamics in these studies, we fit population dynamics at each (ω_1, ω_3) coordinate using two exponential functions, as described in Section 2.5.3 (approach 1). Only

waiting times after 100 fs were considered so as to avoid influence from pulse overlap effects. Examples fits for the higher energy $S_n \leftarrow S_1$ transition for each compound are shown in Figure 4.4A-C of the main text. Figure S4.3 shows additional fits for the ground-state bleach (GSB)/stimulated emission (SE) and excited-state absorption (ESA) features of *p*-PDI and the resultant power spectra.
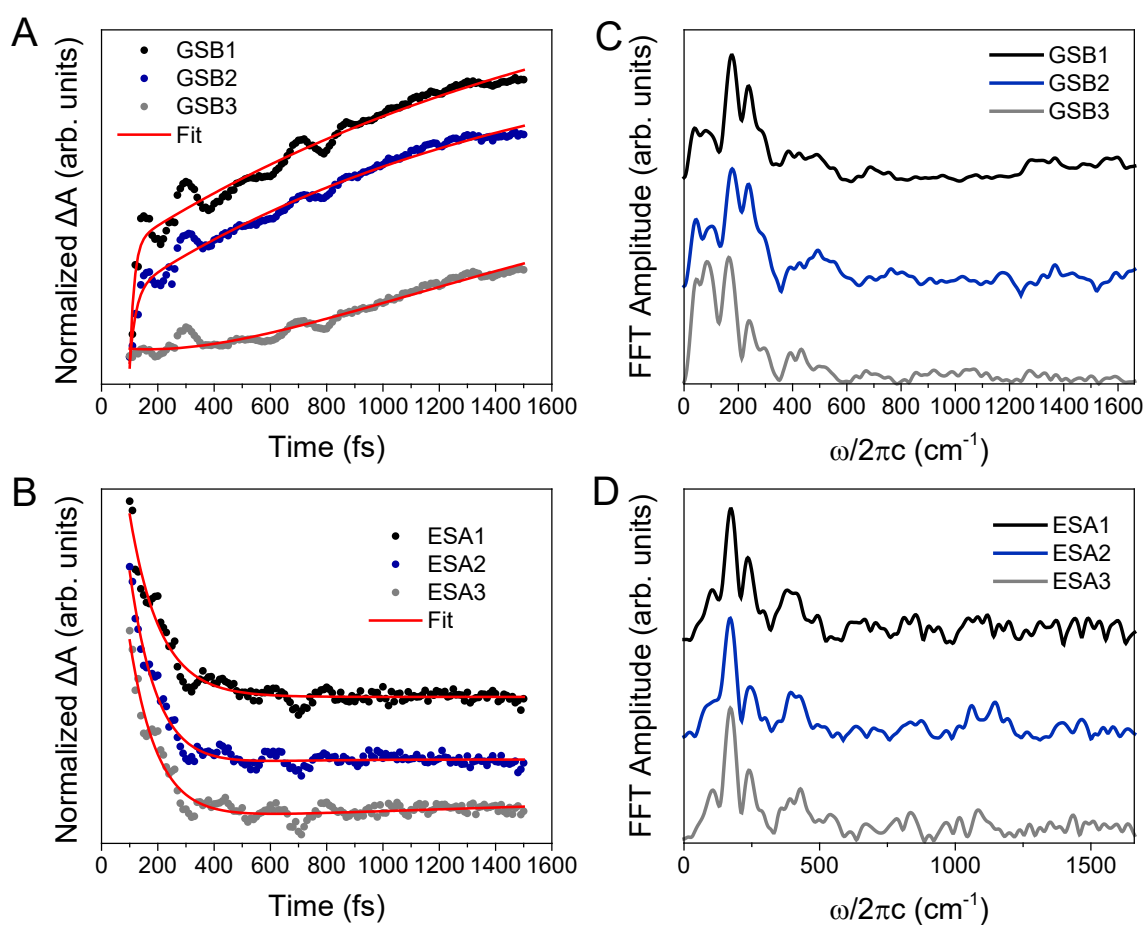
Figure S4.3. Representative (A and B) bi-exponential fits and (C and D) resultant power spectra for single (ω_1, ω_3) coordinates on the GSB/SE (top) and ESA (bottom) features for *p*-PDI.

A.6 Determination of Coulombic coupling

Simulations using a previously described Frenkel-Holstein Hamiltonian formalism[160] were conducted to estimate the dipolar coupling in these dimeric systems. Spectral linewidths were imposed by applying a Gaussian windowing function to the linear response and the absorption spectrum was obtained via a Fast Fourier transform. In these simulations, we included the primary vibration noted from the vibronic structure in the experimental absorption spectra of frequency ~1250 cm^{-1}. We first fit the monomer spectrum to extract a Huang-Rhys parameter of ~0.56. Employing these parameters in the dimer absorption spectra simulations, we calculated dipolar coupling values of ~180 and ~270 cm^{-1} for *p*-PDI and *m*-PDI, respectively. The results of these simulations are shown in comparison to the experimental absorption spectra in Figure S4.4.
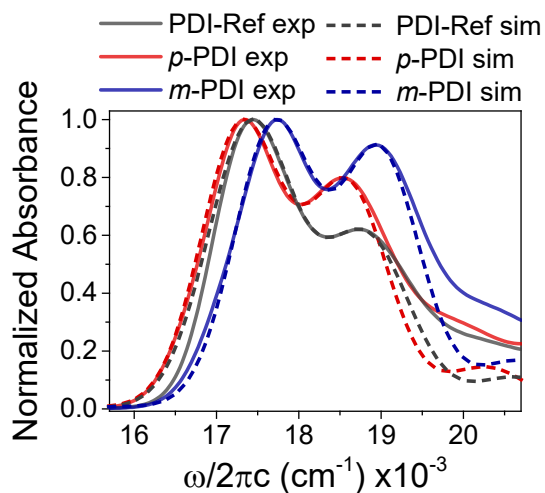
Figure S4.4. Experimental (solid) and simulated (dashed) absorption spectra for **PDI-Ref,** *p*-PDI, and *m*-PDI.

A.7. Additional two-dimensional electronic spectroscopy

Figures S4.5-S4.7 illustrate 2D spectra for **PDI-Ref**, *p*-PDI, and *m*-PDI as a function of the waiting time across the time range of interest to this work. For clarity, all 2DES spectra shown in this manuscript were smoothed with an 11th order moving average. Contours near zero signal magnitudes are suppressed for clarity. Figure S4.7 illustrates that *m*-PDI undergoes symmetry-

breaking charge transfer ($\omega_1 = 17500$ cm^{-1}, $\omega_3 = 12800$ cm^{-1}), but to a negligible amount (<5%) within the temporal window of interest to this work (1.5 ps).
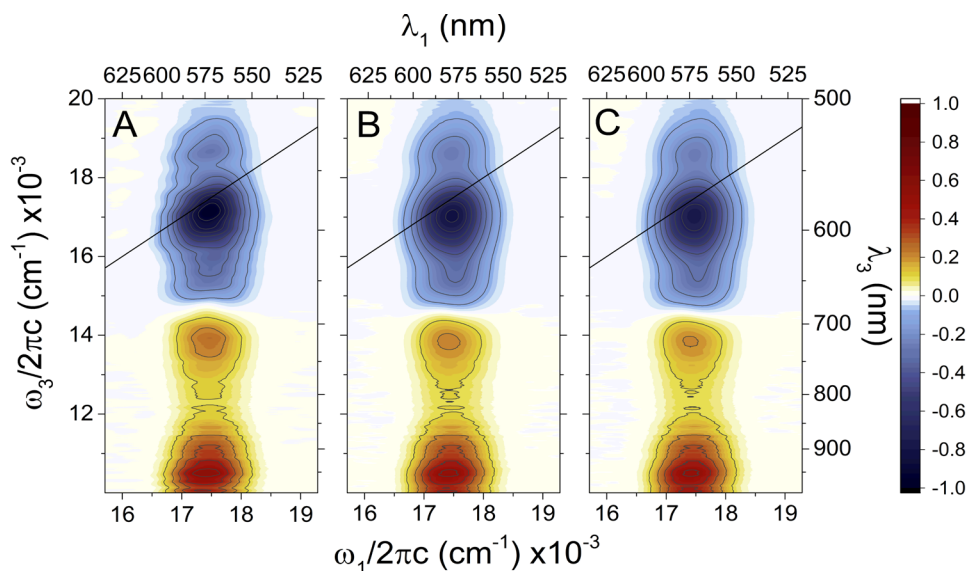
Figure S4.5. Absorptive 2DES spectra for **PDI-Ref** at waiting times of (A) 100, (B) 500, and (C) 1500 fs obtained in THF at 295 K and normalized to absolute maximum signal at 100 fs.
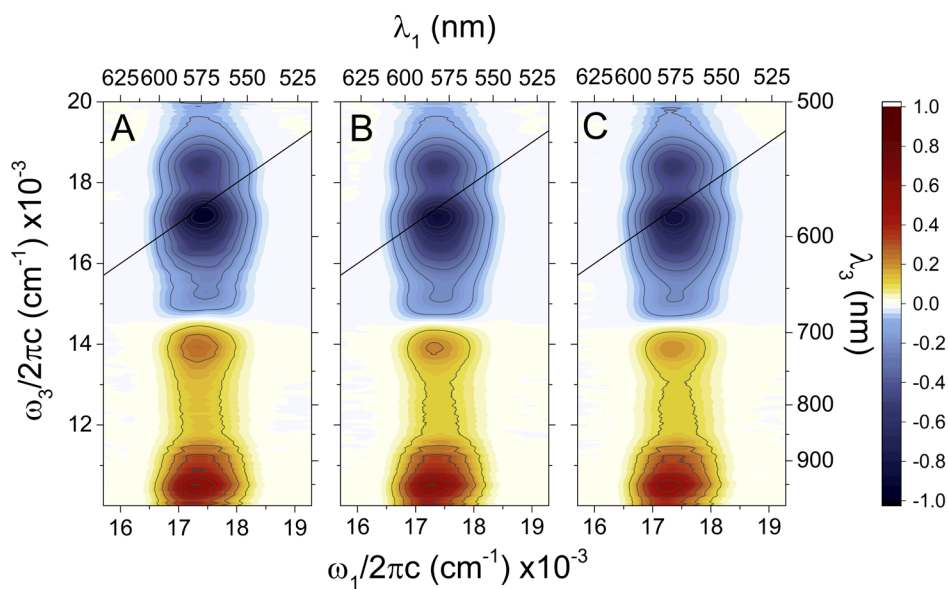
Figure S4.6. Absorptive 2DES spectra for ***p*-PDI** at waiting times of (A) 100, (B) 500, and (C) 1500 fs obtained in THF at 295 K and normalized to absolute maximum signal at 100 fs.
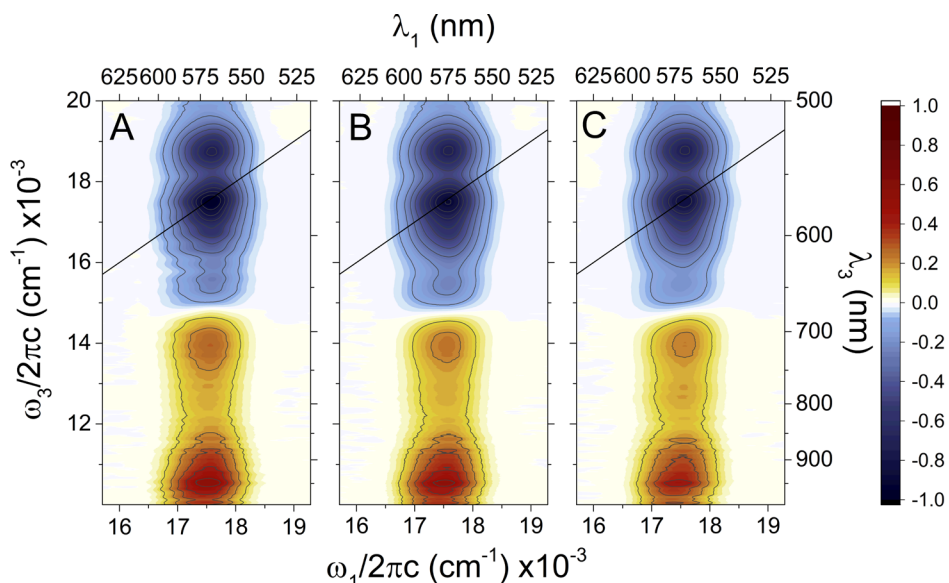
Figure S4.7. Absorptive 2DES spectra for **m-PDI** at waiting times of (A) 100, (B) 500, and (C) 1500 fs obtained in THF at 295 K and normalized to absolute maximum signal at 100 fs.

A.8 Additional quantum beating analyses

To confirm the quantum beating signatures shown in Figures 4.4 and 4.5 were not impacted by laser fluctuations and/or solvent impurities, we conducted these experiments numerous times on different days with different solvent aliquots and laser alignments. A compilation of the replicate power spectra for each compound is shown in Figures S4.8-S4.10. The data shown in the main text are from *scan 1*. Furthermore, Figure S4.11 illustrates the results from a control measurement on neat-THF using the same experimental parameters and post-processing.
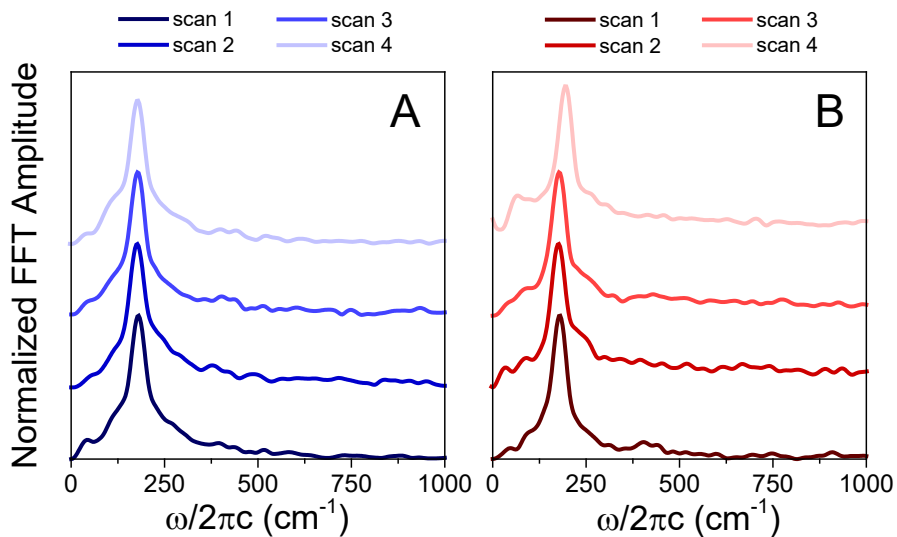
Figure S4.8. Normalized replicate Frobenius norms calculated across the **PDI-Ref** (A) GSB/SE and (B) ESA spectral features.
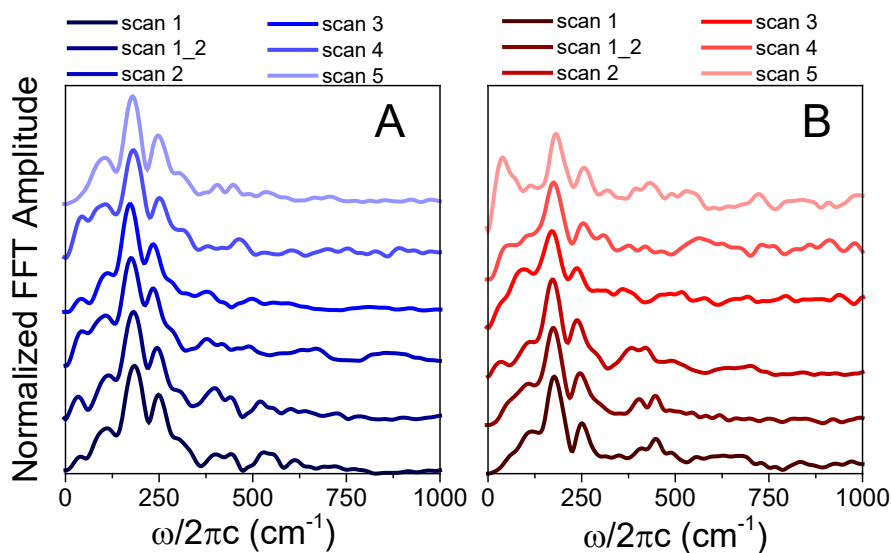
Figure S4.9. Normalized replicate Frobenius norms calculated across the *p*-**PDI** (A) GSB/SE and (B) ESA spectral features. All scans were collected on separate days, except scans 1 and 1_2 which were performed on the same day, but with different sample batches.
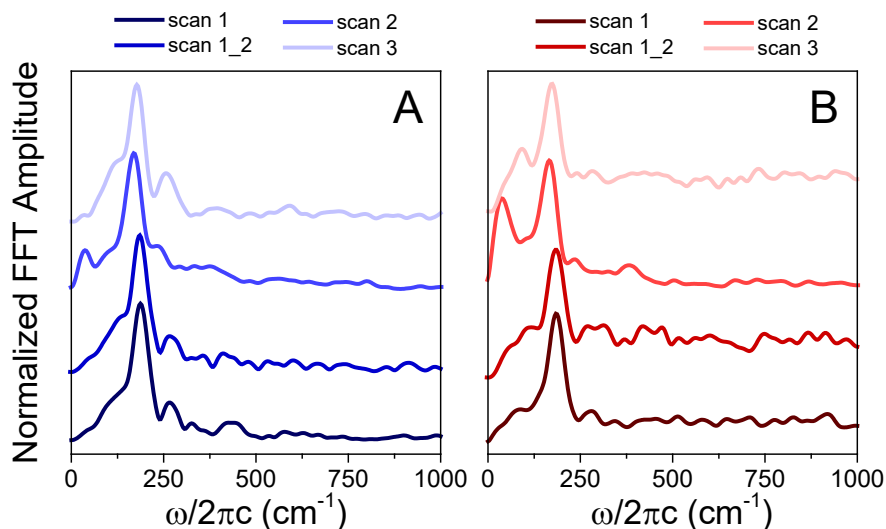
Figure S4.10. Normalized replicate Frobenius norms calculated across the *m*-PDI (A) GSB/SE and (B) ESA spectral features. All scans were collected on separate days, except scans 1 and 1_2 which were performed on the same day, but with different sample batches.
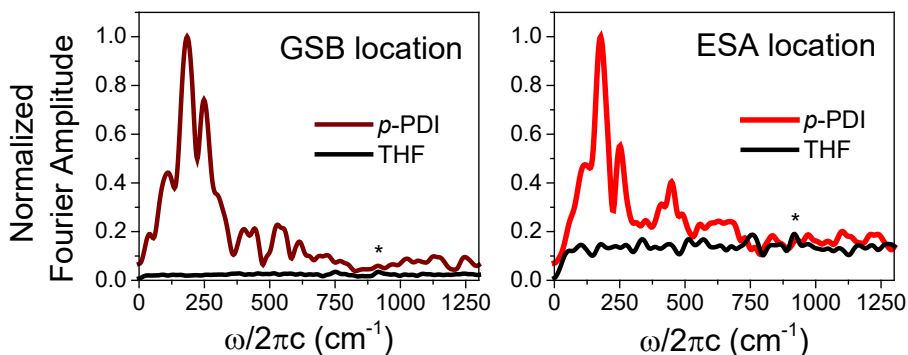
Figure S4.11. Frobenius norms calculated across the *p*-PDI (A) GSB/SE and (B) ESA region for the both *p*-PDI and the corresponding neat THF solvent scan. The power spectra are normalized to the maximum Fourier magnitude in the respective *p*-PDI power spectrum.

To investigate any influence the benzyl linker has on the power spectra in these studies, we conducted identical 2DES experiments on a monomeric compound with propyl groups on the imide positions. A direct comparison of excited-state power spectra for the monomeric compounds is shown in Figure S4.12; we observe no significant differences.
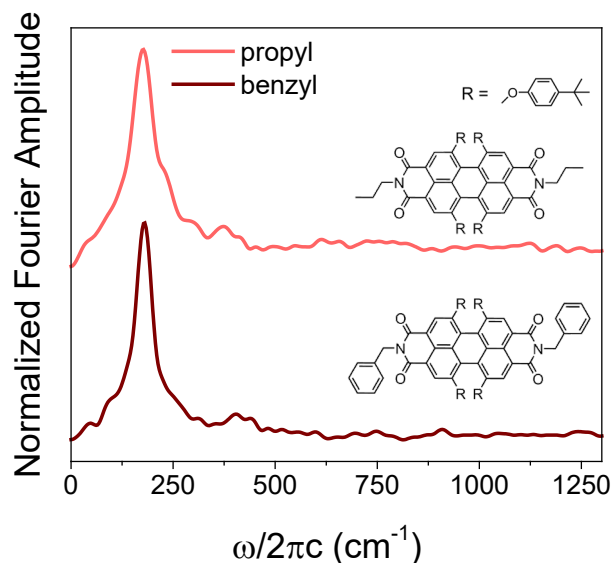
Figure S4.12. ESA Frobenius norms for the monomeric PDI control compounds.

To further confirm that the weaker quantum beating signatures around 400 cm^{-1} in these compounds was not an artifact of noise, we produced beating amplitude maps for **PDI-Ref** and **p-PDI**, as shown in Figure S4.13. For both samples, the amplitude of this frequency does not simply follow the lineshapes of the GSB and SE optical features. Instead, the peaks in the beatmaps occur at positions expected for a vibrational coherence, or vibronic in the case of the dimer. It should be noted that drawing insight about vibronic coupling from these beatmaps is complicated by the significant Stokes shift in these systems (*vide infra*), which results in the excited-state coherence amplitude smearing in the probe dimension below the diagonal. This notion is further supported by the presence of strong quantum beating near the fluorescence maximum in both compounds.
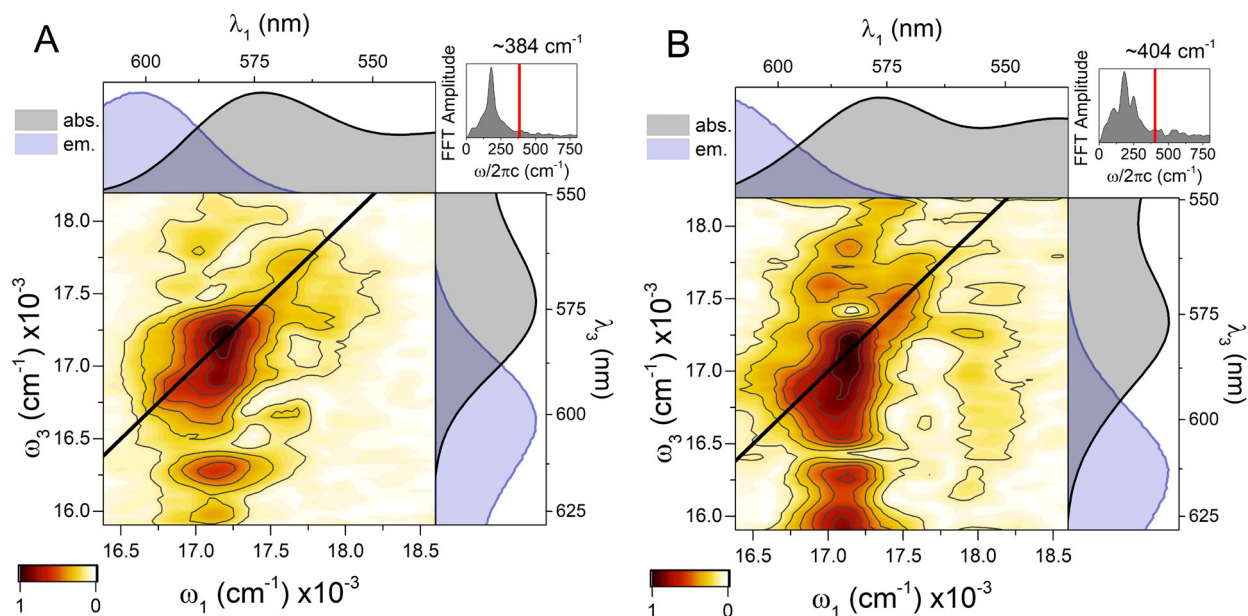
Figure S4.13. Quantum beating amplitude maps at a frequency near 400 cm^{-1} for (A) **PDI-Ref** and (B) *p*-**PDI**. Absorption and emission spectra for both compounds are included.

A.9. High-frequency coherences

To investigate influence from the resonance conditions employed for the main text experiments and any differences in high-frequency coherences in these systems, we conducted further experiments with our 2DES pump pulse centered near 18000 cm^{-1} (~555 nm) to enforce more resonance with higher-lying vibronic states. This pump spanned 17000 to 19100 cm^{-1} with a ~940 cm^{-1} FWHM. Figure S4.14 shows the spectra of the pulses employed as well as SHG-FROG characterization of the pump. All samples were prepared as described in Section 4.2.
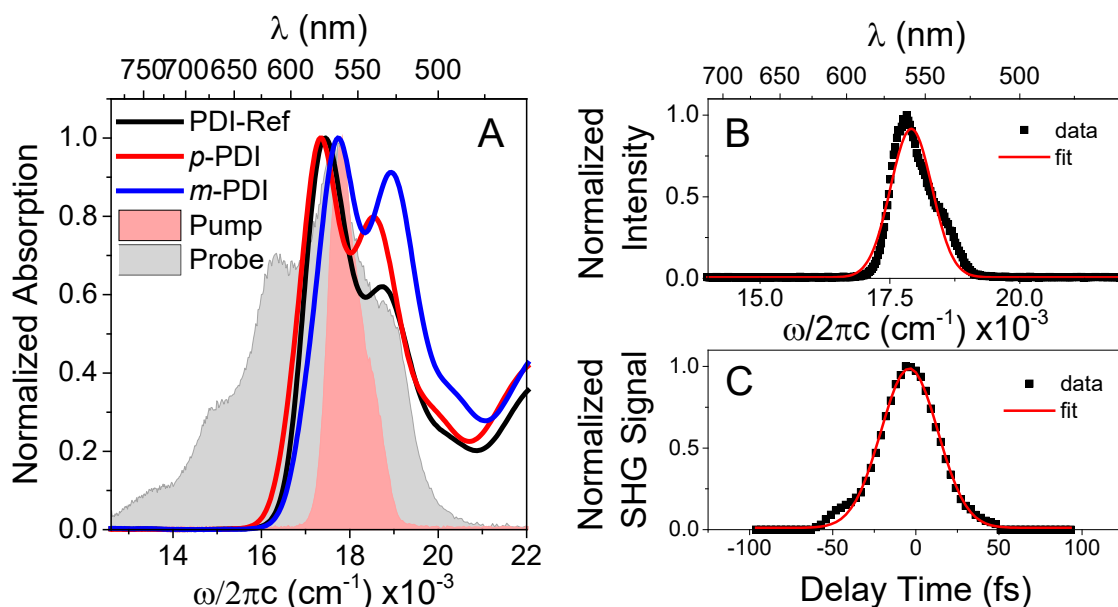
Figure S4.14. (A) Normalized steady-state absorption spectra of **PDI-Ref**, **p-PDI**, and **m-PDI** obtained in THF at room temperature. Pump and probe pulses for the 2DES measurements are superimposed. (B) Raw pump spectrum fit to a Gaussian (~940 cm^{-1} FWHM) and (C) a SHG-FROG summed across all wavelengths and fit to a Gaussian (~40 fs FWHM, corresponding to a ~28 fs pulse duration).

An identical procedure as described for the ~17540 cm^{-1} (~570 nm) 2DES pump experiments was used to obtain excited- and primarily ground-state power spectra for each compound, as shown in Figure S4.15. As mentioned in the main text, the excited-state signals cannot be completely removed from the latter. Despite increased resonance with any higher-lying vibronic states, no appreciable peaks can be observed above ~1000 cm^{-1}, with the exception of the weak peak near ~1500 cm^{-1}. All low frequency results for this experiment agree with the trends discussed in the main text and corroborate the relative enhancement of certain quantum beating signals from the **p-PDI** compound in relation to the other samples. Figure S4.16 illustrates the magnitude of these beating signals from **p-PDI** in comparison to that obtained from the corresponding spectral regions of a neat-THF 2DES blank scan.
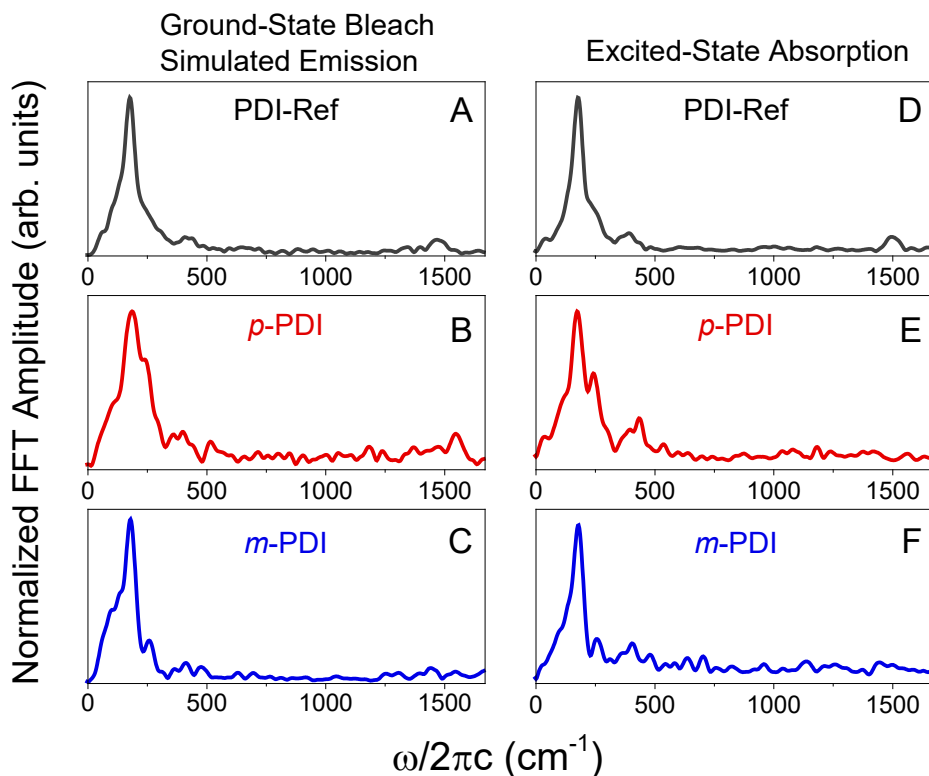
Figure S4.15. Frobenius norms calculated in the frequency domain across a 300 x 400 cm^{-1} region on the (A-C) GSB/SE feature near the diagonal and (D-F) the higher energy $S_n \leftarrow S_1$ ESA feature for each system listed.
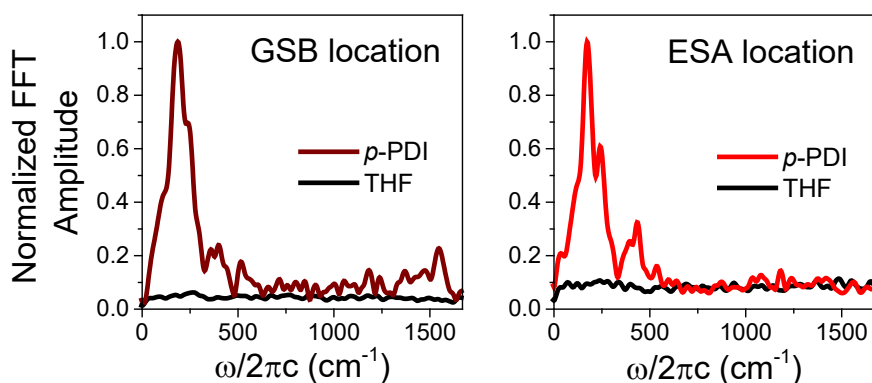
Figure S4.16. Frobenius norms calculated across the *p*-PDI (A) GSB/SE and (B) ESA region for the both *p*-PDI and neat THF pumped at 18000 cm^{-1}. The power spectra are normalized to the maximum Fourier magnitude in the respective *p*-PDI power spectra.

A.10. Frobenius norm region selection

Frobenius norms are used here to avoid bias in selecting a region of the 2D spectrum to analyze coherences as well as for improving the signal-to-noise ratio. All frequency-domain

Frobenius norms span 400 and 300 cm^{-1} in the pump and probe dimensions, respectively, and cover

~350 points in the 2D maps. These regions were selected to be located near the maximum beating

amplitude of the ~430 cm^{-1} oscillation since a signature near this frequency was observed in all of

these compounds, whereas the common ~180 cm^{-1} oscillation shows very broad features in the

frequency amplitude domain and complicates selection of the center. In cases where the signal-to-

noise ratio for this mode was too low, we centered the Frobenius norm near the ~250 cm^{-1} feature

amplitude maximum. In principle, all of these coherence frequencies should have similar

maximum amplitude coordinates within data for each respective compound. Figure S4.17

illustrates representative time- and frequency-domain spectra for *p*-PDI with the norm regions

superimposed. Similar Frobenius norms conducted in the time domain are shown in Figure 4.4A-

C, but these traces were constructed over a region containing only ~18 points (centered at the

specified coordinates) to avoid destructive interference of the time-domain oscillations.
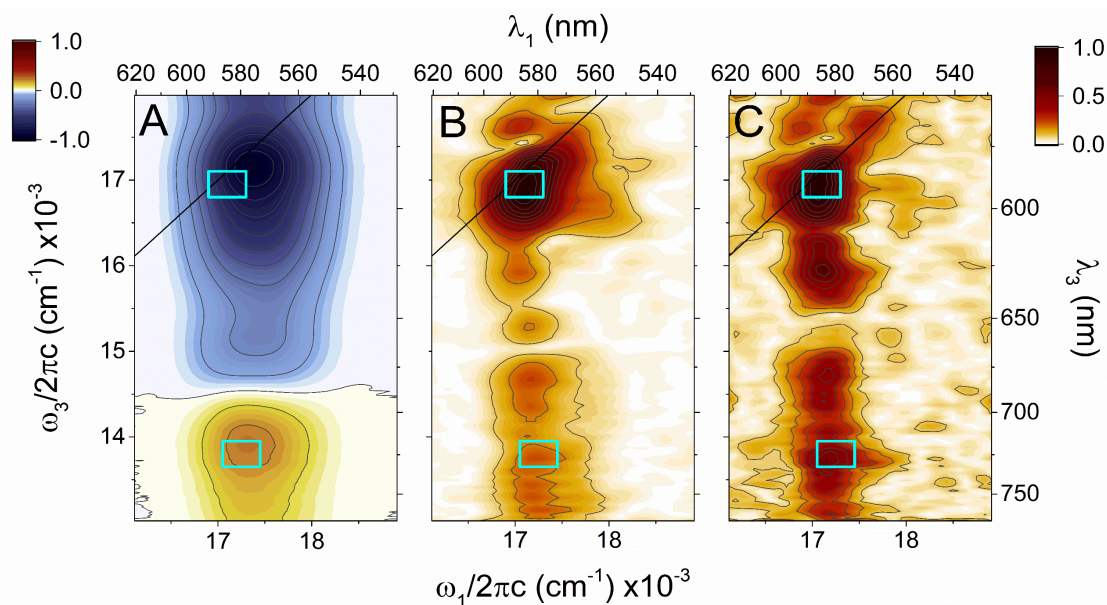
Figure S4.17. (A) Time-domain and (B and C) frequency-domain spectra illustrating region selection for Frobenius norms for *p*-PDI. The frequency amplitude maps reflect the magnitude of oscillatory signals near (B) 257 and (C) 439 cm^{-1}. Cyan rectangles indicate the approximate regions over which the coherence analysis was performed.

A.11. Influence from the dynamic Stokes shift

Figure S4.18 shows a closer comparison of the absorption and fluorescence spectra for **PDI-Ref, *p*-PDI**, and ***m*-PDI**. Stokes shifts of ~850, ~1000, and ~1200 cm^{-1}, respectively, are observed. In order to understand how the coherences on the ground versus excited state will manifest themselves in the frequency-domain beatmaps due to this shift, we characterized the timescale of the dynamic Stokes shift in **PDI-Ref**. Considering that the excited-state coherences stem from coherently produced wavepackets, theory predicts a π phase flip where the wavepacket traverses the minimum of the excited-state potential energy surface.[146, 354] This node in the signal can be used to characterize the timescale of the Stokes shift.[145, 355] Figure S19D shows the oscillatory residuals for **PDI-Ref** after removing the population dynamics from a transient absorption dataset using a function containing two exponential terms convoluted with a Gaussian. The phase jump and amplitude node for the intense ~180 cm^{-1} mode is clearly seen near 16500 cm^{-1} (607 nm). However, at the earliest time point shown, the node is located near 16950 cm^{-1} (590 nm), which is the initial vertical energy between the ground state and the displaced excited state. The node transiently shifts and arrives at its final position after ~150 fs. This shift directly represents the timescale of the dynamics Stokes shift for **PDI-Ref** in THF at room temperature. The origin of this rapid shift is likely inertial solvent dynamics.[145, 355] In the dimers, this is convoluted with relaxation between exciton states.[227]
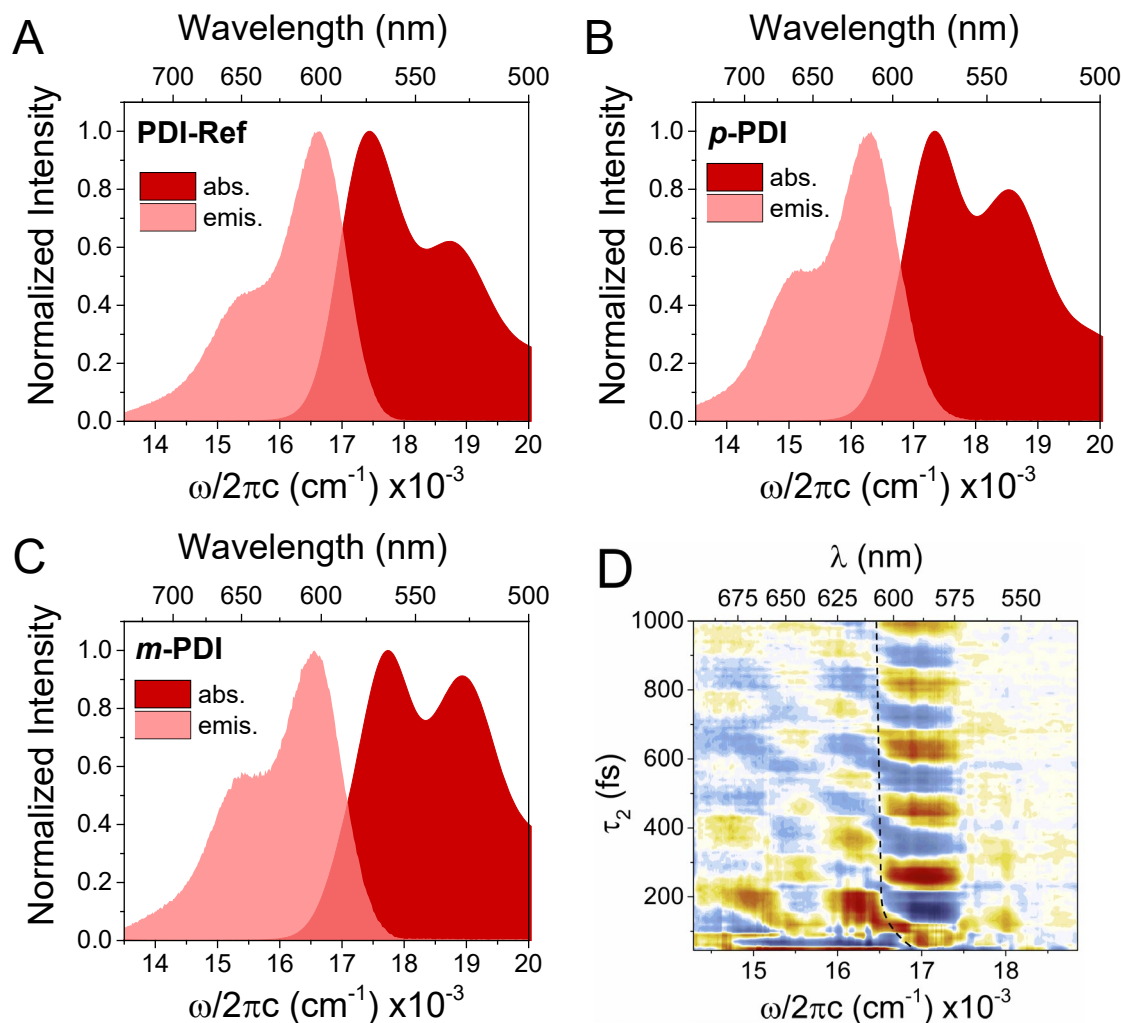
Figure S4.18. Comparison of absorption and fluorescence spectra for (A) **PDI-Ref**, (B) **p-PDI**, and (C) **m-PDI** in THF at room temperature and (D) residuals from a transient absorption scan of **PDI-Ref** post removal of population dynamics. The superimposed dotted line illustrates the approximate location of the amplitude node in the oscillatory signals.

A.12. Additional femtosecond stimulated Raman spectroscopy details and data

Calibration of the CCD array for all FSRS data was performed with at least four neat solvent peaks (DCM, DMF, and THF) and the Rayleigh line. The ground-state FSRS spectra presented in Figure 4.5D-F were obtained via dispersing onto the CCD array with a 2400 gr/mm grating and averaging 100 one-second exposures. Broad optical absorption baselines were

removed via a cubic fit. The spectra were smoothed with adjacent averaging over a 7-point range for clarity.

Figure S4.19 compares cubic baseline-subtracted, unsmoothed, and unnormalized FSRS spectra for each compound compared to that of neat-THF.
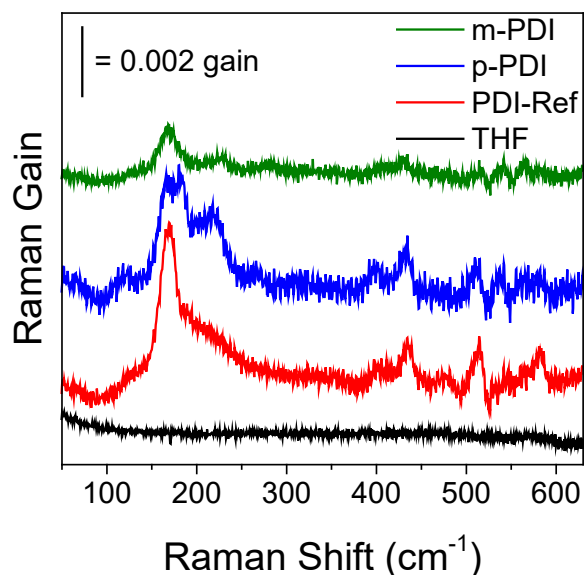
Figure S4.19. Unnormalized and unsmoothed FSRS spectra for **PDI-Ref**, *p*-**PDI**, and *m*-**PDI** in THF at room temperature compared to that of neat-THF.

We conducted excited-state time-resolved FSRS on all three of the compounds studied here to complement the power spectra extracted from the 2DES ESA features (Figure 4.4D-F). Figure S4.20 shows FSRS spectra 0.5 ps after photoexcitation via a 573 nm actinic pump. The 710 nm Raman pump here minimizes resonance with stimulated emission while maximizing that with the higher energy $S_n \leftarrow S_1$ transition in these compounds. Raw data were collected using a 1200 gr/mm grating. The spectra in Figure S4.20 were each generated by averaging 100 one-second exposures, subtracting the corresponding -5 ps trace, removing the broad transient absorption background with a spline fit, and adjacent averaging over a 3-point range for clarity. Despite the

lower signal-to-noise ratio, the peak trends between **PDI-Ref**, *p*-**PDI**, and *m*-**PDI** mostly follow those observed in the 2DES ESA power spectra (Figure 4.4D-F).
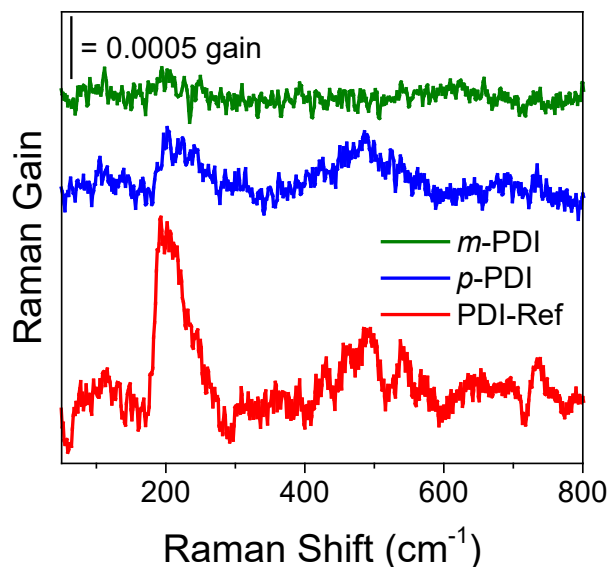
Figure S4.20. Unnormalized time-resolved FSRS spectra for **PDI-Ref**, *p*-**PDI**, and *m*-**PDI** in THF at room temperature 0.5 ps after photoexcitation.

A.13. Normal mode analysis

Figure S4.21A illustrates the computed Raman frequency spectrum from the **PDI-Ref** DFT normal mode analysis. The spectrum was broadened (Gaussian FWHM = 10 cm^{-1}) for ease of comparison to the experimental data and the frequency axis is scaled in accordance with our choice of basis set (x0.96). Figure S4.21B-D provide further depictions of the nuclear motions potentially associated with the peaks observed via 2DES and FSRS. However, the lack of inclusion of the resonance condition in these calculations complicates precise assignment of these modes.
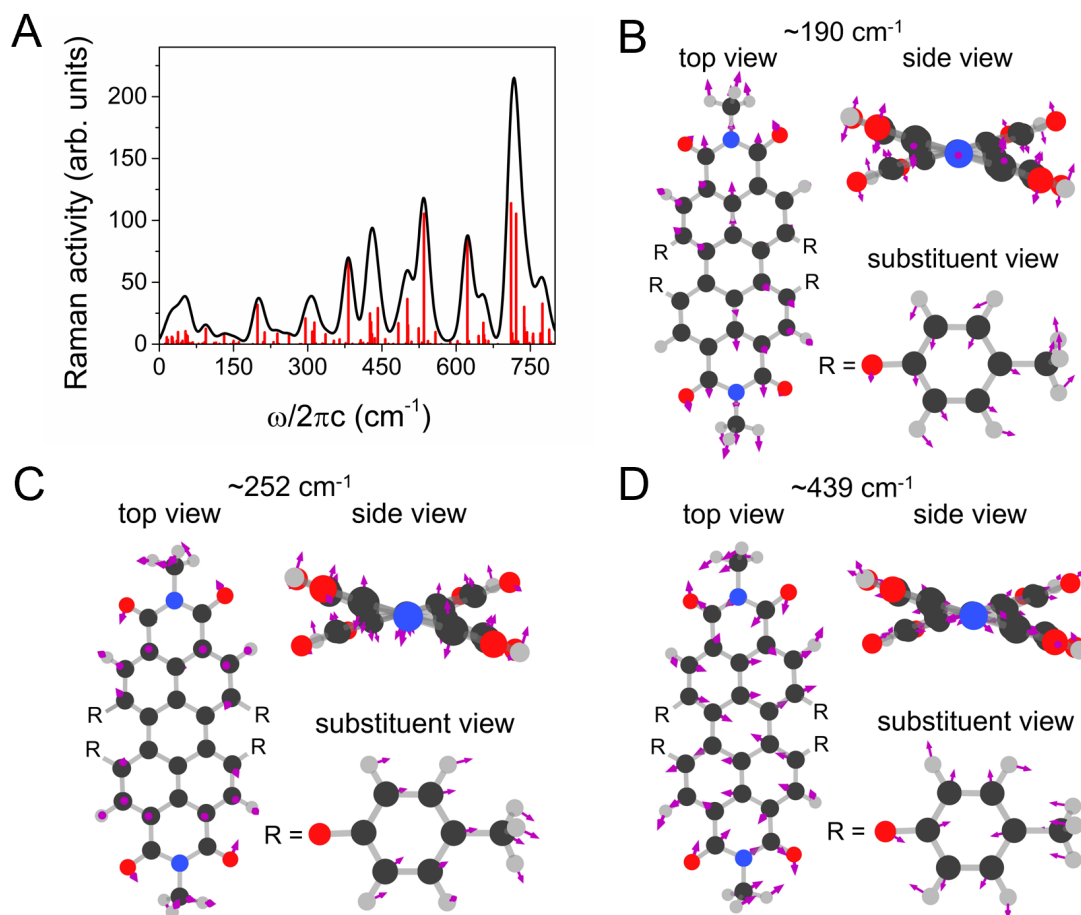
Figure S4.21. (A) Computed Raman spectrum for **PDI-Ref** and nuclear motions associated with vibrational frequencies of (B) ~190, (C) ~252, and (D) ~439 cm^{-1} (scaled by 0.96).

A.14. Computed Values

Table 4.5.1 PDI-Ref, methyl on phenoxy group instead of tert-butyl

ATOM	X	Y	Z					
O	2.16803	-5.6741	-0.70312		C	-0.004	-1.41988	-0.00723
O	-2.19034	-5.67213	0.67877		C	-0.00879	-2.84321	-0.00712
O	2.19415	5.67703	0.6616		C	1.16486	-3.54984	-0.34993
O	-2.16824	5.67678	-0.70759		C	-1.24019	-0.71089	0.14285
O	-3.42461	0.75858	-1.08321		C	-2.35331	-1.43907	0.61051
O	-3.42923	-0.73202	1.07166		C	-2.32501	-2.84297	0.69225
O	3.43219	0.73686	1.06366		C	-1.1879	-3.53994	0.33551
O	3.42485	-0.75684	-1.08777		C	-1.20376	-5.02052	0.35997
N	-0.01821	-5.67232	-0.00926		C	1.17712	-5.03209	-0.37909
N	0.02012	5.6761	-0.02042		C	1.24197	0.71498	0.13905
C	2.30638	-2.85939	-0.70644		C	0.00557	1.42372	-0.00984
C	2.34446	-1.45581	-0.62459		C	-1.23548	0.72282	-0.15637
C	1.23678	-0.71922	-0.15757		C	2.3561	1.44387	0.60321
					C	2.32845	2.84798	0.68138

C	1.19045	3.54425	0.32587		H	-0.82991	-7.49137	-0.68799
C	0.01035	2.84705	-0.01239		H	0.92307	-7.49596	-0.31174
C	-1.16415	3.55309	-0.35365		H	-7.10221	2.8777	0.60784
C	-2.30648	2.86204	-0.70656		H	-7.05568	1.83702	-3.55902
C	-2.34401	1.45859	-0.62261		H	-4.76409	0.89958	-3.29148
C	1.20663	5.02491	0.34688		H	6.99522	1.8697	3.61513
C	-1.1764	5.03531	-0.38537		H	7.14294	2.84953	-0.56384
C	0.05833	7.14176	-0.0165		H	4.88136	1.87436	-0.87263
C	-0.05612	-7.13797	-0.00198		H	-4.86533	-1.87483	-0.87068
C	-4.66886	1.37076	-1.20228		H	-7.13088	-2.84163	-0.57789
C	-5.31877	1.92206	-0.0966		H	7.09996	-2.88296	0.60093
C	-6.59656	2.45154	-0.25565		H	4.8329	-1.91318	0.869
C	-7.24735	2.43388	-1.49874		H	4.76184	-0.90325	-3.29724
C	-6.57317	1.86558	-2.58508		H	7.04795	-1.852	-3.56814
C	-5.28801	1.3379	-2.44772		H	4.71789	0.91425	3.30282
C	4.67496	1.34879	1.2026		H	-4.8302	1.92057	0.87225
C	5.26375	1.33775	2.4654		H	-7.02165	-1.83307	3.59564
C	6.53951	1.87531	2.62752		H	-4.73815	-0.88587	3.29916
C	7.23915	2.43027	1.54721		H	-0.29852	-7.49675	1.00138
C	6.62027	2.42682	0.29072		H	0.30265	7.50282	0.98558
C	5.34798	1.88613	0.10688		H	8.94145	3.57954	0.86162
C	-7.24226	-2.41823	1.53376		H	9.36828	2.20611	1.88923
C	-4.6727	-1.34358	1.2053		H	8.67381	3.65939	2.60978
C	-5.3384	-1.88601	0.10575		H	9.13311	-2.64659	-2.54164
C	-6.61262	-2.42107	0.28072		H	8.55025	-4.14632	-1.81191
C	7.24049	-2.44787	-1.5068		H	9.23793	-2.88325	-0.78883
C	6.59388	-2.4568	-0.26222		H	-9.07593	2.74122	-2.61514
C	5.31859	-1.92039	-0.10126		H	-8.60765	4.11842	-1.61026
C	4.66817	-1.37095	-1.20683		H	-9.3034	2.68098	-0.85992
C	5.28553	-1.34271	-2.45392		H	-9.23221	-2.89405	0.82185
C	6.56737	-1.87653	-2.59304		H	-9.14054	-2.58655	2.5646
C	-6.55397	-1.85336	2.61416		H	-8.54388	-4.11048	1.90002
C	-5.27349	-1.32059	2.46072					
C	-8.63061	3.02183	-1.65555					
C	8.62607	3.00034	1.73512					
C	-8.61195	-3.03026	1.71444					
C	8.61262	-3.05903	-1.67117					
H	3.17183	-3.41862	-1.0392					
H	-3.1942	-3.39717	1.02387					
H	3.19865	3.40288	1.00917					
H	-3.17284	3.42047	-1.03842					
H	0.83093	7.49339	-0.70474					
H	-0.92136	7.49926	-0.32524					

Table 4.5.2. PDI-Ref, Raman frequencies

FREQUENCY (CM⁻¹)	RAMAN ACTIVITY (ARB. UNITS)				
11.79	0.356	333.19	0.175	725.22	2.115
13.81	0.801	336.03	7.949	737.59	30.203
15.04	5.642	351.58	0.488	738.21	13.663
17.33	3.645	352.85	2.731	743.36	4.09
25.41	5.986	364.35	3.864	743.42	9.629
26.79	5.103	376.84	0.699	748.3	0.908
28.03	1.852	382.26	67.775	755.15	6.135
35.31	2.705	390.28	0.303	755.75	8.489
37.77	9.793	405.04	0.72	756.38	2.771
43.75	0.996	406.94	3.239	770.28	3.899
46.93	2.744	412.14	1.09	770.56	8.706
52.88	10.495	421.44	0.769	774.58	32.697
54.67	7.681	425.97	24.822	788.18	11.744
56.31	4.598	427.78	11.996	791.82	1.368
57.2	6.49	428.13	17.7	797.41	0.144
58.99	1.198	428.48	7.697	818.85	2.018
62.47	0.447	429.42	4.621	823.46	14.248
65.15	0.97	430.07	8.062	843.51	19.876
67.69	1.373	435.51	4.798	843.69	16.007
79.36	0.299	441.75	29.197	845.9	10.861
86.83	0.504	456.84	4.022	846.59	0.249
91.67	1.785	463.2	0.238	848.62	10.889
92.51	0.471	472.92	0.235	849.2	0.511
94	12.377	483.36	16.976	851.6	63.012
110.73	0.948	498.57	0.68	857.1	0.201
114.59	1.21	501.47	36.474	859.5	3.438
121.68	0.244	502.85	15.236	863.52	135.148
131.13	6.835	509.95	2.001	888.74	25.707
132.51	0.16	524.25	12.823	894.91	2.233
135.5	0.019	530.92	1.255	915.45	7.835
143.52	0.007	535.05	105.404	924.6	135.253
149.09	1.247	542.4	0.456	925.4	6.336
150.18	2.678	543.17	2.568	925.66	61.844
155.47	0.3	548.16	0.183	926.34	3.802
160.82	1.523	558.22	9.746	957.12	4.998
188.99	0.093	570.21	0.108	958.21	3.491
198.61	31.696	588.3	1.766	959	1.626
210.08	1.714	602.98	2.481	960.33	1.973
212.89	9.521	607.95	0.16	965.44	1.171
230.83	1.663	622.87	83.77	966.47	2.74
238.6	8.538	625.94	2.41	966.6	0.785
241.82	0.156	645.47	6.694	966.92	3.254
262.14	7.759	645.92	2.795	997.54	95.046
283.9	0.064	655.08	17.233	998.59	70.438
287.16	0.069	656.49	7.434	1019.74	4.068
295.52	20.763	657.91	3.571	1020.18	2.279
309.34	10.198	658.74	3.241	1021.39	2.253
312.18	2.438	665.29	2.562	1021.71	2.711
313.61	17.427	684.39	0.074	1022.5	3.274
316	0.768	711.05	113.849	1039.57	4.431
329.41	0.485	713.48	8.711	1039.94	1.641
		718.28	1.782	1040.21	9.566
		718.98	2.433	1040.6	1.65
		721.4	105.417	1043.83	26.067

1066.41	0.145	1372.88	8.001	1649.87	1237.739
1076.18	1.044	1382.9	8.158	1669.22	42.833
1076.21	1.098	1384.81	9299.586	1669.76	565.362
1076.45	0.364	1392.88	270.085	1670.5	60.287
1079.98	1.486	1423.89	743.917	1670.69	598.306
1092.72	202.514	1434.06	12.837	1737.94	31.797
1141.54	0.699	1445.02	52.112	1738.03	215.902
1141.61	8.118	1445.85	43.832	1770.08	2.396
1142.05	0.615	1446.3	99.504	1773.35	1514.181
1142.21	2.442	1447.05	81.834	3042.6	254.888
1147.83	10.03	1449.62	37.341	3043.19	123.445
1153.4	4.968	1452.81	50.157	3043.22	520.902
1157.39	3.624	1455.12	19.829	3043.98	357.377
1159.83	515.341	1457.53	172.82	3087.49	75.188
1165.84	3.913	1457.86	55.97	3087.56	510.651
1165.86	3.165	1459.82	1149.911	3097.7	112.61
1201.11	2.019	1460.33	36.941	3097.97	102.102
1201.33	10.138	1462.58	72.65	3099.99	100.135
1202.17	5.861	1471.74	3.067	3100.72	101.974
1203.33	97.345	1485.06	2132.431	3126.85	62.223
1204.08	5.687	1516.84	26.048	3127.19	79.735
1222.41	85.447	1517.64	25.713	3127.56	29.793
1223.12	1.195	1518.24	26.056	3127.62	110.609
1238.6	5.293	1519.13	27.725	3149.79	106.931
1238.9	3.437	1523.92	26.388	3149.85	99.177
1239.42	0.471	1523.96	23.345	3183.96	127.488
1239.93	92.277	1525.67	14.267	3185.92	148.414
1245	71.82	1525.78	25.937	3185.94	103.252
1247.89	1.417	1525.89	35.851	3186.36	122.855
1254.87	13.364	1526.93	23.785	3187.06	94.715
1258.71	45.757	1529.77	19.56	3187.46	87.443
1259.95	531.334	1529.81	134.659	3187.7	111.237
1280.5	379.672	1553.56	30.367	3190.56	93.635
1309.97	176.475	1553.76	5.397	3213.45	38.691
1317.22	26.738	1555.4	5.324	3213.47	43.586
1319.46	415.373	1559.86	175.179	3217.08	73.95
1324.51	35.487	1561.42	36.756	3217.82	80.94
1337.18	10.742	1561.91	2.96	3218.13	56.405
1338.51	347.091	1581.21	7853.347	3218.17	72.382
1339.29	5.188	1605.52	3.649	3221.85	65.662
1339.45	6.45	1632.19	51.564	3221.9	78.078
1348.54	18.006	1633.22	72.85	3222.42	34.104
1348.97	12.852	1641.41	2232.713	3222.71	40.026
1349.11	82.654	1641.92	2843.171	3249.48	79.754
1349.6	37.873	1643.53	70.546	3249.57	114.413
1350.82	9.741	1644.04	709.425	3249.85	91.019
1366.13	314.704	1644.78	57.289	3250.25	97.696

Appendix B: Supplementary Information for Chapter 5

B.1. Linear and two-dimensional electronic spectroscopy

Solutions of each analyte (less than 150 μM) in chlorobenzene were prepared with optical densities ranging from 0.2 to 0.5 in glass cuvettes with a 1 mm pathlength. The 2DES experiments conducted for this work employed pump pulses centered near 16650 cm^{-1} (600 nm), spanning approximately 4000 cm^{-1} baseline-to-baseline (Figure S5.1). These pulses were 21 fs in duration, as characterized by SHG-FROG (Figure S5.2). The pump and probe were parallel in polarization and the pump energy at the sample was 8 nJ/pulse. 2DES spectra as a function of the inter-pump time delay (t_1) were collected in the rotating frame with a rotation frequency of 13500 cm^{-1} from $t_1 = 0$ to 189 fs with a 3 fs step size for the data discussed in the main text. Scan-specific changes in these parameters are outlined below when applicable. Data were averaged between 2500 and 7500 laser cycles for each 2D spectrum. To evaluate quantum beating signatures, a series of spectra were collected as a function of t_2. This delay was scanned with a range of small waiting timesteps (5, 7, 8, and 10 fs) for laboratory noise analysis (*vide infra*). Experiments were conducted several times on different days with different solvent aliquots to ensure results were not correlated to laser fluctuations or solvent impurities.

B.2. Laser pulse characterization
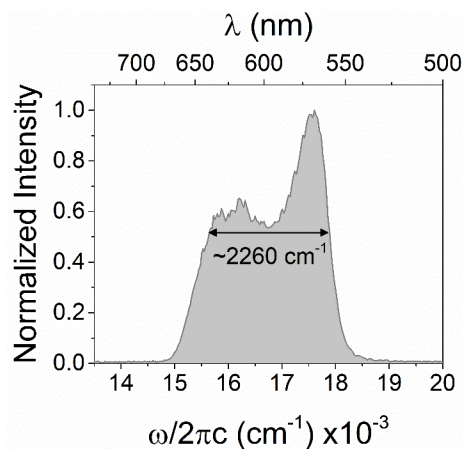
Figure S5.1. A typical pump pulse spectrum. The approximate width at half of the maximum pulse intensity is 2260 cm^{-1}. The baseline-to-baseline coverage is approximately 3720 cm^{-1}.

Figure S5.1 shows a typical chirp-corrected pulse spectrum, centered at 16650 cm^{-1} (600 nm) with a 2260 cm^{-1} full-width at half-maximum (FWHM). Example SHG-FROG traces are provided in Figure S5.2A and B. The measured pulse width of the 2DES pump pulse was approximately 21 fs.
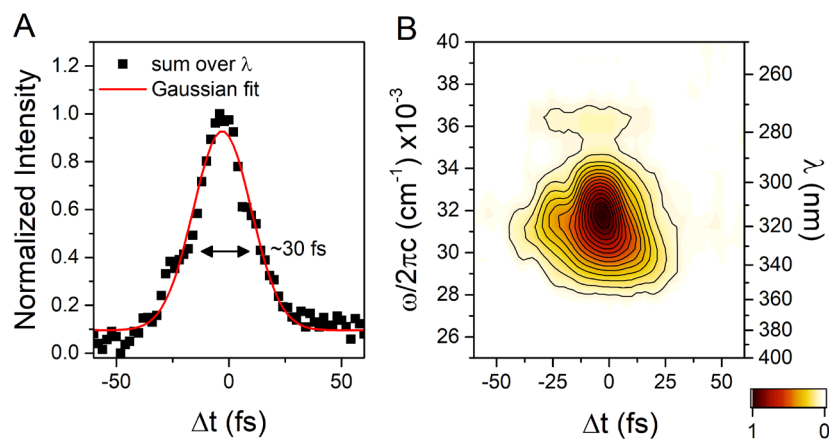
Figure S5.2. (a) SHG-FROG trace of the typical pump pulse employed in these experiments and (b) the summation of the FROG data over the wavelength dimension overlaid with a Gaussian fit (FWHM = 30 fs). The pulse duration was thus approximately 21 fs.

PG-FROG measurements were performed to determine the frequency-dependent instrument response function between the pump and probe pulses under similar experimental
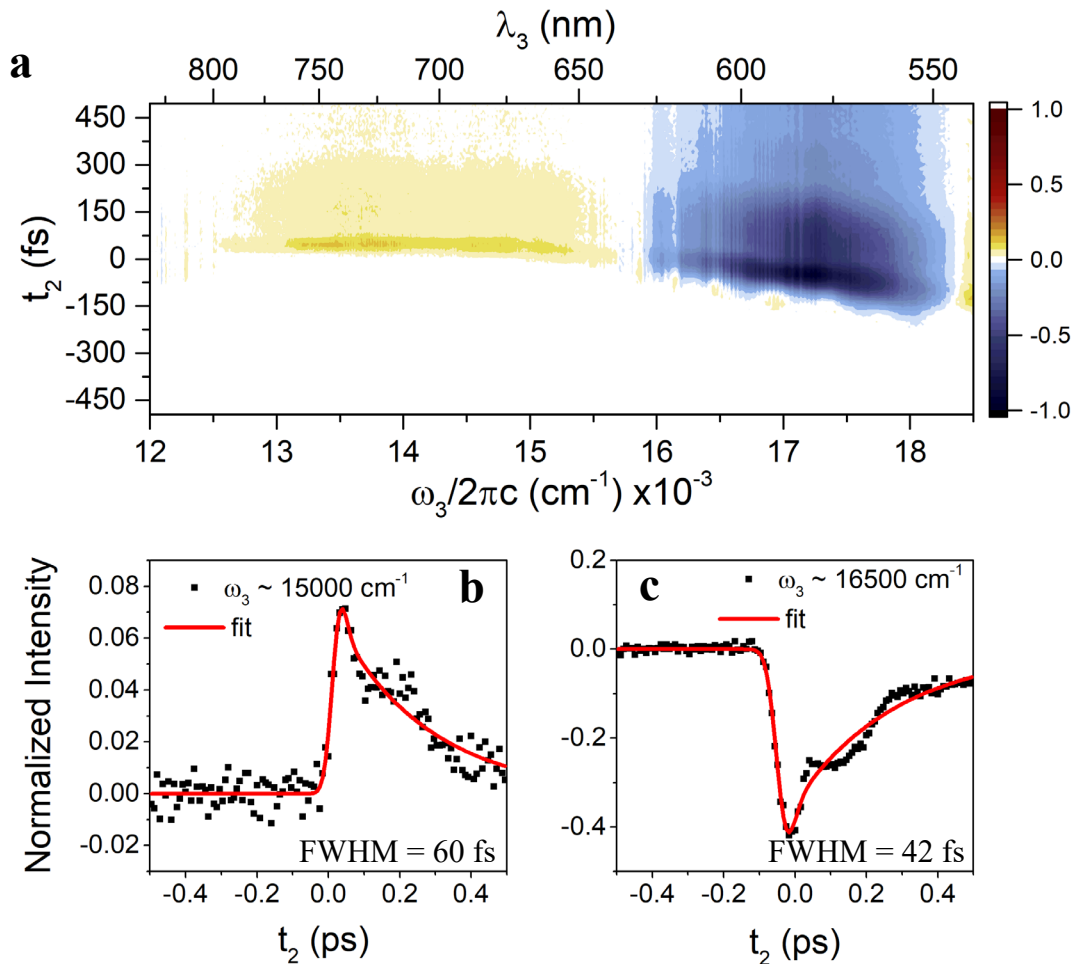
Figure S5.3. (a) Normalized PG-FROG signal across the probe range of interest in this work and time-domain slices near (b) $\omega_3 = 15000$ and (c) $\omega_3 = 16500$ cm^{-1} with the corresponding Gaussian-exponential convolution fits (FWHM of 60 and 42 fs, respectively) superimposed.

conditions to those shown in the main text. Both the pump and probe beams were spatially and temporally overlapped in a 1 mm cuvette filled with neat chlorobenzene solvent. Figure S5.3A and B show the PG-FROG signal (pre-time zero signal subtracted) obtained for the regions of interest to the molecular systems in this study. Fitting the data near $\omega_3 = 15000$ and 16500 cm^{-1} to a gaussian response convoluted with a single exponential, which captures the average quantum beating that ensues beyond gaussian response, we extracted instrument response function (IRF) values of 60 and 42 fs, respectively.

B.3. Femtosecond Stimulated Raman Spectroscopy (FSRS)

Calibration of the CCD array for all FSRS data was performed with at least four neat solvent peaks (DCM, DMF, and THF) and the Rayleigh line. Broad optical absorption baselines were removed via a cubic fit.

B.4. Computational details

All DFT calculations were performed using the Amsterdam Density Functional software package. To lower the computational cost, the C15 swallowtail end groups were substituted with methyl units. Resonance Raman cross sections were computed using the BP86 functional with a DZP basis set in vacuo. Prerequisites to this calculation were geometry optimization and normal mode analysis outputs, where we employed the latter to gauge the accuracy of the former based on the condition of no high-frequency (> 100 cm^{-1}) imaginary modes. To combat the presence of these modes, we scaled the system geometry by an arbitrary percentage of the imaginary mode motion and re-conducted the geometry optimization and frequency analysis. To compute the electronic structure of **TDI$_1$** and **TDI$_2$** in chlorobenzene, we employed the ωb97X-D functional with a DZP basis set. We accounted for solvation effects by using the SOLVENT command in ADF with dielectric and radius values of 5.62 and 3.54 Å, respectively. S_1 and T_1 energies in both the monomeric and dimeric systems were determined by TDDFT vertical excitation energy calculations from the optimized ground-state geometries.

B.5. Data Analysis

To avoid contamination from cross-phase modulation at early times, we cut each vector in the t_2 dimension to near $t_2 = 90$ fs prior to fitting population dynamics (approach 1 in Section 2.5.3). We employed three exponential functions here to capture rapid, sub-200 fs dynamics, likely

stemming from inertial solvent response and SF, in the case of **TDI$_2$**, as well as longer relaxation processes occurring on the order of >1 ps. Example time-domain data, fits, isolated quantum beats, and resulting power spectra averaged over a 40 × 40 cm^{-1} window within the magenta rectangles in Figure 5.2 in the main text are shown in Figure S5.4. Generation of 2DES spectra in the frequency domain for the pump (ω_1) and probe (ω_3) axes requires Fourier transformation of the data with respect to the coherence time delay, which is performed using an in-house MATLAB package described in Section 2.5.
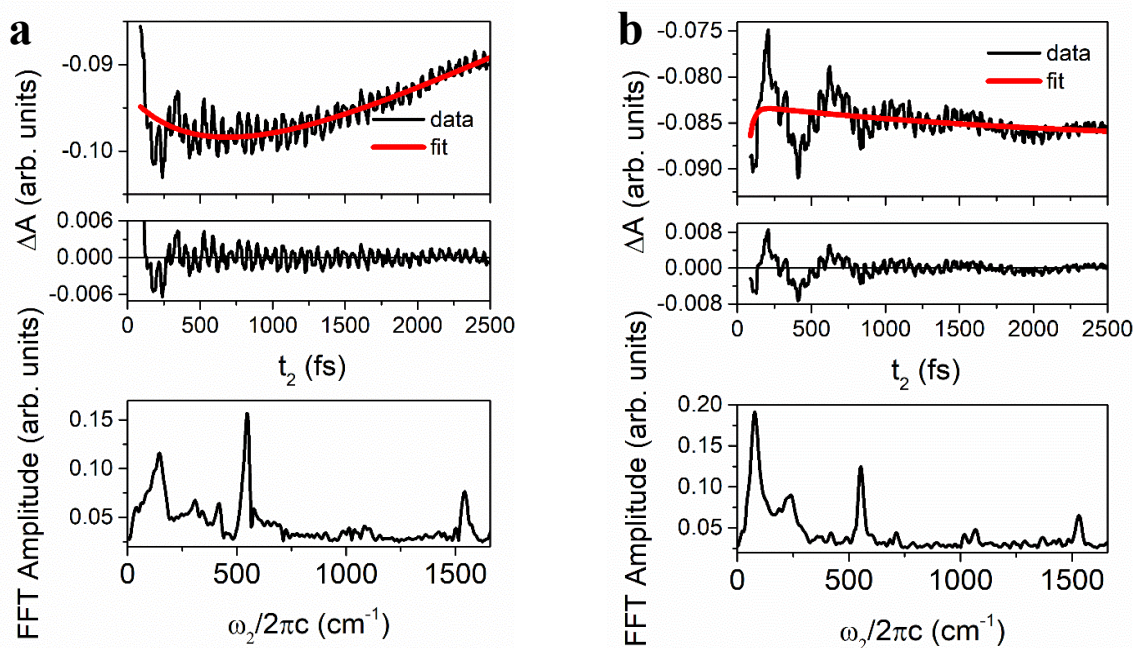
Figure S5.4. Time domain data and multiexponential fit (top panel), isolated quantum beat signals (middle panel), and the frequency power spectrum (bottom panel) for (a) **TDI$_1$** and (b) **TDI$_2$**. These data were averaged over a 100 x 100 cm^{-1} window within the regions highlighted by magenta rectangles in Figure 5.2.

After isolation from population kinetics, Fourier analysis of quantum beating traces with respect to the population time follows a similar procedure for that of the coherence time delay and are zero-padded to a length of 2^{10}. Since data between $t_2 = 0$ and near-90 fs are truncated, we offset

the data within the padded vector by a corresponding number of zeros to ensure no systematic frequency shifts when comparing datasets. For the data discussed in the main text, the unpadded data traces range from 88 to 2504 fs with a timestep of 8 fs, which yields a frequency resolution of about 14 cm^{-1} in the Fourier power spectra. Frequency resolutions for replicate scans are discussed below. To remove bias in representation of the quantum beat signals, all power spectra presented here were calculated by performing frequency-domain Frobenius norms on 400×400 cm^{-1} windows in the pump and probe dimensions. These power spectra thus capture quantum beats within this entire region of the data.

B.6. Time-dependence of two-dimensional electronic spectra

Figures S5.5-S5.6 illustrate 2D spectra for **TDI$_1$** and **TDI$_2$**, respectively, at additional waiting times for the dataset shown in Figure 5.2 in the main text. Prior to plotting, all 2DES spectra in this work were smoothed with an 11th order moving average, arcsinh scaled after amplifying the signals by a factor of 100, and normalized to their respective absolute value change in ΔA. Contours are displayed at 10% intervals unless otherwise stated.
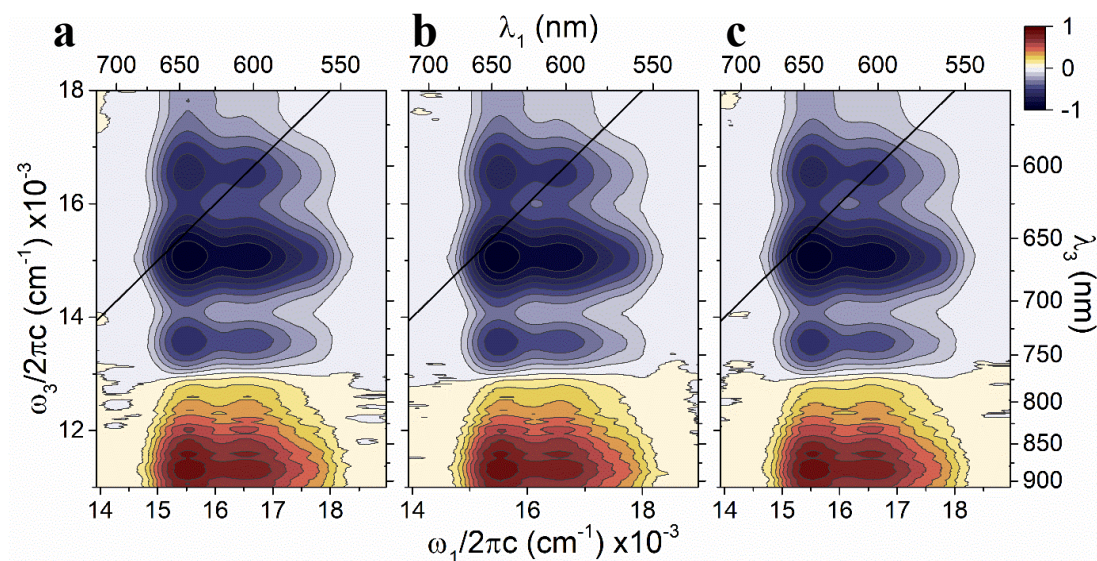
Figure S5.5. 2DES spectra for **TDI₁** in room-temperature chlorobenzene at waiting times of approximately (a) 9.8 ps, (b) 80 ps, and (c) 155 ps.
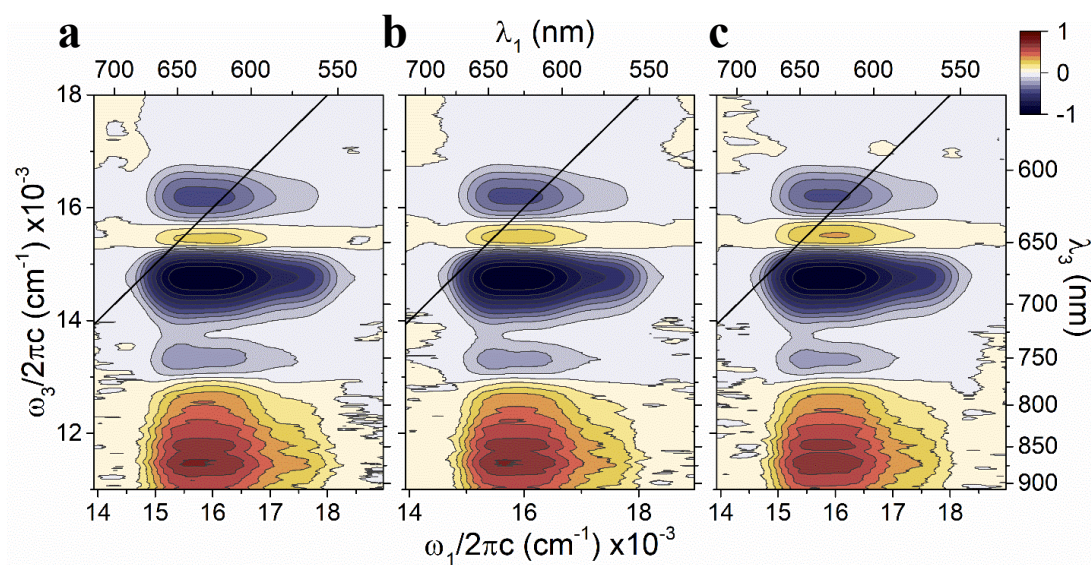
Figure S5.6. 2DES spectra for **TDI₂** in room-temperature chlorobenzene at waiting times of approximately (a) 9.8 ps, (b) 80 ps, and (c) 155 ps.

B.7. Quantum beating control measures

We performed a control 2DES measurement on neat, room temperature chlorobenzene to distinguish impulsively excited solvent Raman modes from the coherences probed from the analytes. Figure S5.7 compares the Frobenius norms for **TDI$_2$** compared to the corresponding norm for neat chlorobenzene, generated using the same procedure as described above over similar (ω_3, ω_1) coordinates. The power spectra are normalized to the common peak near 730 cm^{-1}. This comparison indicates that the quantum beating features discussed in this work indeed originate from the **TDI$_1$** and **TDI$_2$** analytes.
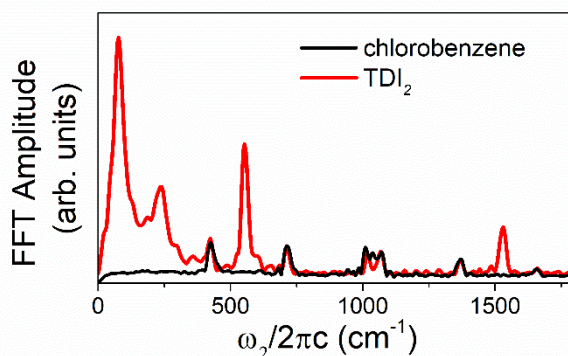
Figure S5.7. Power spectra calculated for **TDI$_2$** and neat chlorobenzene. Spectra are normalized to the solvent feature near 730 cm^{-1}.

As an additional control measure, we performed 2DES experiments on **TDI$_1$** and **TDI$_2$** with several different waiting time step sizes. This procedure offers a method of determining true analyte features, as compared to peaks originating from laboratory noise. As the step size increases in magnitude, noise features will be detected at lower frequencies, while real analyte features will remain nearly constant in frequency (within the resolution of the ω_2 dimension). Power spectra from these experiments are shown in Figure S5.8. We find the signals below approximately 1050 cm^{-1} are attributable to real quantum beat signatures from both analytes and chlorobenzene solvent,

while a persistent noise feature is present in the high-frequency regime. Since we do not observe strong analyte signals above 1050 cm^{-1}, we restrict the x-axes of our power spectra here and in the main text to exclude the feature originating from laboratory noise.
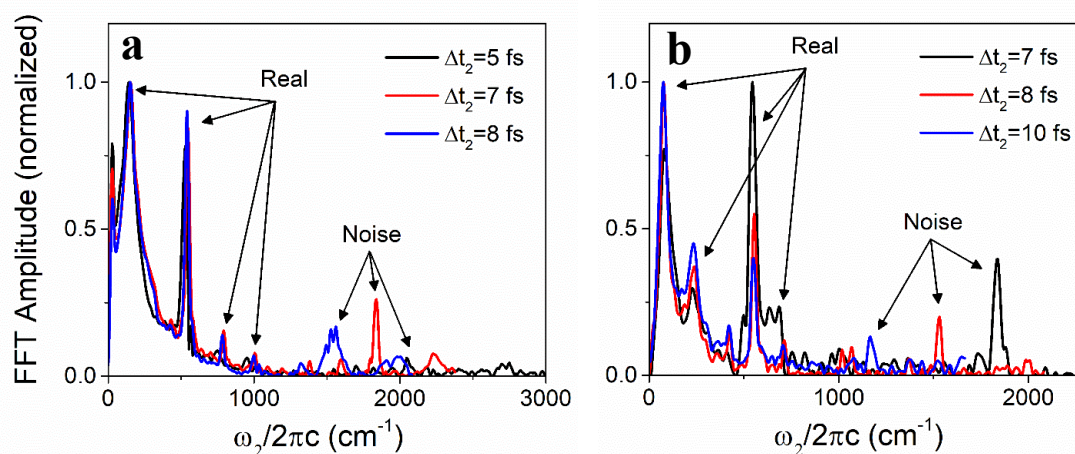
Figure S5.8. Comparison of power spectra for (a) **TDI$_1$** and (b) **TDI$_2$** at several waiting time step sizes. Peaks with frequencies not significantly dependent on the time step are indicated as "real," while features that shift substantially are identified as "noise."

B.8. Replicate quantum beating analyses

To confirm the quantum beating signatures we observed were not impacted by laser fluctuations and/or solvent impurities, we conducted replicate measurements on different days with different solvent aliquots and beamline alignments. Any notable differences in experimental parameters are provided in Table 5.1. In addition to the datasets discussed in the main text (Figure 5.3), Figure S5.9 shows replicate power spectra for both compounds with several different waiting time step sizes. While the relative amplitudes of the features somewhat vary, the peak frequencies remain robust across datasets for both compounds. Using these datasets in conjunction with those presented in the main text, we tabulated average values and standard deviations for the peak frequencies of interest, which are shown in Table 5.2. We find that the standard deviation for each

peak is less than the minimal frequency resolution of the ω_2 dimension (Table 5.1), which we

accordingly assign as the primary source of uncertainty in the peak frequencies.
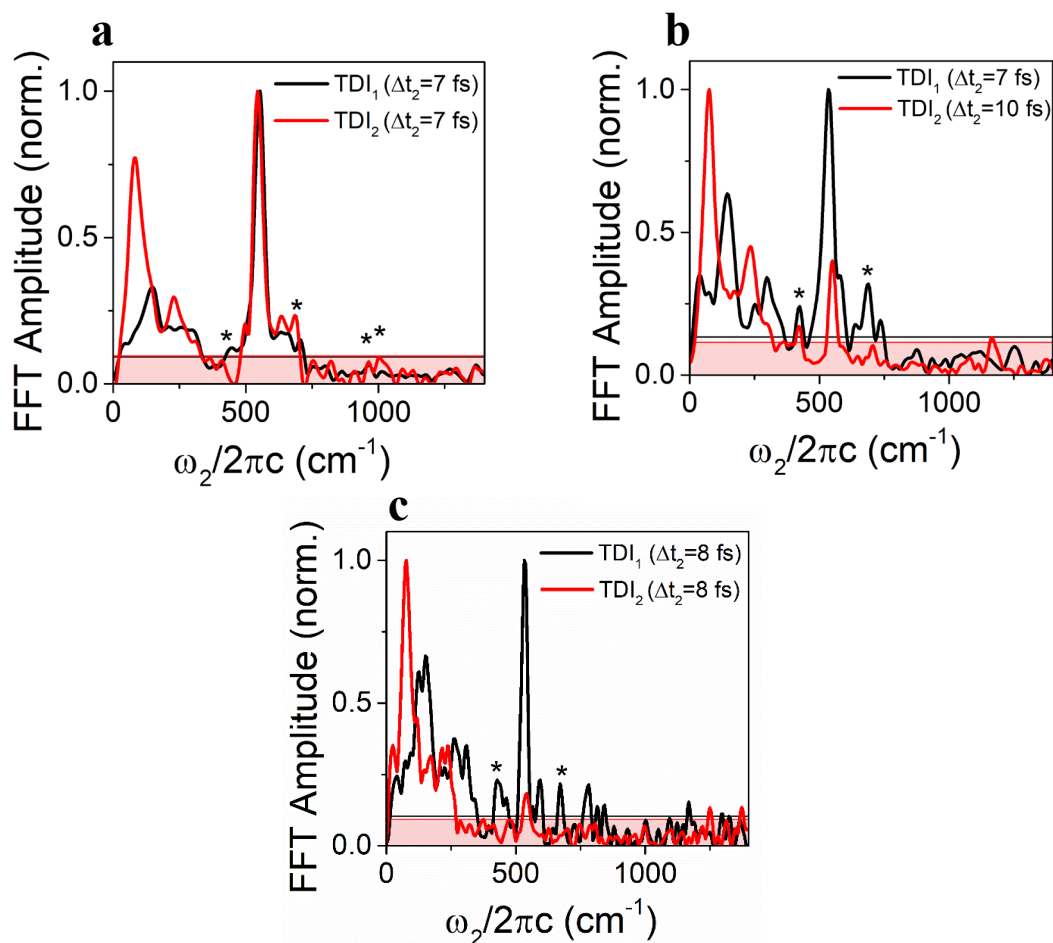
Figure S5.9. Replicate 2DES power spectra for both compounds at waiting time step sizes of (a) 7 fs, (b) 7 and 10 fs for **TDI₁** and **TDI₂**, respectively, and (c) 8 fs. Solvent peaks are marked with asterisks. Additional data-specific experimental parameters are given in Table 5.1.

Table 5.1. Notable differences in experimental parameters for each of the datasets presented in Figure S5.9.

Figure # (sample name)	Rotating frame (cm^{-1})	Δt_1 (fs)	Final t_1 value (fs)	Δt_2 (fs)	Final t_2 value (fs)	$\omega_2/2\pi c$ resolution (cm^{-1})	Phase cycling scheme
S5.9a (**TDI$_1$**)	14000	4	280	7	1505	23	1
S5.9a (**TDI$_2$**)	14000	4	280	7	1505	23	1
S5.9b (**TDI$_1$**)	14800	4	300	7	1505	23	2
S5.9b (**TDI$_2$**)	14200	4	300	10	2000	17	1
S5.9c (**TDI$_1$**)	13500	3	93	8	2504	14	2
S5.9c (**TDI$_2$**)	13500	3	93	8	2504	14	2

Table 5.2. Statistical results for the four quantum beating datasets presented for both **TDI$_1$** and **TDI$_2$**.

TDI$_1$ mean frequency ± std. dev. (cm^{-1})	**TDI$_2$** mean frequency ± std. dev. (cm^{-1})
148 ± 3	78 ± 3
304 ± 4	234 ± 3
542 ± 9	548 ± 5

Figures S5.10 and S5.11 show the corresponding replicate beatmaps for the data shown in Figure S5.9a and S5.9c. Our observation of additional quantum beating intensity near the $^1(T_1T_1)$ ESA feature in the **TDI$_2$** data as compared to that of **TDI$_1$** remains consistent across replicate measurements and different waiting time step sizes (Δt_2 = 7 and 8 fs).
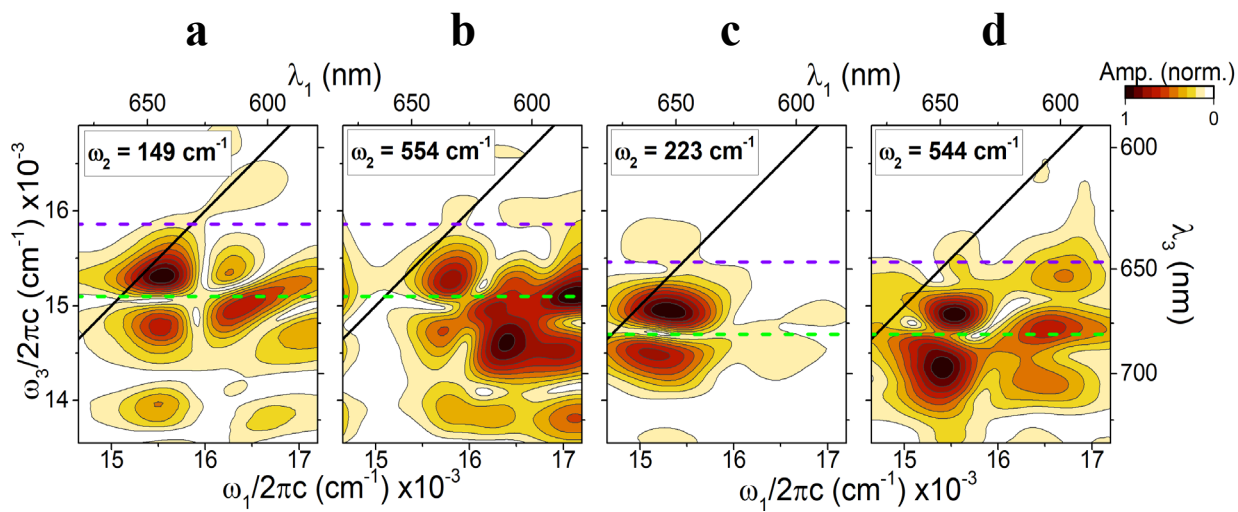
Figure S5.10. Replicate quantum beatmaps for **TDI$_1$** for the (a) 149 and (b) 554 cm^{-1} and **TDI$_2$** at for the (c) 223 and (d) 544 cm^{-1} oscillation frequencies. These beatmaps are calculated from the datasets shown in Figure S9a. The frequency-domain data were smoothed with a 11th order moving average for clarity. Green and purple dashed lines indicate the probe frequencies that correspond to the (0-0) S$_1$ ← S$_0$ and ^{1}(T$_n$T$_1$) ← ^{1}(T$_1$T$_1$) transition energies, respectively.
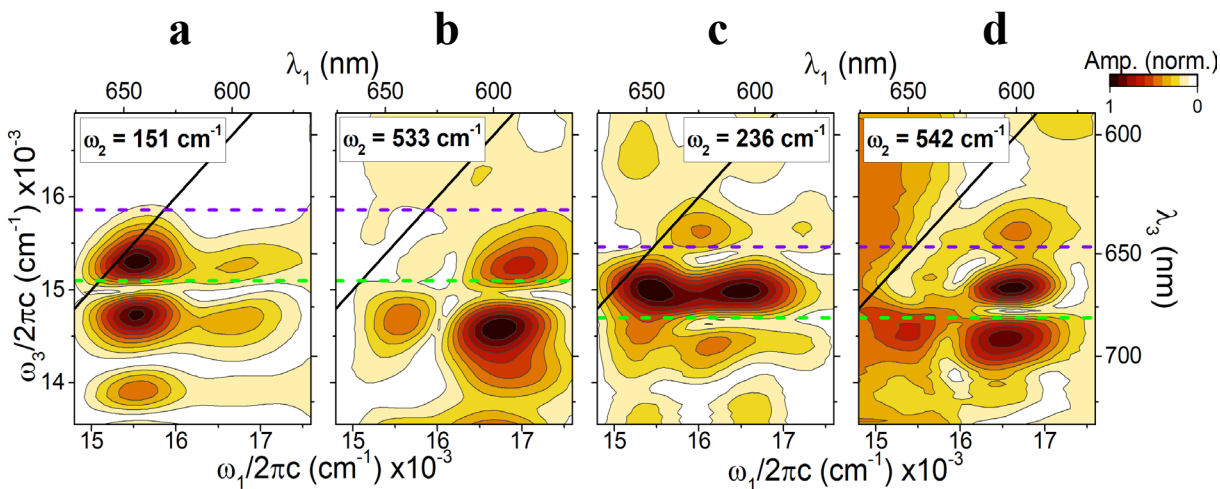
Figure S5.11. Replicate quantum beatmaps for **TDI$_1$** for the (a) 151 and (b) 533 cm^{-1} and **TDI$_2$** at for the (c) 236 and (d) 542 cm^{-1} oscillation frequencies. These beatmaps are calculated from the datasets shown in Figure S5.9c. The frequency-domain data were smoothed with a 7th order moving average for clarity. Green and purple dashed lines indicate the probe frequencies that correspond to the (0-0) S$_1$ ← S$_0$ and ^{1}(T$_n$T$_1$) ← ^{1}(T$_1$T$_1$) transition energies, respectively.

B.9. Replicate early-time two-dimensional electronic spectra

Figures S5.12 and S5.13 show example replicate 2DES spectra for both compounds at

obtained with Δt_2 = 7 and 8 fs, respectively.
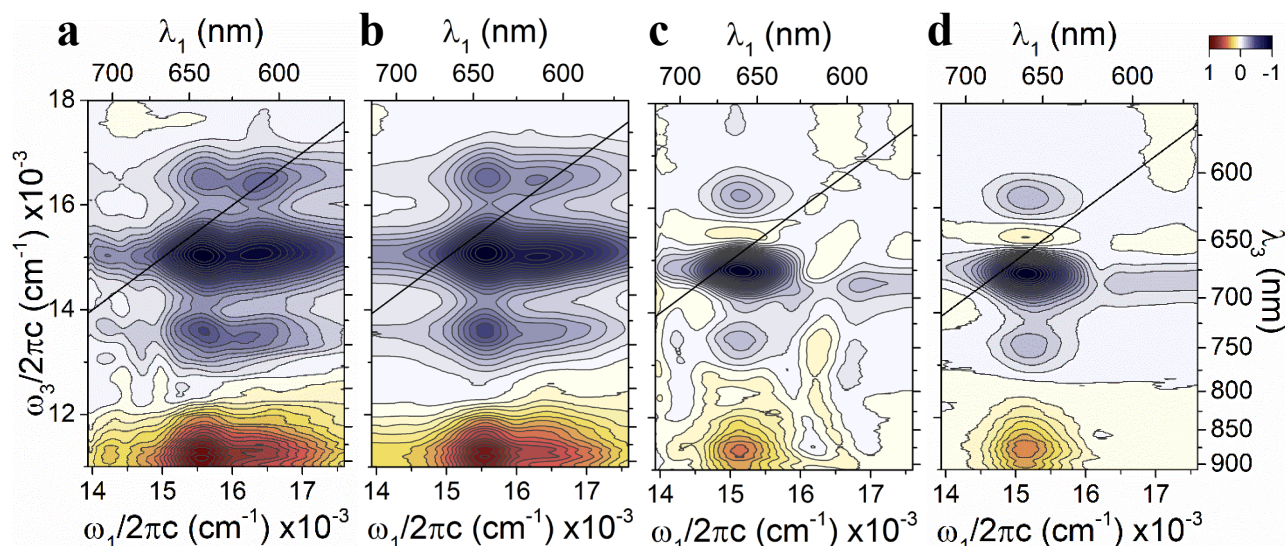
Figure S5.12. Replicate 2DES spectra for **TDI₁** at a waiting time of (a) 84 fs and (b) 1.5 ps and **TDI₂** at a waiting time of (c) 84 fs and (d) 1.5 ps using a 7 fs waiting time step size and a pulse alignment independent from the other measurements. Contours are displayed at 5% intervals to clarify weaker signals.
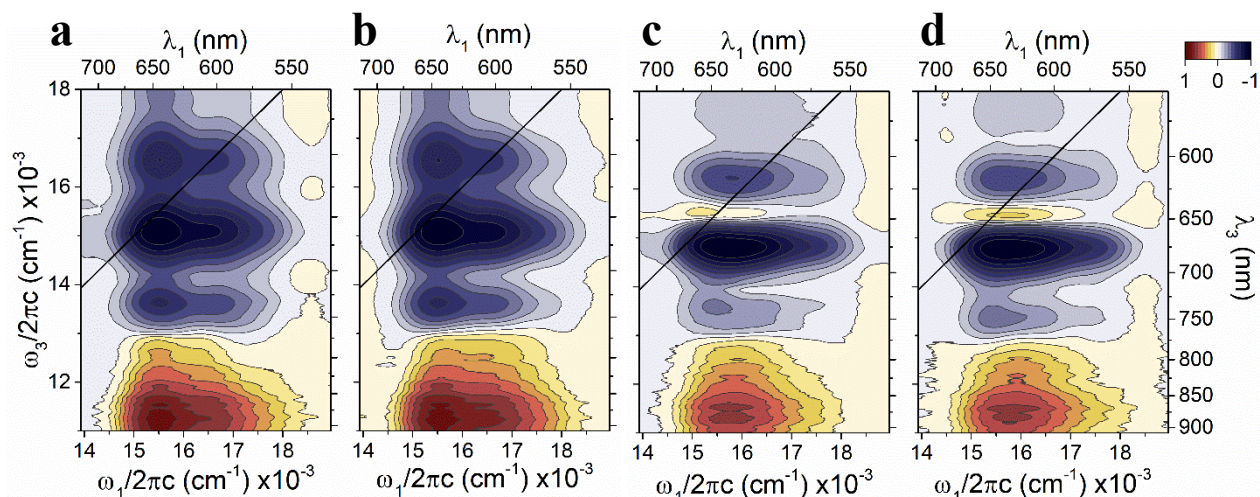
Figure S5.13. Replicate 2DES spectra for **TDI₁** at a waiting time of (a) 88 fs and (b) 1.5 ps and **TDI₂** at a waiting time of (c) 88 fs and (d) 1.5 ps using an 8 fs waiting time step size and a pulse alignment independent from the other replicate measurements.

B.10. 2DES measurements using benzonitrile solvent
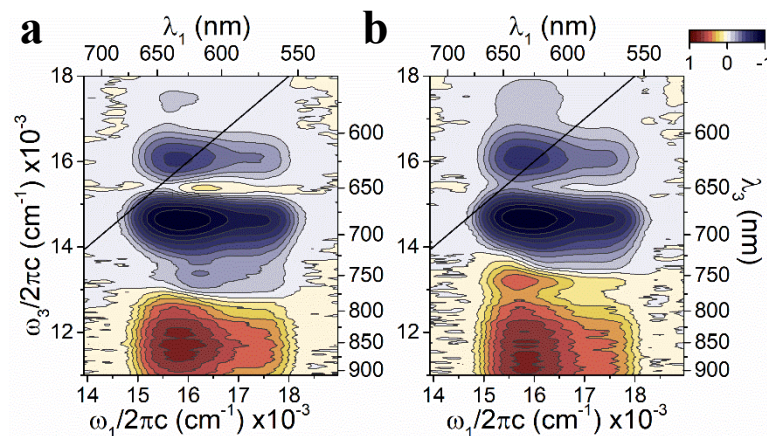
Figure S5.14. 2DES spectra for **TDI$_2$** in room-temperature benzonitrile at waiting times of approximately (a) 1.5 ps, (b) 33 ps.

To elucidate any appreciable contribution of the CT state to the electronic structure of the states populated by SF, we collected 2DES spectra of both compounds in benzonitrile solvent (ε = 25.2) where the CT state energy should be significantly lower compared to the measurements with chlorobenzene solvent. Figures S5.14a and b show 2DES spectra for **TDI$_2$** at waiting times of 1.5 and 33 ps, respectively. We observe the appearance of the $^1(T_1T_1)$ ESA within 1.5 ps after photoexcitation, while the S$_1$ SE remains. These features resemble those observed for **TDI$_2$** in chlorobenzene, suggesting vibronic coupling yields mixed states in higher dielectric environments as well. At later waiting times, we observe population transfer to the CT state, which is primarily identified by the ESA from the anionic species near w_3 = 13100 cm^{-1}. The disappearance of the S$_1$ and $^1(T_1T_1)$ features suggests the CT state does not mix with these states strongly.

B.11. Resonance Raman computations

Figure 5.4a in the main text illustrates the computed resonance Raman spectra for **TDI$_1$** and **TDI$_2$**. These spectra were broadened (Gaussian FWHM = 10 cm^{-1}) for ease of comparison to the experimental data and the frequency axis was scaled in accordance with our choice of functional.[288] Figure S5.15 provides further depictions of the nuclear motions potentially associated with the peaks observed via 2DES and FSRS. The 78 cm^{-1} vibration is readily observed in both the 2DES power and FSRS spectra. As discussed, the high-frequency 1261 cm^{-1} mode is not observed strongly in the 2DES power spectra but is observed via FSRS. The large Raman cross section for this mode in relation to the other calculated motions suggests this mode is primarily responsible for the vibronic progression observed in the linear absorption spectrum for **TDI$_2$**.

78 cm^{-1}

1261 cm^{-1}
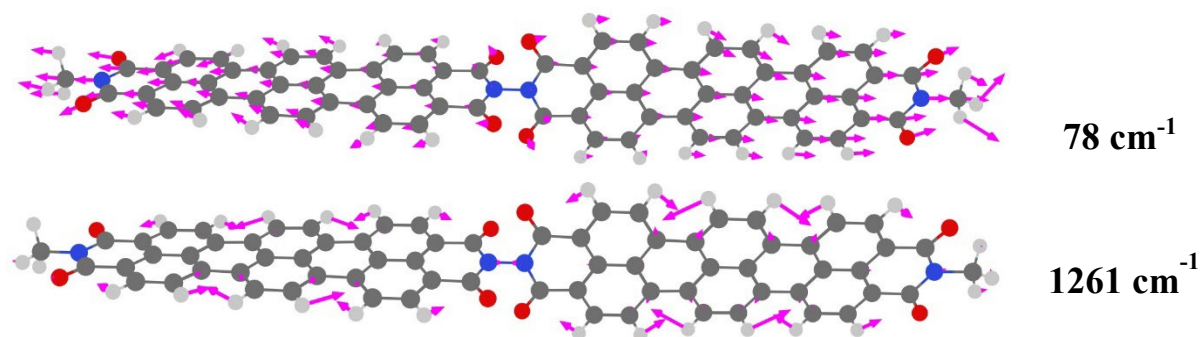
Figure S15. Additional normal mode assignments for the notable peaks that appear in the 2DES power and FSRS spectra for **TDI$_2$**.

B.12. Calculation of J$_{eff}$

Electron- and hole-transfer integrals, V_{LL} and V_{HH} respectively, were calculated using ADF with ωb97X-D functional/DZP basis set. The transfer integrals were calculated at the optimized system geometry as determined using the same functional/basis set combination. We calculated

J_{eff} using Eq. 36, which is formulated in the perturbative limit since the energy gap between the CT and S1 state is larger than the computed transfer integrals.[232]

$$J_{eff} = -\frac{2(V_{LL}V_{LH} - V_{HH}V_{HL})}{[E(CT) - E(TT)] + [E(CT) - E(S1)]} \qquad \text{Eq. 36}$$

where E_{S1}, E_{CT}, and E_{TT} correspond to the electronic energies as calculated at the dimeric geometry.

B.13. Additional simulation details

We propagate the system over an inter-pulse time delay range of 0 to 256 fs with a 1 fs step size. Spectral linewidths were imposed by multiplying the time-domain linear response by a Gaussian windowing function. The width of this windowing function was held constant for all the dimeric systems. The absorption spectrum was obtained via fast Fourier transformation of equation S5.9 after windowing and zero-padding to a vector length of 2^{10}.
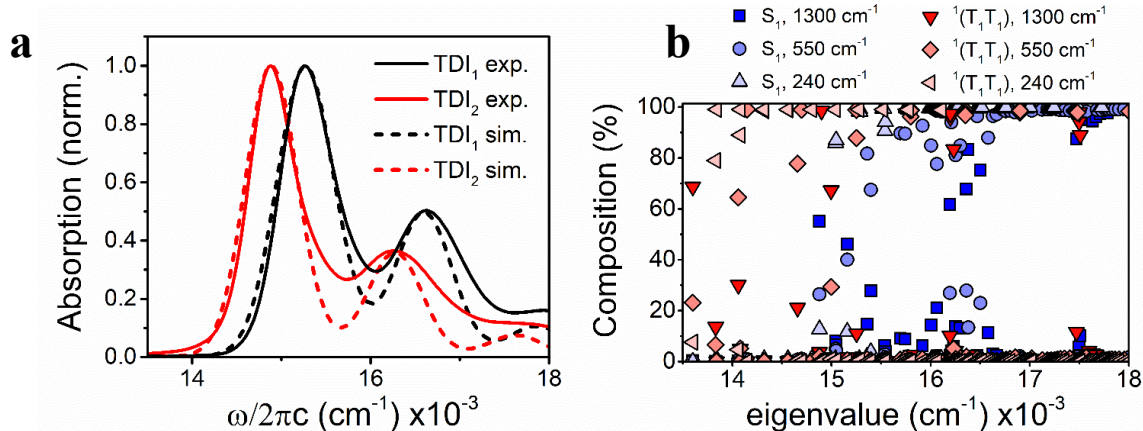
Figure S5.16. (a) Comparison of simulated and experimental linear absorption spectra and (b) the full compositional analysis of the nuclear modes contributing to each eigenvalue discussed in Figures 5.5 and 5.6 in the main text.

We reduced the number of vibronic coupling parameters by defining λ for the 550 and 240 cm^{-1} modes in comparison to λ for the 1300 cm^{-1} using their relative intensities in the experimental FSRS spectrum. By first comparing simulated linear response of **TDI₁**, we calculated Huang-Rhys

factors of 0.420, 0.1270, and 0.0242 for the 1300, 550, and 240 cm^{-1} vibrations, respectively. We then used these factors to simulate the linear response of **TDI$_2$** and calculate the coulombic coupling between the transition dipoles of the monomeric constituents. Figure S5.16a shows a comparison between the experimental and simulated absorption spectra. We determined J = -245 cm^{-1} for **TDI$_2$**, in agreement with the J-type orientation of the transition dipoles.[59] Figure S5.16b provides a complete view of the composition analysis we performed to disentangle nuclear contributions to the eigenstates discussed in the main text.

B.14. Control simulations

We performed several simulations to explore a range of parameter spaces and confirm the trends discussed in the main text were robust to changes in parameters. Namely, we investigated changes in J_{eff} and the nuclear offset, relative to S_0, for S_1 ($\lambda_{S1}^{all}{}^\omega$) versus $^1(T_1T_1)$ ($\lambda_{T1T1}^{all}{}^\omega$) vibrations. Figure S5.17 shows calculated linear response and eigenstate composition for calculations performed with the parameters listed above, but with any changes highlighted. Similarly, Figure S5.18 provides the corresponding nuclear composition analysis for each simulation, where applicable. Figures S5.17a and S5.18a plot the same data shown in Figures 5.5 and 5.6 of the main text, respectively, and represent the starting point for our exploration of parameter spaces. Figure S5.17b shows the corresponding results for a simulation performed with no displacement between the diabatic harmonic potentials. We observe that with no linear vibronic coupling and only weak electronic coupling present, mixing between the S_1 and $^1(T_1T_1)$ is negligible.

The displacement between the S_1 and $^1(T_1T_1)$ states for TDI-based compounds remains unclear. Based on previous works using a similar Hamiltonian, we made the assumption of

equivalent offset from the S_0 state for both the S_1 and $^1(T_1T_1)$ states.[205] In contrast, another study assumed the $^1(T_1T_1)$ state to have zero displacement from the S_0 state.[158] Figures S5.17c and S5.18b show the results of our simulation with this assumption made. We observe that mixing between the diabatic states underlying SF becomes more prevalent in this case. Moreover, the non-negligible contribution of both low- and high-frequency vibrations to the final eigenstates remains observable. Lastly, we conducted these simulations for the intermediate coupling regime between S_1 and $^1(T_1T_1)$ by setting $J_{eff} = 100$ cm^{-1}. Figures S5.17d and S5.18c shows the mixing of electronic and nuclear degrees of freedom is intensified as the effective electronic coupling increases.
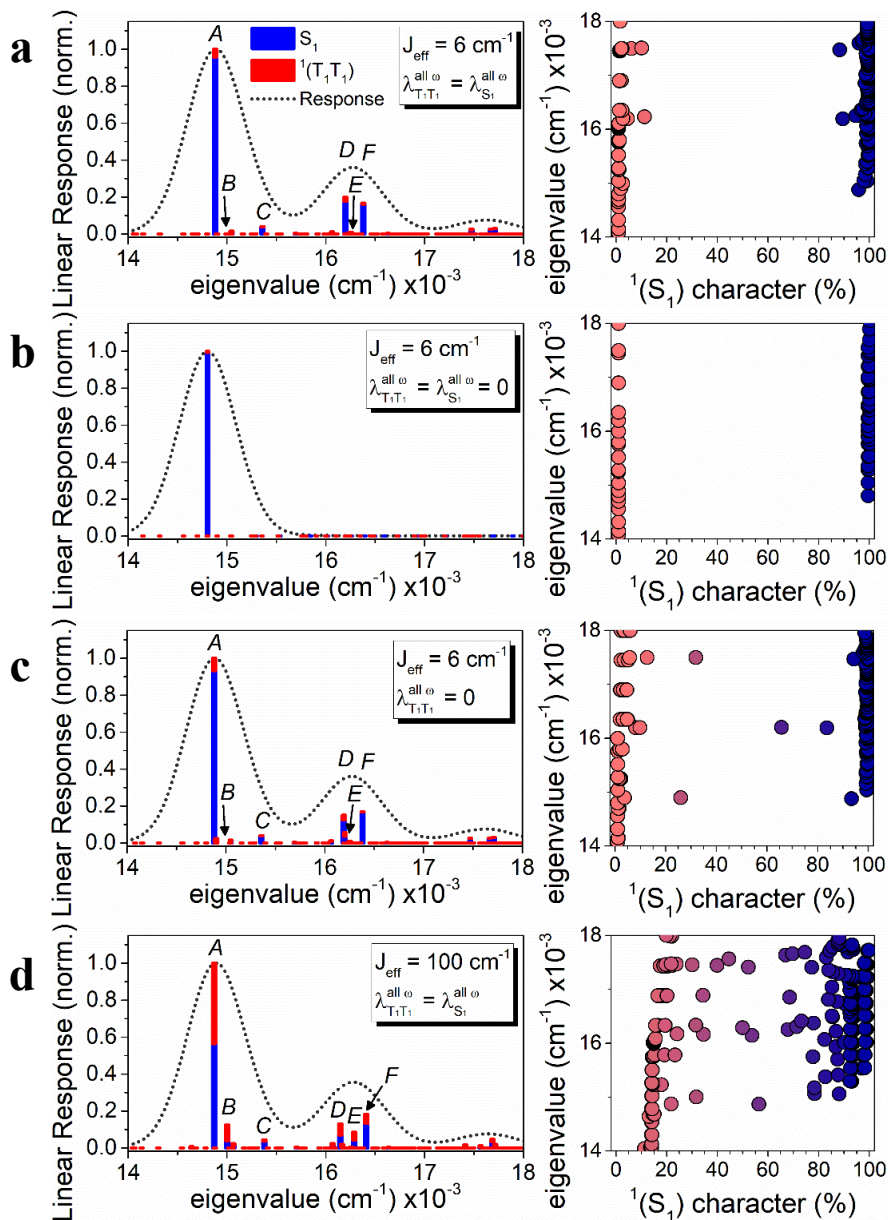
Figure S5.17. Linear response (left) and diabatic contributions (right) for control simulations for the following situations: (a) main text parameters, (b) no linear vibronic coupling, (c) no linear vibronic coupling for the $^1(T_1T_1)$ state, and (d) intermediate electronic coupling between the S_1 and $^1(T_1T_1)$ states.
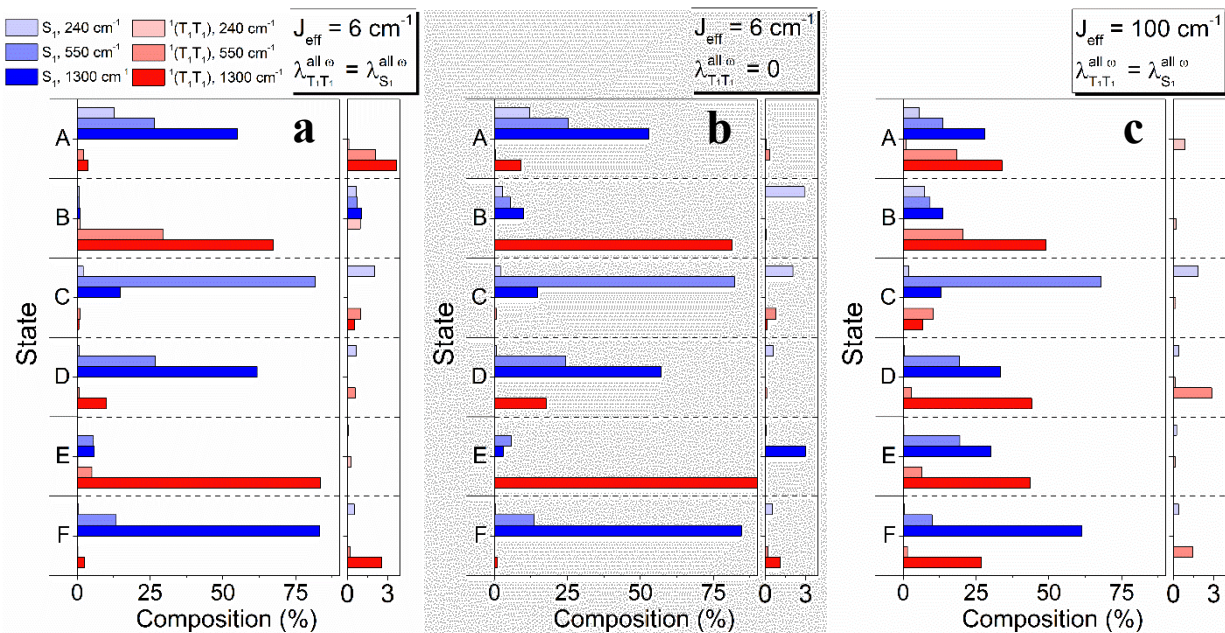
Figure S5.18. Eigenstate nuclear compositions for control simulations for the following situations: (a) main text parameters, (b) no linear vibronic coupling for the $^1(T_1T_1)$ state, and (c) intermediate electronic coupling between the S_1 and $^1(T_1T_1)$ states. States *A* through *F* refer to their respective labels in Figure S5.17.

B.15. Computed geometries and frequencies

Table 5.3. Optimized coordinates for **TDI$_1$** at level of BP86/DZP.

ATOM	X	Y	Z		ATOM	X	Y	Z
O	-0.62858	1.516237	1.717298		C	-7.06115	-0.90626	-0.84194
O	-0.64128	-1.49926	-1.7427		C	-7.06215	0.897037	0.859425
O	-16.3603	-1.65052	-1.58532		C	-7.79667	-1.81899	-1.60296
O	-16.3491	1.685275	1.568293		C	-7.79895	1.807314	1.622173
N	-0.63576	0.010589	-0.00465		C	-7.77443	-0.00488	0.00854
N	-16.3548	0.014022	-0.01596		C	-9.18491	-1.83188	-1.58994
C	0.830146	0.035548	0.014873		C	-9.18717	1.819532	1.607827
C	-1.28239	0.831407	0.934134		C	-9.21341	-0.00523	0.007817
C	-1.27903	-0.8145	-0.94678		C	-9.92459	-0.92866	-0.82115
C	-2.76315	0.817359	0.918233		C	-9.92565	0.918177	0.835752
C	-2.76148	-0.80642	-0.91611		C	-11.3856	-0.91481	-0.8434
C	-3.46261	-1.60105	-1.81318		C	-11.3867	0.907916	0.851861
C	-3.46356	1.607465	1.819499		C	-12.1316	-1.76721	-1.66893
C	-3.4707	0.003287	0.002589		C	-12.1342	1.76261	1.673508
C	-4.85755	-1.62704	-1.80048		C	-12.0866	-0.00177	0.002136
C	-4.85878	1.625695	1.812835		C	-13.5266	-1.75478	-1.67152
C	-4.90181	-0.00056	0.00572		C	-13.5291	1.757307	1.666372
C	-5.60231	-0.85819	-0.89556		C	-13.5184	0.001928	-0.00271
C	-5.60293	0.853661	0.910004		C	-14.2265	-0.88505	-0.84709
					C	-14.229	0.89256	0.836284

C	-15.7073	-0.89598	-0.86778		**H**	-7.28894	2.540706	2.242206
C	-15.7116	0.919526	0.849144		**H**	-9.69148	-2.57363	-2.20253
C	-17.8206	-0.00073	-0.04691		**H**	-9.69472	2.560001	2.221127
H	1.182648	1.050292	-0.20087		**H**	-11.6287	-2.46148	-2.33752
H	1.186009	-0.25249	1.009791		**H**	-11.6327	2.454242	2.345842
H	1.181758	-0.66553	-0.74414		**H**	-14.0918	-2.42515	-2.31847
H	-2.89773	-2.20513	-2.52259		**H**	-14.0947	2.430369	2.309983
H	-2.89832	2.214912	2.525913		**H**	-18.1663	0.214686	-1.06375
H	-5.36266	-2.25945	-2.52667		**H**	-18.1725	0.759006	0.653213
H	-5.36451	2.255345	2.540985		**H**	-18.1829	-0.99369	0.241054
H	-7.28556	-2.55296	-2.22142					

Table 5.4. Computed frequencies for **TDI$_1$** at level of BP86/DZP

FREQUENCY (CM^{-1})	IR ABSORPTION CROSS SECTION (ARB. UNITS)	FREQUENCY (CM^{-1})	IR ABSORPTION CROSS SECTION (ARB. UNITS)	FREQUENCY (CM^{-1})	IR ABSORPTION CROSS SECTION (ARB. UNITS)
2.112	0.00E+00	447.274	2.08E-03	823.323	2.91E-01
13.28	0.00E+00	448.871	6.95E-02	828.108	6.00E+00
38.119	5.06E-03	455.634	9.14E-03	834.49	1.10E+00
41.905	1.24E-03	460.956	1.73E-02	878.017	2.61E-03
60.714	1.90E+00	467.221	3.07E+00	879.956	1.27E-04
64.511	2.15E-03	479.915	2.97E+00	913.555	4.26E-01
73.627	1.12E-02	480.297	2.08E-02	914.312	1.96E-02
74.903	1.03E+00	513.949	4.94E+01	928.676	6.98E+00
76.272	3.11E+00	537.159	1.29E-02	938.361	2.32E+01
89.685	8.03E-01	540.508	8.50E-04	939.774	5.74E-01
118.525	2.07E+00	554.274	1.05E-03	940.943	2.84E+00
120.009	4.07E+00	566.262	1.94E+00	943.555	7.89E-02
146.917	4.44E-01	567.517	2.10E+01	944.526	9.75E-01
154.829	5.44E-01	577.143	2.43E-01	977.89	6.07E-03
164.565	1.11E+00	588.209	4.35E-04	1001.45	3.43E-02
166.667	1.09E-01	611.912	1.36E-03	1027.356	1.70E+02
167.772	1.62E+01	613.578	6.28E-01	1034.546	2.15E+02
177.654	1.09E+00	616.618	9.93E-03	1037.376	3.37E-01
238.643	2.04E-01	620.372	7.97E-02	1069.977	2.36E+01
240.952	2.85E-02	661.211	8.03E-01	1079.911	9.78E-03
257.285	1.85E-01	673.918	1.41E+01	1115.142	1.15E-02
262.003	2.48E-03	675.032	2.79E+00	1115.505	1.56E-01
271.6	6.51E-03	677.181	2.48E+00	1138.705	2.94E-02
307.781	4.95E-01	705.364	2.87E-03	1142.596	1.99E-01
314.471	1.62E+00	709.74	5.82E+00	1145.071	8.02E+00
318.383	3.08E-01	719.525	3.92E+01	1149.335	1.14E+01
318.682	3.86E-01	722.835	9.63E+00	1164.952	4.44E-02
350.131	2.25E+01	728.947	1.94E-02	1178.678	1.16E-01
356.262	8.37E-02	733.657	7.09E-01	1186.015	1.63E+00
366.811	2.51E-02	750.043	4.44E-02	1198.7	7.40E+01
377.554	1.27E-03	783.267	8.64E-02	1209.86	1.41E+00
398.016	1.38E+02	785.319	3.82E+01	1216.802	2.54E-02
399.274	2.77E+01	788.104	9.53E+01	1219.766	1.33E-01
413.97	1.21E+01	797.48	4.72E-03	1227.297	7.75E+00
419.014	8.80E+00	805.082	4.06E-02	1250.045	8.24E-01
422.097	8.24E-02	809.806	2.45E+00	1252.464	1.08E+02
438.045	4.75E-02	813.391	6.75E+00	1259.725	2.99E-02
		817.24	1.61E+00	1273.184	3.03E-03
		818.387	1.21E+00	1283.219	5.49E+00
		820.769	7.72E+01	1292.21	7.68E+01

1299.162	1.96E-02	**1448.952**	4.38E-01	**1682.173**	27.73824
1306.886	3.23E+02	**1452.439**	4.42E+00	**2991.79**	4.017736
1309.553	2.27E+00	**1458.917**	2.66E-01	**2991.875**	86.1785
1328.343	8.67E-01	**1459.031**	2.43E+01	**3070.026**	7.111136
1338.077	6.48E+02	**1497.186**	5.93E+01	**3070.099**	0.452504
1338.989	5.54E-01	**1504.521**	2.77E-01	**3122.406**	4.714071
1343.336	1.97E-02	**1526.39**	2.82E+00	**3122.501**	12.0607
1357.874	1.85E+00	**1537.206**	5.59E-03	**3126.067**	1.685295
1370.205	1.33E+02	**1552.767**	6.59E+00	**3126.495**	1.434423
1373.409	5.79E-01	**1556.107**	1.48E+02	**3128.511**	1.720486
1388.906	2.18E+02	**1557.726**	1.71E+00	**3128.906**	2.621448
1392.882	1.73E+00	**1563.943**	2.18E-02	**3132.918**	9.764446
1400.032	2.45E-02	**1569.207**	9.05E+02	**3133.008**	0.141406
1410.741	2.87E+02	**1583.719**	1.01E+00	**3141.251**	0.065343
1433.902	9.24E-02	**1588.322**	6.22E-02	**3141.302**	0.314649
1439.494	4.03E+00	**1588.815**	2.42E-02	**3147.012**	0.664093
1440.891	5.24E-04	**1643.946**	355.5519	**3147.208**	0.727989
1447.812	1.69E+01	**1644.719**	410.3664	**3153.136**	0.797779
1448.062	8.86E+00	**1679.816**	966.8055	**3153.427**	3.027098

Table 5.5. Computed resonance Raman cross sections for **TDI₁** at level of BP86/DZP

FREQUENCY (CM⁻¹)	RESONANCE RAMAN CROSS SECTION AT 670 NM (ARB. UNITS)				
60.71	4.68E-33	467.22	4.10E-34	913.55	7.61E-33
64.51	7.85E-33	479.92	5.96E-32	914.31	3.46E-33
73.63	2.78E-31	480.3	1.98E-30	928.68	1.30E-33
74.9	4.28E-32	513.95	5.58E-34	938.36	1.50E-34
76.27	1.29E-31	537.16	2.78E-30	939.77	4.08E-33
89.69	4.28E-33	540.51	2.22E-29	940.94	2.34E-33
118.53	1.12E-32	554.27	2.39E-33	943.55	7.39E-33
120.01	3.56E-34	566.26	5.63E-34	944.53	2.67E-33
146.92	9.64E-33	567.52	2.83E-33	977.89	2.17E-30
154.83	7.28E-33	577.14	9.03E-36	1001.45	5.63E-33
164.56	1.48E-32	588.21	1.18E-30	1027.36	2.94E-35
166.67	1.77E-29	611.91	4.03E-34	1034.55	3.30E-33
167.77	1.11E-31	613.58	9.87E-35	1037.38	1.64E-33
177.65	1.43E-32	616.62	4.48E-33	1069.98	2.85E-35
238.64	7.50E-35	620.37	1.02E-31	1079.91	1.01E-30
240.95	8.70E-33	661.21	5.39E-34	1115.14	7.26E-36
257.29	2.82E-35	673.92	4.71E-35	1115.51	2.64E-36
262	6.23E-34	675.03	1.29E-33	1138.7	3.79E-33
271.6	1.05E-31	677.18	1.77E-34	1142.6	1.69E-32
307.78	5.39E-32	705.36	1.95E-30	1145.07	4.78E-35
314.47	8.19E-34	709.74	4.11E-34	1149.34	1.33E-34
318.38	3.28E-33	719.52	7.57E-34	1164.95	3.92E-33
318.68	1.07E-32	722.84	1.44E-33	1178.68	4.06E-33
350.13	3.11E-34	728.95	1.52E-32	1186.02	1.06E-34
356.26	1.05E-32	733.66	1.97E-32	1198.7	8.69E-34
366.81	3.47E-33	750.04	2.95E-34	1209.86	1.14E-34
377.55	2.57E-32	783.27	1.88E-34	1216.8	2.97E-30
398.02	1.28E-32	785.32	9.67E-34	1219.77	1.35E-30
399.27	5.14E-32	788.1	1.86E-33	1227.3	5.24E-33
413.97	1.22E-35	797.48	2.29E-31	1250.05	4.92E-31
419.01	2.27E-35	805.08	3.23E-31	1252.46	1.25E-32
422.1	1.89E-32	809.81	2.79E-34	1259.72	3.94E-29
438.05	1.85E-33	813.39	1.76E-35	1273.18	1.38E-28
447.27	4.91E-31	817.24	1.52E-33	1283.22	8.86E-34
448.87	1.94E-34	818.39	7.52E-33	1292.21	1.88E-31
455.63	2.28E-33	820.77	4.79E-35	1299.16	1.04E-32
460.96	1.67E-33	823.32	1.30E-31	1306.89	7.36E-33
		828.11	1.93E-34	1309.55	1.62E-34
		834.49	1.47E-33	1328.34	5.70E-30
		878.02	5.15E-31	1338.08	3.34E-33
		879.96	2.59E-32	1338.99	5.43E-30

1343.34	5.42E-32	**1447.81**	2.85E-33	**1556.11**	3.51E-31
1357.87	4.67E-35	**1448.06**	6.21E-33	**1557.73**	1.28E-29
1370.2	1.36E-31	**1448.95**	4.50E-33	**1563.94**	2.96E-32
1373.41	2.23E-29	**1452.44**	7.13E-34	**1569.21**	3.98E-33
1388.91	2.02E-32	**1458.92**	2.65E-31	**1583.72**	6.15E-34
1392.88	5.98E-30	**1459.03**	3.86E-33	**1588.32**	8.76E-31
1400.03	3.47E-31	**1497.19**	2.70E-35	**1588.82**	2.97E-31
1410.74	1.50E-33	**1504.52**	4.01E-33	**1643.95**	2.60E-32
1433.9	4.52E-30	**1526.39**	2.22E-33	**1644.72**	2.19E-32
1439.49	6.07E-32	**1537.21**	1.40E-28	**1679.82**	2.40E-32
1440.89	1.59E-32	**1552.77**	9.82E-31	**1682.17**	8.38E-31

Table 5.6. Optimized coordinates for **TDI₂** at level of BP86/DZP

ATOM	X	Y	Z		ATOM	X	Y	Z
N	-16.38557	0.02055	-0.01541		C	-4.89040	1.63488	1.79979
C	-17.85161	0.00223	-0.04057		C	-4.89121	-1.64594	-1.79088
H	-18.20885	-0.98349	0.27571		C	-3.49543	-0.00548	0.00410
H	-18.20247	0.78134	0.63829		C	-3.49671	1.61295	1.81309
H	-18.20311	0.18918	-1.06121		H	-5.39637	2.27393	2.51899
C	-15.74085	0.98373	0.78294		C	-3.49744	-1.62431	-1.80441
C	-15.73960	-0.94100	-0.80907		H	-5.39749	-2.28371	-2.51103
C	-14.25798	0.95499	0.77063		C	-2.79323	-0.82521	-0.91406
O	-16.37681	1.79749	1.44816		C	-2.79298	0.81452	0.92181
C	-14.25843	-0.92966	-0.79110		H	-2.93402	2.22426	2.51778
O	-16.39355	-1.73992	-1.47541		H	-2.93513	-2.23449	-2.51039
C	-13.54844	0.01046	-0.00806		C	-1.31592	-0.84418	-0.95528
C	-13.55691	1.87571	1.53698		C	-1.31577	0.83414	0.96200
C	-13.56013	-1.85542	-1.55344		O	-0.65269	-1.51218	-1.73142
C	-12.11670	0.00583	-0.00411		N	-0.69262	-0.00437	0.00281
H	-14.12145	2.59703	2.12684		O	-0.65236	1.50244	1.73761
C	-12.16198	1.87413	1.54998		N	0.69257	-0.00389	0.00301
H	-14.12658	-2.57241	-2.14695		C	1.31582	0.96486	-0.82399
C	-12.16502	-1.86258	-1.55874		C	1.31594	-0.97038	0.83253
C	-11.41571	0.95581	0.79899		C	2.79327	0.93363	-0.79453
C	-11.41729	-0.94864	-0.80368		O	0.65242	1.74183	-1.49125
H	-11.66012	2.61609	2.16584		C	2.79336	-0.93747	0.80474
H	-11.66413	-2.60714	-2.17230		O	0.65263	-1.74870	1.49834
C	-9.95441	0.93809	0.81206		C	3.49547	-0.00160	0.00545
C	-9.95574	-0.93820	-0.81064		C	3.49671	1.84042	-1.57521
C	-9.24335	-0.00140	0.00175		C	3.49676	-1.84353	1.58624
C	-9.21442	1.82657	1.59731		C	4.92863	-0.00054	0.00665
C	-9.21652	-1.83000	-1.59290		H	2.93443	2.54084	-2.19176
C	-7.80423	-0.00371	0.00351		C	4.89064	1.85577	-1.56460
C	-7.82658	1.80400	1.62089		H	2.93444	-2.54436	2.20229
H	-9.71967	2.56136	2.21891		C	4.89068	-1.85672	1.57810
H	-9.72254	-2.56296	-2.21609		C	5.63183	0.96537	-0.77643
C	-7.82846	-1.81162	-1.61342		C	5.63184	-0.96530	0.79109
C	-7.09076	0.89746	0.85303		H	5.39619	2.58094	-2.19721
C	-7.09147	-0.90664	-0.84476		H	5.39627	-2.58097	2.21173
H	-7.31765	2.52784	2.25250		C	7.09190	0.99763	-0.72750
H	-7.32032	-2.53655	-2.24446		C	7.09199	-0.99644	0.74361
C	-5.63123	0.85476	0.90194		C	7.80465	0.00043	0.00780
C	-5.63177	-0.86588	-0.89274		C	7.82930	1.98442	-1.38757
C	-4.92829	-0.00566	0.00454		C	7.82929	-1.98235	1.40507
					C	9.24368	-0.00003	0.00716

C	9.21712	2.00741	-1.35517	C	13.55683	-2.11421	1.19165
H	7.32167	2.77223	-1.93875	H	11.65926	-2.94811	1.69067
H	7.32162	-2.76920	1.95758	C	14.25795	-1.07344	0.59848
C	9.21701	-2.00649	1.37110	C	14.25732	1.05828	-0.60562
C	9.95586	1.03756	-0.67190	H	14.12373	2.91745	-1.64509
C	9.95558	-1.03841	0.68524	H	14.12114	-2.93151	1.63951
H	9.72363	2.80555	-1.89235	C	15.74086	-1.10598	0.60031
H	9.72357	-2.80469	1.90816	C	15.73846	1.07708	-0.61465
C	11.41655	1.06514	-0.63557	O	16.37761	-2.02804	1.10399
C	11.41598	-1.06951	0.64398	N	16.38468	-0.01315	-0.00985
C	12.11675	-0.00356	0.00247	O	16.39225	1.98661	-1.12009
C	12.16292	2.10284	-1.21026	C	17.85094	0.01096	-0.02991
C	12.16185	-2.10907	1.21575	H	18.20249	0.03015	-1.06723
C	13.54831	-0.00632	-0.00140	H	18.20763	0.91455	0.47580
C	13.55811	2.10275	-1.19394	H	18.20164	-0.88678	0.48205
H	11.66053	2.94364	-1.68228				

Table 5.7. Computed vibrational frequencies for **TDI$_2$** at level of BP86/DZP

FREQUENCY (CM^{-1})	IR ABSORPTION CROSS SECTION (ARB. UNITS)	FREQUENCY (CM^{-1})	IR ABSORPTION CROSS SECTION (ARB. UNITS)	FREQUENCY (CM^{-1})	IR ABSORPTION CROSS SECTION (ARB. UNITS)
-20.414	-5.49E-03	238.602	7.02E-04	460.932	1.52E-01
1.581	0.00E+00	240.141	1.18E-03	462.255	8.56E+01
3.274	0.00E+00	248.342	1.90E-01	464.54	2.50E+00
16.064	0.00E+00	249.274	2.65E-01	473.31	2.06E+01
17.931	0.00E+00	262.181	1.02E-01	476.517	4.85E-03
20.802	2.60E-03	262.848	3.82E-01	478.153	1.12E-01
23.139	1.33E-02	269.496	4.40E-02	479.436	1.10E+00
27.257	3.11E-04	270.884	9.37E-03	479.681	1.85E+00
36.628	9.01E-03	302.167	1.74E+00	509.256	6.68E+01
41.153	8.48E-03	304.428	2.51E+00	509.537	1.48E+02
45.501	1.56E-01	306.832	1.40E-01	534.255	5.71E-02
57.939	1.38E+00	307.757	1.28E-02	535.471	2.80E-02
62.135	1.35E+00	322.079	3.18E+00	536.84	3.56E-02
67.408	5.62E-01	325.873	3.79E+00	538.158	1.60E+00
69.003	3.68E-02	327.638	3.92E+00	538.913	6.53E-02
72.76	3.52E-02	329.62	1.78E-02	552.464	1.12E-02
73.759	5.50E-01	353.449	1.38E+00	553.378	1.47E-02
74.352	3.36E-01	353.847	5.61E-01	566.405	8.43E-01
75.825	7.05E-02	357.331	1.51E+01	566.462	1.24E+00
76.316	2.18E+00	358.915	3.45E+00	577.16	6.94E-02
86.483	2.46E+00	375.675	7.25E-01	578.182	3.08E-01
89.767	8.75E-03	375.849	1.32E+00	578.857	4.66E+01
99.934	2.84E-02	396.32	1.21E+01	581.716	2.25E-01
103.835	9.39E-02	396.702	1.78E+01	611.937	2.09E-02
112.116	3.05E+00	398.421	7.81E-01	612.498	3.02E+00
113.87	3.21E+00	399.972	1.13E+01	612.63	4.08E-01
150.499	1.72E+00	402.887	5.47E+02	614.417	3.98E-01
151.116	2.62E+00	414.583	6.08E+00	616.711	4.87E-02
160.176	2.98E+00	415.142	1.18E+00	617.406	2.10E-02
161.075	4.70E+00	418.142	9.26E+00	618.689	5.21E-04
164.633	5.16E+00	418.395	3.52E+00	619.845	4.43E-02
167.499	1.11E+01	420.743	1.67E+00	650.331	2.11E+02
170.819	4.61E-02	422.559	4.52E-02	660.259	2.78E-01
173.789	8.04E+00	427.22	4.40E-02	661.771	9.29E-01
175.073	5.72E-01	436.439	8.51E-01	670.337	9.97E+00
185.993	4.58E-02	437.272	6.12E-02	671.993	9.64E+00
186.711	3.25E-01	450.191	3.47E-02	672.056	3.36E+00
218.365	1.11E-03	450.574	3.46E-02	674.209	4.32E+01
		456.796	5.98E-02	679.484	5.86E+00
		458.418	3.13E-02	679.842	4.92E+00
		459.606	7.51E-02	702.887	4.36E-04

707.472	2.17E+00	892.462	4.94E+00	1179.223	6.66E+00
708.534	2.90E-04	908.613	8.87E-03	1179.472	7.94E+00
714.276	2.23E+01	909.323	1.55E-02	1181.185	2.47E+02
715.183	2.53E+01	912.26	1.94E-02	1186.658	1.85E+00
716.111	1.22E+02	912.907	3.79E-02	1186.813	1.29E+00
719.065	6.36E+01	938.094	2.53E-02	1198.78	5.47E+01
721.44	1.56E+01	940.845	3.31E-02	1199.724	5.71E+01
721.984	1.67E+01	941.166	9.86E-03	1212.786	2.78E+00
730.197	7.30E-01	941.546	1.92E+00	1214.301	1.58E+01
732.408	2.88E-01	941.686	3.47E+00	1218.557	4.47E+00
734.478	2.44E-01	943.137	7.00E-01	1218.87	5.32E+00
755.772	1.80E+00	943.382	8.15E-02	1227.697	5.12E+00
756.194	1.42E+00	943.645	1.04E+01	1228.72	4.82E+00
782.349	1.03E+00	944.106	1.40E+01	1230.984	7.96E-02
783.114	3.79E+00	944.451	4.70E+00	1251.411	6.06E+01
784.835	8.11E-01	944.575	8.79E+00	1251.753	3.42E+01
785.11	8.75E+01	955.944	6.96E+00	1255.988	1.25E+02
785.702	1.37E+02	983.162	4.68E-03	1260.965	8.84E-01
787.551	8.01E+01	1009.403	5.67E+01	1271.983	1.12E+01
796.977	2.13E-03	1009.423	2.93E+01	1273.845	5.74E-01
798.381	3.97E+00	1018.603	3.54E+02	1282.192	5.31E+00
799.216	4.21E-02	1033.772	5.18E+01	1282.754	5.27E+00
803.3	7.84E-02	1033.984	5.31E+01	1289.994	1.04E+03
809.02	2.49E+00	1042.73	4.01E-02	1292.223	1.23E+02
809.121	3.25E+00	1069.025	1.60E+01	1297.513	1.23E+03
817.152	2.60E-01	1069.115	1.71E+01	1297.681	7.50E-01
818.76	1.16E+01	1073.796	4.64E+01	1298.985	3.54E-03
819.572	7.83E+01	1085.376	3.66E-02	1303.971	4.90E-01
819.947	8.94E+00	1114.967	1.51E-01	1309.759	1.96E+00
820.117	4.14E+01	1115.472	6.41E-02	1310.476	2.06E+00
820.515	5.01E+01	1123.907	6.39E+01	1323.278	1.52E+02
821.146	1.25E+00	1125.104	5.99E+01	1325.082	9.47E-01
821.684	4.14E-01	1138.061	3.62E+00	1335.663	2.02E+03
822.616	2.01E+00	1138.19	2.94E+00	1338.302	3.98E-01
822.995	3.36E+00	1138.942	7.56E+01	1338.904	1.12E+01
827.968	1.36E+01	1143.126	1.41E+00	1340.084	1.41E+00
828.448	5.50E+00	1144.873	6.62E+01	1342.107	7.94E-01
833.989	6.64E-01	1147.215	5.28E-01	1342.264	1.05E+00
834.574	3.83E-01	1150.435	2.65E+01	1357.192	1.71E+00
875.573	5.59E-03	1150.463	3.03E+01	1357.619	1.68E+00
886.788	2.28E+01	1166.724	5.97E+00	1368.435	3.34E+02
892.233	7.68E+00	1167.045	5.36E+00	1368.913	3.95E+00

1374.144	2.68E+00	**1536.762**	3.30E+00	**3070.015**	3.71E+00
1374.25	9.93E+01	**1536.912**	2.37E+00	**3072.432**	3.68E+00
1391.199	3.45E+00	**1552.657**	1.78E+01	**3120.306**	7.88E+00
1391.952	1.69E+01	**1552.908**	1.01E+01	**3121.635**	9.73E+00
1393.032	3.77E+01	**1556.369**	4.03E+02	**3125.119**	9.39E+00
1393.175	4.38E+01	**1556.562**	3.22E+01	**3125.347**	1.49E+00
1407.007	4.18E+00	**1558.713**	4.31E+01	**3128.019**	2.86E+00
1407.235	4.89E+02	**1559.135**	3.16E+00	**3128.334**	1.17E+00
1430.601	4.39E-01	**1563.947**	5.88E-01	**3129.584**	1.24E+00
1431.432	6.58E+00	**1564.094**	5.42E-01	**3129.628**	1.90E+00
1438.332	5.80E-01	**1568.523**	2.62E+03	**3129.852**	2.79E+00
1438.678	9.15E-01	**1570.335**	1.28E+01	**3130.251**	2.75E+00
1440.946	5.10E-02	**1583.198**	1.17E+00	**3132.342**	3.36E+00
1440.986	5.67E-02	**1583.271**	9.92E-01	**3133.007**	2.61E+00
1447.977	1.38E+01	**1588.497**	1.08E+01	**3134.362**	9.14E+00
1448.115	1.21E+01	**1588.679**	2.47E+00	**3134.767**	5.52E+00
1448.975	9.67E-02	**1588.833**	2.58E+00	**3140.197**	9.08E-01
1449.252	1.03E-01	**1589.02**	2.63E+00	**3140.479**	9.68E-01
1451.779	2.69E+00	**1643.948**	3.78E+02	**3142.791**	2.42E-01
1451.86	2.67E+00	**1644.213**	3.82E+02	**3143.072**	2.60E-01
1458.309	1.25E+01	**1680.546**	1.22E+03	**3147.348**	1.29E+00
1458.485	1.27E+01	**1681.086**	1.67E+02	**3147.459**	2.58E+00
1497.707	5.80E+01	**1682.941**	3.07E+02	**3148.9**	1.46E+00
1498.002	5.95E+01	**1684.401**	3.06E+02	**3149.096**	1.45E+00
1504.811	1.60E+00	**1695.802**	9.42E+02	**3150.486**	2.61E+00
1505.036	8.57E-01	**1721.734**	8.32E-01	**3150.599**	1.43E+00
1526.563	3.59E+00	**2991.489**	5.02E+01	**3154.749**	1.82E+00
1526.707	3.23E+00	**2992.935**	5.42E+01	**3154.984**	2.11E+00

Table 5.8. Computed resonance Raman cross sections for **TDI$_2$** at level of BP86/DZP

FREQUENCY (CM^{-1})	RESONANCE RAMAN CROSS SECTION AT 670 NM (ARB. UNITS)	FREQUENCY (CM^{-1})	RESONANCE RAMAN CROSS SECTION	FREQUENCY (CM^{-1})	RESONANCE RAMAN CROSS SECTION
62.13	2.24E-32	322.08	3.92E-33	536.84	6.85E-32
67.41	7.09E-32	325.87	3.57E-33	538.16	1.74E-30
69.00	1.78E-33	327.64	6.20E-33	538.91	4.65E-29
72.76	1.09E-31	329.62	4.81E-31	552.46	3.36E-33
73.76	6.31E-31	353.45	1.59E-33	553.38	2.32E-33
74.35	4.28E-31	353.85	1.01E-33	566.40	8.54E-33
75.83	2.08E-29	357.33	8.77E-33	566.46	1.33E-34
76.32	1.07E-30	358.92	8.06E-33	577.16	5.59E-34
86.48	7.64E-33	375.68	2.96E-32	578.18	7.78E-34
89.77	1.07E-30	375.85	2.60E-32	578.86	8.81E-33
99.93	1.95E-32	396.32	3.60E-32	581.72	2.51E-30
103.83	2.29E-32	396.70	2.02E-32	611.94	1.55E-33
112.12	2.12E-33	398.42	1.09E-31	612.50	4.02E-33
113.87	2.23E-34	399.97	4.14E-34	612.63	1.27E-33
150.50	2.70E-33	402.89	5.91E-33	614.42	2.36E-32
151.12	2.98E-33	414.58	1.78E-35	616.71	5.44E-34
160.18	1.58E-32	415.14	5.05E-33	617.41	1.84E-33
161.07	3.17E-33	418.14	4.18E-34	618.69	2.36E-33
164.63	7.38E-33	418.39	8.82E-34	619.85	3.10E-32
167.50	9.86E-33	420.74	8.86E-34	650.33	1.26E-33
170.82	2.29E-32	422.56	5.02E-33	660.26	2.53E-33
173.79	2.10E-32	427.22	1.72E-30	661.77	3.70E-33
175.07	1.48E-32	436.44	4.68E-34	670.34	4.14E-34
185.99	6.01E-33	437.27	4.39E-33	671.99	2.09E-35
186.71	3.08E-33	450.19	3.26E-34	672.06	7.64E-34
218.37	2.11E-29	450.57	2.84E-34	674.21	4.56E-34
238.60	5.00E-32	456.80	1.41E-34	679.48	1.49E-33
240.14	5.84E-32	458.42	5.32E-33	679.84	1.75E-33
248.34	5.41E-34	459.61	3.74E-33	702.89	3.75E-30
249.27	7.61E-34	460.93	2.07E-33	707.47	3.95E-33
262.18	2.34E-33	462.25	1.56E-34	708.53	2.97E-31
262.85	2.81E-34	464.54	1.14E-31	714.28	4.29E-34
269.50	5.72E-33	473.31	1.46E-32	715.18	1.34E-33
270.88	2.60E-32	476.52	3.21E-30	716.11	1.49E-34
302.17	3.04E-33	478.15	9.99E-32	719.07	3.10E-34
304.43	6.08E-33	479.44	4.17E-32	721.44	4.69E-34
306.83	5.51E-32	479.68	1.35E-31	721.98	5.79E-34
307.76	4.96E-31	509.26	3.73E-31	730.20	2.87E-33
		509.54	1.79E-31	732.41	3.46E-33
		534.25	6.11E-30	734.48	1.49E-31
		535.47	8.56E-30	755.77	1.44E-33

756.19	8.78E-34	**943.64**	6.64E-34	**1228.72**	2.35E-33
782.35	4.14E-34	**944.11**	1.01E-32	**1230.98**	1.23E-29
783.11	4.80E-34	**944.45**	4.20E-33	**1251.41**	7.93E-32
784.84	7.25E-32	**944.58**	1.50E-33	**1251.75**	3.95E-31
785.11	2.47E-34	**955.94**	8.26E-34	**1255.99**	2.68E-32
785.70	4.11E-34	**983.16**	9.11E-30	**1260.96**	1.30E-28
787.55	2.33E-35	**1009.40**	1.68E-33	**1271.98**	1.89E-30
796.98	2.50E-31	**1009.42**	7.59E-34	**1273.85**	3.52E-28
798.38	4.80E-33	**1018.60**	8.48E-35	**1282.19**	7.16E-34
799.22	2.49E-33	**1033.77**	1.40E-33	**1282.75**	5.24E-34
803.30	1.10E-31	**1033.98**	1.46E-33	**1289.99**	9.69E-33
809.02	4.10E-35	**1042.73**	1.02E-30	**1292.22**	2.66E-31
809.12	8.67E-35	**1069.03**	3.28E-34	**1297.51**	1.84E-33
817.15	4.34E-32	**1069.12**	1.47E-34	**1297.68**	1.02E-32
818.76	1.96E-32	**1073.80**	1.52E-33	**1298.98**	1.05E-32
819.57	7.90E-35	**1085.38**	2.39E-30	**1303.97**	2.36E-31
819.95	4.95E-32	**1114.97**	3.54E-35	**1309.76**	2.63E-34
820.12	1.16E-32	**1115.47**	2.86E-36	**1310.48**	2.66E-34
820.51	9.30E-34	**1123.91**	8.49E-34	**1323.28**	1.09E-32
821.15	1.77E-31	**1125.10**	1.26E-33	**1325.08**	1.96E-29
821.68	2.53E-31	**1138.06**	6.51E-33	**1335.66**	9.95E-33
822.62	1.42E-34	**1138.19**	6.59E-33	**1338.30**	5.30E-30
823.00	5.33E-35	**1138.94**	8.47E-34	**1338.90**	1.55E-31
827.97	9.76E-35	**1143.13**	1.83E-32	**1340.08**	1.08E-29
828.45	2.69E-34	**1144.87**	1.75E-34	**1342.11**	1.72E-32
833.99	1.76E-33	**1147.21**	1.96E-31	**1342.26**	2.92E-32
834.57	1.94E-33	**1150.43**	1.62E-33	**1357.19**	2.41E-33
875.57	1.92E-30	**1150.46**	1.22E-33	**1357.62**	3.25E-33
886.79	3.53E-35	**1166.72**	6.09E-33	**1368.43**	7.73E-32
892.23	6.23E-33	**1167.05**	4.52E-33	**1368.91**	8.05E-30
892.46	3.08E-33	**1179.22**	4.33E-34	**1374.14**	6.71E-29
908.61	1.82E-32	**1179.47**	2.15E-34	**1374.25**	1.95E-30
909.32	2.76E-33	**1181.18**	1.16E-33	**1391.20**	8.95E-30
912.26	3.36E-32	**1186.66**	4.64E-34	**1391.95**	6.66E-31
912.91	3.83E-33	**1186.81**	5.49E-34	**1393.03**	3.62E-30
938.09	6.99E-32	**1198.78**	8.76E-34	**1393.17**	2.23E-30
940.85	5.99E-35	**1199.72**	5.10E-34	**1407.01**	2.58E-31
941.17	2.10E-33	**1212.79**	2.82E-30	**1407.23**	3.27E-34
941.55	5.60E-34	**1214.30**	4.92E-31	**1430.60**	8.07E-30
941.69	2.35E-34	**1218.56**	8.02E-32	**1431.43**	4.44E-32
943.14	5.28E-33	**1218.87**	8.67E-32	**1438.33**	5.63E-31
943.38	1.10E-32	**1227.70**	2.42E-33	**1438.68**	4.37E-31

1440.95	1.68E-32	**1526.56**	6.91E-33	**1583.20**	1.88E-33
1440.99	1.91E-32	**1526.71**	2.71E-33	**1583.27**	2.05E-33
1447.98	1.32E-32	**1536.76**	1.63E-28	**1588.50**	2.41E-31
1448.12	3.05E-33	**1536.91**	2.15E-28	**1588.68**	5.30E-31
1448.97	3.78E-33	**1552.66**	6.06E-32	**1588.83**	5.59E-31
1449.25	2.52E-33	**1552.91**	2.13E-32	**1589.02**	2.61E-31
1451.78	6.39E-33	**1556.37**	1.32E-30	**1643.95**	2.29E-32
1451.86	4.29E-33	**1556.56**	4.62E-30	**1644.21**	2.30E-32
1458.31	1.77E-31	**1558.71**	3.62E-30	**1680.55**	1.35E-31
1458.48	1.40E-31	**1559.13**	3.42E-29	**1681.09**	9.94E-31
1497.71	1.65E-34	**1563.95**	6.19E-33	**1682.94**	1.54E-32
1498.00	3.74E-34	**1564.09**	1.11E-32	**1684.40**	1.54E-32
1504.81	4.70E-33	**1568.52**	1.14E-31	**1695.80**	1.62E-33
1505.04	5.92E-33	**1570.34**	3.29E-30	**1721.73**	4.32E-30

Table 5.9. Optimized coordinates for **TDI₁**; Level of theory: ωb97X-D /DZP, SOLVENT (radius = 3.54 Å, dielectric = 5.62)

ATOM	X	Y	Z	ATOM	X	Y	Z
N	-16.27068	-0.06292	0.09882	C	-4.88604	0.05141	-0.05983
C	-17.72751	-0.11549	0.10832	C	-4.86011	1.67151	1.72892
H	-18.05352	-1.05298	0.54978	C	-4.86838	-1.56485	-1.85203
H	-18.09167	0.71939	0.69164	C	-3.47260	0.05280	-0.06442
H	-18.10148	-0.05234	-0.90990	C	-3.46812	1.63335	1.75351
C	-15.63225	0.97592	0.76010	H	-5.36190	2.29988	2.44817
C	-15.62535	-1.07561	-0.59031	C	-3.47669	-1.52365	-1.88583
C	-14.15496	0.98310	0.72427	H	-5.37357	-2.19366	-2.56851
O	-16.26365	1.83750	1.33686	C	-2.78058	-0.74649	-0.99558
C	-14.15046	-1.04816	-0.61459	C	-2.77631	0.85298	0.86277
O	-16.27004	-1.94317	-1.14401	H	-2.92177	2.22718	2.47293
C	-13.44776	-0.02308	0.04243	H	-2.93395	-2.11548	-2.60963
C	-13.46832	1.98171	1.36322	C	-1.31253	-0.74764	-1.03700
C	-13.46242	-2.02886	-1.27871	C	-1.30822	0.84723	0.90305
C	-12.03424	-0.00460	0.01738	O	-0.64830	-1.37464	-1.82473
H	-14.01659	2.75555	1.88182	N	-0.69095	0.04889	-0.06758
C	-12.07423	2.00153	1.35339	O	-0.64054	1.46980	1.69140
H	-14.00907	-2.81618	-1.77852	N	0.68005	0.03873	-0.06191
C	-12.06878	-2.01366	-1.31562	C	1.31126	1.05902	-0.78212
C	-11.34214	1.02928	0.70263	C	1.28897	-0.99074	0.66511
C	-11.34028	-1.02180	-0.69071	C	2.77923	1.03518	-0.73972
H	-11.58283	2.80669	1.87611	O	0.65525	1.87913	-1.37556
H	-11.57478	-2.80917	-1.85056	C	2.75732	-0.98724	0.64039
C	-9.87339	1.02469	0.70463	O	0.61453	-1.80173	1.25033
C	-9.87281	-0.98395	-0.73713	C	3.46524	0.01940	-0.04531
C	-9.17113	0.02583	-0.02365	C	3.48167	2.01494	-1.39238
C	-9.14952	1.97214	1.39187	C	3.43845	-1.97544	1.30301
C	-9.14948	-1.91214	-1.45057	C	4.88052	0.01044	-0.03596
C	-7.75048	0.03752	-0.03963	H	2.94455	2.78903	-1.92225
C	-7.75925	1.94788	1.42124	C	4.87318	2.01865	-1.37441
H	-9.64521	2.75609	1.94250	H	2.88499	-2.74276	1.82592
H	-9.64483	-2.69849	-1.99793	C	4.82978	-1.99626	1.30404
C	-7.76078	-1.86598	-1.50948	C	5.58844	1.04107	-0.71122
C	-7.04424	0.98692	0.74548	C	5.56593	-1.02854	0.64945
C	-7.04610	-0.90013	-0.84038	H	5.37653	2.81287	-1.90168
H	-7.25430	2.71760	1.98461	H	5.31674	-2.79499	1.83982
H	-7.25654	-2.62414	-2.08888	C	7.05634	1.03785	-0.68232
C	-5.58134	0.91788	0.82467	C	7.03380	-1.04360	0.64259
C	-5.58507	-0.81736	-0.93914	C	7.75011	-0.00623	-0.01302
				C	7.78868	2.02828	-1.29483

C	7.74439	-2.04555	1.26203	C	13.44852	-2.09380	1.27711
C	9.17289	-0.01380	-0.00029	H	11.55364	-2.90895	1.76742
C	9.17816	2.02608	-1.27524	C	14.14782	-1.08296	0.67207
H	7.30117	2.84075	-1.80986	C	14.16916	1.00626	-0.57392
H	7.23951	-2.85597	1.76335	H	14.04949	2.82071	-1.66673
C	9.13379	-2.05831	1.26693	H	13.98733	-2.89640	1.76064
C	9.88919	1.03215	-0.64389	C	15.62493	-1.10851	0.68714
C	9.86621	-1.06797	0.65483	C	15.64441	1.00866	-0.55771
H	9.68317	2.83527	-1.77855	O	16.24504	-2.01242	1.20877
H	9.62152	-2.87618	1.77320	N	16.27675	-0.04535	0.07972
C	11.35791	1.03383	-0.62297	O	16.30001	1.89128	-1.07348
C	11.33474	-1.08349	0.66434	C	17.73414	-0.01481	0.08730
C	12.03993	-0.02805	0.02813	H	18.10687	-0.05904	-0.93253
C	12.09911	2.03529	-1.21720	H	18.07336	0.90698	0.55094
C	12.05443	-2.09118	1.27420	H	18.08673	-0.86859	0.65001
C	13.45359	-0.03478	0.04265				
C	13.49311	2.02403	-1.19308				
H	11.61552	2.85865	-1.71830				

Appendix C: Supplementary Information for Chapter 6

C.1. Additional experimental details

During pulse shaping, masks to compensate for the frequency-dependent Bragg angle[223] were employed to help compress the pulse (Figure S6.1). To minimize the detrimental effects of spatial chirp and walk-off on observing wavepacket signatures, we fixed the angle between the pump and probe beamlines to less than three degrees. Example 2DES spectra for each signal contribution, which were separated as described in Section 2.5.1, are shown in Figures S6.2 and S6.3. Replicate experiments (*vide infra*) were conducted on different days with different solvent aliquots to ensure results were not correlated to laser fluctuations or solvent impurities. A representative SHG-FROG trace is shown in Figure S6.1, where the measured pulse width was approximately 10 fs. Across all experimental trials, the pulse duration ranged between approximately 10 and 15 fs.
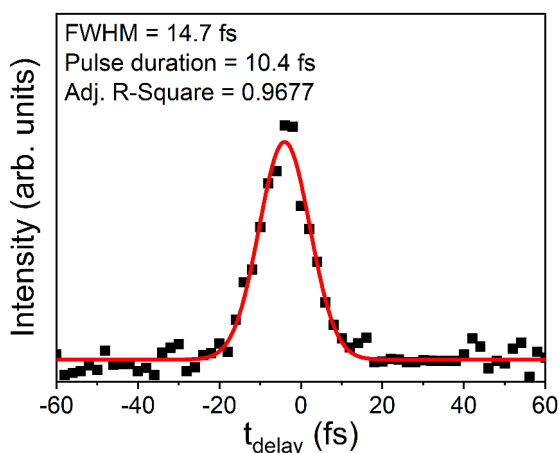
Figure S6.1. An example SHG-FROG trace at 313 nm for the pump pulse overlaid with a Gaussian fit (FWHM = 14.7 fs), indicating a pulse duration of approximately 10 fs.

C.2. Additional theoretical details

Based on our extraction of Huang-Rhys factors using comparisons between the simulated and experimental absorption spectra (*vide infra*), we defined λ for the 550 cm^{-1} mode in relation to that of the 1350 cm^{-1} vibration using their relative intensities in the experimental femtosecond stimulated Raman spectroscopy (FSRS) data. Using the methods described in Chapter 3, we simulated the linear response of TDI (Figure 6.3a) and extracted Huang-Rhys factors of 0.42 and 0.13 for the 1350 and 550 cm^{-1} vibrations, respectively. Table 6.1 shows a summary of all parameters used to dress the model Hamiltonians and calculate response functions.

Table 6.1. An overview of the parameters employed in these simulations

Hamiltonian Parameter	Value	Response calculation parameter	Value/range
ε_{S_1}	15125 cm^{-1}	t_1, t_3	0 to 186 fs
ε_{S_n}	26625 cm^{-1}	t_2	0 to 1000 fs
ω	550, 1350 cm^{-1}	Δt	3 fs
λ_{550,S_1}	0.356	Δ (t_1, t_3 evolution)	2000 cm^{-1}
λ_{1350,S_1}	0.648	t_c (t_1, t_3 evolution)	40 fs
λ_{550,S_n}	0.712	Δ (t_2 evolution)	100 cm^{-1}
λ_{1350,S_n}	1.296	t_c (t_2 evolution)	300 fs
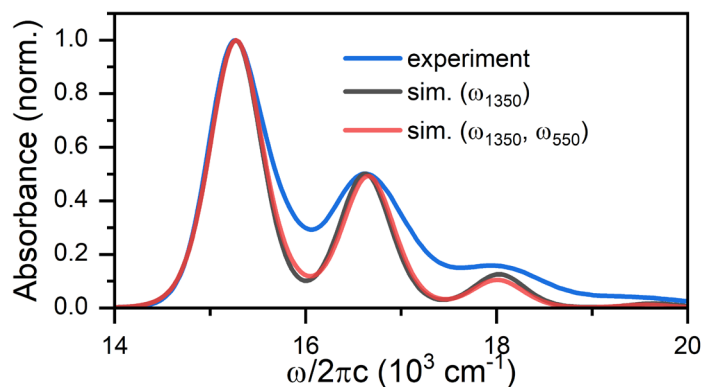
Figure S6.2. A comparison of two simulated linear absorption spectra for TDI and an experimental spectrum. One simulation (gray) included solely the 1350 cm^{-1} vibration ($\lambda^2 = 0.497$), while the second (red) included both the 1350 ($\lambda^2 = 0.420$) and 550 cm^{-1} ($\lambda^2 = 0.127$) vibrations.

Figure S6.3 illustrates schematics for an example multiple-DHO model for two arbitrary vibrations, α and β. Allowing a maximum of two vibrational quanta for each mode, the basis set for this system has ten kets, where each is color-coded to indicate which vibration they describe. Both α (red) and β (blue) vibrations are characterized by three configurations on the both the electronic ground and excited states. Importantly, both vibrations share global zero-point kets on these two electronic states, which are highlighted in purple. Translating this basis set into a multiple-DHO Hamiltonian (Equation 20, Section 3.3.1) generates the matrix on the right of Figure S6.3, which uses the same color-coded scheme to indicate non-zero entries (except for the diagonal value for site 1 which serves as a reference point with energy equal to zero). Sites one through five correspond to electronically ground-state configurations, making this block of the Hamiltonian diagonal since the ground electronic surface is unshifted in the nuclear coordinate system. In contrast, the block encompassed by sites six through ten contains off-diagonal elements that arise from the linear vibronic coupling, or rather the shifted nature of the electronically excited state. Importantly, while the α and β vibrations are defined to be independent in the site basis, both have off-diagonal coupling elements with the global zero-point vibrational configuration on the electronic excited state ($|1,0,0\rangle$), as indicated by the black arrows originating from the $|1,1,0\rangle$ and $|1,0,1\rangle$ kets (and the H.C. bras). The values of these matrix entries are equivalent to $\omega_m \lambda_m$ for vibration m. When $\omega_\alpha \lambda_\alpha$ and $\omega_\beta \lambda_\beta$ are *both* greater than zero, meaning that both oscillators have non-zero HR factors, diagonalization of the Hamiltonian in Figure S3 results in eigenstates of mixed vibrational character, with the degree of mixing dependent on both λ_α and λ_β.
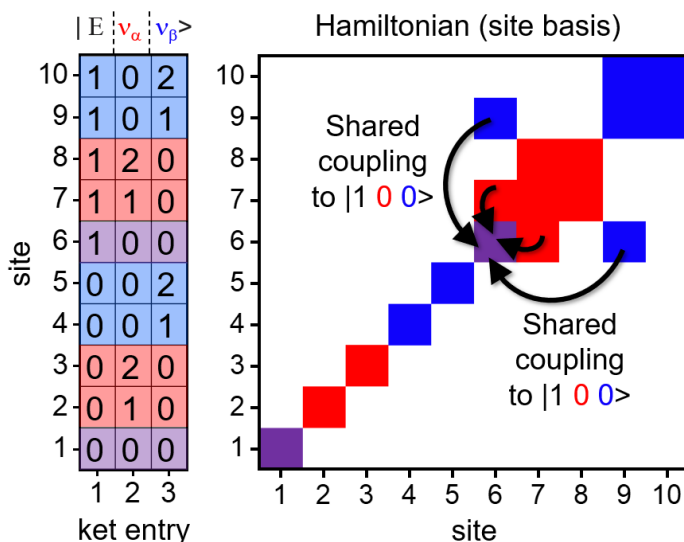
Figure S6.3. A schematic illustrating an example multiple-DHO basis set (two vibrations with two quanta each) and site-basis Hamiltonian. The diagrams are color coded with red and blue signifying the 550 and 1350 cm^{-1} vibrational coordinates, respectively, while purple indicates relevance to both vibrations. The colored indices in the Hamiltonian indicate non-zero values, except for the diagonal purple entry for site 1 which is set to zero as a reference point for all other entries.

C.3. Data Analysis

We achieved pump energy resolution (ω_1) and isolated quantum beating signatures as described in Section 2.5. In our use of approach 2 for subtracting population kinetics, we included oscillatory components below a threshold frequency of 150 cm^{-1} within our fit. This was done to combat the occasional tendency of rapid population dynamics to be fit as quickly dephasing, low-frequency oscillations. We additionally truncated each vector in the t_2 dimension to near $t_2 = 100$ fs to avoid contamination from cross-phase modulation and offset the data by a corresponding number of zeros to ensure no systematic frequency shifts when comparing datasets. We zero-padded time-domain quantum beats to either twice the original vector length, in the case of quantum beatmaps, or 2^{10} for calculation of the Frobenius norm power spectra. For the data discussed in the main text, the unpadded data traces ranged from 100 to 1600 fs with a timestep of

8 fs, which implies a frequency resolution of about 21 cm^{-1} in the Fourier power spectra. We calculated all experimental 2DES power spectra using a Frobenius norm over a 200 x 200 cm^{-1} window in the pump and probe frequency dimensions. This window was centered at the location of the maximum beating amplitude of the 543 cm^{-1} oscillation. This approach avoids bias in the representation of power spectra from the 2DES dataset and additionally increases the signal-to-noise ratio.

C.4. Additional and replicate 2DES spectra

Figure S6.4 illustrates an expanded view of Figure 6.3b, showing the ESA features of the experimental and simulated 2DES spectra. Figure S6.5 provides additional time-domain 2DES spectra for TDI in THF from two different experimental trials. Figure S6.6 shows the rephasing and non-rephasing contributions to the absorptive signals shown in Figures S6.5b and S6.5c.
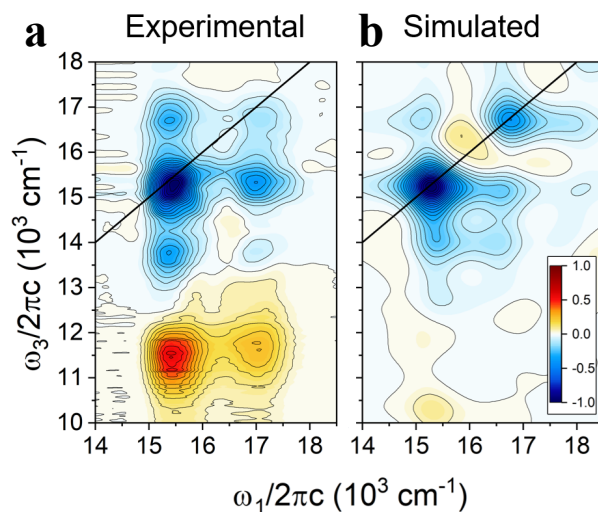
Figure S6.4. (a) Experimental and (b) simulated 2DES spectra at a waiting time $t_2 = 100$ fs. Contours are plotted at 5% intervals with 10% contour lines darkened. The spectrum in (a) is smoothed with an 11th order moving average with a Gaussian filter.
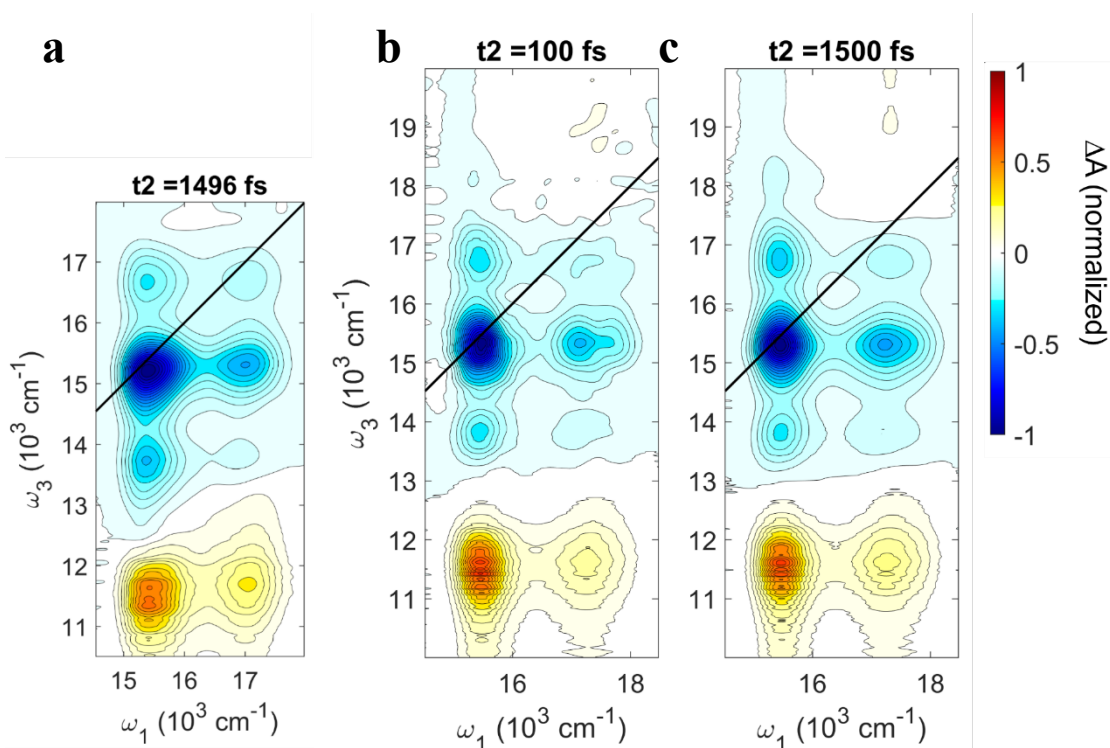
Figure S6.5. Absorptive TDI (in THF) 2DES spectra for (a) the dataset discussed in the main text and (b and c) a replicate trial at waiting times of (a) 1496, (b) 100, and (c) 1500 fs. All spectra are smoothed in the probe dimension with a gaussian filtered moving average.
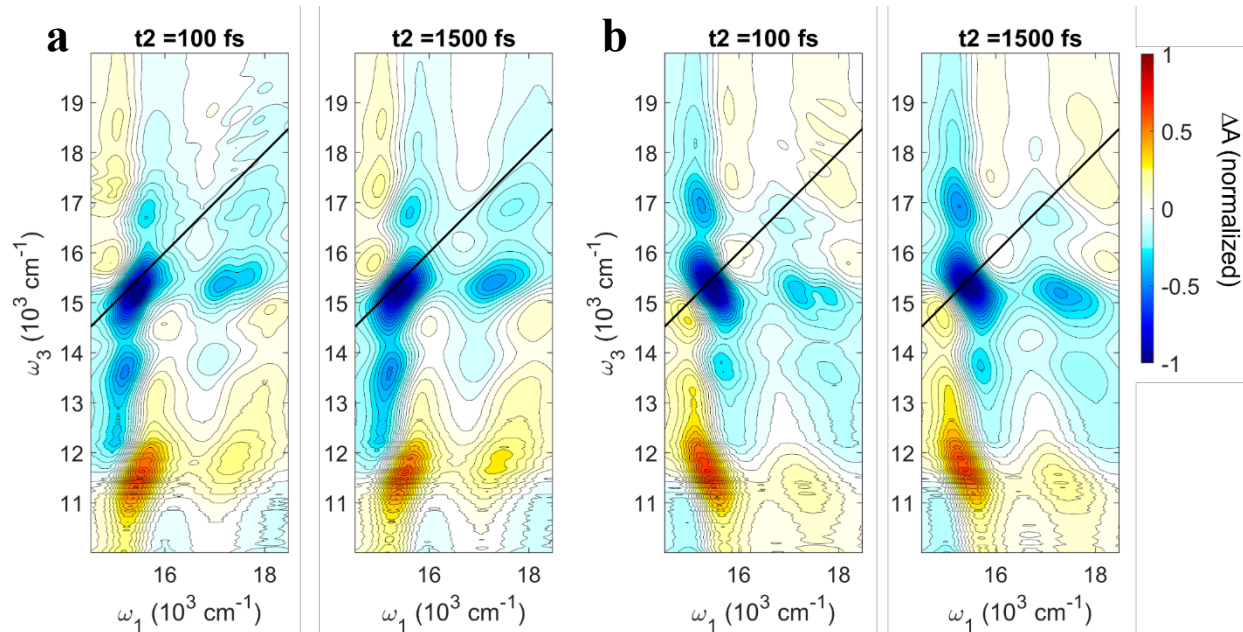
Figure S6.6. Real (a) Rephasing and (b) non-rephasing 2DES spectra for TDI in THF at waiting times near 100 and 1500 fs. All spectra are smoothed in the probe dimension with a gaussian filtered moving average.

C.5. Additional power spectra

Figure S6.7 shows a power spectrum from a replicate measurement of TDI in THF. Despite the difference in t_2 step size ($\Delta t_2 = 5$ fs), the prominent features remain near within the frequency
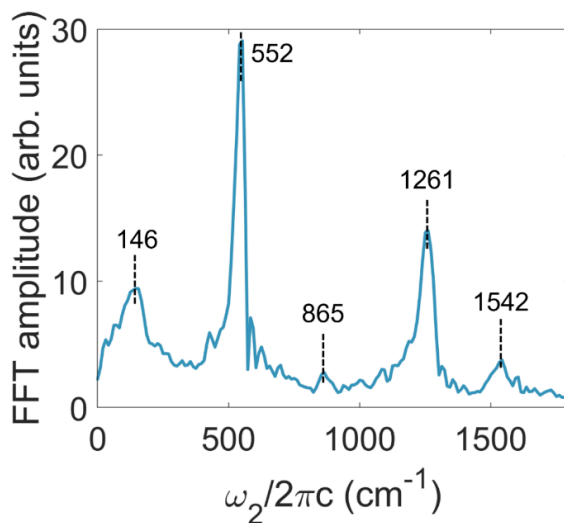
Figure S6.7. A replicate experimental power spectrum for TDI in THF. These data were collected with a t_2 time step size of 5 fs.

resolution of the peaks observed from the power spectrum obtained with $\Delta t_2 = 8$ fs (Figure 6.4a). We note that the peaks near 865 and 1260 cm^{-1} likely correspond to the 800 and 1300 cm^{-1} modes in Figure 6.4a. Similarly, the dataset shown in Figures S6.5 and S6.6 identify these peaks near 800 and 1270 cm^{-1}. The frequency differences between these results may originate from the frequency resolution in the ω_2 domain and/or variations in experimental conditions between the independent measurements. We expect excited-state signatures, such the 800 cm^{-1} beat frequency, to be particularly sensitive to the latter explanation due to their more rapid dephasing and lesser amplitude relative to quantum beats from ground-state vibrational coherences. In addition to the impact from the aforementioned factors, the window over which the power spectra are calculated (ω_1 and ω_3 ranges for 2DES, ω_3 range for TA) may drive the observed differences in relative amplitude of the feature between 800 and 860 cm^{-1}. We do not concentrate on variations in relative amplitude because the conclusions from this work do not rely significantly on the relative amplitude of quantum beats.

To further confirm that the Fourier features observed in our 2DES measurements were not the product of laboratory noise, we examined the quantum beating signatures in three consecutive transient absorption measurements with $\Delta t_2 = 5$, 6, or 7 fs (Figure S6.8). Importantly, no features were observed to vary significantly in frequency as a function of the step size, indicating that the quantum beats originate from solute and/or solvent coherences.[356] Moreover, Figure S6.9 verifies that all peaks, with exception to the feature near 900 cm^{-1}, originate from the TDI solute.
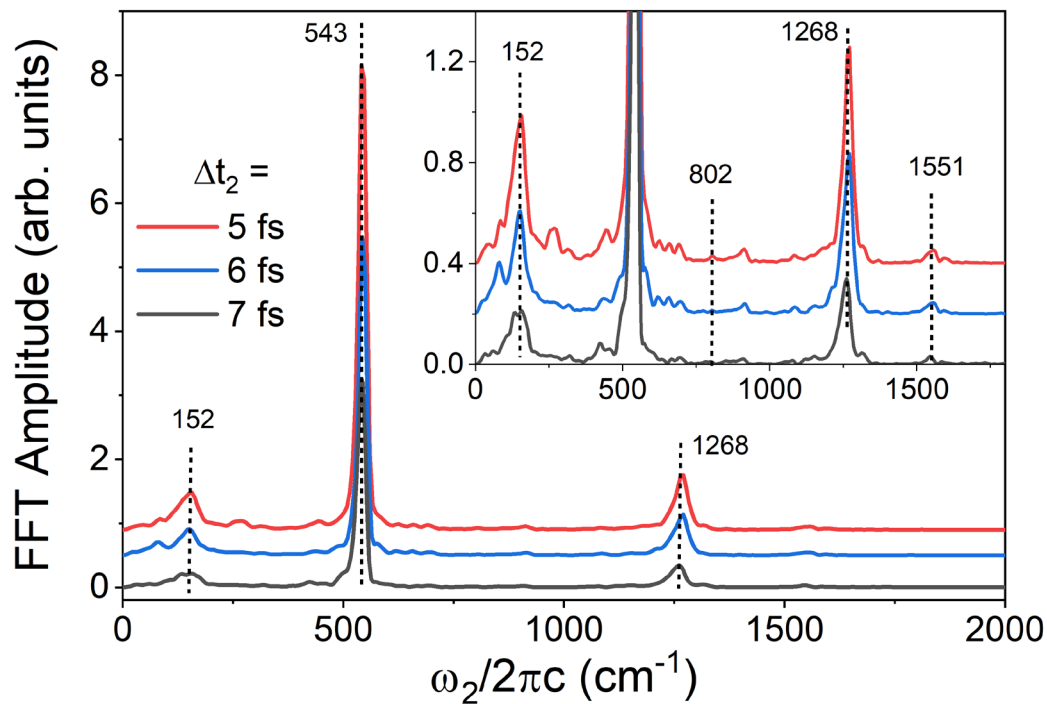
Figure S6.8. Power spectra for TDI in THF obtained from transient absorption scans ranging from 100 to 2500 fs in waiting time domain with step sizes of 5, 6, or 7 fs. Each trace was obtained by integrating the FFT signals across the probe region between $\omega_3 = 13000$ and 16000 cm^{-1}.
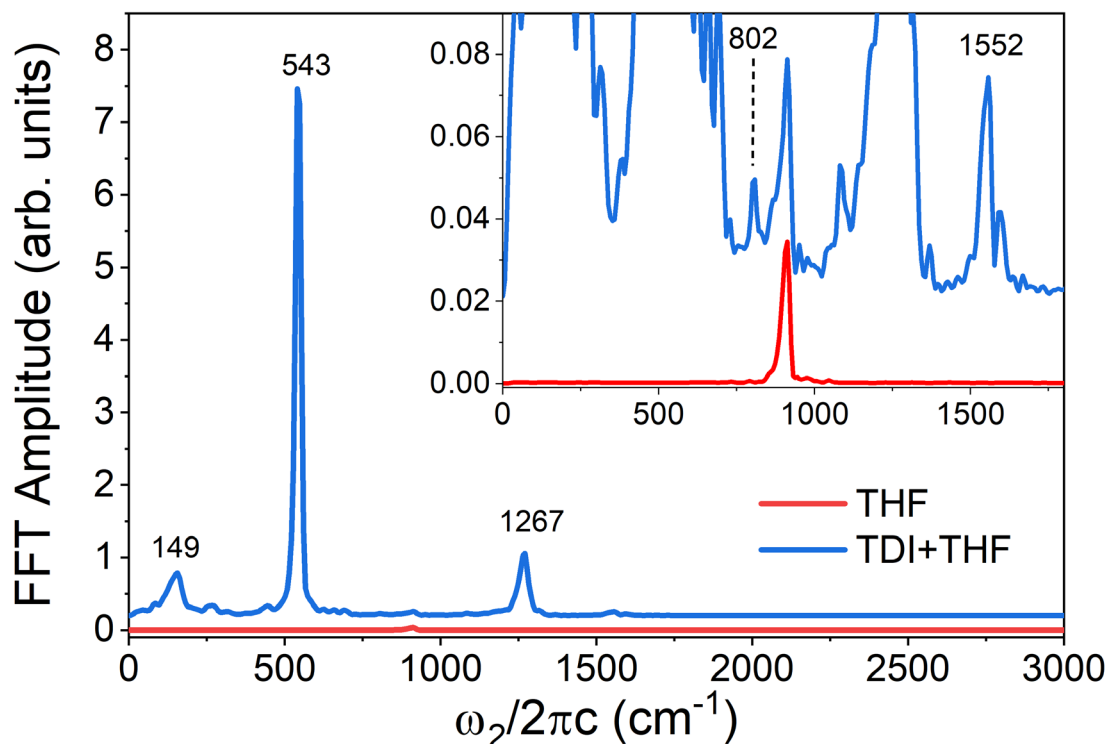
Figure S6.9. Experimental power spectra for TDI in comparison to a neat THF blank.

C.6. Additional and replicate quantum beatmaps

Figure S6.10a illustrates the single-DHO picture for both the 550 and 1350 cm^{-1} vibrations in the case that their wavepacket motions are completely independent. The experimental absorptive quantum beatmap for the 550 cm^{-1} oscillation frequency of TDI is shown in Figure S6.10b, which is in good agreement with our previous experimental work.[157] In line with our discussions of the rephasing beatmaps in Figure 6.5, we find that the single-DHO model is unable to predict several features of the experimental beatmap, particularly those located far from the diagonal line. In contrast, the beatmap obtained from the multiple-DHO simulation (Figure S6.10d) reproduces many of these features, as highlighted by the colored circles in both Figures S6.10b and S6.10d.

In the case of the comparison denoted by the purple circles, we attribute the difference in probe

frequencies between the peaks to the ~300 cm^{-1} Stokes shift characteristic of TDI in THF,[157, 283]

which is not included within the simulation. Additional differences between the positions of the

identically colored circles between Figure S6.10b and S6.10d are attributed to imperfections of the

theory, primarily the fact that we only treated two of the several FC-active vibrations of TDI.

Another possible factor is the large linewidth associated with electronic transitions. In the absence

of an ab initio treatment of the system-bath interactions, additional deviations between the center

locations of the experimental and theoretical beatmap features are possible.
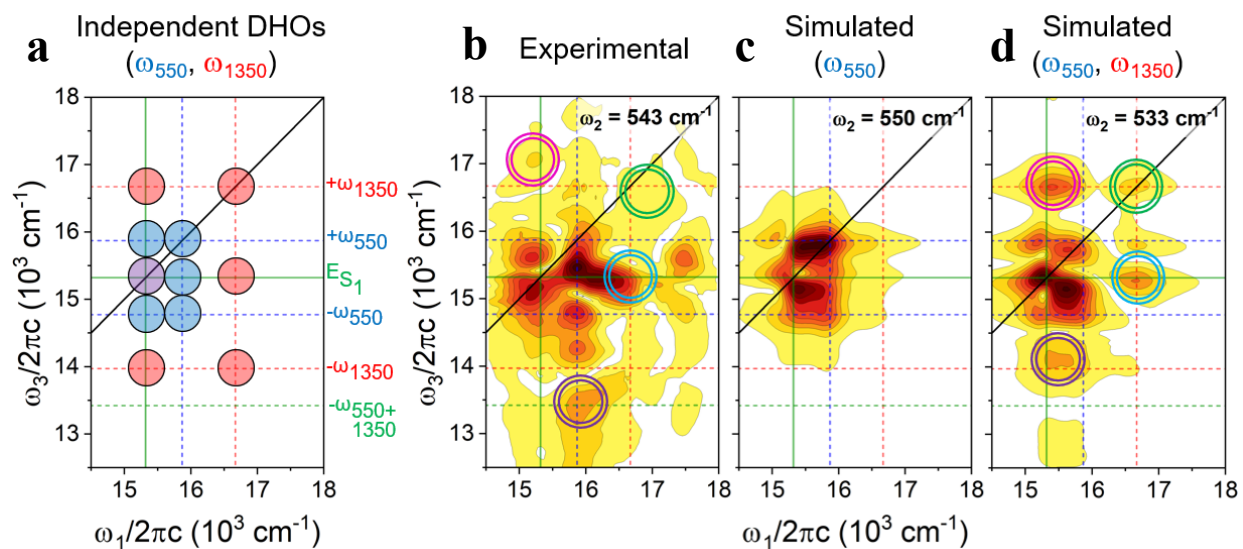
Figure S6.10. Absorptive quantum beatmaps from (a) a schematic picture of individual 550 and 1350 cm^{-1} vibrations, (b) experimental 2DES data, and third-order signals simulated with the (c) single-DHO and (d) multiple-DHO Hamiltonians. The solid green lines indicate the 0-0 singlet electronic transition energy for all vibrations. Dotted lines are color-coded to match the code used in the titles (blue = 550 cm^{-1} mode, red = 1350 cm^{-1} mode) and indicate energies that represent either one or two frequency quanta away from the 0-0 singlet transition energy in either the pump (vertical lines) or probe (horizontal lines) axis. Colored circles in (b) and (d) highlight features that are not accounted for within the single-DHO approximation.

While the separation of rephasing and non-rephasing signals from experimental 2DES data

collected in the pump-probe geometry is a well-established process,[50, 224] analysis of quantum

beating signatures in these signal components is less common. To this end, Figure S6.11 shows

two absorptive quantum beatmaps for the 550 cm^{-1} mode of TDI collected with both phase cycling

schemes discussed in Section 2.5.1. The agreement between these beatmaps indicates the ability

of scheme 2 (Eq. 11) to reproduce absorptive quantum beating signatures as the sum of the real

rephasing and non-rephasing signals. We believe this result indicates that the separation of

rephasing and non-rephasing quantum beats via scheme 2 is a valid approach.
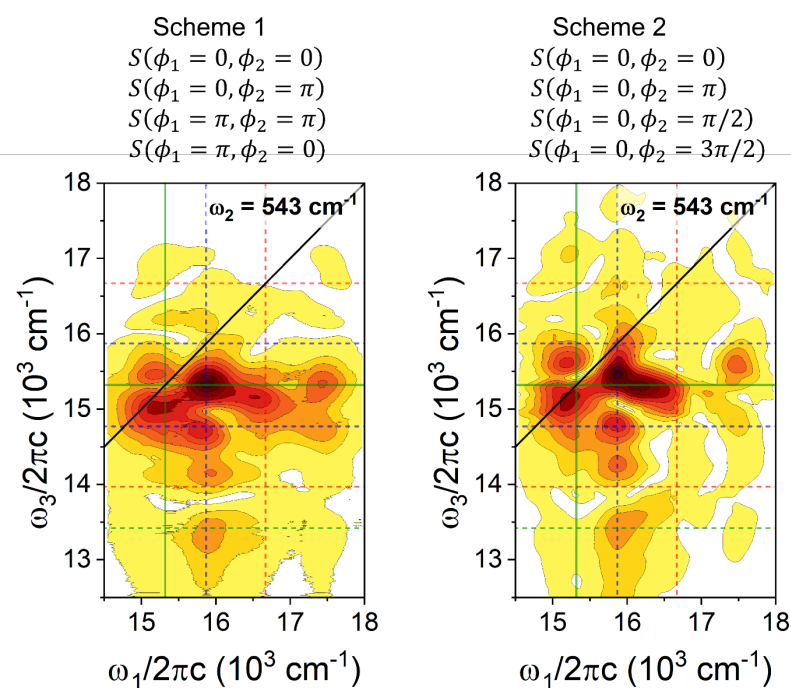
Figure S6.11. Comparison between absorptive TDI beatmaps obtained using the phase cycling schemes detailed above each figure. Scheme 1 yields purely absorptive signal while the real portions of the rephasing and non-rephasing signals from scheme 2 were combined to extract the absorptive signal.

Figure S6.12 provides the non-rephasing counterparts to the experimental rephasing

beatmaps presented in the main text, while Figures S6.13 and S6.14 show replicate quantum

beatmaps for all signal components from two different measurements. In addition, Figure S6.15

provides beatmaps for several additional beat frequencies observed in the power spectrum shown

in Figure 6.4.
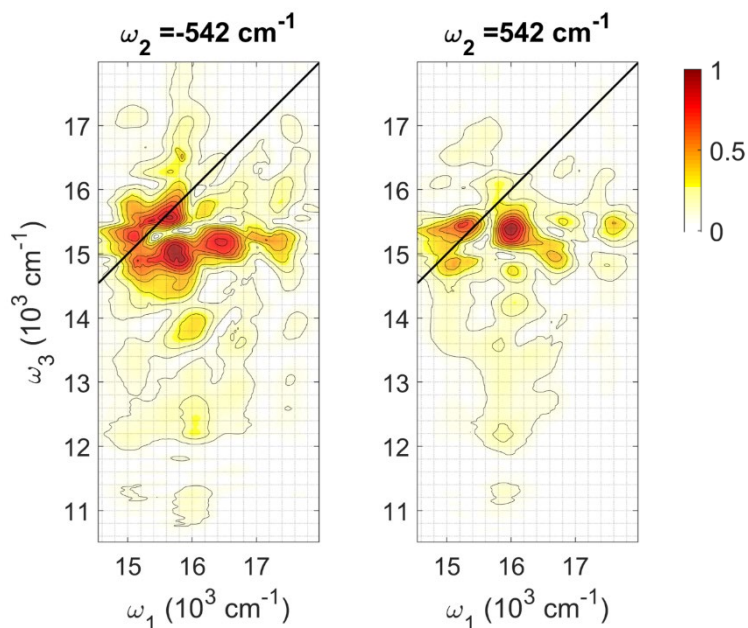
Figure S6.12. Experimental non-rephasing quantum beatmaps, associated with the data presented in Figures 6.5 and 6.6 within the main text, at the beat frequencies of -542 (left) and +542 cm^{-1} (right). These data were collected with a t_2 time step size of 8 fs.
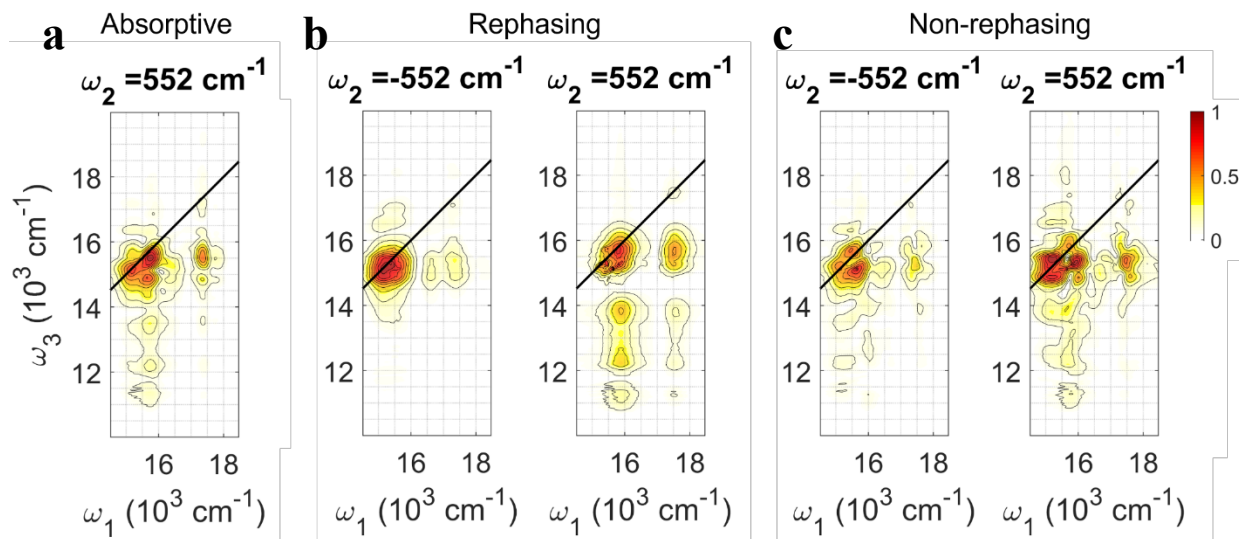
Figure S6.13. Replicate experimental (a) absorptive, (b) rephasing, and (c) non-rephasing quantum beatmaps for TDI dissolved in THF at the oscillation frequencies indicated above each plot. These data were collected with a t_2 time step size of 5 fs.
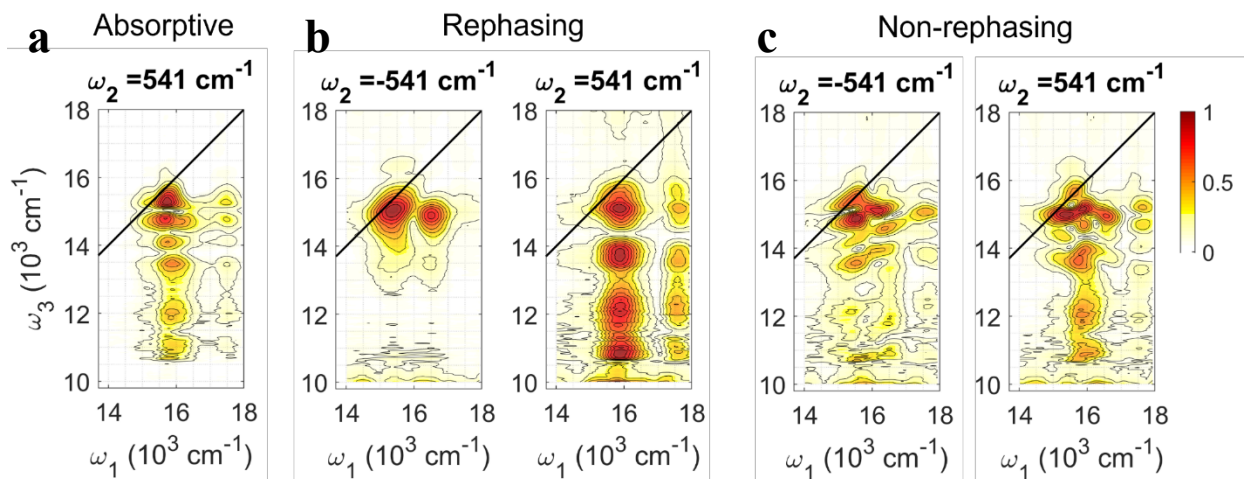
Figure S6.14. Replicate experimental (a) absorptive, (b) rephasing, and (c) non-rephasing quantum beatmaps for TDI dissolved in toluene at the oscillation frequencies indicated above each plot. These data were collected with a t_2 time step size of 8 fs.
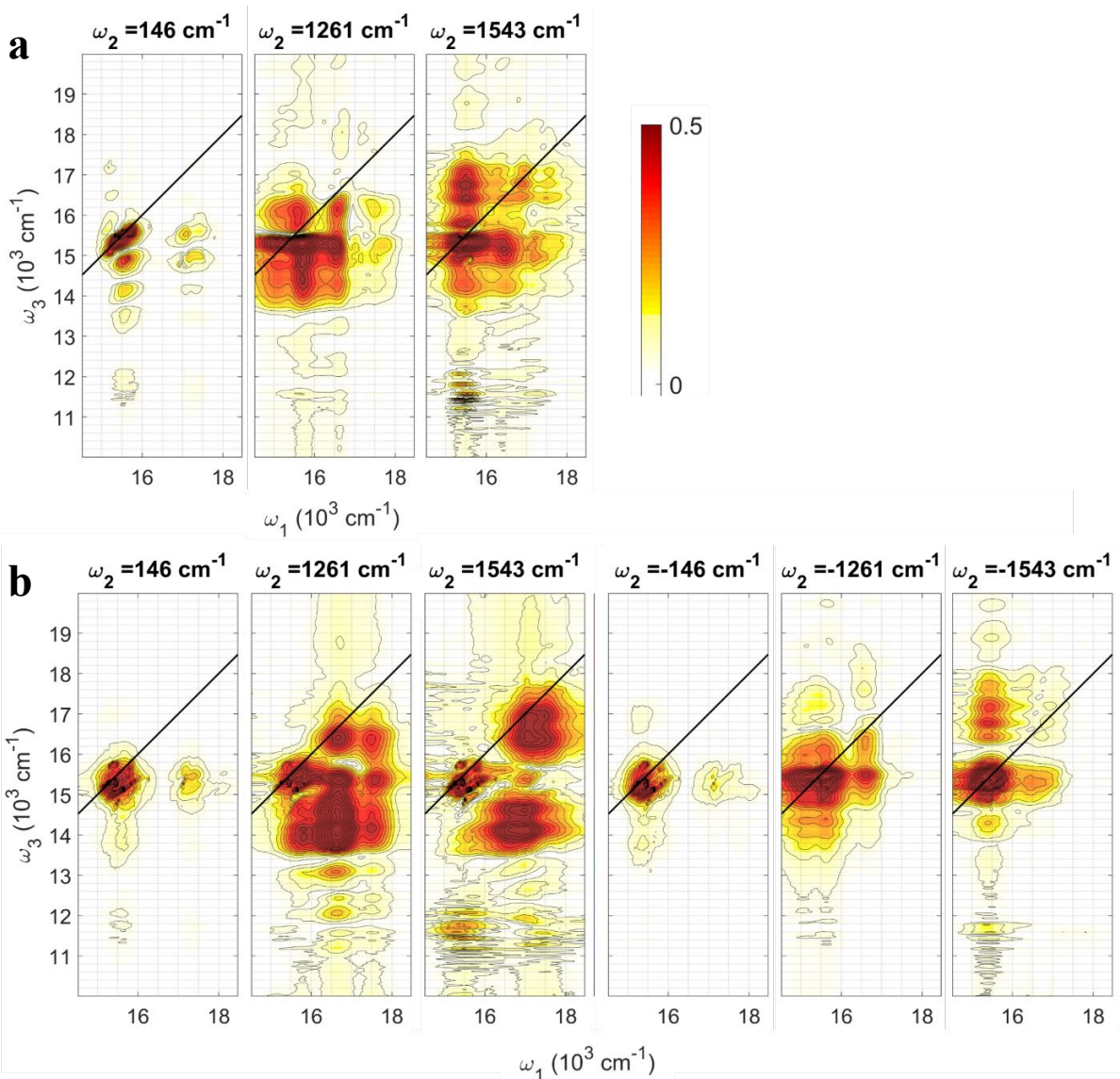
Figure S6.15. Additional (a) absorptive and (b) rephasing quantum beatmaps for TDI in THF at beat frequencies denoted above each plot.

C.7. Additional simulated quantum beatmaps

Figure S6.16 shows simulated non-rephasing TDI quantum beatmaps using both the single-DHO (a) and multiple-DHO (b) models. Similar to the insights drawn from the rephasing and absorptive beatmaps for these models, the non-rephasing simulations indicate that harmonic

coupling between the 550 and 1350 cm^{-1} modes yields additional features in both the $\omega_2 = -533$ and $+533$ cm^{-1} beatmaps.
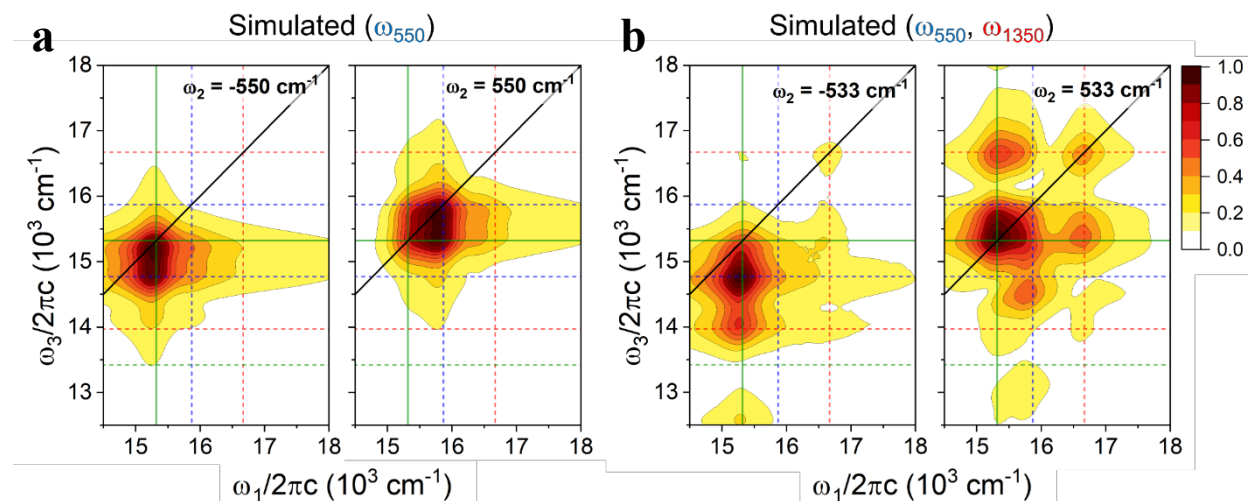
Figure S6.16. Simulated non-rephasing beatmaps for the (a) single-DHO and (b) multiple-DHO Hamiltonians. Beatmaps for both -550 and +550 cm^{-1} beat frequencies are provided.

Figure S6.17 shows a decomposition of the multiple-DHO TDI simulation into positive and negative beat frequencies for each response function defined by Equations 29-34 (Section 3.4). We note that while our analysis here focused predominantly on the GSB and SE response functions, we find that vibronic coupling between harmonic oscillators also impacts the beatmaps extracted from ESA pathways, as shown in Figures S6.17e and f. Explorations of this influence on the ESA beatmaps are ongoing.
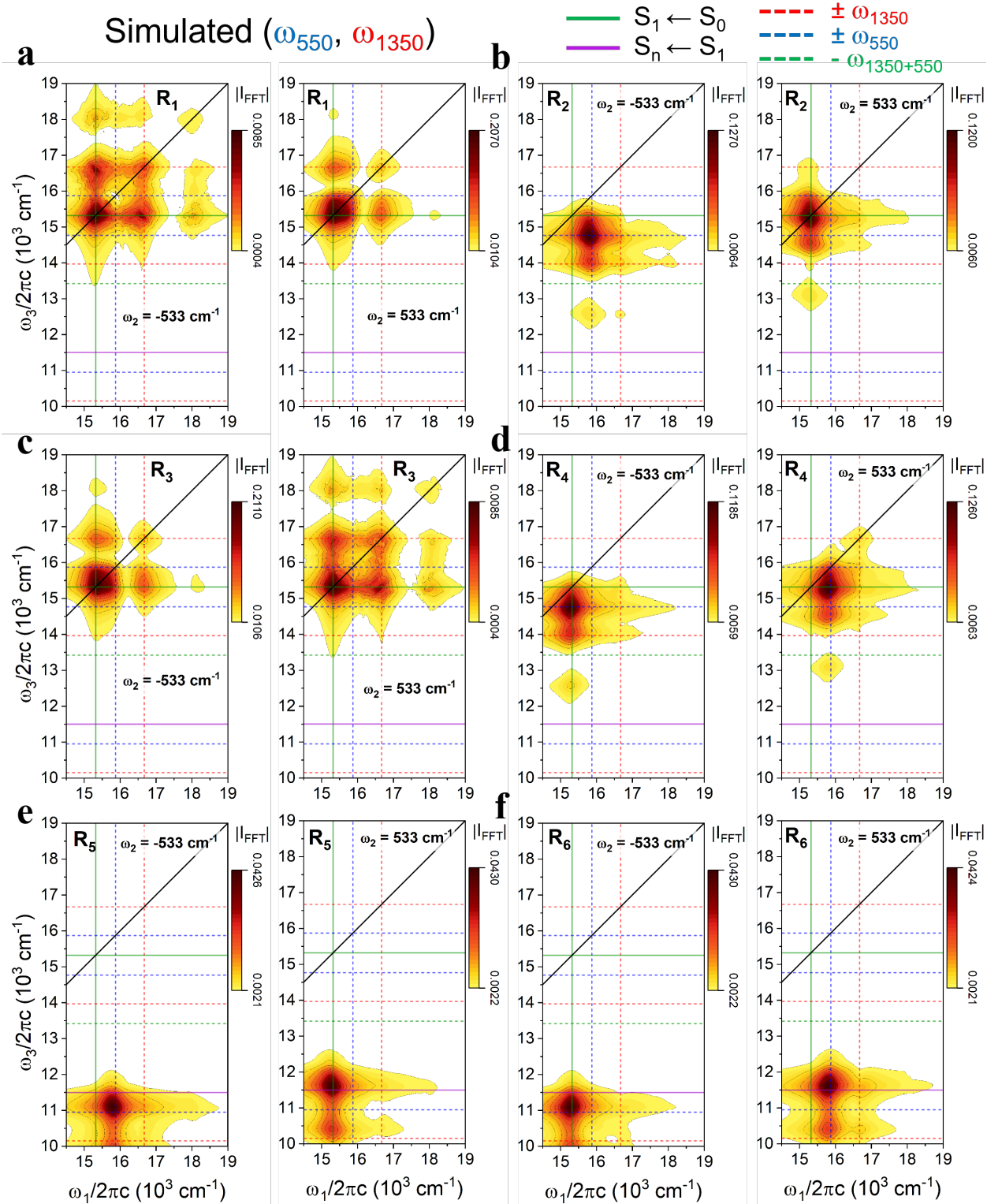
Figure S6.17. Quantum beatmaps for the multiple-DHO TDI simulation for $\omega_2 = -533$ and $+533$ cm^{-1} for the (a) R1, (b) R2, (c) R3, (d) R4, (e) R5, and (f) R6 portions of the total response function. All spectra are normalized to maximum beat signal in the full simulated dataset.

C.8. Additional experimental and theoretical comparisons

Figures S6.18 compares the experimental and simulated absorptive beatmaps for the ~800 cm^{-1} signal oscillations. While differences are apparent between the two beatmaps, such as the broader distribution of amplitude along the ω_1 axis in the experimental results, we observe qualitative agreement.
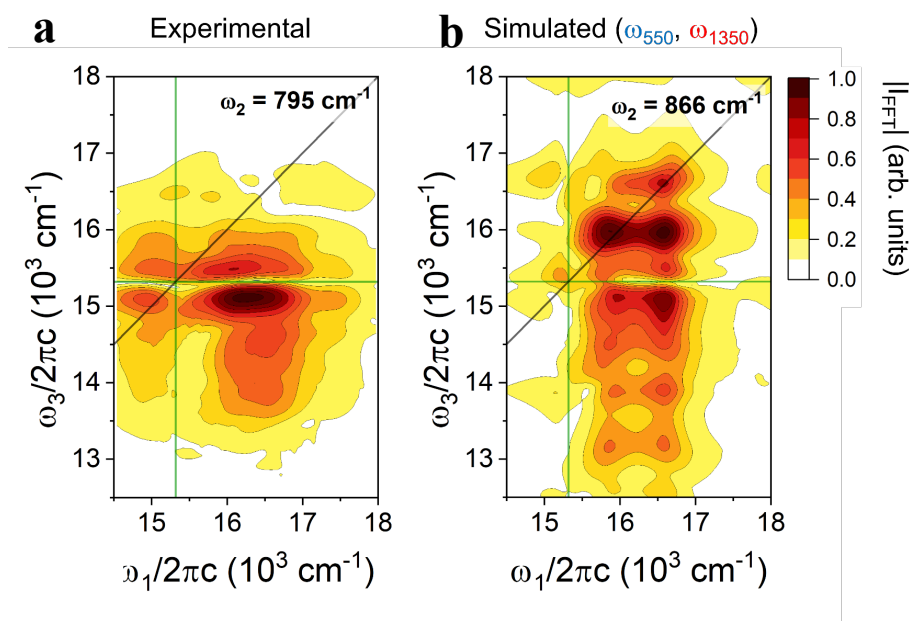
Figure S6.18. (a) Experimental and (b) simulated beatmaps for the ~800 cm^{-1} signal oscillation observed for TDI. Both plots are normalized to their respective maximum amplitude.

Appendix D: Original Research Proposal

D.1. Title and abstract

Disentangling the roles of vibrations in ultrafast photochemistry using resonant fifth-order spectroscopy

Many important photochemical reactions have been shown to be mediated by a complex interplay of vibrational and electronic degrees of freedom. However, tools the probe excited-state evolution along multidimensional potential energy surfaces in real time are scarce. As such, the precise roles that vibronic and vibrational couplings play in photochemical processes, such as photosynthesis and charge transfer, remain obscure. Two-dimensional impulsive stimulated Raman spectroscopy (2D-ISRS) was recently demonstrated to reveal coupling between vibrational coordinates during ultrafast photoisomerization of photoactive yellow protein. Owing to the lack of descriptive 2D-ISRS theories, the physical origin of many features in experimental 2D-ISRS results remains unclear. This proposed research aims to develop efficient codes for simulating 2D-ISRS signals that emerge from common molecular Hamiltonians. By confirming the ability of the simulations to reproduce experimental observations, the insights gained through this research will offer valuable guidance for future 2D-ISRS studies.

D.2 Introduction, Background, and Significance of the Research

The functions and possible utility of coupling between electronic and vibrational (vibronic) degrees of freedom is of broad interest for improving macroscopic technologies, such as solar photovoltaics,[238] using quantum mechanical phenomena.[222] Vibronic coupling is suggested to have profound impacts on important chemical reactions, such as energy and charge transfer in natural[13, 19] and artificial photovoltaics.[215] Several theoretical studies have predicted that the spatiotemporal delocalization induced by nonadiabatic interactions can enhance the efficiency of energy[106, 195] and charge[155] transport through coupled molecular networks. A previous investigation of a well-known, high-performing OPV blend, P3HT:PCBM, posited that the ultrafast electron transfer from the P3HT donor to the PCBM acceptor is reliant on bridging of the HOMO-LUMO gap by an intramolecular vibration.[215] There is a clear need to improve our current understanding of vibronic phenomena and, in turn, pave the way for establishing vibronic coupling as a tunable design parameter.

The notion that nonadiabatic photochemistry can be enabled by a resonant vibration[107, 258] emerged from expansive research of vibronic coupling in natural photosynthetic organisms.[13, 16] As more focus has been shifted to synthetic molecular aggregates, an increasing number of studies are finding that an *interplay* of multiple vibrational coordinates[305, 357] is needed to capture the mechanisms of several ultrafast photochemical processes, including singlet fission,[157, 159, 165, 203, 208] and electron transfer.[164] However, as even small molecules have an enormous number of normal modes (3N-6 with N equal to the number of atoms), separating the roles of reactive vibrations from motions that merely "spectate" population evolution is an ongoing challenge.[68, 164, 208, 305, 357] This challenge is amplified by the tendency of signatures from vibrational couplings to be obscured by

single-mode wavepackets in established experimental techniques such as two-dimensional electronic spectroscopy (2DES).

While two-dimensional infrared spectroscopy (2DIR) and two-dimensional electronic-vibrational (2DEV)[108, 111, 124, 358, 359] directly probe couplings between vibrations, the precise *function(s)* of these couplings can remain ambiguous from the perspective of these approaches. In contrast, two-dimensional impulsive stimulated Raman spectroscopy (2D-ISRS) is an emerging technique that uses multidimensional wavepacket evolution to simultaneously the nature *and* chemical function of coupled nuclear trajectories.[130, 360] Experimental 2D-ISRS results were first reported in 2019, where Kuramochi and coworkers revealed the presence of low- and high-frequency vibrational couplings during the excited-state isomerization of photoactive yellow protein (PYP).[131] However, the sheer complexity of the 2D-ISRS signals precluded interpretation of features other than a single cross-peak and therefore obscured the role of these couplings in the photoisomerization process. Fully realizing the insight afforded by this technique requires descriptive and comprehensive theoretical simulations of spectra for relevant multichromophoric systems. To date, theoretical descriptions of 2D-ISRS signals have yet to be developed beyond the harmonic oscillator (HO) model.[130]

D.3 Scientific Objectives

This research proposal aims to study the *information content* and *capacity* of 5$^{\text{th}}$-order two-dimensional impulsive stimulated Raman spectroscopy (2D-ISRS) to **reveal chemically reactive vibrational coordinates**. This overall objective is broken down into three specific aims:

Phase 1: To develop an efficient theoretical framework for simulating 2D-ISRS signals.

Phase 2: To explore the predictive power of 2D-ISRS theory by reproducing trends from

experiments of ultrafast photoisomerization of photoactive yellow protein (PYP).

Phase 3: To simulate 2D-ISRS spectra for a wide range of molecular Hamiltonians and identify

salient features that most effectively distinguish molecular properties of interest.

D.4. Previous Work

2D-ISRS is a newly developed technique that derives from time-resolved impulsive

stimulated Raman spectroscopy (TR-ISRS), which is a well-established technique that has been

used to study structural evolution during photochemical processes such as charge transfer,[298, 299,]

[303] excimer formation,[303] singlet fission,[203] proton transfer,[360] and photoisomerization.[361, 362] Figure

D.1(a) illustrates that both TR-ISRS and 2D-ISRS experiments use actinic pump (AP), Raman

pump (RP), and probe (P) pulses. As shown by Figure D.1(b), the AP pulse promotes the system

from the ground state ($|G\rangle$) to the electronic excited state ($|E\rangle$ in this example), where vibrational

coherences may be launched in addition to populations (off-diagonal and diagonal density matrix

elements, respectively, in the energy-eigenstate basis). This non-equilibrium configuration evolves
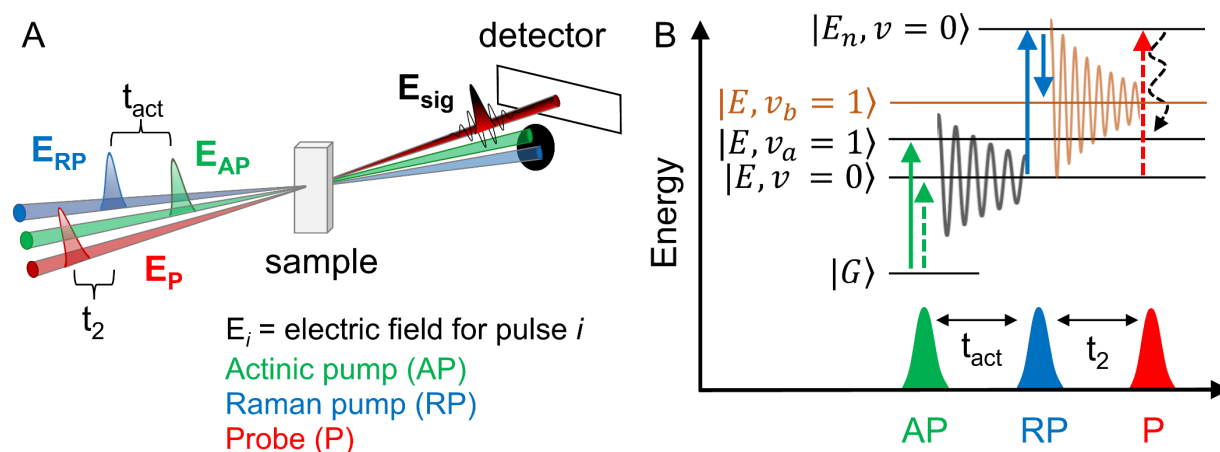
Figure D.1. (a) Pulse schematic for TR-ISRS and 2D-ISRS. (b) Example wave-mixing energy level (WMEL) diagram for 2D-ISRS.

over the time delay t_{act}, after which a RP pulse (resonant with a $E_n \leftarrow E$ transition) stimulates vibrational wavepackets on $|E\rangle$ that evolve over t_2 prior to interacting with the P pulse and emitting a signal photon.

By examining the Fourier power of wavepackets along t_2, numerous groups have used TR-ISRS to measure structural dynamics as a function of t_{act}. The key difference between TR-ISRS and 2D-ISRS is that the latter can selectively reveal and correlate wavepacket evolution over *both* t_{act} and t_2. Kuramochi and coworkers[131] recently used this capability to study the ultrafast *trans-to-cis* photoisomerization of p-coumaric acid (pCA), which is embedded in PYP. By compressing both the actinic (ca. 35 fs) and Raman pump (ca. 7 fs) pulses, the authors extracted 2D-ISRS quantum beatmaps (Figure D.2A) that correlate pumped (AP) and probed (RP) wavepackets that evolve over t_{act} and t_2, respectively. Off-diagonal peaks in this representation therefore indicate coupling between discrete vibrational modes.[131] As indicated by a white arrow in Figure D.2A,
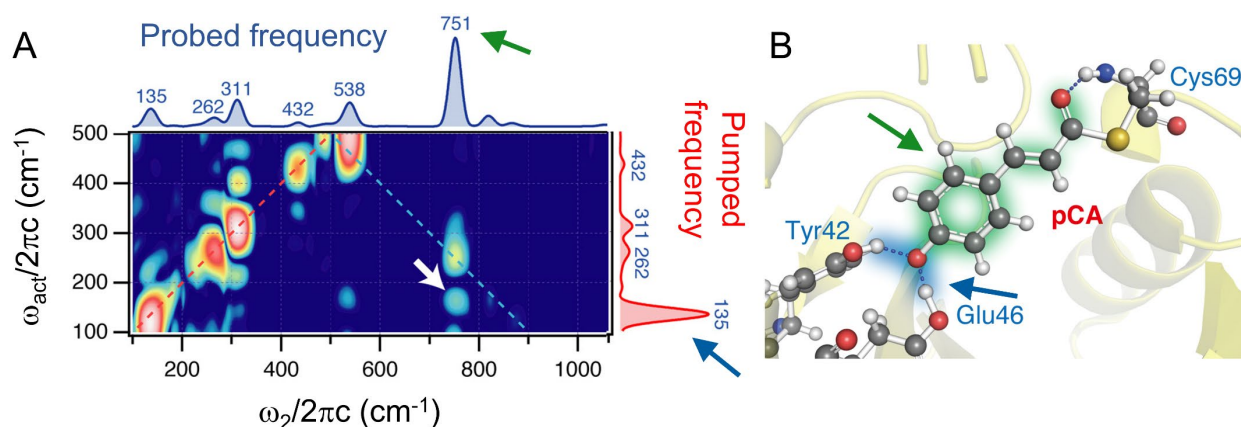
Figure D.2. (A) 2D-ISRS signal correlating wavepacket motions during t_{act} and t_2 for the pCA chromophore embedded in PYP. Diagonal features arise predominantly from coherence depletion pathways, while cross-peaks indicate couplings between wavepackets. (B) A schematic of PYP with the pCA chromophore and amino acid residues in the foreground. A white arrow in (A) indicates the crosspeak of interest in the report from Kuramochi and coworkers, which indicates coupling between the C-O stretch mode of pCA (green glow in B) and low-frequency intermolecular motions of the anchoring amino acid hydrogen bond network (blue glow in B). Figure adapted from Kuramochi, H. et al. *Sci. Adv.* **2019**, 5 (6), eaau4490.

Kuramochi and coworkers identified a cross-peak between the phenolic C-O stretch mode of pCA and low-frequency intermolecular motions of the anchoring amino acid hydrogen bond network. The green and blue glow within Figure D.2B illustrates the relevant atoms within PYP that participate in these coupled pCA (green) and hydrogen bond (blue) motions.

The presence of the cross-peak indicated in Figure D.2A was interpreted as evidence that anharmonic coupling between a pCA vibration and low-frequency motion of the hydrogen-bonded amino acids may underlie the pCA photoisomerization event in PYP. Considering that numerous peaks (diagonal and off-diagonal) in the 2D-ISRS spectrum shown in Figure D.2A were not able to be explained by Kuramochi and coworkers, the detailed picture of the potential energy surface (PES) that 2D-ISRS may afford appears to be obscured by complex and sensitive experimental signatures. Naturally, theoretical simulations based on key molecular models are indispensable in such situations, as has been repeatedly demonstrated by studies of 3rd-order quantum beats with 2DES.[107, 158, 160, 161, 187, 206] To the knowledge of the author, the first and only theoretical simulations for 2D-ISRS spectra were reported by Fumero and coworkers in 2020.[130] The quantum mechanical model developed by the authors includes three electronic states that are displaced in nuclear coordinate space and each dressed with vibrational modes *within the harmonic approximation*. Figure D.3A and D illustrates two cases within this model with differing Duschinsky rotation angles,[328] which is a well-known phenomenon that engenders mixing between excited-state vibrations (based on projections to the ground-state vibrations). Fumero and coworkers arrived at three main conclusions from this work: (1) Peaks in 2D-ISRS spectra are intricate even for the minimal displaced harmonic oscillator model; (2) 2D-ISRS is highly sensitive to Duschinsky rotations and resulting vibrational mixings; (3) All diagonal and off-diagonal peaks in 2D-ISRS

spectra should be describable to avoid misassignments of spectra to molecular models. Though thorough and insightful, the work from Fumero et. al., only scratches the surface of molecular models that are routinely used to rationalize signatures from 3rd-order optical spectroscopies.[308,160] Theoretical treatment of 2D-ISRS spectra for molecular aggregates have yet to be addressed in any capacity.

Model: Harmonic oscillator θ_D = Duschinsky rotation angle
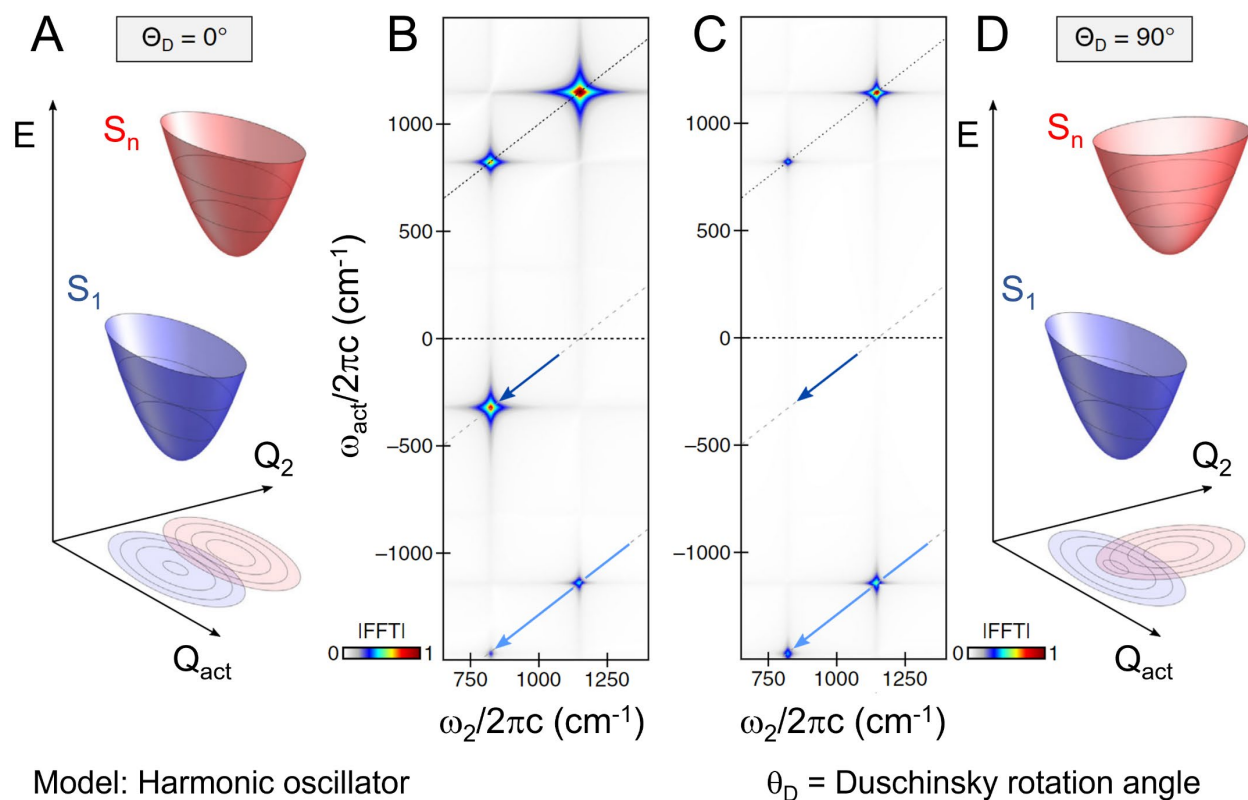
Figure D.3. Potential energy surfaces for displaced harmonic oscillator models with (A) zero and (D) 90° Duschinsky rotation angles, alongside the corresponding (B and C) simulated 2D-ISRS spectra. Figure adapted from Fumero, G. et. al., *Phys. Rev. X* **2020**, *10*, 011051.

D.5. Proposed Research

Theoretical simulations are of paramount importance to studies of ultrafast photochemistry.[107, 143, 160, 187] Over the past 15 years, widespread controversy[1, 16, 188, 352] surrounding the role of coherence in photosynthesis is attributable to interpretations of complex

spectroscopic signals *without* descriptive theories. It is therefore an opportune time to develop descriptive and far-reaching theories for 2D-ISRS spectra, with focus placed on physical interpretation of the 5th-order signals as well as guiding experimentation.

D.5.1. Phase 1 (year one)

As described in Section D.3, the proposed research is scaffolded into three phases. **During Phase 1**, our team will build upon and connect existing software packages to efficiently develop a Python-based 2D-ISRS simulation code. We will employ a similar sum-over-states approach as described by Fumero and coworkers, where the total 2D-ISRS signal is obtained by separately simulating and then combining all 5th-order Liouville pathways. We will formulate the 5th-order molecular response functions using Liouville pathways previously described.[363] One example pathway for 2D-ISRS of a three-state displaced harmonic oscillator is diagrammed in Figure D.4A,
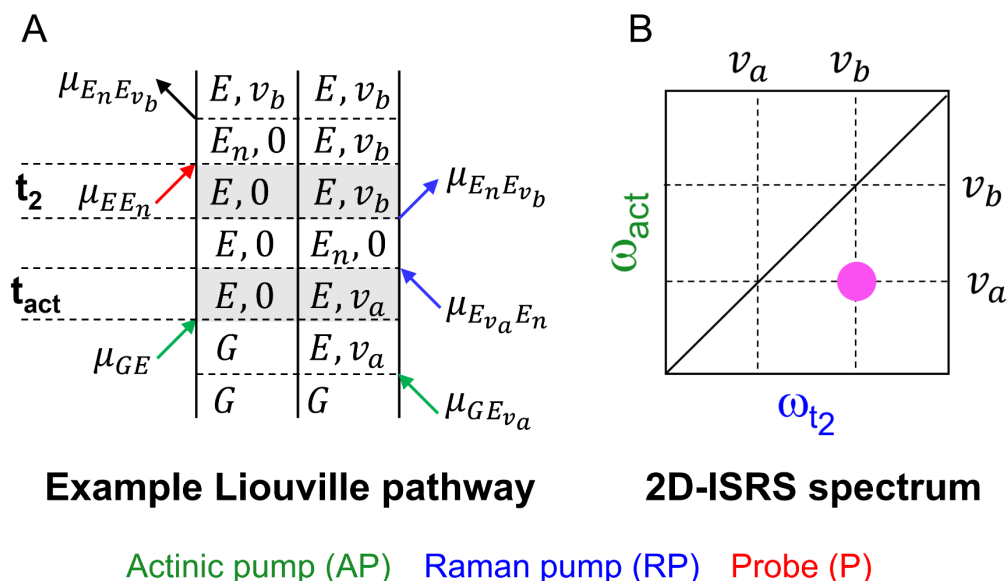
Figure D.4. (A) An example Liouville pathway for 2D-ISRS (corresponding to the WMEL diagram in Figure D.1.) and (B) the location of the corresponding cross-peak in the 2D-ISRS signal. Density matrix elements that are propagated through time in (A) are shaded gray.

where the two periods of time evolution (t_{act} and t_2) feature different off-diagonal density matrix elements and therefore lead to a cross-peak in the corresponding 2D-ISRS plot (Figure D.4B).

Python simulations of 2D-ISRS will first be performed on the harmonic oscillator model as outlined by Fumero and coworkers.[130] We will formulate the basis states using the occupation number representation, which enables the system Hamiltonian and transition dipole matrices to be easily formulated and tuned by reading the basis set of interest. A total of two time-delays are required (t_{act} and t_2) to simulate 2D-ISRS signals, which we expect to be computationally tractable as simulations of 2DES signals require three time dimensions.[152, 160] We will verify the accuracy of our simulations by direct comparison to results provided by Fumero and coworkers.[130]

To benchmark the computational costs of 2D-ISRS simulations, we will first treat system-bath interactions phenomenologically in Phase 1. Upon achieving efficient simulations with this approach, we will then incorporate system-bath interactions by interfacing our Python code with the *Quantum Toolbox in Python* (QuTip),[364] which is well-established and has been used recently to simulate ultrafast electron transfer dynamics along a two-dimensional potential energy surface.[164] We will first use the Redfield master equation module in QuTip, though several other methods are available if more or less accuracy (computational cost) is desired.

Even the minimal displaced harmonic oscillator Hamiltonian will necessitate high-dimensional basis sets, since all excited electronic states must be dressed with at least two vibrations. In turn, we anticipate obstacles involving computational resources will often arise. We are prepared with several contingency plans if 2D-ISRS simulations do not converge within the timescale of days. Approximations can be made on a model-to-model basis, as we will discuss further in the context of Phases 2 and 3. For the displaced harmonic oscillator simulations of Phase

1, the number of vibrational quanta for each mode can be tailored to lower the dimensionality of the Hamiltonian. Previous studies have also shown that a shifted vibrational basis can be used to maintain accuracy while lowering the number of vibrational quanta.[160] We additionally can parallelize 2D-ISRS simulations over a time delay, such as tact, and/or during the population removal procedure to enable significant reduction in computational times. For MATLAB-based simulations of 2DES signals, we have found that parallelization over only six cores speeds up removal of population dynamics by a factor of five (Figure D.5).
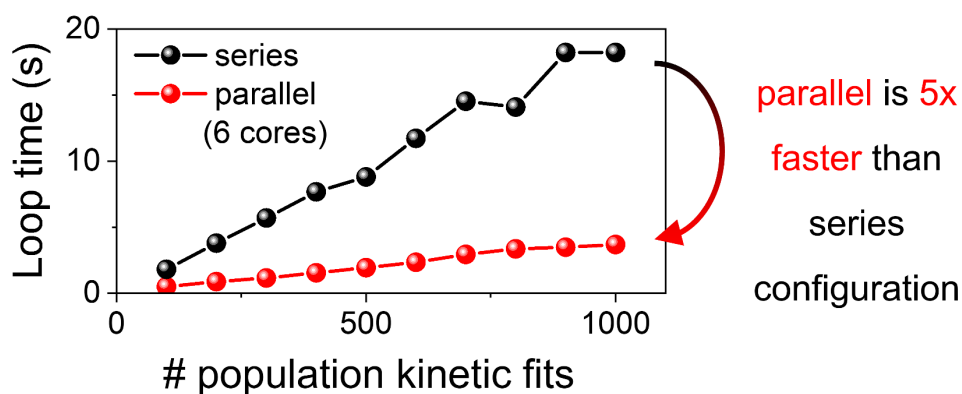
Figure D.5. Comparison of computational time required to separate population kinetics from wavepacket evolution using series and parallel configurations. Parallelization over six cores shortens the computational time by a factor of five compared to the series configuration.

D.5.2. Phase 2 (year one)

In Phase 2 of the proposed research, we will benchmark the accuracy of our 2D-ISRS simulations for model that include photochemical processes. We will simulate 2D-ISRS spectra for the *trans-to-cis* photoisomerization of pCA embedded in PYP and compare to published experimental measurements.[131] Previous studies have suggested that this process proceeds via low-frequency "trigger" and "guiding" vibrations,[365] which is supported by the cross-peak identified in experimental 2D-ISRS measurements of PYP (Figure D.2A).[131] We will therefore formulate a

model Hamiltonian for this system that contains five electronic states: one ground, two singlet (for both the *trans-* and *cis-*conformers), and two high-lying singlet states for each conformer. Each singly excited state will be dressed with one high- and two low-frequency modes, where one of the latter is treated as a non-Condon coordinate that triggers the coupling between the *trans* and *cis* states. The ground and high-lying singlet electronic states will be dressed with these modes, but with minimal vibrational quanta since the Boltzmann population and resonance condition of the Raman pump pulse limits the relevant vibrational levels for these states. The 5th-order response of this molecular Hamiltonian will be calculated with impulsive light-matter interactions based on the experimental resonance conditions. With population dynamics captured with the Redfield formalism in QuTip, we will simulate 2D-ISRS spectra for PYP and compare them to the experimental results, with specific focus on the presence, or lack thereof, of cross-peaks. The sum-over-states approach will allow us to isolate which Liouville pathways contribute to the cross-peaks; the importance of specific molecular parameters can be gauged by changing the nature of the vibrational Hamiltonian and examining the effect on the 2D-ISRS spectra.

We anticipate significant computational cost challenges in Phase 2 and, as such, plan to upgrade our 2D-ISRS Python code to run on a cluster managed either by the local academic institution or by governmental agencies, such as the United States Department of Energy. This approach will allow us to parallelize our simulations across tens to hundreds of computing cores.

D.5.3. Phase 3 (year two)

Due to the sensitivity of quantum beats in spectroscopic signals to properties of the molecular Hamiltonian,[15, 146, 154] there is broad and ongoing interest[152, 308, 366] in simulating 3rd-order quantum beat spectra across a wider range of physical models than are traditionally

explored[154] (i.e., beyond the HO and electronic dimer). **Phase Three of the proposed research** extends this motivation to the context of 5th-order 2D-ISRS. We will simulate 2D-ISRS spectra across a wide range of microscopic models, including those listed in Table D.1. in conjunction with specific questions to be answered.

Table D.1. Pairings of system Hamiltonians and system-bath interactions that will be examined in Phase Three, along with key questions to be addressed with each pairing.

System Hamiltonian	System-bath treatment	Key question(s)
Anharmonic multi-mode monomer	Phenomenological Redfield (QuTiP)	How do purely harmonic versus anharmonic couplings between vibrations manifest in 2D-ISRS spectra?
Single- and multi-mode Frenkel exciton (FE) dimer	Phenomenological	How do changes in the PES from transition dipole coupling (J_{Coul}) emerge in 2D-ISRS spectra? What salient features indicate H- versus J-aggregation regimes?
Single- and multi-mode Frenkel exciton dimer	Redfield (QuTiP)	How do the diagonal and anti-diagonal peak widths in 2D-ISRS inform upon vibrational relaxation processes?
Single- and multi-mode Frenkel exciton-charge-transfer (FECT) dimer	Phenomenological	How do short-range charge-transfer couplings (J_{CT}) manifest in 2D-ISRS? Can PES distortions by J_{Coul} versus J_{CT} be differentiated with 2D-ISRS?
Multi-mode FE trimer	Redfield (QuTiP)	How is the extent of energy transfer impacted by selective excitation or suppression of wavepackets along t_{act} and t_2?

The system and system-bath pairings listed in Table D.1 are intentionally designed to address questions that have historically challenged research endeavors using 3rd-order spectroscopy. The key questions seek to address aspects of the molecular potential energy surface (PES) that are often obscured or completely invisible to 3rd-order techniques, such as the strength of long-range Coulombic versus short-range charge-transfer couplings.[59, 65, 67] The final row of Table D.1 describes our aim to

characterize and quantify the impacts that wavepackets driven in 2D-ISRS experimentation have on the extent of photochemical reactions.

As the sum-over-states approach for simulating the molecular response is invariant to changes in molecular models, transitioning between 2D-ISRS simulations of two different models will require (1) formulating the new system, system-bath, and bath Hamiltonians and (2) defining the appropriate transition dipole matrices. In this fashion, the workflow for Phase Three is designed to accomplish high-throughput screening of molecular models that are ubiquitously used in ongoing research using 3rd-order spectroscopies. Answers to the questions posed in Table D.1 will guide both experimental and molecular design for future implementations of 2D-ISRS, ultimately saving an innumerable amount of research hours and taxpayer dollars.

The success of Phase 3 relies on sufficient computational resources and parallelization approaches, as will be established in Phase 2. It may be necessary to explore approximations that can simplify the molecular models and/or response simulations without losing significant information. For example, implementation of "*effective*" vibrational modes[305, 357] has been shown to reduce the dimensionality of multi-mode Hamiltonians while still capturing the emergent photophysics from coupled modes. Recent studies have also shown that selective truncation of basis sets[333] may also reduce cost while maintaining important information.

D.6. Summary and Conclusions

The extent to which numerous important photophysical phenomena emerge from a complex interplay of vibrational and electronic degrees of freedom is continuing to be realized. However, couplings between nuclear coordinates and, in turn, the precise functions of specific vibronic couplings in photochemistry remain elusive. Two-dimensional impulsive stimulated

Raman spectroscopy (2D-ISRS) is an emerging technique that provides a uniquely detailed picture of excited-state evolution along multidimensional potential energy surfaces. Nonetheless, the complexity of spectral features in 2D-ISRS experiments has already been shown to preclude accurate translation of 2D-ISRS spectra to chemical insight. The proposed research aims to develop efficient theoretical frameworks for 2D-ISRS, confirm accuracy through direct comparison to experimental data, and explore 2D-ISRS spectra across a wide range of molecular models to guide future experiments and molecular design. Timely development of theoretical methods alongside emerging experimental progress will expedite the realization of 2D-ISRS as a frontrunning probe of molecular dynamics.

Curriculum Vitae

Jonathan Schultz

jonathan.schultz@duke.edu
612-707-7054

EDUCATION

Northwestern University   Evanston, IL
Ph.D. in Chemistry   July 2022
Thesis: "*Revealing Vibronic Coupling and Coherence in Molecular Aggregates with Multidimensional Spectroscopy: Experiment and Theory*"

University of Minnesota-Twin Cities   Minneapolis, MN
Bachelor of Science in Chemical Engineering and B.S. in Chemistry   May 2017
GPA: 3.733, *cum laude*
Senior thesis: "*Nanoparticle Applications Spanning Enhanced Ultrafast Sensing and Groundwater Remediation*"

RESEARCH EXPERIENCE

Postdoctoral Researcher   July 2022-present
Duke University; Advisor: Prof. David N. Beratan
- Employ quantum dynamics simulations and density functional theory to reveal transport mechanisms in materials and biological systems

Ph.D. Researcher   July 2017-July 2022
Northwestern University; Advisors: Profs. Michael R. Wasielewski and Mark A. Ratner
- Used multidimensional optical and femtosecond Raman spectroscopies to investigate coherence phenomena in synthetic organic materials
- Performed original numerical simulations and density functional theory computations to rationalize experimental findings

Undergraduate Researcher   December 2015-May 2017
University of Minnesota Twin Cities; Advisor: Prof. Renee R. Frontiera
- Explored time-resolved plasmon dynamics for application in solar energy harvesting

Undergraduate Researcher   September 2014-December 2015
University of Minnesota Twin Cities; Advisor: Prof. R. Lee Penn
- Elucidated the dependence of iron oxide reactivity on foreign particles in simulated groundwater systems

NSF REU Student   May 2015-August 2015
Pennsylvania State University; Advisor: Prof. Benjamin J. Lear
- Discovered the effect of Fe_3O_4 nanoparticle size on the efficiency of thermal energy dissipation for use in tunable photothermal reactions

TEACHING EXPERIENCE

Northwestern Teaching Consultant   September 2021-July 2022
- Served as a feedback conduit between undergraduate students and course instructors by facilitating in-class reflections and assembling the outcomes into a final report

Teaching Certificate Program Participant   September 2021-June 2022
- Honed pedagogical values through specialized seminars, literature explorations, and development of an original course design

Graduate research mentor in the Wasielewski group   September 2018-July 2022
- Provided guidance and promote curiosity to graduate students through frequent discussions about research concepts, results, and directions
- Trained students on specialized laser instrumentation and computational methods through hands-on learning

Northwestern Graduate Teaching Fellow   May 2020-June 2021
- Facilitated a funded teaching project involving design and production of *research connection* films that place graduate research projects in the context of chemistry course concepts ([YouTube channel](#) and [website](#))
- Gathered statistical evidence that viewing the videos increased *conceptual understanding*, *contextual awareness*, and *interest in research opportunities* for undergraduate general chemistry students

Science Club mentor   September 2017-March 2020
- Taught groups of middle school students how to develop hypotheses, design experiments, and analyze results in weekly workshops throughout the academic year
- Guided students through independent research projects

CHEMunity mentor   September 2018-August 2021
- Assimilate incoming graduate students into doctoral studies and aid with the group selection process

Science in the classroom teacher   October 2019-March 2020
- Lead science experiments for 3rd and 4th grade students to teach the scientific method and inspire future involvement in science

Undergraduate and graduate research webinar speaker   April 2020
- Hosted a virtual presentation and discussion about graduate and undergraduate research opportunities for University of Minnesota undergraduate chemistry students

Chem 350 – Molecular Electronics lead TA   April 2019-May 2019
- Guided students through spectroscopic experiments, data analytics, and interpretation of results
- Awarded for excellence in student teaching based on undergraduate student feedback and consultation with chemistry faculty

Chem 132, 161, 162 – General Chemistry TA   September 2017-May 2018
- Led students through intro-level chemistry curriculum through weeklylaboratory experiments and recitations
- Provided student feedback at office hours and through graded reports

American Chemical Society Project SEED mentor   June 2016-August 2016
- Trained a visiting summer high school student in experimental and analytical research methods in the Penn lab
- Provided guidance for developing hypotheses and designing experiments

Chemists in the Library program mentor   January 2015-September 2016
- Traveled to underprivileged neighborhoods to introduce children and parents to basic principles of chemistry

STUDENTS MENTORED

Graduate Students

James O'Connor	Northwestern – Wasielewski group	2019-2022
Jeremy Fisher	Northwestern – Wasielewski group	2018-2022
Arnold Chan	Northwestern – Chen group	2018-2019
Jonah Greenberg	Northwestern – Gingrich group	2019-2020

High School Students

Xatziri Viveros	Washington Technology Magnet High School	2016

PUBLICATIONS

Online Publication List: Google Scholar | ORCID: 0000-0002-3386-5460 | LinkedIn
(*Corresponding Author; †Equal contribution)

14. Parker, K. A.; **Schultz, J. D**.; Singh, N.; Wasielewski, M. R.*; Beratan, D. N.* Mapping Simulated Two-Dimensional Spectra to Molecular Models Using Machine Learning. *J. Phys. Chem. Lett.* **2022**, doi.org/10.1021/acs.jpclett.2c01913

13. Kim, T.[†]; Lin, C.[†]; **Schultz, J. D**.; Young, R. M.; Wasielewski, M. R.* π-Stacking-Dependent Vibronic Couplings Drive Excited-State Dynamics in Perylenediimide Assemblies. *J. Am. Chem. Soc.* **2022**, *144 (25)*, 11386–11396

12. Lin, C.[†]; Kim, T.[†]; **Schultz, J. D**.; Young, R. M.; Wasielewski, M. R.* Accelerating symmetry-breaking charge separation in a perylenediimide trimer through a vibronically coherent dimer intermediate. *Nat. Chem*. **2022**, *14*, 786–793

11. **Schultz, J. D**.; Kim, T.; O'Connor, J. P.; Young, R. M.; Wasielewski, M. R.* Coupling between harmonic vibrations influences quantum beating signatures in two-dimensional electronic spectra. *J. Phys. Chem. C.* **2022**, *126 (1),* 120-131

10. Petrosko, S. H.; D. Coleman, B. D.; Drout, R. J.; **Schultz, J. D.**; Mirkin, C. A.* Spherical Nucleic Acids: Integrating Nanotechnology Concepts into General Chemistry Curricula. *J. Chem. Educ.* **2021***, 98 (10),* 3090–3099

9. Zhao, X.[†]; O'Connor, J. P.[†], **Schultz, J. D.**[†]; Bae, Y. J.; Lin, C.; Young, R. M.*; Wasielewski, M. R.* Temperature Tuning of Coherent Mixing between States Driving Singlet Fission in a Spiro-Fused Terrylenediimide Dimer. *J. Phys. Chem. B* **2021***, 125 (25),* 6945–6954

8. **Schultz, J. D.**[†]; Shin, J. Y.[†]; Chen, M.; O'Connor, J. P.; Young, R. M.; Ratner, M.A.; Wasielewski, M. R.* Influence of Vibronic Coupling on Ultrafast Singlet Fission in a Linear Terrylenediimide Dimer. *J. Am. Chem. Soc.* **2021***, 143 (4),* 2049–2058

7. Bae, Y. J.; Shimizu, D.; **Schultz, J. D**.; Kang, G.; Zhou, J.; Schatz, G. C.; Osuka,A.; Wasielewski, M. R.* Balancing Charge Transfer and Frenkel Exciton Coupling Leads to Excimer Formation in Molecular Dimers: Implications for Singlet Fission. *J. Phys. Chem. A* **2020***, 124 (41)*, 8478–8487

6. **Schultz, J. D**.; Coleman, A. F.; Mandal, A.; Ratner, M. A; Young, R. M.*; Wasielewski, M. R.* Steric Interactions Impact Vibronic and Vibrational Coherences in Perylenediimide Cyclophanes. *J. Phys. Chem. Lett.* **2019***, 10,* 7498-7504

5. Mandal, A.; **Schultz, J. D.**; Wu, Y.-L.; Coleman, A. F.; Young, R. M.*; Wasielewski, M. R.* Transient Two-Dimensional Electronic Spectroscopy: Coherent Dynamics at Arbitrary Times along the Reaction Coordinate. *J.Phys. Chem. Lett.* **2019**, *10*, 3509-3515

4. Phelan, B. T.[†]; **Schultz, J. D.**[†]; Zhang, J.; Huang, G.-J.; Young, R. M.*; Wasielewski, M. R.* Quantum Coherence in Ultrafast Photo-driven Charge Separation. *Faraday Discuss*. **2019**, *216*, 319-338.

3. Mandal, A.; Chen, M.; Foszcz, E. D.; **Schultz, J. D.**; Kearns, N. M.; Young, R.M.*; Zanni, M. T.; Wasielewski, M. R.* Two-Dimensional Electronic Spectroscopy Reveals Excitation Energy-Dependent State Mixing during Singlet Fission in a Terrylenediimide Dimer. *J. Am. Chem. Soc.* **2018**, *140*, 17907-17914

2. Johnson, R. J. G.; **Schultz, J. D.**; Lear, B. J.* Photothermal effectiveness of magnetite nanoparticles: Dependence upon particle size probed by experiment and simulation. *Molecules* **2018**, *23 (5),* 1234

1. Strehlau, J. H.; **Schultz, J. D.**; Vindedahl, A. M.; Arnold, W. A.; Penn, R. L.* Effect of nonreactive kaolinite on 4-chloronitrobenzene reduction by Fe(II) in goethite-kaolinite heterogeneous suspensions. *Environ. Sci.: Nano* **2017***, 4,* 325-334

HONORS AND AWARDS

Time-Resolved Vibrational Spectroscopy First-Place Poster Award	Sept. 2019
Northwestern University Donald E. Smith Teaching Award	May 2019
Northwestern University Chair's Fellowship	Apr. 2017
National Science Foundation Graduate Research Fellowship	Mar. 2017
Undergraduate Research Opportunity Scholarship	Apr. 2016 & Nov. 2014
252nd ACS PHYS Division Poster Award	Aug. 2016
Valspar Science & Engineering Student Scholarship	Apr. 2016
David A. and Merece H. Johnson Scholarship	Apr. 2016
Lee Ponto Scholarship	Apr. 2016
Undergraduate Research Opportunity Program Scholarship	Apr. 2016, Nov. 2014
Fridley Scholarship	Mar. 2016, Mar. 2015
Barry Goldwater Scholarship Nominee	Dec. 2015
Sigma Xi Rising Stars Award	Mar. 2015
University of Minnesota Presidential Academic Scholarship	Sept. 2013

ACADEMIC PRESENTATIONS

"*Vibronic coupling drives ultrafast singlet fission in a linear terrylenediimide dimer*," Invited virtual presentation, American Chemical Society National Meeting 2021; August 23, 2021

"*Unveiling Coherence with Two-Dimensional Electronic Spectroscopy*," Invited virtual presentation, Center for Molecular Quantum Transduction; January 21, 2021

"*Vibronic Coupling in Ultrafast Organic Photophysics*," Invited virtual presentation, University of Minnesota Twin Cities; April 24, 2020

Steric Interactions Impact Vibronic and Vibrational Coherences in Perylenediimide Cyclophanes," Time-Resolved Vibrational Spectroscopy 2019; Auckland, NZ, September 9 and 10, 2019

"*Time-resolved Surface-Enhanced Raman Spectroscopy*," Richard P. Van Duyne Symposium; Minneapolis, MN, September 2016

"*Time-resolved Surface-Enhanced Raman Spectroscopy*," ACS National Meeting, PHYS Poster Symposium; Philadelphia, PA, August 24, 2016

"*Time-resolved Surface-Enhanced Raman Spectroscopy*," UMN Summer Research Poster Expo; University of Minnesota, Minneapolis, MN, August 11, 2016

"*Size Effect of Fe_3O_4 Nanoparticles on Photothermal Decomposition of Polypropylene Carbonate*," REU Symposium; Penn State University, University Park, PA, July 30, 2015

"*Reactivity of Iron Oxides in Complex Groundwater Systems*," UMTC Undergraduate Poster Symposium; University of Minnesota, Minneapolis, MN, April 22, 2015

WORKSHOPS FACILITATED

Developing a Productive and Welcoming Lab Environment   Sept. 2020
Turning Your Recitation into a Learning Discussion   Sept. 2020
Giving Effective Advice: Targeting Feedback Toward Student Growth   Mar. 2021
Transforming the Traditional Lecture into an Engaged Learning Tool   Apr. 2021

ACADEMIC ACTIVITIES

Science communication team leader   May 2021-present
- Collaborated with a team of graduate researchers to produce accessible, scientific articles for the general public (online link)

Diversity, Equity, and Inclusion statement committee   June 2021
- Contributed to the writing and ratification of the DEI statement for the Center for Synthesizing Quantum Coherence (online link)